9 April 2010 | $10

Science

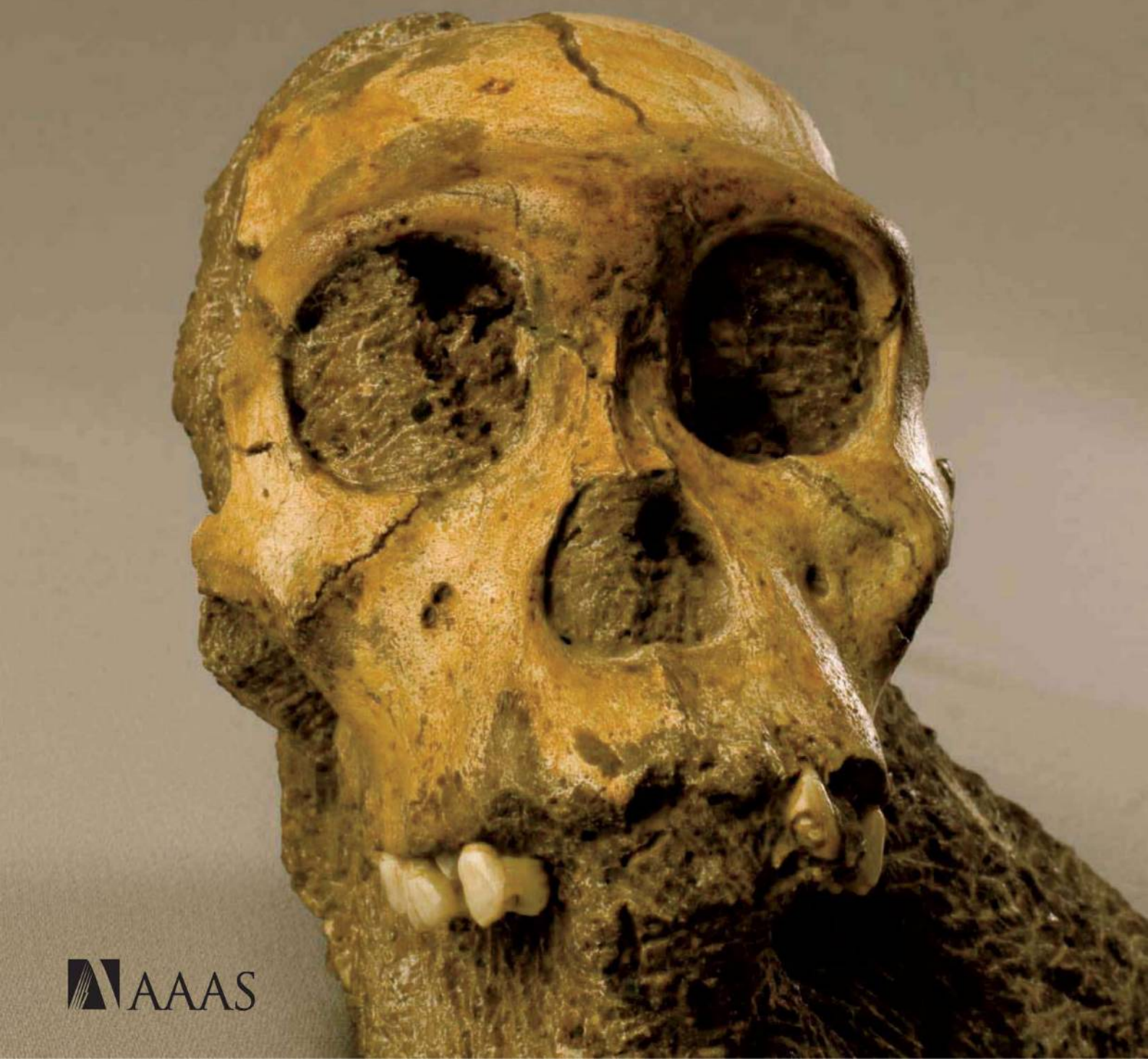

AAAS

Analyzing genetic differences

Genotyping sample and assay technologies by QIAGEN

Rely on trusted automated and manual workflow solutions for:

- **Sample collection and stabilization**
- **Genomic DNA purification, DNA storage, and whole genome amplification**
- **PCR amplification and automated QIAxcel® fragment analysis**
- **HRM® and Pyrosequencing® detection**

Making improvements in life possible — www.qiagen.com

QIAGEN®

Sample & Assay Technologies

cell sciences®

ultra pure cytokines

Produced in barley, these proteins are animal, bacterial, and viral free, and are ultra pure, with extremely low endotoxin.

www.cellsciences.com

Cell Sciences offers innovative, unique growth factors and hard-to-produce recombinant proteins, bypassing the use of bacterial or animal cell systems. These ultra pure proteins contain no contamination from other growth factors and negligible amounts of endotoxin.

Background: barley endosperm

The host organism, barley, with its specialized endosperm storage tissue, provides many unique features including proficient protein machinery, with eukaryotic folding, and a distinct route for long-term protein protection and storage. A biochemically inert environment, void of endotoxins, low protease activity and secondary metabolite content, and a simple protein profile, aid in downstream processing. Barley has also a G.R.A.S. (generally recognized as safe) status from the FDA.

Cell Sciences ultra pure growth factors and cytokines are produced for use in basic and applied medical scientific research, cell culture media and diagnostics.

- serum free
- animal, bacterial & viral free
- extremely low endotoxin (<0.005 ng/ug)
- highly biologically active
- easier regulatory clearance
- perfect for cell culture, drug development, stem cell research, animal research
- for use in all *in vitro* cellular studies
- for use in all *in vivo* animal studies

Ultra pure cytokines & growth factors

FGF1, human
FGF2, human
FLT3 ligand, human
GCSF, human
IFNA2, human
IFN gamma, human
IGF1, human
IL1-alpha, human
IL2, human
IL3, human
IL4, human
IL5, human
IL6, human
IL7, human
IL9, human
IL16, human
IL22, human
KGF, human
M-CSF, human
NRG1/HRG beta 2, human
SCF, mouse
SF20/IL25, human
TNF-alpha, human
TNF-beta, human
VEGF121, human
VEGF165, human

CELL SCIENCES INC • 480 NEPONSET STREET, BUILDING 12A, CANTON, MA 02021 • INFO@CELLSCIENCES.COM

TOLL FREE: (888) 769-1246 • TEL: (781) 828-0610 • FAX: (781) 828-0542 • WEB WWW.CELLSCIENCES.COM

GE Healthcare
Life Sciences

Inspired Ägain

Who better to draw inspiration for the new ÄKTA™ avant system than from customers using the 30,000 ÄKTA systems already in use around the world? Well, you spoke and we listened. The new ÄKTA avant system for process development is faster — enabling quicker insights. It minimizes the chance of error, even while working at higher speeds. And it allows for direct, reliable scalability. At GE Healthcare, our focus is on helping scientists achieve even more, faster. It's a commitment we have in our genes. And all this is backed by the service, support, and investment in the future that being part of GE can bring.

Want to know more? Why not talk with us today. Visit **www.gelifesciences.com/aktaavant**

I **ÄKTA** I Amersham I Biacore I IN Cell Analyzer I Whatman I GE Service I

The New ÄKTA avant

imagination at work

First published September 2009
GE Healthcare Bio-Sciences AB, Björkgatan 30, 751 84 Uppsala, Sweden
GE12-09

EDITORIAL

NEWS OF THE WEEK

NEWS FOCUS

LETTERS

BOOKS *ET AL.*

POLICY FORUM

PERSPECTIVES

CONTENTS continued >>

page 160

page 175

COVER

Cranium of *Australopithecus sediba* (specimen UW88-50), a new species of australopith found at the Malapa site in South Africa. Two partial skeletons, dated to about 1.9 million years ago, share many derived features with *Homo* and may thus shed light on the evolution of that genus. See the related Research Articles on pages 195 and 205 and the related News story on page 154.

Photo: Brett Eloff, courtesy of Lee Berger and the University of the Witwatersrand

DEPARTMENTS

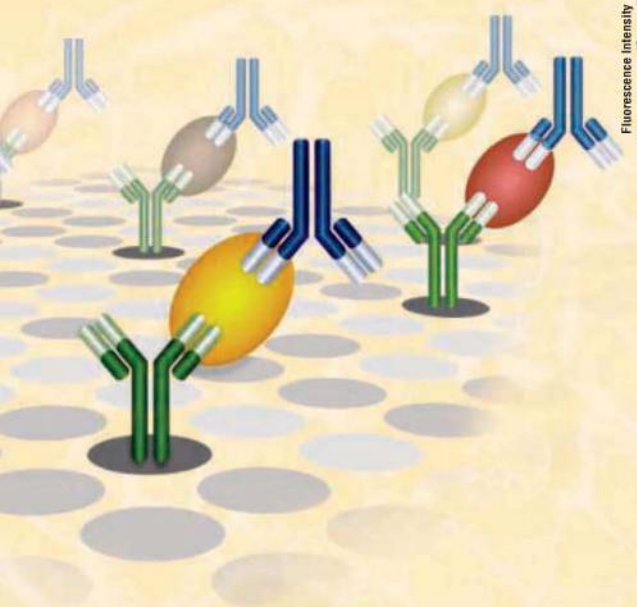

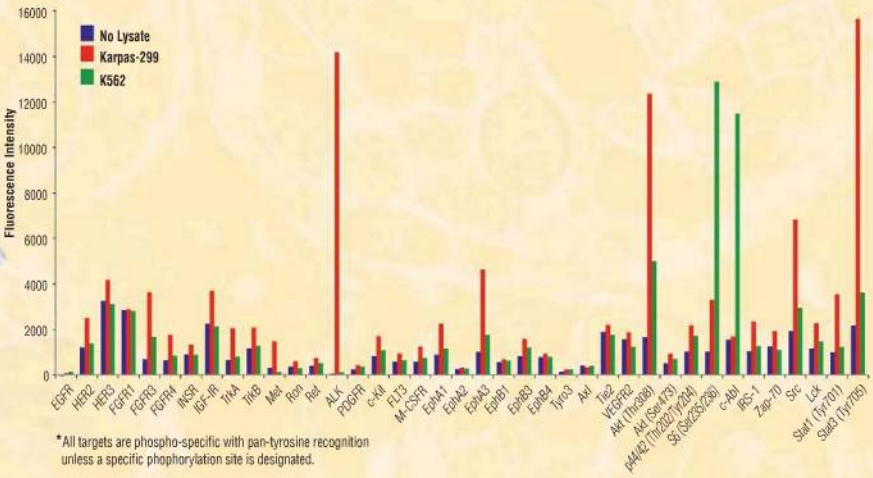

*All targets are phospho-specific with pan-tyrosine recognition unless a specific phophorylation site is designated.

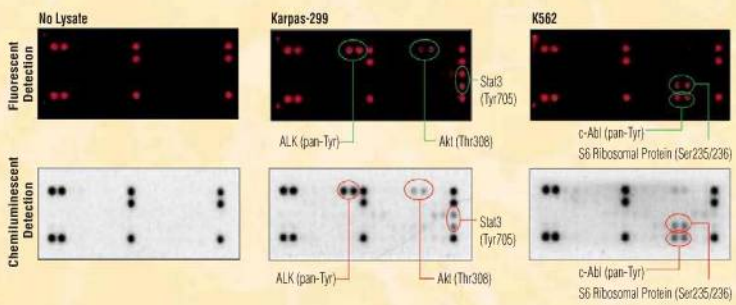

New PathScan® RTK Signaling Antibody Array Kits

...from Cell Signaling Technology®

New PathScan® RTK Signaling Antibody Array Kits are slide-based antibody arrays founded on the sandwich immunoassay principle.

- Arrays are produced and optimized in-house, incorporating the highest quality antibodies and ensuring results you can trust.
- Arrays allow the analysis of phosphorylation levels of 39 proteins per assay, saving valuable time and reagents.
- Arrays are designed to detect receptor tyrosine kinases (RTKs) and key downstream signaling molecules, allowing the most comprehensive readout of signaling events.
- Technical support is provided by the same scientists who developed and produce the product, which translates into a thorough, fast and accurate response.
- Chemiluminescent detection kit offers convenient and easy detection without specialized instrumentation.
- Fluorescent detection kit offers a broad linear range for the most accurate quantification.

Unparalleled product quality, validation and technical support.

Above: Analysis of Karpas-299 and K562 cells using the PathScan® RTK Signaling Antibody Array Kits reveals various phosphorylated RTKs and signaling nodes. The fluorescent readout and corresponding quantification were obtained using PathScan® RTK Signaling Antibody Array Kit (Fluorescent Readout) #7949 (middle and upper panels). The chemiluminescent readout was obtained using PathScan® RTK Signaling Antibody Array Kit (Chemiluminescent Readout) #7982 (lower panel).

Visit us at AACR Booth #1211

Meet our product scientists who will answer questions and provide in-depth insight into some of our most innovative products and services.

Featuring PathScan® RTK Signaling Antibody Array Kits

Monday, April 19th, 9 a.m. - 5 p.m.

for more information visit...

www.cellsignal.com

China www.cst-c.com.cn | **Europe** www.cellsignal.eu | **Japan** www.cstj.co.jp

Cell Signaling TECHNOLOGY®

U.S.: 978-867-2300 | **E-mail:** info@cellsignal.com

REVIEW

RESEARCH ARTICLES

REPORTS

CONTENTS continued >>

pages 180 & 216

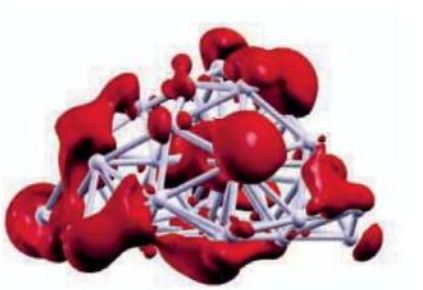

page 224

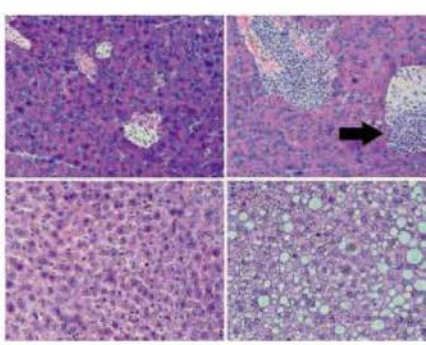

pages 179 & 228

"The fastest separations and the gold standard method.

That's **electroforward** thinking."

Next-generation precast gels. No special buffers required.

Introducing long shelf life Mini-PROTEAN™ TGX (**T**ris-**G**lycine e**X**tended) Gels from Bio-Rad. The innovative TGX formulation delivers consistent, linear separation without the need for expensive, specialized buffers.

Get results faster with:

- Run times as short as 15 minutes
- Transfer in as little as 15 minutes
- New bottom-opening cassette design for faster setup and less handling for downstream applications

Gel with us at **www.miniprotean.com**.

Research. Together.

SCIENCEONLINE

SCIENCEXPRESS
www.sciencexpress.org

Recent Hot-Spot Volcanism on Venus from VIRTIS Emissivity Data
S. E. Smrekar et al.
Satellite observations suggest that Venus is a geologically active planet.
10.1126/science.1186785

Coadministration of a Tumor-Penetrating Peptide Enhances the Efficacy of Cancer Drugs
K. N. Sugahara et al.
Anticancer drugs are more effective in mice when they are injected with a peptide that helps the drugs penetrate the tumor.
10.1126/science.1183057

Five-Vertebrate ChIP-seq Reveals the Evolutionary Dynamics of Transcription Factor Binding
D. Schmidt et al.
Binding of two liver-specific transcription factors in several vertebrate species reveals complex regulatory evolution.
10.1126/science.1186176

Reconstitution of Outer Membrane Protein Assembly from Purified Components
C. L. Hagan et al.
Assembly of a β-barrel membrane protein in a cell-free system does not require added energy.
10.1126/science.1188919

SCIENCENOW
www.sciencenow.org
Highlights From Our Daily News Coverage

Mass of the Common Quark Finally Nailed Down
Physicists measure fundamental bits of nuclear matter to within 1.5%.

Notorious Drug Stanches Bleeding
Thalidomide eases symptoms of rare blood vessel disease.

East Coast Winds Would Support a Stable Power Grid
Regionally interconnected turbines could supply power for much of the country.

SCIENCESIGNALING
www.sciencesignaling.org
The Signal Transduction Knowledge Environment

RESEARCH ARTICLE: Stabilization of VEGFR2 Signaling by Cerebral Cavernous Malformation 3 Is Critical for Vascular Development
Y. He et al.
CCM3, which is associated with inherited cerebrovascular defects, prevents ligand-mediated degradation of a receptor involved in blood vessel formation.

RESEARCH ARTICLE: AAA+ Proteins RUVBL1 and RUVBL2 Coordinate PIKK Activity and Function in Nonsense-Mediated mRNA Decay
N. Izumi et al.
Two ATPases regulate molecular complexes that ensure genome integrity and accurate gene expression.

RESEARCH ARTICLE: Regulation of G Protein–Coupled Receptor Signaling—Specific Dominant-Negative Effects of Melanocortin 2 Receptor Accessory Protein 2
J. A. Sebag and P. M. Hinkle
Two homologous accessory proteins exert opposing effects on the responsiveness of the melanocortin 2 receptor to the hormone ACTH.

PERSPECTIVE: A Trojan Horse for Parkinson's Disease
Y. Hu and Y. Tong
Inhibition of the kinase activity of LRRK2 may be neuroprotective.

SCIENCECAREERS
www.sciencecareers.org/career_magazine
Free Career Resources for Scientists

Scientists Embrace Openness
C. Wald
Some scientists go to great lengths to make everything they do in the lab transparent.

All in the Details: Careers in Regulatory Science
N. Volkers
Regulations at every step of drug development mean jobs for regulatory scientists.

From Researcher to Outreacher
L. Laursen
A career in outreach makes connecting science with the public a full-time job.

SCIENCETRANSLATIONAL MEDICINE
www.sciencetranslationalmedicine.org
Integrating Medicine and Science

PERSPECTIVE: Rod-Derived Cone Viability Factor for Treating Blinding Diseases—From Clinic to Redox Signaling
T. Léveillard and J.-A. Sahel
A neuroprotective protein may be broadly useful for treating degenerative retinal diseases caused by mutations in a number of different genes.

COMMENTARY: Training Translators for Smart Drug Discovery
C. Skarke and G. A. FitzGerald
Human capital is a rate-limiting constraint in translational medicine and therapeutics.

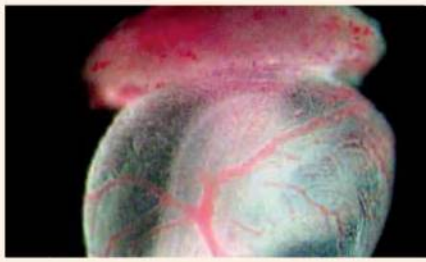

SCIENCESIGNALING
Building blood vessels.

RESEARCH ARTICLE: Klf15 Deficiency Is a Molecular Link Between Heart Failure and Aortic Aneurysm Formation
S. M. Haldar et al.
Klf15 deficiency causes cardiomyopathy and aortopathy by a shared mechanism and defines a novel therapeutic pathway.

RESEARCH ARTICLE: Airway PI3K Pathway Activation Is an Early and Reversible Event in Lung Cancer Development
A. M. Gustafson et al.
A cancer-associated signaling pathway is reversibly activated in the normal airways of smokers before they develop lung cancer.

SCIENCEPODCAST
www.sciencemag.org/multimedia/podcast
Free Weekly Show
Download the 9 April *Science* Podcast to hear about a newly discovered species of hominid, the evolution of behavior, a tournament of social learning strategies, and more.

SCIENCEINSIDER
news.sciencemag.org/scienceinsider
Science Policy News and Analysis

SCIENCE (ISSN 0036-8075) is published weekly on Friday, except the last week in December, by the American Association for the Advancement of Science, 1200 New York Avenue, NW, Washington, DC 20005. Periodicals Mail postage (publication No. 484460) paid at Washington, DC, and additional mailing offices.

Domestic individual membership and subscription (51 issues): $146 ($74 allocated to subscription). Domestic institutional subscription (51 issues): $910; Foreign postage extra: Mexico, Caribbean (surface mail) $55; other countries (air assist delivery) $85. First class, airmail, student, and emeritus rates on request. Canadian rates with GST available upon request, GST #1254 88122. Publications Mail Agreement Number 1069624. **Printed in the U.S.A.**

Change of address: Allow 4 weeks, giving old and new addresses and 8-digit account number. **Postmaster:** Send change of address to AAAS, P.O. Box 96178, Washington, DC 20090–6178. **Single-copy sales:** $10.00 current issue, $15.00 back issue prepaid includes surface postage; bulk rates on request. The identification code for *Science* is 0036-8075. *Science* is indexed in the *Reader's Guide to Periodical Literature* and in several specialized indexes.

AAAS
ADVANCING SCIENCE, SERVING SOCIETY

CREDIT: YUN HE/YALE UNIVERSITY

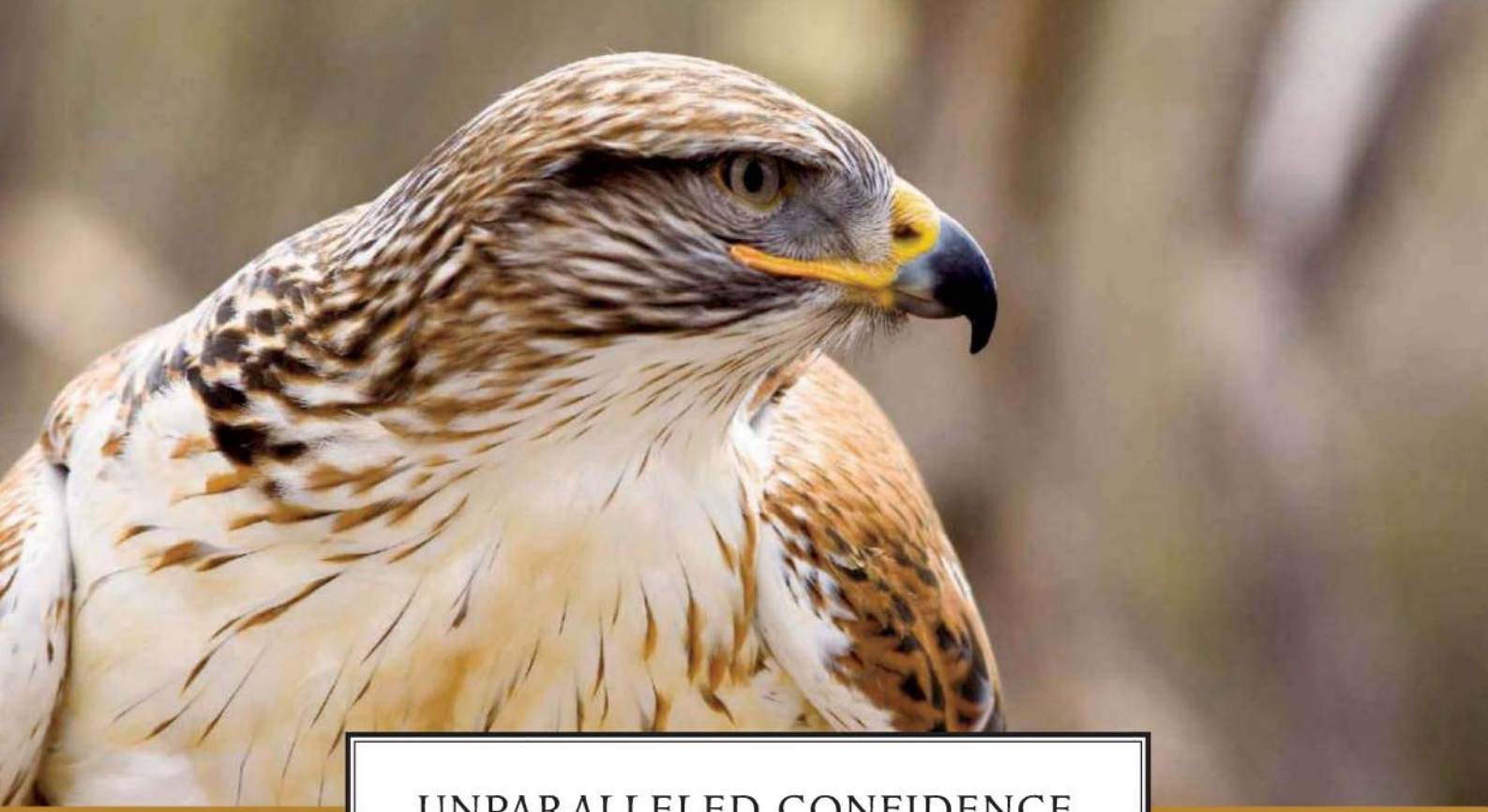

UNPARALLELED CONFIDENCE

PCR Reagents

There are already enough variables in PCR, don't let polymerase performance be one of them. Choose from one of the largest selections of polymerases for PCR applications from the leader in enzyme technology and bring unparalleled confidence to your experiments.

Not all PCR polymerases are created equal

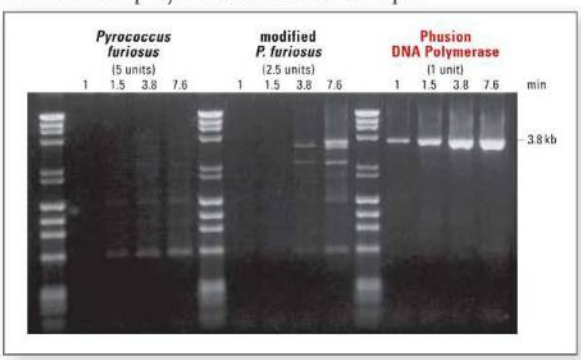

Amplification of a 3.8 kb fragment from human beta globin gene clearly illustrates the extreme speed and robustness offered by using Phusion DNA Polymerase.

Phusion is a registered trademark of Finnzymes Oy.

NEB has the polymerase for your application:

- **Routine**
- **Hot start**
- **Fast**
- **High-fidelity**
- **Long or difficult templates**
- **High throughput**
- **Extraction-free PCR**
- **Master Mixes**

Visit confidentPCR.com to learn more, and to find PCR-related special offers.

CELEBRATING 35 YEARS

NEW ENGLAND BioLabs® Inc.
enabling technologies in the life sciences

Like Father, Like Mother, Like Child >>

Transcriptional regulation is mediated by chromatin structure, which may affect the binding of transcription factors, but the extent of how individual-to-individual genetic variation affects such regulation is not well understood. **Kasowski *et al.*** (p. 232, published online 18 March) investigated the binding of two transcription factors across the genomes of human individuals and one chimpanzee. Transcription factor binding was associated with genomic features such as nucleotide variation, insertions and deletions, and copy number variation. Thus, genomic sequence variation affects transcription factor binding and may explain expression difference among individuals. **McDaniell *et al.*** (p. 235, published online 18 March) provide a genome-wide catalog of variation in chromatin and transcription factor binding in two parent-child trios of European and African ancestry. Up to 10% of active chromatin binding sites were specific to a set of individuals and were often inherited. Furthermore, variation in active chromatin sites showed heritable allele-specific correlation with variation in gene expression.

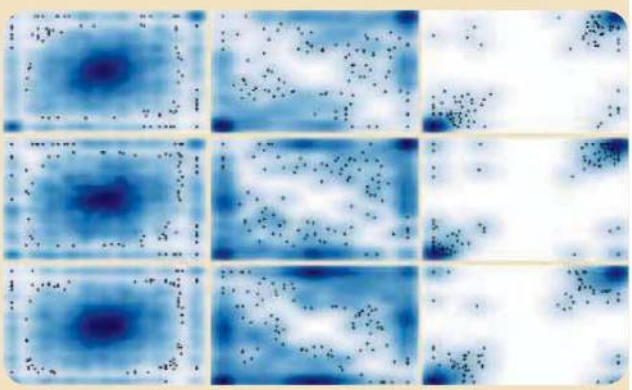

CREDIT (TOP TO BOTTOM): MCDANIELL *ET AL.*; SHEPS *ET AL.*

Ultrafast Imaging

Optical microscopy is generally limited in resolution by the wavelength of light incident on the substrate. Because these wavelengths, even in the ultraviolet, are on the order of hundreds of nanometers, electron beams have long been used instead to probe structural detail at the smallest scale. While offering exceptional spatial resolution, electrons repel one another and so cannot be compressed in time as easily as a pulse of light. Electron microscopy has thus traditionally been a comparatively static characterization method. **Zewail** (p. 187) reviews recent technological developments in stripping down the electron pulses used for imaging that have been able to introduce time resolution of trillionths of a second to this spatially precise technique. Local transformations ranging from graphite film oscillations to iron phase transitions have been tracked in this manner.

From *Australopithecus* to *Homo*

Our genus *Homo* is thought to have evolved a little more than 2 million years ago from the earlier hominid *Australopithecus*. But there are few fossils that provide detailed information on this transition. **Berger *et al.*** (p. 195; see the cover) now describe two partial skeletons, including most of the skull, pelvis, and ankle, of a new species of *Australopithecus* that are informative. The skeletons were found in a cave in South Africa encased in sediments dated by **Dirks *et al.*** (p. 205) to about 1.8 to 1.9 million years ago. The fossils share many derived features with the earliest *Homo* species, including in its pelvis and smaller teeth, and imply that the transition to *Homo* was in stages.

It Pays to Be a Copy Cat

Does it pay to copy what others do? **Rendell *et al.*** (p. 208) elected to copy Robert Axelrod's 1979 tournament in which strategies for playing the iterated prisoner's dilemma game were pitted against each other until an overall winner emerged—the tit-for-tat strategy. In the 2008 tournament, 100 social learning strategies designed to cope with a changing environment competed against each other; the winning strategy involved sampling the behaviors of other players periodically, rather than exploring the environment alone.

Heat Flow in Graphene

Unsupported graphene sheets show exceptional thermal transport properties, but are these properties maintained when a graphene sheet is in contact with a substrate? **Seol *et al.*** (p. 213; see the Perspective by **Prasher**) measured the thermal conductivity of graphene supported on silicon dioxide and found that, while the conductivity was considerably lower than that of free-standing graphene, it was still greater than that of metals such as copper. A theoretical model suggested that the out-of-plane flexing vibrations of the graphene play a key role in thermal transport. Thus, graphene may help in applications such as conducting heat away from electronic circuits.

Mussel Fibers

While it is possible to make strong fibers or threads from organic materials, most suffer from high wear abrasion. Marine mussels attach themselves to rocky seashores using a series of byssal threads. Despite the constant rubbing caused by the motion of the tides, the threads show high wear resistance. **Harrington *et al.*** (p. 216, published online 4 March; see the Perspective by **Messersmith**) now find that the threads are protected by a proteinaceous outer cuticle that is rich in the amino acid 3,4-dihydroxyphenylalanine (dopa), which is known to be a strong adhesive. The cuticle is also rich in metal ions, primarily Fe^{3+}. The dopa-metal cross-links helped to form the tough outer coating.

CO_2 Lends a Hand

Solvent plays a complex and multifaceted role in facilitating charge transfer events. One obstacle to understanding its influence is that solvent molecules are in constant motion; just teasing out their arrangement in space at the point in time when an electron hops from one substrate to another is often a great challenge. **Sheps *et al.*** (p. 220; published online 4 March) have studied a highly simplified prototype system, in which a single CO_2 molecule coordinates, as a solvent might, to an IBr^- ion in the gas phase. A combination of ultrafast photoelectron spectroscopy and theoretical simulations was applied that suggests that even this solitary interaction is sufficient to induce electron transfer from iodide to bromine during a dissociation reaction. Energy channeled through CO_2-bending vibrations promoted formation of $I(CO_2)$ and Br^-.

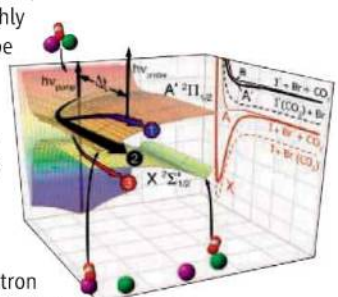

Continued on page 135

www.454.com

GS Junior Sequencing System

The Next Big Thing in Sequencing *is small.*

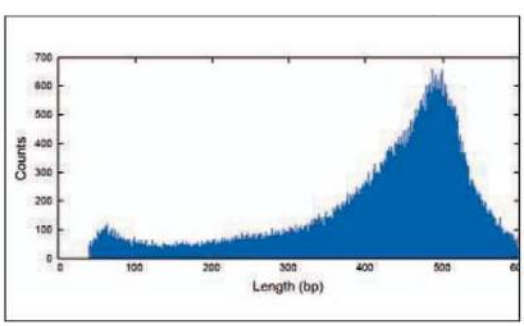

Figure 1: Example Read Length Distribution of 100,000 reads from *E. coli* K-12 (genome size approximately 4.5 Mb), from a single GS Junior System run.

Bring the power, performance, speed, and long reads of the GS FLX Titanium chemistry to your benchtop with the newest addition to the Roche genome sequencing portfolio – the **GS Junior Sequencing System**.

- **Make the most of your sequencing projects with our 400- to 500-base-pair read lengths (Figure 1).**
- **Benefit from established technology that has enabled hundreds of peer-reviewed publications.**
- **Accelerate your next discovery using the system's comprehensive suite of dedicated data analysis software.**

For complete information on the GS Junior System and all of the Roche sequencing solutions, visit ***www.gsjunior.com*** or contact your local Roche representative today.

For life science research only.
Not for use in diagnostic procedures.

454 SEQUENCING

Roche Diagnostics GmbH
Roche Applied Science
Werk Penzberg
82372 Penzberg, Germany

Roche

Continued from page 133

Silver Cluster Catalysts for Propylene Oxide

The formation of ethylene oxide—in which an oxygen atom bridges the double bond of ethylene—can be made directly and efficiently from ethylene and oxygen with the aid of silver catalysts (typically comprising a small silver cluster on aluminum oxide). Similar approaches are not so successful for making propylene oxide—an important starting material for polyurethane plastics, which are made from chlorinated intermediates. **Lei *et al.*** (p. 224) report that silver trimers, Ag_3, deposited on alumina are active for direct propylene oxide formation at low temperatures with only a low level of formation of CO_2 by-product, unlike larger particles that form from these clusters at higher temperatures. Density functional calculations suggest that the open-shell nature of the clusters accounts for the improved reactivity.

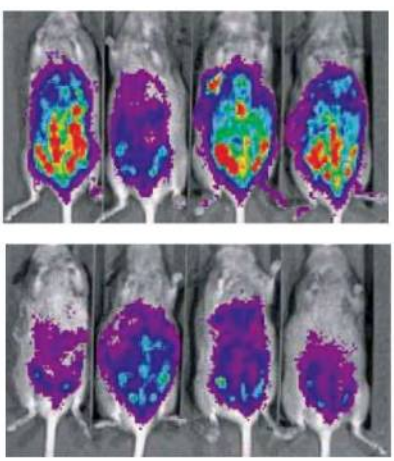

Speedy TCR Transgenic Mouse Manufacture

T cell receptor (TCR) transgenic mice are one of the most useful and ubiquitous tools of the immunologist. This is because the majority of T cells that develop in these mice express T cell receptors with known antigen specificity, and thus the mice can be used to study antigen-specific immune responses. The downside of TCR transgenic mice is that they can be difficult and time-consuming to generate and the antigen specificities of their T cells are often not physiologically relevant. **Kirak *et al.*** (p. 243) now describe the use of somatic cell nuclear transfer to create TCR transgenic mice with specificity for antigens known to be important in the immune response against the parasite *Toxoplasma gondii*. This method generates mice with greater ease and speed than conventional TCR transgenic mice and can be applied to generate mice with T cells specific to antigens from a variety of infectious diseases.

Debugging Metabolic Disease

Obesity, now officially recognized as an epidemic in many developed nations, is a key component of "metabolic syndrome," an array of metabolic disturbances that increase an individual's risk of developing diabetes and heart disease. The rise in obesity rates has been largely attributed to the growing imbalance between food intake and energy expenditure, but recent provocative work has suggested a possible link between obesity and the composition of microbes residing within the gut. **Vijay-Kumar *et al.*** (p. 228, published online 4 March; see the Perspective by **Sandoval and Seeley**) now find that mutant mice deficient in a component of the innate immune system (which defends the body against microbial pathogens) develop hallmark features of metabolic syndrome, accompanied by changes in gut microbiota. Notably, transfer of gut microbiota from the mutant mice to wild-type mice conferred several features of metabolic syndrome to the recipients. Thus, the development of metabolic syndrome may indeed be influenced by gut microbes that are regulated by the innate immune system.

Arsenic on the Fingers

Arsenic, an ancient drug used in traditional Chinese medicine, has attracted wide interest because it has therapeutic activity in patients with acute promyelocytic leukemia (APL). The drug acts by promoting degradation of an oncogenic protein, PML-RARα, a fusion protein containing sequences from the PML zinc finger protein and retinoic acid receptor α, which is found specifically in APL cells and helps drive their growth. **Zhang *et al.*** (p. 240; see the Perspective by **Kogan**) now explain how arsenic initiates the molecular events leading to PML-RARα degradation. Arsenic was found to bind directly to cysteine residues within zinc finger domains of PML. Arsenic binding then induced oligomerization of PML, which in turn enhanced its association with an enzyme that helps catalyze SUMOylation, a posttranslational modification that can target proteins for degradation.

CREDIT: KIRAK *ET AL.*

What is your taste?

BGI'S GENOMICS BAR

华大基因 BGI

tech@genomics.cn
www.genomics.cn
86-755-25273395

Would 128 Illumina HiSeq 2000 Sequencing Systems, 500 bioinformaticians and the use of cutting-edge software programs developed by BGI satisfy your taste?

One of the world's biggest genome centers is looking for collaborators!

Arthur D. Levinson has been at Genentech (South San Francisco, CA) since 1980, was its chief executive officer from 1995 to 2009, and is now the company's chairman.

Cancer Therapy Reform

LAST MONTH, THE U.S. FOOD AND DRUG ADMINISTRATION (FDA) ANNOUNCED THAT IT PLANS to draft new guidelines for testing and approving the use of multidrug treatments for diseases. For cancer treatment, the need for this approach and its attendant guidelines are based on an advanced understanding of the disease that has emerged from 30 years of research. If we are to achieve breakthrough cancer therapies, current FDA regulations must change.

An extensive characterization of the altered signaling pathways in cancer cells has spurred the development of targeted pharmaceutical agents that disrupt individual aberrant pathways. This strategy is predicated on preclinical evidence that the malignant properties of tumors depend on such pathway alterations. Examples of effective targeted agents include imatinib (Gleevec), which targets the enzyme c-Abl in chronic myelogenous leukemia, and trastuzumab (Herceptin), which targets the protein HER2 in certain breast cancers.*

In the best cases, targeted agents have changed the natural history of the diseases they were designed to treat. However, too often, the clinical benefit has been modest, if not disappointing. This lack of efficacy is increasingly explained by our current understanding of biological mechanisms. A cell decides whether to proliferate, differentiate, remain in a resting state, or die depending on the output from signaling networks that are characterized by pathway redundancies and cross-talk. These features can overcome the effect of single-agent interventions. For example, inhibitors of the enzyme mitogen-activated protein kinase kinase (MEK) have proven disappointing as single agents against pancreatic and non–small-cell lung cancer, despite frequent MEK pathway activation in these cancers. Mouse models have shown that combining a MEK inhibitor with an agent that targets part of another signaling pathway [phosphoinositide 3-kinase (PI3K)] can result in substantial tumor regression by inhibiting parallel signaling pathways. Other potential drug combination approaches to enhance efficacy and prevent rapid development of resistance include targeting different points of the same signaling pathway with different drugs or using drugs that target the same altered protein but in different ways.

Current regulatory burdens confound attempts to develop two new molecular entities (NMEs) as a combination therapy. The "combination rule" of the FDA's Code of Federal Regulations was designed for therapies that use fixed-dose combinations (drugs combined into one physical form), but it also applies to non–fixed-dose combinations of drugs. The contribution of each drug to the combination product must be determined for regulatory approval. Hence, large multi-arm, factorial-designed phase III clinical trials are required to provide statistical proof that the combination product is superior to standard-of-care therapy and to each drug administered separately. This has been acceptable for drugs that treat non–life-threatening diseases, such as hypertension, but it is less acceptable for diseases such as late-stage cancer, where treatment with potentially ineffective therapies should be kept to a minimum.

The FDA's willingness to devise guidelines that examine the totality of data (clinical and nonclinical) when assessing the contribution of each NME to an effective combination, without requiring statistical superiority for the combination over each single drug, is welcome news and will probably spur more collaboration between companies to develop these novel combinations. The FDA's recent announcement of a new initiative (in partnership with the U.S. National Institutes of Health) to accelerate the process from scientific discovery to the availability of new therapies is also good news. I urge the FDA to expedite the development of new approaches that will enable efficient clinical evaluation and potential approval of the combination of two NMEs to treat cancer, while maintaining appropriate standards to ensure patient safety. It is time for regulatory science to catch up with basic science in the quest for breakthrough cancer therapies for the patients who desperately need them.

– Arthur D. Levinson

10.1126/science.1189749

*Genentech produces Herceptin and is developing inhibitors of MEK (GDC-0973) and PI3K (GDC-0941 and GDC-0980).

DOES YOUR FINANCIAL GUIDANCE MAKE THE GRADE?

Bring your total financial picture into focus with Fidelity.

It takes a deep understanding of both personal investing and retirement planning to give higher education professionals like you the full picture. We'll guide you with the benefit of over 60 years of experience to help you create a more complete plan for your goals. Why settle for less?

Expect More—and Get It Free with Fidelity

One-on-one Consultation	To review both your workplace and personal savings as part of a comprehensive plan
Investment Help	To choose low-cost investments, from bonds and annuities to stocks and mutual funds
Professional Guidance*	From retirement income planning to charitable giving and estate planning

NEVER SETTLE

SCHEDULE YOUR COMPLIMENTARY CONSULTATION TODAY.

800.823.0172
FIDELITY.COM/RESERVE

Turn here℠

Fidelity INVESTMENTS

Before investing, consider the funds' investment objectives, risks, charges and expenses. Contact Fidelity for a prospectus containing this information. Read it carefully.

Products or services mentioned above may not be applicable depending on your particular financial situation. Restrictions may apply. Please contact Fidelity for additional information.

*Although it may be provided in one-on-one consultations, guidance provided by Fidelity is educational in nature, is not individualized, and is not intended to serve as the primary or sole basis for your investment or tax-planning decisions.

545542

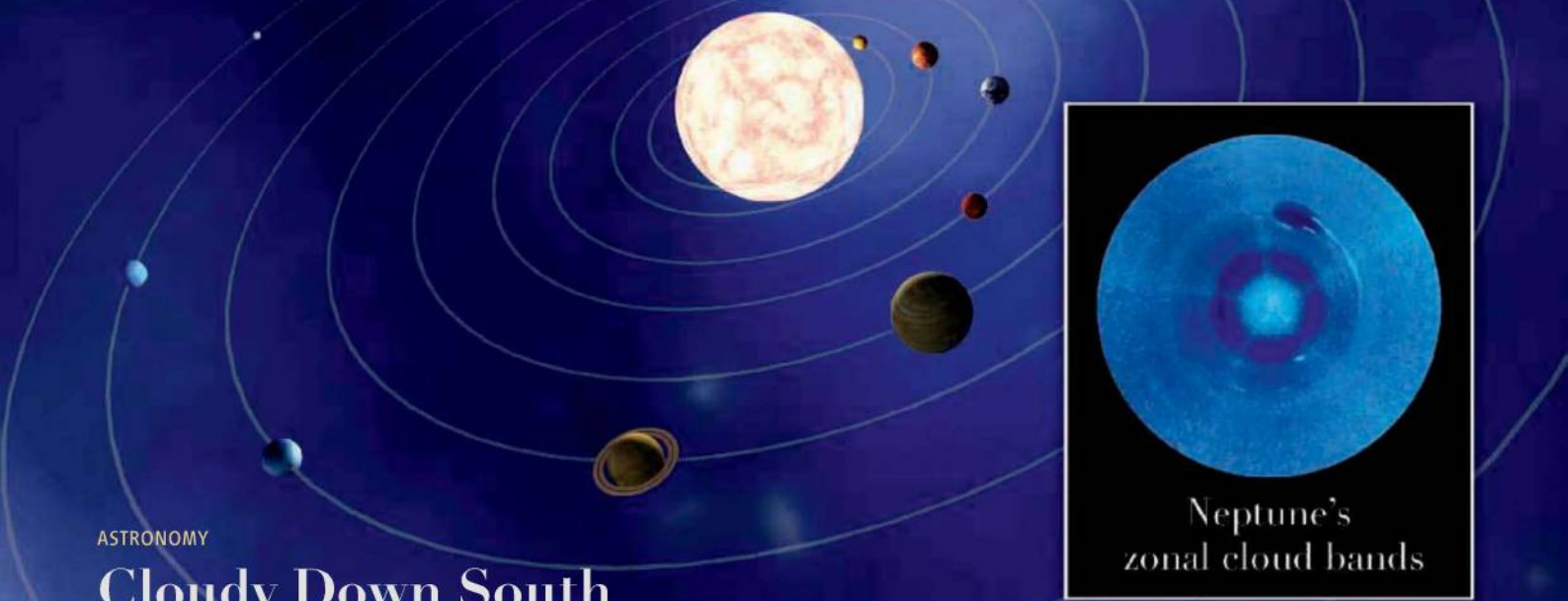

ASTRONOMY

Cloudy Down South

Neptune receives much less radiation from the Sun than either Jupiter or Saturn. Like these two large planets, though, it has a meteorologically active atmosphere, with clouds, storms and possibly a global circulation pattern. Most of Neptune's clouds evolve on a time scale of hours. One cloud, however, has appeared to persist since at least 1989, when it was first detected by the spacecraft Voyager 2. This cloud is located within a few degrees of the south pole, where the troposphere is known to be warmer and where, by analogy with Saturn's south polar environment, researchers suspect that a vortex may exist. Using the Keck Telescope in Hawaii, Luszcz-Cook *et al.* observed Neptune's south pole in the near-infrared, thereby probing the upper and lower troposphere. Images taken over 3 days in July 2007 show the south polar cloud splitting in two and then coming together again. The altitude observed is consistent with cloud formation due to upwelling and condensation of methane gas. Thus, rather than representing a single stable cloud, the bright feature observed by Voyager marks a site of persistent cloud activity, which may be related to a Neptunian south polar vortex and an organized circulation pattern. — MJC

Icarus 10.1016/j.icarus.2010.03.007 (2010).

CREDITS (TOP TO BOTTOM): ISTOCKPHOTO (INSET) VOYAGER PROJECT/NASA; VALLET *ET AL.*, *PNAS* **107**, 5124 (2010)

IMMUNOLOGY

Watching of the Sentinels

Natural killer T cells (NKTs) are a subset of unconventional T cells. They express a limited T cell receptor repertoire and recognize lipid (rather than protein) antigens presented by the nonclassical major histocompatability complex CD1d. Although NKTs have been implicated in antimicrobial, inflammatory, and autoimmune responses, their dynamics during an immune response and the antigen-presenting cell (APC) populations that mediate their activation are not well defined.

Lee *et al.* have visualize d the response of NKTs in the liver to infection with *Borrelia burgdorferi* (the causal agent of Lyme's disease), whereas Barral *et al.* followed NKTs in lymph nodes in response to particulate lipid antigens. In mice infected with *Borrelia*, they proliferated rapidly and produced cytokines; in response to antigen, NKTs slowed down and formed long-lasting contacts with their relevant APCs, which in both cases were macrophages. In the liver, sinusoid-localized Kupffer cells activated NKTs, whereas lymph node NKTs were activated by a subset of macrophages located in the subcapsular sinus. — KLM

Nat. Immunol. **11**, 295; 303 (2010).

CANCER

Runaway Remodeling

Bone metastases are a common feature of many advanced-stage cancers and are among the most painful and debilitating complications. Tumor cells alter bone tissue by unbalancing the bone remodeling process that occurs naturally throughout adult life. In the context of osteolytic (bone-destroying) metastases, this disruption occurs through an enhanced production of osteoclasts—the cells that resorb bone—or through a suppressed production of osteoblasts—the cells that build bone. The molecular mechanism by which tumor cells alter the abundance of these cell types is the subject of two recent studies using mouse models of cancer.

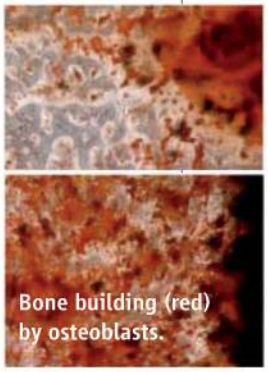

Bone building (red) by osteoblasts.

Vallet *et al.* found that multiple myeloma cells cause bone marrow stromal cells to secrete activin A, which is a member of the transforming growth factor–β family of cytokines and which inhibits the differentiation of cells into osteoblasts. In independent work on breast cancer–associated bone disease, Min *et al.* found that Tie2, a receptor tyrosine kinase that is expressed at high levels in breast cancer, is also expressed in bone marrow cells that normally differentiate into osteoclasts and is in fact required for osteoclast production. Inhibition of either activin A or Tie2 signaling with soluble decoy receptors led to the amelioration of osteolytic bone disease, suggesting that these two molecules may be useful therapeutic targets. — PAK

Proc. Natl. Acad. Sci. U.S.A. **107**, 5124 (2010); *Cancer Res.* **70**, 2819 (2010).

Continued on page 141

RNAi screening lies at the beginning of discovery research. MISSION® RNAi offers the most validated and comprehensive screening tools available including lentiviral, shRNA, siRNA, miRNA, and esiRNA libraries and panels. Spend your time on discovery with streamlined workflows and greater confidence in your results. MISSION RNAi technologies – release your screening potential.

wherebiobegins.com/biosilencing

SIGMA-ALDRICH®

SIGMA® Life Science Where bio begins™

Continued from page 139

BIOMEDICINE

Liquid Biopsy

Certain cancers spread through the migration of circulating tumor cells (CTCs). Once shed from either primary or metastatic sources into the bloodstream, these cells can become lodged in bone, lungs, brain, or liver. The rarity of the cells, at concentrations of one per billion blood cells, has hindered their use in quantitative evaluations. Stott *et al.* have now developed an automated imaging system for prostate cancer CTCs. The cells are isolated with a microfluidic chip that extracts them from the leukocytes and red blood cells. They are then stained to highlight the nuclei and prostrate-specific antigens (PSAs), as the distance between the two markers can be used to identify and verify each whole cell.

Significant PSA heterogeneity was detected across the CTCs taken from a range of patients, and there was also considerable variability in the rate of decline of CTCs after surgery. However, the authors were able to track significant decreases in CTCs in patients with metastatic cancer after hormone therapy, with only modest decreases in CTCs after chemotherapy. The authors envision scaling up this automated method for tracking the migration of CTCs. — MSL

Sci. Transl. Med. **2**, 25ra23 (2010).

ECOLOGY

No Plant Is an Island

Most land plants form mutualistic associations with fungi, in which the partners rely on each other for mineral and nutrient exchange, as well as for the endowment of beneficial properties such as heat tolerance and protection from pests. These arbuscular mycorrhizal fungi (AMFs) in turn host at least two types of endosymbiotic prokaryotes: a β-proteobacterium and a distinctive coccoid Gram-positive entity. Naumann *et al.* have found the latter in the cytoplasm of many AMF lineages, and sequence analysis shows that despite possessing a cell wall, these bacterium-like organisms cluster with the *Mollicutes*. These bacteria appear to have been associated with AMFs since the Devonian, 400 million years ago; for this partnership to have persisted so long, there must be significant fitness benefits. Furthermore, this association is an intimate one as the bacteria live in the fungal cytoplasm with no discernable membrane enclosing them. This discovery raises several questions about the evolution of key bacterial and fungal lineages, as well as the evolution of plants and the functional nature of this ecologically key suite of symbioses. — CA

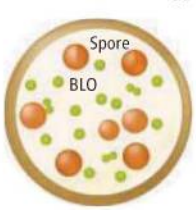

CREDIT: NAUMANN *ET AL.*, *ISME J.* 10.1038/ISMEJ.2010.21 (2010)

ISME J. 10.1038/ismej.2010.21 (2010).

PHYSIOLOGY

Old and Fat

Adipose tissue secretes the hormone leptin, which regulates food intake and energy use. The loss of leptin signaling through its receptor can cause obesity and diabetes in mice and is associated with obesity in humans, too. The leptin receptor signals in part via three tyrosine residues that become phosphorylated after leptin binds. The effects are complex because other signaling components bind to the phosphorylated residues: One attracts the JAK2 protein kinase and STAT transcription factors, and a second (Tyr^{985}) appears to transduce both positive and negative signals, and also inhibits the receptor itself. Tyr^{985} is bound by the SOCS3 protein, which inhibits the activation of STAT3, and by the protein tyrosine phosphatase SHP2, which antagonizes JAK-STAT signaling. You *et al.* engineered mice to block phosphorylation of Tyr^{985}. When young, these animals were leaner than controls and showed increased responses to leptin; however, as the animals aged, the opposite was true. They ate more than controls and expended less energy. Obesity induced by a high-fat diet was also more severe in the older mutant mice than in controls. Hence, Tyr^{985} may be important for the normal adjustment of metabolic control as mice age. — LBR

Mol. Cell. Biol. **30**, 1650 (2010).

GEOLOGY

Alpine Growth Spurts

Traditionally, the formation of metamorphic rock was thought to occur slowly and steadily, driven by the gradual rates of tectonics or conductive heat flow. However, recent research has shown that more rapid transformation is possible when fluid movement through the crust is involved. Pollington and Baxter show that this probably occurred in the Austrian Alps, where metamorphism broadly reflects gradual continental collision and tectonic exhumation of deep seated rocks. The authors used the Sm-Nd isotopic system to date garnets from old cores to young rims, with improved accuracy. The garnets overall grew during about 8 million years, but the individual dates show that most of the growth actually occurred during two short pulses. The first, which may have lasted less than a few hundred thousand years, seems to reflect the infiltration of fluids during the beginning of exhumation. — BH

Earth Planet. Sci. Lett. **293**, 63 (2010).

FROM START TO FINISH, ENDNOTE X3 KEEPS YOUR RESEARCH ON THE FAST TRACK.

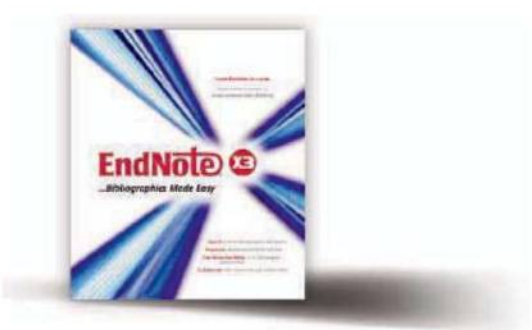

Download your free demo or buy online today
www.endnote.com

Out of the blocks, EndNote enables you to set your cites on discovery with connectivity to high quality data from the Web of Knowledge℠ and thousands of online library catalogs worldwide.

EndNote X3 is meters ahead with a personal EndNote Web account that simplifies collaboration and formats bibliographies in over 3,900 styles. EndNote Web also organizes publication lists for the free ResearcherID author community so you can view your personal citation metrics, complete with dynamic Times Cited detail from the Web of Knowledge. It doesn't stop there. You'll find new speed in Cite While You Write™ for Apple® Pages '09, Microsoft® Word and OpenOffice.org Writer 3 for Windows. Keep the lead in your race to discovery with integrated informaton solutions from Thomson Reuters.

Visit booth #1244 at AACR 2010 and put Thomson Reuters on your reference team today! You may even win your own copy of EndNote.

800-722-1227 • 760-438-5526 • rs.info@thomson.com

THOMSON REUTERS

High Efficiency Gene Transfer into Stem Cells

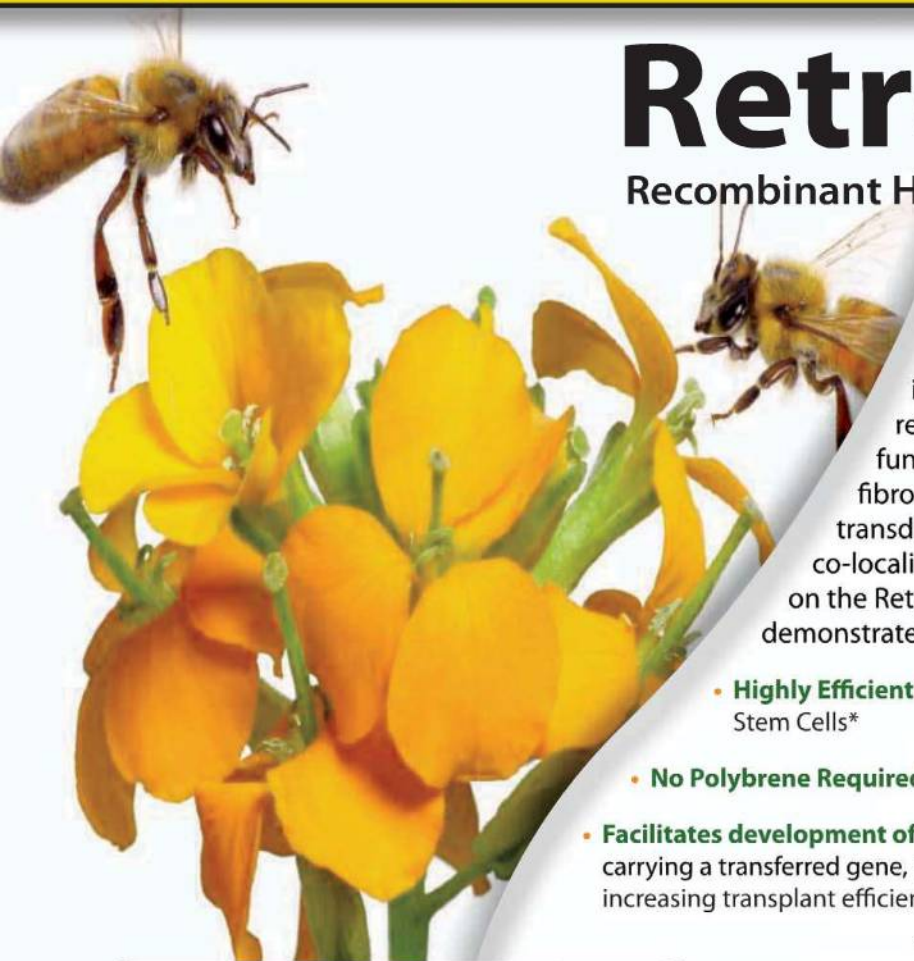

RetroNectin®

Recombinant Human Fibronectin Fragment

Use of RetroNectin®-based gene transduction protocols dramatically enhances the efficiency of retrovirus or lentivirus-mediated gene transfer into mammalian cells. RetroNectin® is a recombinant polypeptide consisting of three functional domains derived from the human fibronectin. RetroNectin®'s enhancement of gene transduction efficiency is hypothetically due to co-localization of retroviral particles and target cells on the RetroNectin® molecule. Recent experiments demonstrate Retronectin®'s efficacy on stem cells.

- **Highly Efficient Retroviral or Lentiviral Gene Transfer** into Stem Cells*
- **No Polybrene Required** for Transduction
- **Facilitates development of innovative protocols** for proliferation of cells carrying a transferred gene, maintaining the function of the cells, and increasing transplant efficiency

* carrying VLA-4 and/or VLA-5 cell surface receptors

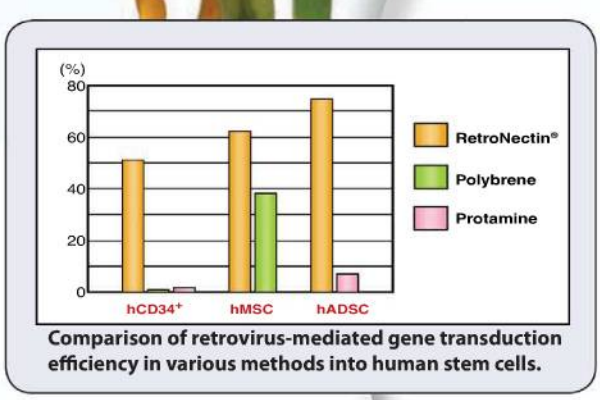

Comparison of retrovirus-mediated gene transduction efficiency in various methods into human stem cells.

RetroNectin® enables and enhances retrovirus-mediated gene transfer into stem cells which express lower levels of GALV envelope receptor, such as hCD34+ or hADSC

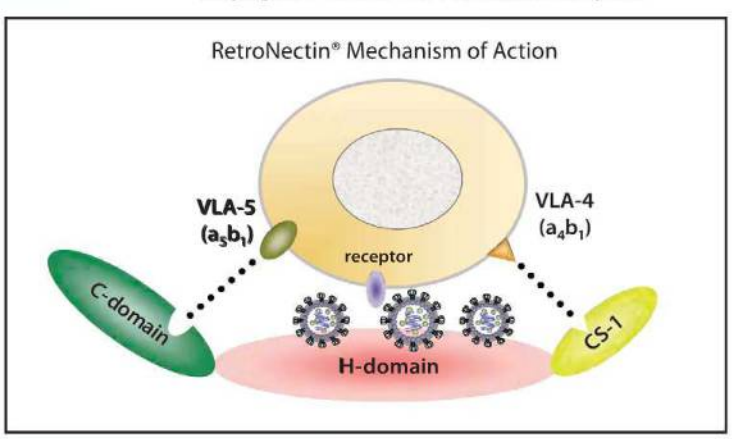

TaKaRa

For more information
www.takarabio.com

Japan:
Takara Bio Inc.
+81 77 543 7247
www.takara-bio.com

Europe:
Takara Bio Europe S.A.S.
+33 1 3904 6880
www.takara-bio.eu

USA:
Clontech Laboratories, Inc
A Takara Bio Company
888-251-6618
www.takara-bio.us

China:
Takara Biotechnology
(Dalian) Co., Ltd.
+86 411 8764 1681
www.takara.com.cn

Korea:
Takara Korea
Biomedical Inc.
+82 2 2081 2525
www.takara.co.kr

www.sciencemag.org

Science

1200 New York Avenue, NW
Washington, DC 20005
Editorial: 202-326-6550, FAX 202-289-7562
News: 202-326-6581, FAX 202-371-9227
Bateman House, 82-88 Hills Road
Cambridge, UK CB2 1LQ
+44 (0) 1223 326500, FAX +44 (0) 1223 326501

Subscription Services For change of address, missing issues, new orders and renewals, and payment questions: 866-434-AAAS (2227) or 202-326-6417, FAX 202-842-1065. Mailing addresses: AAAS, P.O. Box 96178, Washington, DC 20090-6178 or AAAS Member Services, 1200 New York Avenue, NW, Washington, DC 20005

Institutional Site Licenses please call 202-326-6755 for any questions or information

Reprints: Author Inquiries 800-635-7181
Commercial Inquiries 803-359-4578

Permissions 202-326-7074, FAX 202-682-0816

Member Benefits AAAS/Barnes&Noble.com bookstore www.aaas.org/bn; AAAS Online Store www.apisource.com/aaas/ code MKB6; AAAS Travels: Betchart Expeditions 800-252-4910; Apple Store www.apple.com/eppstore/aaas; Bank of America MasterCard 1-800-833-6262 priority code FAA3YU; Cold Spring Harbor Laboratory Press Publications www.cshlpress.com/affiliates/aaas.htm; GEICO Auto Insurance www.geico.com/landingpage/go51.htm?logo=17624; Hertz 800-654-2200 CDP#343457; Office Depot https://bsd.officedepot.com/portalLogin.do; Seabury & Smith Life Insurance 800-424-9883; Subaru VIP Program 202-326-6417; VIP Moving Services www.vipmayflower.com/domestic/index.html; Other Benefits: AAAS Member Services 202-326-6417 or www.aaasmember.org.

science_editors@aaas.org	(for general editorial queries)
science_letters@aaas.org	(for queries about letters)
science_reviews@aaas.org	(for returning manuscript reviews)
science_bookrevs@aaas.org	(for book review queries)

Published by the American Association for the Advancement of Science (AAAS), *Science* serves its readers as a forum for the presentation and discussion of important issues related to the advancement of science, including the presentation of minority or conflicting points of view, rather than by publishing only material on which a consensus has been reached. Accordingly, all articles published in *Science*—including editorials, news and comment, and book reviews—are signed and reflect the individual views of the authors and not official points of view adopted by AAAS or the institutions with which the authors are affiliated.

AAAS was founded in 1848 and incorporated in 1874. Its mission is to advance science, engineering, and innovation throughout the world for the benefit of all people. The goals of the association are to: enhance communication among scientists, engineers, and the public; promote and defend the integrity of science and its use; strengthen support for the science and technology enterprise; provide a voice for science on societal issues; promote the responsible use of science in public policy; strengthen and diversify the science and technology workforce; foster education in science and technology for everyone; increase public engagement with science and technology; and advance international cooperation in science.

Information for Authors
See pages 352 and 353 of the 15 January 2010 issue or access www.sciencemag.org/about/authors

EDITOR-IN-CHIEF **Bruce Alberts**
EXECUTIVE EDITOR **Monica M. Bradford** NEWS EDITOR **Colin Norman**
MANAGING EDITOR, RESEARCH JOURNALS **Katrina L. Kelner**
DEPUTY EDITORS **R. Brooks Hanson, Barbara R. Jasny, Andrew M. Sugden**

Editorial senior editors/commentary Lisa D. Chong, Brad Wible; **senior editors** Gilbert J. Chin, Pamela J. Hines, Paula A. Kiberstis (Boston), Marc S. Lavine (Toronto), Beverly A. Purnell, L. Bryan Ray, Guy Riddihough, H. Jesse Smith, Phillip D. Szuromi (Tennessee), Valda Vinson, Jake S. Yeston; **associate editors** Kristen L. Mueller, Jelena Stajic, Nicholas S. Wigginton, Laura M. Zahn; **research associate** Alexis Wynne Mogul; **book review editor** Sherman J. Suter; **associate letters editor** Jennifer Sills; **editorial manager** Cara Tate; **senior copy editors** Jeffrey E. Cook, Cynthia Howe, Harry Jach, Lauren Kmec, Barbara P. Ordway, Trista Wagoner; **copy editor** Chris Filiatreau; **editorial coordinators** Carolyn Kyle, Beverly Shields; **publications assistants** Ramatoulaye Diop, Joi S. Granger, Emily Guise, Jeffrey Hearn, Michael Hicks, Lisa Johnson, Scott Miller, Jerry Richardson, Jennifer A. Seibert, Brian White, Anita Wynn; **editorial assistants** Emily C. Horton, Patricia M. Moore, Miriam Weinberg; **executive assistants** Alison Crawford; **administrative support** Maryrose Madrid; **editorial fellow** Melissa R. McCartney

Editorial director, web & new media Stewart Wills; **senior web editor** Tara S. Marathe; **web editor** Robert Frederick; **web development manager** Martyn Green; **web developer** Andrew Whitesell

News deputy news editors Robert Coontz, Eliot Marshall, Jeffrey Mervis, Leslie Roberts; **contributing editors** Elizabeth Culotta, Polly Shulman; **news writers** Yudhijit Bhattacharjee, Adrian Cho, Jennifer Couzin, David Grimm, Constance Holden, Jocelyn Kaiser, Richard A. Kerr, Eli Kintisch, Greg Miller, Elizabeth Pennisi, Robert F. Service (Pacific NW), Erik Stokstad, Jue Wang; **intern** Lauren Schenkman; **contributing correspondents** Jon Cohen (San Diego, CA), Daniel Ferber, Ann Gibbons, Sam Kean, Robert Koenig, Andrew Lawler, Mitch Leslie, Charles C. Mann, Virginia Morell, Gary Taubes; **copy editors** Linda B. Felaco, Melvin Gatling, Melissa Raimondi; **administrative support** Scherraine Mack; **bureaus** San Diego, CA: 760-942-3252, FAX 760-942-4979; Pacific Northwest: 503-963-1940

Production director James Landry; **senior manager** Wendy K. Shank; **assistant manager** Rebecca Doshi; **senior specialists** Steve Forrester, Chris Redwood, Anthony Rosen; **Preflight director** David M. Tompkins; **manager** Marcus Spiegler; **specialist** Jason Hillman

Art director Yael Kats; **associate art director** Laura Creveling; **senior illustrators** Chris Bickel, Katharine Sutliff; **illustrator** Yana Greenman; **senior art associates** Holly Bishop, Preston Huey, Nayomi Kevitiyagala; **art associates** Kay Engman, Matthew Twombly; **photo editor** Leslie Blizard

***Science* International**

Europe (science@science-int.co.uk) **editorial: international managing editor** Andrew M. Sugden; **senior editor/commentary** Julia Fahrenkamp-Uppenbrink; **senior editors** Caroline Ash, Stella M. Hurtley, Ian S. Osborne, Peter Stern; **associate editor** Maria Cruz; **locum editor** Helen Pickersgill; **editorial support** Deborah Dennison, Rachel Roberts, Alice Whaley; **administrative support** John Cannell, Janet Clements, Louise Hartwell; **news: europe news editor** John Travis; **deputy news editor** Daniel Clery; **contributing correspondents** Michael Balter (Paris), John Bohannon (Vienna), Martin Enserink (Amsterdam and Paris), Gretchen Vogel (Berlin); **intern** Tim Wogan

Latin America contributing correspondent Antonio Regalado

Asia Japan Office: Asca Corporation, Tomoko Furusawa, Rustic Bldg. 7F, 77 Tenjin-cho, Shinjuku-ku, Tokyo 162-0808, Japan; +81 3 6802 4616, FAX +81 3 6802 4615, inquiry@sciencemag.jp; **asia news editor** Richard Stone (Beijing: rstone@aaas.org); **contributing correspondents** Dennis Normile [Japan: +81 (0) 3 3391 0630, FAX +81 (0) 3 5936 3531; dnormile@gol.com]; Hao Xin [China: +86 (0) 10 6307 4439 or 6307 3676, FAX +86 (0) 10 6307 4358; cindyhao@gmail.com]; Pallava Bagla [South Asia: +91 (0) 11 2271 2896; pbagla@vsnl.com]

EXECUTIVE PUBLISHER **Alan I. Leshner**
PUBLISHER **Beth Rosner**

Fulfillment Systems and Operations (membership@aaas.org); **director** Waylon Butler; **customer service supervisor** Pat Butler; **specialists** Latoya Casteel, LaVonda Crawford, Vicki Linton, April Marshall; **data entry supervisor** Cynthia Johnson; **specialists** Shirlene Hall, Tarrika Hill, William Jones

Business Operations and Administration director Deborah Rivera-Wienhold; **business systems and financial analysis director** Randy Yi; **manager, business analysis** Eric Knott; **manager, business operations** Jessica Tierney; **financial analysts** Priti Pamnani, Celeste Troxler; **rights and permissions: administrator** Emilie David; **associate** Elizabeth Sandler; **marketing director** Ian King; **marketing managers** Allison Pritchard, Alison Chandler, Julianne Wielga; **marketing associates** Aimee Aponte, Mary Ellen Crowley, Wendy Wise; **senior marketing executive** Jennifer Reeves; **director, site licensing** Tom Ryan; **director, corporate relations** Eileen Bernadette Moran; **publisher relations, eresources specialist** Kiki Forsythe; **senior publisher relations specialist** Catherine Holland; **publisher relations, east coast** Phillip Smith; **publisher relations, west coast** Philip Tsolakidis; **fulfillment supervisor** Iquo Edim; **fulfillment coordinator** Celeste MacDonald; **marketing manager** Christina Schlecht; **electronic media: manager** Lizabeth Harman; **project manager** Trista Snyder; **assistant manager** Lisa Stanford; **senior production specialists** Ryan Atkins, Christopher Coleman, **computer specialist** Walter Jones; **production specialists** Nichele Johnston, Kimberly Oster; **director, web and new media** Will Collins

advertising director, worldwide ad sales Bill Moran
commercial editor Sean Sanders: 202-326-6430
project director, outreach Brianna Blaser

Product (science_advertising@aaas.org); **midwest** Rick Bongiovanni: 330-405-7080, FAX 330-405-7081; **east coast/e. canada** Laurie Faraday: 508-747-9395, FAX 617-507-8189; **west coast/w. canada** Lynne Stickrod: 415-931-9782, FAX 415-520-6940; **uk/europe/asia** Roger Goncalves: TEL/FAX +41 43 243 1358; **japan** ASCA Corporation, Nanako Ide +81 (0) 3 6802 4616, FAX +81 (0) 3 6802 4615; ads@sciencemag.jp; **senior traffic associate** Deiandra Simms

worldwide associate director of *Science* Careers Tracy Holmes: +44 (0) 1223 326525, FAX +44 (0) 1223 326532

Classified (advertise@sciencecareers.org); **u.s.: midwest/east coast** Tina Burks: 202-326-6577; **west/south central** Nicholas Hintibidze: 202-326-6533; **sales coordinators** Rohan Edmonson, Shirley Young; **europe/row sales:** Susanne Kharraz, Dan Pennington, Alex Palmer; **sales assistant** Lisa Patterson; **japan** ASCA Corporation, Jie Chin +81 (0) 3 6802 4616, FAX +81 (0) 3 6802 4615; careerads@sciencemag.jp; **advertising support manager** Karen Foote: 202-326-6740; **advertising production operations manager** Deborah Tompkins; **senior production specialist/graphic designer** Amy Hardcastle; **senior production specialist** Robert Buck; **senior traffic associate** Christine Hall

It becomes you.

Introducing the 3500 Series Genetic Analyzer.

Get ready to make an amazing discovery: the new 8-capillary and 24-capillary 3500 Series Genetic Analyzers take DNA analysis to an entirely new level of performance. A level where your daily workflow seems like a natural extension of your own intuition. Where precise, quality-assured data inspires greater confidence. And where a new consumables design and intuitive software interface keep you current and in control.

Take a closer look, and you'll find the new 3500 and 3500xL Genetic Analyzers are like second nature. Which is our first priority when it's your data.

Discover the 3500 System at **www.appliedbiosystems.com/3500Series**

Easy-to-Use Consumables

Control at Your Fingertips

Quality-Assured Data

applied biosystems™
part of life technologies™

Submission deadline August 1

Your name here.

The GE & Science Prize for Young Life Scientists. Because brilliant ideas build better realities.

Imagine standing on the podium at the Grand Hotel in Stockholm, making your acceptance speech for the GE & Science Prize for Young Life Scientists. Imagine having your essay read by your peers around the world. Imagine discussing your work in a seminar with other prize winners and Nobel Laureates. Imagine what you could do with the $25,000 prize money. Now stop imagining. If you were awarded your Ph.D. in molecular biology in 2009, then submit your 1000-word essay by August 1, and you can make it reality.

Want to build a better reality? Go to www.gescienceprize.org

GE & Science Prize for Young Life Scientists

imagination at work

Science AAAS

* For the purpose of this prize, molecular biology is defined as "that part of biology which attempts to interpret biological events in terms of the physico-chemical properties of molecules in a cell".

(McGraw-Hill Dictionary of Scientific and Technical Terms, 4th Edition).

28-9402-06AB

American Association for Cancer Research
www.aacr.org

Members Worldwide Devoted to Conquering Cancer

With over 30,000 members in nearly 90 countries, AACR is devoted to encouraging collaborations among scientific communities around the world. AACR membership enables investigators, both domestic and international, to participate more fully in the universal conquest of cancer, promote a global dialogue of regional and international cancer issues, and extend worldwide access to AACR programs and resources. AACR offers six membership categories to support each aspect of our members' professional development and enhancement in cancer research. Special membership dues rates are available for investigators located in countries with emerging economies.

Dues Structure for Members*

	Standard Dues	Emerging Economies: Upper Middle Income	Emerging Economies: Lower Middle Income	Emerging Economies: Low Income
Active	$265	$50	$30	$20
Associate	$50	$25	$15	$10

Affiliate rates are $115 and Student Membership is free.
These rates apply to all income levels.

*Visit www.aacr.org for a listing of countries with emerging economies as designated by the World Bank.

AACR's programs and services foster the exchange of knowledge and new ideas among scientists dedicated to cancer research, provide training opportunities for the next generation of cancer researchers, and increase public understanding of cancer.

Why you should Join AACR

By becoming a member of the AACR you will receive the following member benefits:

- **Substantially Reduced Registration Rates** offered to members only for participation in upcoming conferences and meetings.
- **The Privilege of Sponsoring an Abstract** for AACR Annual Meetings and special conferences.
- **Professional Advancement sessions** on grant writing, scientific publishing, starting-up and managing a successful lab and more are held at no cost to our members.
- **Funding and Award Opportunities** for Scientific Achievement, such as career development, research fellowships, scholar-in-training, and travel grants.
- **Education and Training** through workshops and special courses to provide young investigators with opportunities to develop skills in clinical trial design, molecular biology, pathobiology, and related fields.
- **Exclusive discounts** on subscriptions to our six renowned peer-reviewed scientific journals, and a complimentary digital subscription to CR, a magazine for cancer survivors, patient advocates, their families, physicians, and scientists.
- **Network internationally** with scientists and join any of six Association groups committed to promoting dialogue and scholarship among cancer researchers and to supporting the efforts of underrepresented populations in the cancer research community.

Apply Now!

Attending the 101st Annual Meeting? Visit **AACR Central** in the Exhibit Hall or the Membership Booth in the registration area (West Hall) to apply or visit **www.aacr.org/membership.**

American Association for Cancer Research Membership Department
615 Chestnut Street, 17th Floor • Philadelphia, PA, USA 19106-4404 • Phone: 215-440-9300 • Fax: 215-440-9412
E-mail: membership@aacr.org • www.aacr.org

EDITED BY CONSTANCE HOLDEN

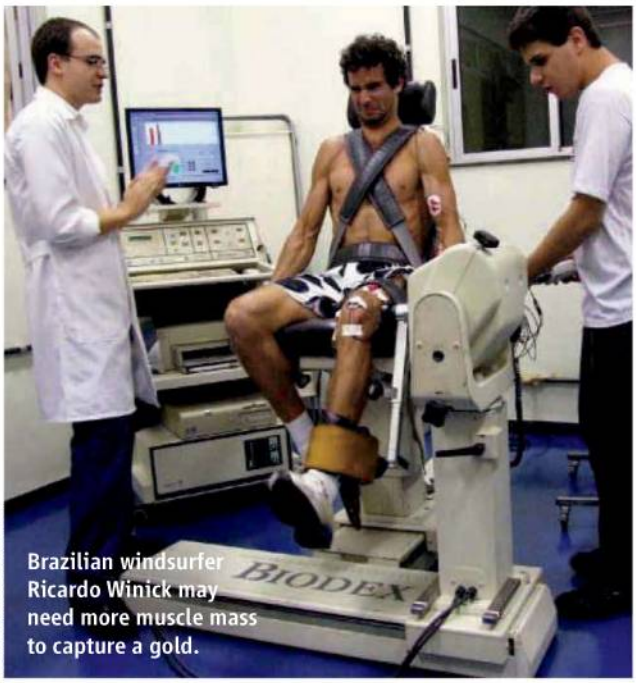

Brazilian windsurfer Ricardo Winick may need more muscle mass to capture a gold.

Olympics Lab in Rio

Brazil may be an emerging global economic power, but in Olympic medals, its performance is strictly second rate. At the 2008 Beijing summer games, Brazil ranked 17th in the medal count, just ahead of Kenya.

Now that Rio de Janeiro is set to host the games in 2016, Brazil's government is turning to science to help crank up its medal output. Last month, it announced it will spend $7 million outfitting a new Olympic Laboratory in Rio. "We have a strategic vision to be in the top 10 sports powers by 2016," says Maurício França of Brazil's Research and Projects Financing Agency.

The center, to be housed in a swimming complex built for the 2007 Pan American Games, will be equipped with high-speed cameras for physiological studies as well as a biochemistry lab to analyze data from athletes including swimmers, volleyball players, and judo competitors. In many cases, França notes, Brazilians have been missing the winner's podium by just centimeters or seconds. "We think that science can make the difference."

LOWERING THE BAR

"Should childbirth be considered a stressor sufficient to meet the criteria for PTSD?"

—Article in the February 2010 *Archives of Women's Mental Health*, whose special topic is psychiatry's *Diagnostic and Statistical Manual of Mental Disorders*, the *International Classification of Diseases*, and "the female psyche: quo vadis?"

Mathematics 'Nobel'

John Torrence Tate, 85, is this year's winner of the $1 million Abel Prize for mathematics, awarded by the Norwegian Academy of Science and Letters.

Tate taught at Harvard University for 36 years before joining the University of Texas, Austin. He retired last year. Tate, who is being recognized for "his vast and lasting impact on the theory of numbers" has his name attached to many ideas in number theory, starting with Tate's Thesis, his celebrated 1950 Princeton University doctoral thesis. According to a commentary by mathematician Marcus du Sautoy of the University of Oxford in the United Kingdom, prime numbers (numbers divisible only by themselves or 1) are to math what the elements are to chemistry. Because they are infinite, however, they can't be put in a table; "instead, we must look for patterns … [in] the way the primes are laid out through the universe of numbers." Tate is "the Galileo of number theory," says du Sautoy, because his work "has provided tools and insights which have allowed the mathematicians of this generation to see further into the universe of numbers than ever before."

A prize ceremony will be held in Oslo on 25 May.

The Price of Eggs

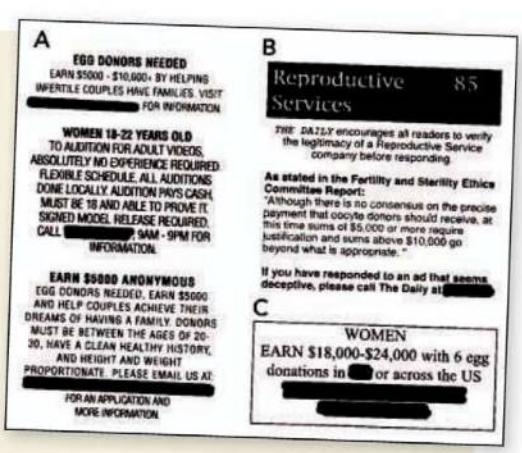
A

EGG DONORS NEEDED
EARN $5000 - $10,000+ BY HELPING INFERTILE COUPLES HAVE FAMILIES. VISIT [redacted] FOR INFORMATION

WOMEN 18-22 YEARS OLD
TO AUDITION FOR ADULT VIDEOS. ABSOLUTELY NO EXPERIENCE REQUIRED. FLEXIBLE SCHEDULE. ALL AUDITIONS DONE LOCALLY. AUDITION PAYS CASH. MUST BE 18 AND ABLE TO PROVE IT. SIGNED MODEL RELEASE REQUIRED. CALL [redacted] 9AM - 9PM FOR INFORMATION

EARN $5000 ANONYMOUS
EGG DONORS NEEDED. EARN $5000 AND HELP COUPLES ACHIEVE THEIR DREAMS OF HAVING A FAMILY. DONORS MUST BE BETWEEN THE AGES OF 20-30, HAVE A CLEAN HEALTHY HISTORY, AND HEIGHT AND WEIGHT PROPORTIONATE. PLEASE EMAIL US AT: [redacted] FOR AN APPLICATION AND MORE INFORMATION

B

Reproductive Services 85

THE DAILY encourages all readers to verify the legitimacy of a Reproductive Service company before responding.

As stated in the Fertility and Sterility Ethics Committee Report:
"Although there is no consensus on the precise payment that oocyte donors should receive, at this time sums of $5,000 or more require justification and sums above $10,000 go beyond what is appropriate."

If you have responded to an ad that seems deceptive, please call The Daily at [redacted]

C

WOMEN
EARN $18,000-$24,000 with 6 egg donations in [redacted] or across the US
[redacted]

While bioethicists continue to agonize over whether women should be compensated for donating oocytes to research, the U.S. market for eggs for assisted reproduction is flourishing. According to an article in the spring issue of the *Hastings Center Report*, some donors are offered tens of thousands of dollars, and the likelihood of having a high SAT score may be more important than appearance or ethnicity in determining the value of a student's oocytes.

Aaron D. Levine, assistant professor of public policy at the Georgia Institute of Technology in Atlanta, obtained copies of student newspapers from 366 colleges and universities around the country. He found 111 ads soliciting egg donors in 65 different student newspapers, in what he believes is the "first national cross-sectional sample" of such ads. He found that top fees were offered at the institutions with the highest average SAT scores of incoming students, and he calculated that every increase of 100 SAT points increased the bounty by $1930. That amount roughly doubled if the advertisements were placed on behalf of a specific couple. One ad, which ran in *The Harvard Crimson*, *The Daily Princetonian*, and *Yale Daily News*, offered $35,000 to an attractive athletic donor with an SAT score over 1400.

Levine says he doesn't think the situation has changed much since 2006 when most of the data were collected: He recently spoke at Duke University, where he saw two ads, for $10,000 and $15,000 each. At nearby but lower-SAT-scoring University of North Carolina, oocytes were sought for only $2500.

CREDITS (TOP TO BOTTOM): BRAZILIAN OLYMPIC COMMITTEE; CHARLIE FONDVILLE/THE ABEL PRIZE/THE NORWEGIAN ACADEMY OF SCIENCE AND LETTERS; *HASTINGS CENTER REPORT* (MARCH–APRIL 2010)

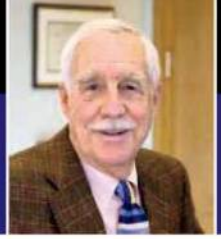

Judge throws out gene patents 153

A new human ancestor 154

SCIENTIFIC LITERACY

NSF Board Draws Flak for Dropping Evolution From *Indicators*

Americans are less likely than people in the rest of the world to believe that humans evolved from earlier species and that the universe began with a big bang. Those findings appear repeatedly in surveys of scientific literacy, and until this year they also showed up in the National Science Foundation's biennial compilation of the state of global science.

But the 2010 edition of *Science and Engineering Indicators* omits any mention of those two hot-button issues in its chapter on public attitudes toward science and technology. A section describing the survey results and related issues was edited out of the massive volume by the National Science Board (NSB), NSF's oversight body and the official publisher of *Indicators*. Board members say the answers don't properly reflect what Americans know about science and, thus, are misleading. But the authors of the survey disagree, and those struggling to keep evolution in the classroom say the omission could hurt their efforts.

"Discussing American science literacy without mentioning evolution is intellectual malpractice," says Joshua Rosenau of the National Center for Science Education, an Oakland, California–based nonprofit that has fought to keep creationism out of the science classroom. "It downplays the controversy." The 2008 edition of *Indicators*, for example, discussed "Evolution and the Schools" along with its analysis of the two survey questions, and the 2006 edition contained an article titled "Evolution Still Under Attack in Science Classrooms."

NSB officials counter that their decision to drop the survey questions on evolution and the big bang from the 2010 edition was based on concerns about accuracy. The questions were "flawed indicators of scientific knowledge because the responses conflated knowledge and beliefs," says Louis Lanzerotti, an astrophysicist at the New Jersey Institute of Technology in Newark and chair of the board's Science and Engineering Indicators (SEI) committee. John Bruer, a philosopher and president of the James McDonnell Foundation in St. Louis, Missouri, and the lead reviewer for the chapter, says he recommended removing the text and related material because the survey questions "seemed to be very blunt instruments, not designed to capture public understanding" of the two topics.

The board's action surprised science officials at the White House, to whom the board officially submits *Indicators*. "The [Obama] Administration counts on the National Science Board to provide the fairest and most complete reporting of the facts they track," says Rick Weiss, a spokesperson and analyst at the White House Office of Science and Technology Policy. In recent weeks, OSTP has asked for and received an explanation from the board about why the text was deleted.

Science has obtained a copy of the deleted text, which does not differ substantially from what has appeared in previous *Indicators*. The two questions (see graphic) have been part of an NSF-funded survey on scientific understanding and attitudes toward science since 1983. The deleted section notes that the 45% of Americans who answered "true" to the statement: "Human beings, as we know them today, developed from earlier species of animals" is similar to the percentage in previous years and much lower than in Japan (78%), Europe (70%), China (69%), and South Korea (64%). A similar gap exists for the response to the statement: "The universe began with a big explosion," with which only 33% of Americans agreed.

Bruer proposed the changes last summer, shortly after NSF sent a draft version of *Indicators* containing this text to OSTP and other government agencies. In addition to removing a section titled "Evolution and the Big Bang," Bruer recommended that the board drop a sentence noting that "the only circumstance in which the U.S. scores below other countries on science knowledge comparisons is when many Americans experience a conflict between accepted scientific knowledge and their religious beliefs (e.g., beliefs about evolution)." At a May 2009 meeting of the board's *Indicators* committee, Bruer said that he "hoped indicators could be developed that were not as value-charged as evolution."

Bruer, who was appointed to the 24-member NSB in 2006 and chairs the board's Education and Human Resources Committee, says he first became concerned about the two survey questions as the lead reviewer for the same chapter in the 2008 *Indicators*. At the time, the board settled for what Bruer calls "a halfway solution": adding a disclaimer that many Americans didn't do well on those questions because the underlying issues brought their value systems in conflict with knowledge. As evidence of that conflict, Bruer notes a 2004 study described in the 2008 *Indicators* that found 72% of Americans answered correctly when the statement about humans evolving from earlier species was prefaced with the phrase "according to the theory of evolution." The 2008 volume explains that the different percentages of correct answers "reflect factors beyond unfamiliarity with basic elements of science."

George Bishop, a political scientist at the University of Cincinnati in Ohio who has studied attitudes toward evolution, believes the board's argument is defensible. "Because

CREDITS (TOP TO BOTTOM): GENERAL SOCIAL SURVEY, 2008; THINKSTOCK

of biblical traditions in American culture, that question is really a measure of belief, not knowledge," he says. In European and other societies, he adds, "it may be more of a measure of knowledge."

The scientist who first drew up the survey question thinks the board has made a big mistake. "Evolution and the big bang are not a matter of opinion," says Jon Miller, a science literacy researcher at Michigan State University in East Lansing who conducted the survey until 2001. "If a person says that the earth really is at the center of the universe, … how in the world would you call that person scientifically literate?" Miller asks.

Tom Smith of the National Opinion Research Center in Chicago, Illinois, which conducts the science knowledge survey for *Indicators* as part of the NSF-funded General Social Survey, does not believe the two questions are flawed. Prefacing the evolution and big bang statements with qualifiers might degrade the responses, he says, because "that could have the effect of tipping respondents off about the right answer." He says NSF hasn't asked him to make any changes in the survey, which is now in the field for planned use in the 2012 *Indicators*.

Not yet, at least. Both Lanzerotti and Lynda Carlson, director of NSF's statistical office that manages the survey and produces *Indicators*, say it is time to take a fresh look at the survey questions. Last week, after his interview with *Science*, Lanzerotti asked the head of NSF's Social, Behavioral and Economic Sciences Directorate to conduct a "thorough examination" of the questions through "workshops with experts."

Will the 2012 *Indicators* include a section on evolution? Lanzerotti, whose 6-year term ends next month, would like to see the topic handled "in the proper way," using the different measuring instrument. In hindsight, he says, the 2010 *Indicators* should have explained why the two questions had been dropped.

Miller believes that removing the entire section was a clumsy attempt to hide a national embarrassment. "Nobody likes our infant death rate," he says by way of comparison, "but it doesn't go away if you quit talking about it." **–YUDHIJIT BHATTACHARJEE**

CLIMATE CHANGE

Scientists Ask Minister to Disavow Predecessor's Book

PARIS—Battles over the science of global warming are raging around the world, and France is the latest hot spot. Two months ago, former French science minister Claude Allègre published *L'imposture climatique* (*The Climate Fraud*), a scathing attack on the climate research field and the Intergovernmental Panel on Climate Change (IPCC). Allègre, an emeritus geochemist from the Institute of Earth Physics of Paris (IPGP), describes the field as a "mafia-like" system built around a "baseless myth." Exasperated climate scientists have shot back, claiming the book itself is full of factual mistakes, distortions of data, and plain lies. And last week, more than 500 French researchers signed a letter asking Science Minister Valérie Pécresse to disavow Allègre's book by publicly expressing her confidence in French climate science.

Science minister from 1997 to 2000, Allègre is a frequent guest on French radio and TV shows and has written more than 20 popular science books; his new climate book has sold more than 110,000 copies. But the letter to Pécresse says Allègre and IPGP Director Vincent Courtillot—a self-described "moderate global warming skeptic" who also expressed doubts about IPCC's conclusions in a book last year—have made "false accusations" and "have forgotten the basic principles of scientific ethics, breaking the moral pact that binds every scientist to society."

One key complaint about Allègre's book, which consists of a series of interviews with journalist Dominique de Montvalon, is that its hand-drawn graphics misrepresent data. A graph showing how temperatures rose and fell since 500 C.E., for example, is adapted from a 2008 paper in *Climate Dynamics* by Swedish paleoclimatologist Håkan Grudd. After he was alerted to Allègre's graph, Grudd noticed that until 1900 it largely matched his version. After that, the two started diverging, and whereas Grudd's graph ended in 2004, Allègre's continued with sharply declining temperatures, in an apparent extrapolation of global cooling, until 2100. In a statement he sent to *Science*, Grudd calls the changes "misleading and unethical." Other climate scientists found similar problems. Louise Sime of the British Antarctic Survey says a graph Allègre attributed to her "is not an accurate drawing of anything. … It has nothing to do with my work."

Allègre did not respond to requests for comments. In an e-mail posted on the blog of Sylvestre Huet, a science journalist at *Libération*, Allègre did not deny the discrepancies but said the hand-drawn graphs are nothing more than "virtual support for the written argument." He also told *Libération* the letter to Pécresse was a "useless and stupid petition." Climatologists, he was further quoted, "have wasted a lot of public money, and they're afraid of losing their funding, afraid of losing their jobs." Courtillot says that he finds it "quite astonishing" that scientists asked Pécresse, a politician, to take sides in a scientific debate.

Pécresse has expressed her trust in French climate science and has asked the Academy of Sciences to organize a debate about the research. But she will not choose sides, a ministry spokesperson says: "The minister cannot decide who's right and wrong in a scientific debate." **–MARTIN ENSERINK**

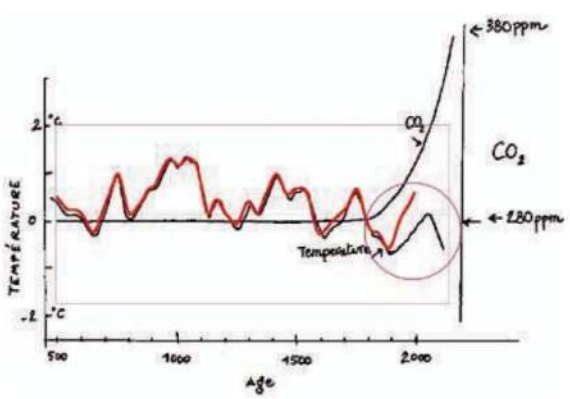

Up or down? Paleoclimatologist Håkan Grudd says his temperature graph (red) doesn't match one drawn by Claude Allègre (black).

CREDIT: HÅKAN GRUDD

Eppendorf & *Science* Prize for Neurobiology

Get recognized!

US$ 25,000 Prize

2009 Winner
Richard Benton, Ph.D.
Assistant Professor
University of Lausanne
Switzerland

Kurstin Roe Photography

eppendorf & Science PRIZE FOR NEUROBIOLOGY

Deadline for entries
June 15, 2010

It's easy to apply! Learn more at
www.eppendorf.com/prize

Congratulations to Dr. Richard Benton on winning the 2009 Eppendorf & *Science* Prize for his studies on odor detection in the fruit fly, *Drosophila*. His findings have revealed unexpected evolutionary parallels between insect chemosensation, immune recognition and synaptic transmission.

The annual international Eppendorf & *Science* Prize for Neurobiology honors young scientists for their outstanding contributions to neurobiology research based on methods of molecular and cell biology. The winner and finalists are selected by a committee of independent scientists, chaired by *Science*'s Senior Editor, Dr. Peter Stern.

To be eligible, you must be 35 years of age or younger. If you're selected as this year's winner, you will receive US$ 25,000, have your work published in the prestigious journal *Science* and be invited to visit Eppendorf in Hamburg, Germany.

eppendorf
In touch with life

Science
AAAS

PATENTS

Cancer Gene Patents Ruled Invalid

A legal bombshell hit the biotech world last week: A federal judge in New York City used sweeping language to invalidate a handful of human gene patents, casting doubt on hundreds more. The decision applies only in New York state and is sure to be appealed—a process that could take years. Still, it undercuts the idea that DNA sequence can be owned.

Judge Robert Sweet of the federal district court in New York City ruled that key discoveries from the mid-1990s, the *BRCA1* and *BRCA2* genes associated with breast and ovarian cancers, are not truly inventions. They are "products of nature," he writes in a blunt 29 March opinion. Legal claims generally refer to genes as "isolated DNA" to support the idea that sequence information is a product of human ingenuity, not nature. But many scientists view this as a "lawyer's trick," Sweet observes. He seems to agree. The BRCA genes in this case, he writes, "are not markedly different from native DNA as it exists in nature." And for that reason he concludes that they are "unpatentable."

That is exactly the outcome sought by a group of cancer patients, medical experts, and others who jointly brought this suit. Their case was presented to the court by the American Civil Liberties Union (ACLU) and the Public Patent Foundation (PUBPAT) of Yeshiva University's Benjamin N. Cardozo School of Law in New York City (*Science*, 22 May 2009, p. 1000). They argued that the patents should never have been granted. Their chief target was the diagnostic company Myriad Genetics in Salt Lake City, Utah, which has exclusive use of the BRCA genes. The second defendant was the University of Utah Research Corp. in Salt Lake City, which owns the patents. In addition, ACLU-PUBPAT sued the U.S. government, saying that by granting a monopoly on BRCA genes, the Patent and Trademark Office had violated everyone's freedom of speech.

The critics zeroed in on the way Myriad blocked the work of independent researchers and diagnostic groups. For example, the suit tells how Myriad halted work by Haig Kazazian and Arupa Ganguly at the University of Pennsylvania (both plaintiffs). In the late 1990s, using their own methods, the Penn group offered BRCA screening to individuals for a fee, but not as a commercial enterprise. Myriad asked Penn to sign a license agreement, but the researchers declined, saying Myriad's terms were too restrictive. Myriad sued, and Penn halted the screening. Today, Ganguly is "very happy" that the court stepped in—but considers it late: "I could have done something with BRCA 10 years ago," Ganguly says, but she has now moved on. Such impacts harmed the public interest, ACLU and PUBPAT argue. Sweet listed the "public harm" controversies in detail but set them aside as "not resolvable" in this proceeding. He also dismissed the suit against the government as moot.

Myriad brushed off the defeat, saying it will appeal and that only seven of its 23 key patents were rejected. The company uses a private database of mutations and medical outcomes to analyze client DNA and gauge a person's risk for cancer. Myriad says it steers clients to early care and claims that "countless lives have been saved" as a result. For families with less common BRCA mutations, the company charges $3000 or more per test. In 2008, according to Sweet's opinion, Myriad's costs for providing tests was about $32 million and its revenue was $222 million.

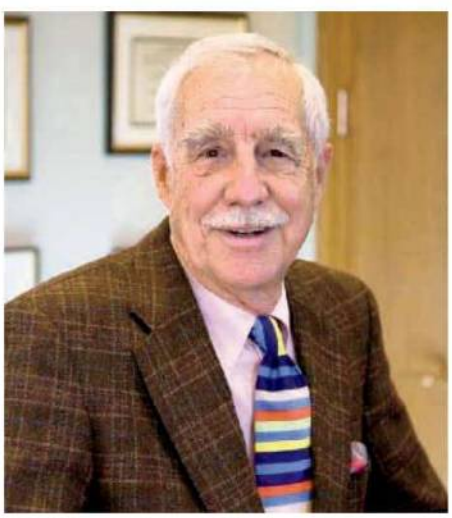

CREDIT: COURTESY ROBERT W. SWEET

Puncturing legal doctrine. Isolated DNA cannot be patented, Judge Robert Sweet says, because it is a product of nature.

Biotech legal experts were surprised by Sweet's decision, partly because gene patents have been around for so long. Li Westerlund, vice president for global intellectual property at Bavarian Nordic, a vaccinemaker, expressed a common bewilderment: "It seems very hard to argue that something that has been patented for decades should not be patentable," she said. The decision threatens to make a risky business even more uncertain, she said.

The first U.S. gene patent was granted in 1980, and the first BRCA patent in 1998. In Europe, researchers and health agencies bitterly resisted enforcement of BRCA patents, and the European Patent Office narrowed but did not quash BRCA patents (*Science*, 24 June 2005, p. 1851). Today, there are roughly 3000 to 5000 patents on human genes, estimates Robert Cook-Deegan, director of the Center for Genome Ethics, Law, and Policy at Duke University in Durham, North Carolina. ACLU claims that the New York decision is "the first time a court has found patents on genes unlawful." Some people were also surprised by Judge Sweet's logic. He argues that Myriad's legal case focused too much on chemistry and structure but failed "to acknowledge the unique characteristics of DNA that differentiate it from other chemical compounds." DNA, he writes, has "unique qualities as a physical embodiment of information" that direct the synthesis of other molecules in the body. It is DNA's information—not chemistry—that people want to patent, and Sweet believes that information comes from nature.

If upheld on appeal, this decision could spike a lot of patents. The Biotechnology Industry Organization in Washington, D.C., warned about this in a brief to the court before the decision, saying that a decision in favor of ACLU-PUBPAT could undermine "the viability of the domestic biotechnology industry" and "would put at risk the validity of a whole host of patents on isolated natural substances."

Knocking down isolated gene patents could actually be good for some companies, says Cook-Deegan. "While this does threaten certain business models—the gene-at-a-time testing models—I think those don't have much of a survival value anyway." He believes companies doing full genome sequence analysis and multiallele testing, such as Allumina, Affymetrix, 23andMe, and Navigenics, will benefit if the courts clear away small sequence claims. "It's good news in that it will reframe the debate, … which had been largely premised on tired old arguments about isolated DNA," Cook-Deegan says.

Many observers—including both Westerlund and Cook-Deegan—predict that the special patent court that will probably review this decision, the Court of Appeals for the Federal Circuit, will likely be more sympathetic to the company. Ultimately, the case could go all the way to the Supreme Court; no one's predicting what may happen at that stage. **–ELIOT MARSHALL**

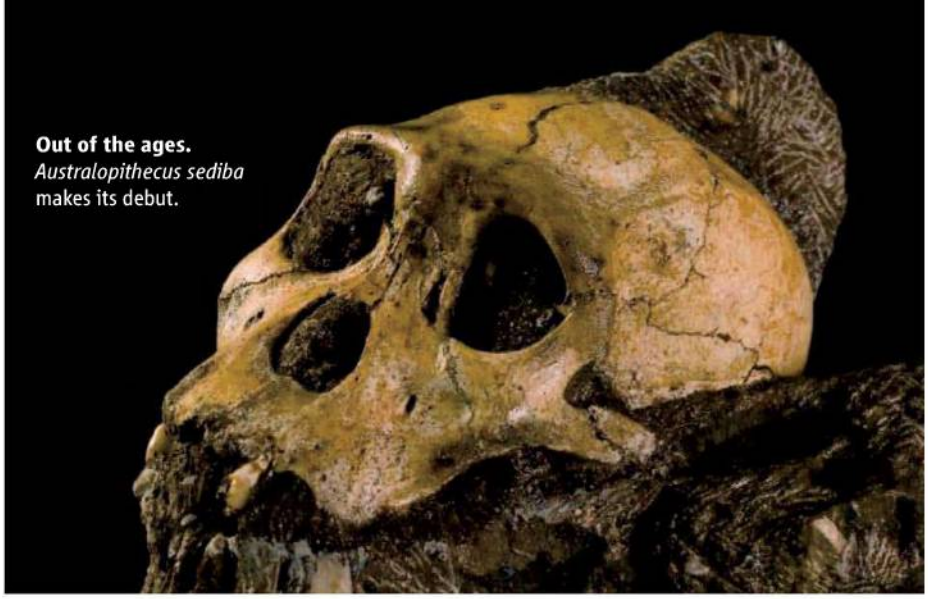

Out of the ages. *Australopithecus sediba* makes its debut.

PALEOANTHROPOLOGY

Candidate Human Ancestor From South Africa Sparks Praise and Debate

"Dad, I found a fossil!"

Lee Berger glanced over at the rock his 9-year-old son, Matthew, was holding and figured the bone sticking out of it was probably that of an antelope, a common find in ancient South African rocks. But when Berger, a paleoanthropologist at the University of the Witwatersrand, Johannesburg, took a closer look, he recognized it as something vastly more important: the collar bone of an ancient hominin. Then he turned the block around and spotted a hominin lower jaw jutting out. "I couldn't believe it," he says.

Now on pages 195 and 205 of this issue of *Science*, Berger and his co-workers claim that these specimens, along with numerous other fossils found since 2008 in Malapa cave north of Johannesburg and dated as early as 2 million years ago, are those of a new species dubbed *Australopithecus sediba*. *Sediba* means "wellspring" in the Sesotho language, and Berger's team argues that the fossils have a mix of primitive features typical of australopithecines and more advanced characteristics typical of later humans. Thus, the team says, the new species may be the best candidate yet for the immediate ancestor of our genus, *Homo*.

That last claim is a big one, and few scientists are ready to believe it themselves just yet. But whether the new hominins are *Homo* ancestors or a side branch of late-surviving australopithecines, researchers agree that because of their completeness—including a skull and many postcranial bones—the fossils offer vital new clues to a murky area in human evolution. "This is a really remarkable find," says paleontologist Meave Leakey of the National Museums of Kenya in Nairobi, who thinks it's an australopithecine. "Very lovely specimens," says biological anthropologist William Kimbel of Arizona State University (ASU), Tempe, who thinks they are *Homo*.

Such different views of how to classify these fossils reflect a still-emerging debate over whether they are part of our own lineage or belong to a southern African side branch. The oldest *Homo* specimens are scrappy and enigmatic, leaving researchers unsure about the evolutionary steps between the australopithecines and *Homo*. Some think that the earliest fossils assigned to that genus, called *H. habilis* and *H. rudolfensis* and dated to as early as 2.3 million years ago, are really australopithecines. "The transition to *Homo* continues to be almost totally confusing," says paleoanthropologist Donald Johanson of ASU Tempe, who has seen the new fossils. So it is perhaps no surprise that the experts disagree over whether the new bones represent australopithecines or early *Homo*. And for now, at least, they don't seem to mind the uncertainty. "All new discoveries make things more confusing" at first, says anthropologist Susan Antón of New York University.

The finds stem from a project Berger embarked on in early 2008 with geologist Paul Dirks, now at James Cook University in Townsville, Australia, to identify new caves likely to hold hominin fossils. Malapa, just 15 kilometers northeast of famous hominin sites such as Sterkfontein, had been explored by lime miners in the early 20th century; they apparently threw the block that Matthew Berger found out of the cave. (Matthew was originally included as a co-author on one of the papers, but *Science*'s reviewers nixed that idea, Berger says.)

When Berger's team excavated inside the cave, it found more of that first individual, a nearly complete skull and a partial skeleton of a boy estimated to be 11 or 12 years old, plus an adult female skeleton, embedded in cave sediments. These fossils are reported in *Science*. The researchers also found bones of at least two other individuals, including an infant and another adult female, that are yet to be published.

Dirks enlisted several experts to help date the fossils. Labs in Bern, Switzerland, and Melbourne, Australia, independently performed uranium-lead radiometric dating, taken from cave deposits immediately below the fossils. They yielded dates of 2.024 million and 2.026 million years respectively, with maximum error margins of ±62,000 years. Paleomagnetic studies suggest that layers holding the fossils were deposited between 1.95 million and 1.78 million years ago, and animal bones found with the hominins were consistent with these dates.

The uranium-lead dating is "credible" and indicates that the fossils are no more than 2 million years old, says geochronologist Paul Renne of the Berkeley Geochronology Center in California, citing the strong reputations of the Bern and Melbourne groups. But Renne regards the paleomagnetic work, which relies on correctly identifying ancient polarity reversals in Earth's magnetic field, as less convincing. The cave's stratigraphy might not be complete enough to formally rule out a much younger paleomagnetic signal for the fossils, he says. Geochemist Henry Schwarcz of McMaster University in Hamilton, Canada, notes that the team suggests that the hominin bodies might have been moved by river flows after they fell into the cave from holes in the earth above. If so, the fossils may not be tightly associated with the dated deposits below and above them, Schwarcz says. But Dirks rejects that suggestion, pointing out that the bones were partly articulated with each other, implying that they were buried soon after death.

For now, many researchers are accepting the dates and moving on to consider the team's hypothesis that *A. sediba* represents a new species transitional between australopithecines and early *Homo*. That idea fits with Berger's long-held—and controversial—view that *A. africanus*, rather than the earlier species to which

CREDIT: L. BERGER ET AL., *SCIENCE*

"Lucy" belongs, *A. afarensis*, was the true ancestor of *Homo*. (Some of Berger's other past claims have sparked strong criticism, including a highly publicized 2008 report of small-bodied humans on Palau, which Berger thought might shed light on the tiny hobbits of Indonesia. But other researchers say the Palau bones belong to a normal-sized modern human population.)

The team's claims for *A. sediba* are based on its contention that the fossils have features found in both genera. On the australopithecine side, the hominin boy's brain, which the team thinks had reached at least 95% of adult size, is only about 420 cubic centimeters in volume, less than the smallest known *Homo* brain of about 510 cc. The small body size of both skeletons, a maximum of about 1.3 meters, is typical of australopithecines, as are the relatively long arms. The team says *A. sediba* most resembles *A. africanus*, which lived in South Africa between about 3.0 million and 2.4 million years ago and is the most likely ancestor for the new species.

Fossil finder. Nine-year-old Matthew Berger at the moment of discovery at Malapa cave.

CREDIT: LEE BERGER

But *A. sediba* differs from *A. africanus* in traits that also link it to *Homo*. Compared with other australopithecines, *A. sediba* has smaller teeth, less pronounced cheekbones, and a more prominent nose, as well as longer legs and changes in the pelvis similar to those seen in later *H. erectus*. This species, also known in Africa as *H. ergaster* and considered an ancestor of *H. sapiens*, first appears in Africa about 1.9 million years ago. Some features of *A. sediba*'s pelvis, such as the ischium (bottom portion), which is shorter than in australopithecines, "do look like they are tending more in a *Homo* direction," says Christopher Ruff, a biological anthropologist at Johns Hopkins Medical School in Baltimore, Maryland.

The claimed *Homo*-like features suggest to some people that the fossils belong in that genus rather than *Australopithecus*. "I would have been happier with a *Homo* designation," based on the small size of the teeth and also their detailed structure, such as the shape of their cusps, says Antón. "It's *Homo*," agrees Johanson, citing features such as the relative thinness of the hominin's lower jaw.

But others are unconvinced by the *Homo* argument. The characteristics shared by *A. sediba* and *Homo* are few and could be due to normal variation among australopithecines or because of the boy's juvenile status, argues Tim White, a paleoanthropologist at the University of California, Berkeley. These characters change as a hominin grows, and the features of a young australopithecine could mimic those of ancient adult humans. He and others, such as Ron Clarke of Witwatersrand, think the new fossils might represent a late-surviving version of *A. africanus* or a closely related sister species to it, and so will be chiefly informative about that lineage. "Given its late age and *Australopithecus*-grade anatomy, it contributes little to the understanding of the origin of genus *Homo*," says White.

Putting *A. sediba* into *Homo* would require "a major redefinition" of that genus, adds paleoanthropologist Chris Stringer of the Natural History Museum in London. At no earlier than 2 million years old, *A. sediba* is younger than *Homo*-looking fossils elsewhere in Africa, such as an upper jaw from Ethiopia and a lower jaw from Malawi, both dated to about 2.3 million years ago. Berger and his co-workers agree that the Malapa fossils themselves cannot be *Homo* ancestors but suggest that *A. sediba* could have arisen somewhat earlier, with the Malapa hominins being late-surviving members of the species.

The team thought long and hard about putting the fossils into *Homo* but decided that given the small brain and other features, the hominin was "australopithecine-grade," says team member Steven Churchill of Duke University in Durham, North Carolina. However they are classified, the Malapa finds "are important specimens in the conversation" about the origins of our genus, says Antón, and "will have to be considered in the solution."

–MICHAEL BALTER

ScienceNOW

From *Science*'s Online Daily News Site

Mass of the Common Quark Finally Nailed Down

Using supercomputers and mind-bogglingly complex simulations, researchers have calculated the masses of particles called "up quarks" and "down quarks" that make up protons and neutrons with 20 times greater precision than the previous standard. The new numbers could be a boon to theorists trying to decipher particle collisions at atom smashers like Europe's Large Hadron Collider or trying to develop deeper theories of the structure of matter.
http://bit.ly/commonquark

Notorious Drug Stanches Bleeding

Despite its horrifying history of causing birth defects, thalidomide has recently made a comeback as a treatment for diseases such as the cancer multiple myeloma. Now, a new study suggests that the drug may also ease the symptoms of a genetic disease called hereditary hemorrhagic telangiectasia—a discovery that could guide researchers to novel therapies for HHT and other vascular diseases.
http://bit.ly/goodthalidomide

Wind Turbines Would Support A Stable Grid

Individual wind turbines and even whole wind farms remain at the mercy of local weather for how much electricity they can generate. But researchers have confirmed that linking up such farms along the entire U.S. East Coast could provide a surprisingly consistent source of power. In fact, such a setup could someday replace much of the region's existing generating capacity, which is based on coal, natural gas, nuclear reactors, and oil. http://bit.ly/windnetwork

That Tortilla Costs More Than You Think

Which costs more, a dollar's worth of sugar or a dollar's worth of paint? That's not a trick question: The sugar costs more, if you count the liters of water that go into making it, according to a new study. Uncovering the water behind the dollars in sectors including cotton farming and moviemaking could help industries use water more wisely.
http://bit.ly/watercost

Read the full postings, comments, and more at **news.sciencemag.org/sciencenow**.

"It's a magical box."
—Miho Terunuma, D.D.S., Ph.D.

Emotional reactions to instrumentation from scientists are rare. Yet with Thermo Scientific NanoDrop Spectrophotometers, they are becoming commonplace. That's because scientists who own a NanoDrop™ are passionate about its simplicity. These instruments reduce analysis time and minimize sample waste with fast, easy and accurate micro-volume nucleic acid and protein sample quantitation. Just ask Dr. Terunuma:

"Before NanoDrop, measuring samples was inconvenient and wasn't easy. The first time I used the NanoDrop I was amazed. Only 1 µl sample and so fast. Every time I purify DNA I use the NanoDrop. It's fast, easy and small. Now, I always use the NanoDrop. It's the best instrument, and I don't have to use much sample."

"I was surprised how easy and fast it was to use the NanoDrop."

Try any NanoDrop instrument for free:* www.thermo.com/nanodrop

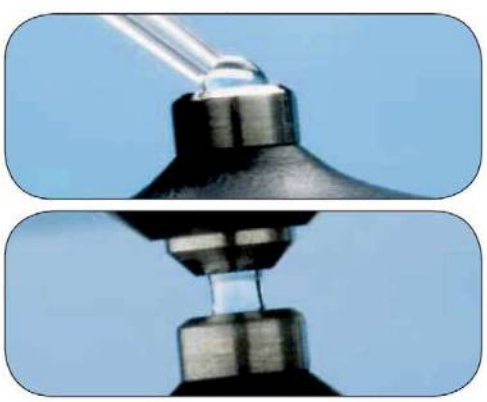

Thermo Scientific NanoDrop UV-Vis Spectrophotometers offer easy, reliable micro-volume analysis, with sample size as low as 0.5 µl and measurement time of less than 5 seconds—no dilutions.

Moving science forward

Thermo SCIENTIFIC

Part of Thermo Fisher Scientific

PLANETARY SCIENCE

Fresh Signs of Volcanic Stirrings Are Radiating From Venus

Scientists long viewed Venus as a possible twin of Earth, but in recent decades the differences have begun outweighing the similarities. Venus is so hot that lead would melt on its surface, and geologists eventually pronounced Venus to be free of plate tectonics. Is there nothing these siblings have in common?

In a paper published online this week in *Science* (www.sciencemag.org/cgi/content/abstract/science.1186785), researchers report new evidence that Venus is still reshaping its surface—as well as cooling its interior—through volcanic outpourings like Hawaii's or Iceland's. One contingent of planetary scientists has long held that most of the venusian surface renewed itself half a billion years ago in a single volcanic paroxysm and has been nearly dormant since, but the *Science* authors argue that Venus also resembles Earth in steadily resurfacing itself.

Planetary scientists are welcoming additional evidence of a geologically youthful Venus. "These lava flows have to be young," says planetary scientist M. Darby Dyar of Mount Holyoke College in South Hadley, Massachusetts. "The most likely explanation is volcanism going on right now."

Present-day volcanism had seemed plausible. Radar imaging by the Magellan probe in the early 1990s revealed nine "hot spots," low rises each a couple of thousand kilometers across. Lava flows had obviously streamed from the hot spot centers. Magellan gravity measurements also indicated that plumes of hot rock are slowly rising beneath venusian hot spots, much as plumes rise beneath Hawaii and Iceland to feed their eruptions.

But researchers couldn't put an age on the flows. So planetary scientist Suzanne Smrekar of NASA's Jet Propulsion Laboratory in Pasadena, California, and colleagues looked at observations of three hot spots by the Visible and Infrared Thermal Imaging Spectrometer (VIRTIS) on the European Space Agency's Venus Express, which is still in orbit. VIRTIS found that the hot spots radiate distinctly more heat than the rest of the planet does. The group infers that the hot spot flows are probably still relatively fresh and unweathered by the 460°C temperature and crushing carbon dioxide atmosphere.

Lookin' hot, and young. Extensive venusian lava flows (within dashed line) radiate heat more efficiently (pinks), implying they are less weathered and therefore young.

CREDIT: S. E. SMREKAR *ET AL.*, *SCIENCE*

No one has weathered enough Venus-like rock under venusian conditions to say just how recently the hot-spot lavas flowed. But when Smrekar and her colleagues assumed wide ranges of plausible lava volumes and lava production rates in their calculations, they got flow ages ranging from a few million years down to 2500 years. For a planet that's been around 4.6 billion years, that's young. The group goes further by suggesting that such widespread expanses of young-looking lava must have been produced by a steady, long-term, relatively slow volcanic outpouring rather than a single long-ago catastrophe.

"They certainly have identified some very young flows," says planetary scientist Mark Bullock of the Southwest Research Institute in Boulder, Colorado. "That's exciting." It means that, like Earth, Venus is actively cooling its interior and reshaping its exterior through volcanism. But is such plume-fed, hot-spot volcanism the only way Venus has operated? "I don't think we know," says planetary scientist Sean Solomon of the Carnegie Institution for Science in Washington, D.C. He and others see too many assumptions, uncertainties, and extrapolations in the case against venusian catastrophism. Someone, they say, needs to start cooking up a lot more venusian rock.

–RICHARD A. KERR

NATURAL DISASTERS

Scientists Count the Costs of Chile's Quake

Chilean scientists have estimated that the magnitude-8.8 earthquake that rocked the country on 27 February caused some $200 million in damage to research facilities and equipment. Researchers are asking the government for emergency funding and for the establishment of a seismology center that would, among other things, run the nation's tsunami warning system.

The quake shook laboratories, burned down an important chemistry center, and wrecked an oceanographic station, potentially setting back Chilean science by years (*Science*, 12 March, p. 1308).

Scientists Unified for the Reconstruction of Chile, a lobby group formed following the disaster, said this week that it will send a list of seven recommendations to Chile's minister of education to get research in the country back on track. The list includes additional grants for students whose projects are on hold and an emergency $90 million line of credit so researchers can replace damaged equipment. "We lost very expensive instruments that you can only buy in the U.S., Europe, or Japan," says Alfonso Droguett, a communications official at the University of Chile.

The recommendations grew out of a meeting held in mid-March in Santiago chaired by Raúl Morales Segura, dean of sciences at the University of Chile. The group now includes the country's leading scientific societies and universities.

Among the scientists' recommendations is to transfer control of the tsunami warning system from the navy to a new national seismology center run by scientists. The navy came under intense criticism for failing to provide an early warning of the tsunami that followed the quake. "We want a system where the scientists, not the uniformed people, are in charge," says Droguett. In principle, such a system would be similar to the one in the United States, where tsunami warnings are handled by the National Oceanic and Atmospheric Administration.

–ANTONIO REGALADO

U.S. CENSUS

Asking the Right Question Requires Right Mix of Science and Politics

On 1 April, the United States celebrated Census Day. At a cost of $14.7 billion, the 2010 Census represents the federal government's largest civilian undertaking. The stakes are high. The enumeration will determine how congressional districts are apportioned, as well as how nearly half a trillion dollars in federal funds should be disbursed.

The U.S. Constitution mandates a decennial census, and Thomas Jefferson directed the first one in 1790. But the process for choosing questions has never been spelled out. The two-page form mailed out last month to every household in the country—"10 questions in 10 minutes"—asks for basic demographic information. For most social science and survey researchers, however, the meat lies in the second arm of the census, called the American Community Survey (ACS). It's a monthly sampling of 3 million households a year that asks residents 75 questions about everything from their incomes and disabilities to how long it takes them to get to work.

The ACS replaced what used to be called the "long form," a detailed questionnaire that went to one in every six households once a decade along with the 10-question "short" form. The 2000 Census was the last one to employ the long form; the monthly ACS succeeded it in 2005. Except for the question about racial identity, the contents of the short form seldom change. But the ACS is a living document. So the procedure for determining its content can have a big impact on what information is collected.

One significant change since the ACS replaced the long form has been the expansion of the executive branch into shaping the questions—an area that historically has been the sole purview of Congress. Federal officials say the shift, triggered by a push from the National Science Foundation (NSF) for a new question on the ACS, promises to improve the overall quality of data gathering. At the same time, Congress isn't likely to relinquish its role in this intensely personal communication with the American public.

Watching anxiously from the sidelines are the social science and survey research communities that rely upon the data. "It's one of the great black holes of all time," says Ed Spar, executive director of the Council of Professional Associations on Federal Statistics, about how the process looks to outsiders. He and others hope that the new procedures, still being ironed out, will be well defined and more transparent.

A matter of degree

Lynda Carlson, the head of NSF's Division of Science Resources Statistics, has seen the process from up close. In 2005 the career civil servant, known fondly to her peers as the Energizer bunny of the federal statistics community, had an idea to improve NSF's National Survey of College Graduates (NSCG). The longitudinal survey, conducted for NSF by the Census Bureau, follows the career paths of those with scientific training or in scientific occupations. Its sample is drawn from the long form of the decennial census, which asks residents for their highest level of education attained.

The survey helps NSF carry out its mission to monitor the health of the U.S. scientific workforce. Unfortunately, the census question didn't distinguish those who majored in biology or chemical engineering from those who studied, say, English literature. As a result, the Census Bureau used proxies—type of job, income, and so on—to create the pool that NSF wanted tracked. Indeed, only one in three graduates surveyed in past years had majored in a relevant science and engineering field or was working in the sector. Wouldn't it be great, thought Carlson, if the census also asked people for their field of degree?

Historically, it has taken an act of Congress to place a question on the census. Although that legislative mandate isn't codified anywhere, Congress has long operated on the principle that its members, because they are elected by the populace, should have the final say in determining the content. "If there wasn't legislation, it didn't go on the long form," explains Susan Schechter, chief of the ACS office at the Census Bureau.

Of course, those decisions are subject to the vagaries of the political process. Sometimes Congress bows to the wishes of an individual member. That happened when then-Senator Bob Dole (R–KS) won approval more than a decade ago for a three-part question about grandparents who provide care for their grandchildren. Other times it responds to outside pressure, as when the telecommunications industry and federal communications officials campaigned successfully for a census question on Internet and computer access as part of the 2008 Broadband Data Improvement Act.

Accordingly, Carlson's first step in 2005 was to contact the Senate panel that oversees NSF. She eventually persuaded its staff to include a mandate for an ACS question about field of degree in a bill then under consideration by Congress reauthorizing NSF's programs. But the idea ran into opposition from the House subcommittee that oversees the census. "We hadn't even had a year of validated data from ACS," recalls John Cuaderes, then staff director of the House panel. "Adding a question to a new survey creates the possibility of screwing it up."

Length was also an issue. As any survey researcher will tell you, making a questionnaire longer—ACS is already 28 pages—can undermine the quality of the answers. In particular, it can mean a lower response rate. But because filling out the census is mandatory—nonresponders can be fined up to $5000—the chief impact of a longer survey is that the government must spend more money to chase down those who didn't answer the first time around.

Legislators who had fought for the ACS as an improvement to the decennial census were wary of the fiscal impact of adding a

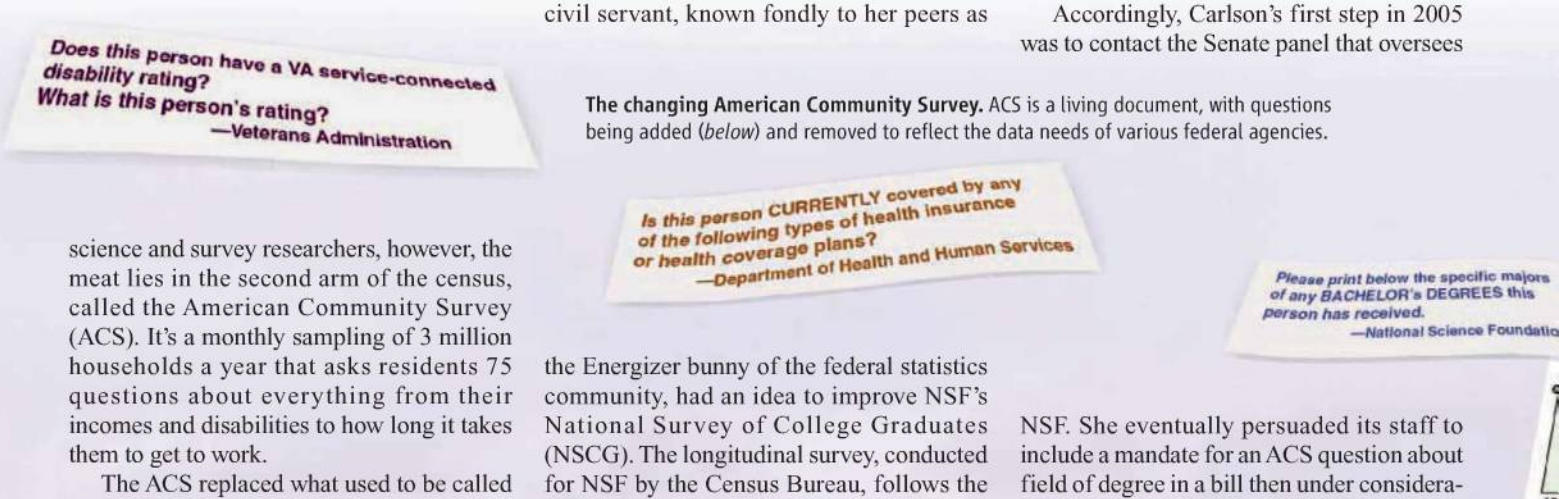

The changing American Community Survey. ACS is a living document, with questions being added (*below*) and removed to reflect the data needs of various federal agencies.

question, says Cuaderes, now Republican deputy staff director on the full committee. "If that happens, then the appropriators could say, 'It's getting too expensive. Let's kill it.' " At the same time, he says that legislation seemed like overkill for the problem that NSF wanted to solve.

A gentleman's agreement

Fortunately for NSF, the executive branch had created a process that could, in theory, provide an alternative path for revising the ACS. In 2000, as the Census Bureau retired the long form and began gearing up for the ACS, the White House set up an interagency statistical committee under the Office of Management and Budget (OMB) to oversee this new survey instrument. After first documenting the legislative history of each question on the ACS, OMB in 2003 asked each of the 30 agencies to identify questions that might need to be revised, dropped, or added, along with a 5-year timeline for possible implementation with the consent of Congress.

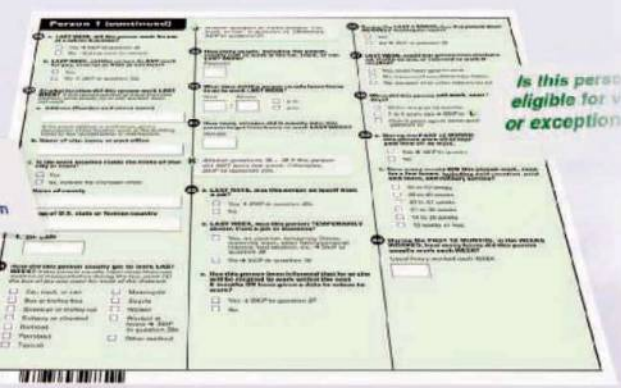

A 1980 law already gives OMB the authority to vet almost any request for information from a federal agency to make sure that it doesn't impose an undue burden on the public. But that authority had never been applied to the census. "Initially, we adhered to the existing policy that any changes [in the census] would require legislation," explains an OMB official familiar with how the committee operates.

Although he had balked at NSF's request for legislation, Cuaderes agreed to look for another way to get a field-of-degree question on the ACS. That search eventually led to discussions with OMB about how to handle an agency request that hadn't been enshrined in legislation.

A deal was eventually struck in 2006. Simply put, says Schechter, "we came up with a gentleman's agreement that OMB would take the heat and be responsible for deciding what would be added to the ACS. And the federal government, through OMB, agreed it would be very restrictive [about using that authority] because of the mandatory nature of the collection."

That agreement gave NSF the green light to design and field-test its question. Finally, in January 2009 the field-of-degree question appeared on the ACS. The new mechanism also allowed the Census Bureau to move ahead with three new questions that had passed muster with the interagency review. The questions—on health insurance coverage, marital history, and disabilities stemming from military service—made their ACS debuts in 2008.

Schechter says this second, parallel track gives the federal survey community a larger role in the decision-making process and promises to improve the value of the ACS to the government. The pending question on Internet access, mandated by the 2008 broadband law, she suggests, might have benefited from such vetting. "Is that the most important new question to ask?" she says. "Maybe, but it never even got reviewed by the federal committee."

To be sure, even survey researchers can disagree about the suitability of a particular question. For example, statistics council head Spar isn't sure that ACS is the right place for NSF's question on field of degree. "Why do you need that information at the tract level [the smallest unit of the census, typically a portion of a city block]?" he asks. "What are they going to do with it?" Carlson says that NSCG needs to report on tiny population subgroups, say, female Hispanic geologists (their identities remain confidential). "Over time," she adds, "it will also give us better geographic estimates."

Once the 2010 Census is history, the federal statistics committee plans to discuss other ways to improve the ACS. One option is annual or biennial supplements that explore a particular topic, say, education or volunteerism, but that do not become part of the permanent ACS. "The key is to keep the burden down and keep the quality up," says the OMB statistics official. "Despite the public's willingness to cooperate, people have their limits. The ACS is a national treasure, and we risk [diminishing] the quality of the survey if we load it up."

–JEFFREY MERVIS

ScienceInsider

From the *Science* Policy Blog

The United Kingdom plans to create the **world's largest marine reserve**—an area larger than California—in its territorial waters in the Indian Ocean. The Chagos Archipelago boasts the largest coral atoll in the world and many smaller reefs. http://bit.ly/b5pGOY

The National Science Foundation has quantified for the first time the **scope of interdisciplinary research** by asking U.S. graduate students about their doctoral dissertations. http://bit.ly/aADZw4

The editor of ***Medical Hypotheses***, who got into hot water for publishing a paper by AIDS "denialist" Peter Duesberg, could be sacked unless he changes reviewing practices at the journal. http://bit.ly/aJxdgW

Agricultural officials in California have abandoned plans to eradicate the **invasive light brown apple moth** and now hope to "contain, control and suppress" the pest. http://bit.ly/9KAlEb

A U.K. parliamentary panel examining the **hacking of e-mails** at the University of East Anglia's Climatic Research Unit says researchers should make all of their evidence available to global warming skeptics and the public. http://bit.ly/d33ePl

The leading **public research universities in the United States** are holding five regional meetings this month as part of a campaign for increased government support. http://bit.ly/bCzkcp

For the fifth consecutive year, the **number of international students applying to U.S. graduate schools** has risen, fueled by a boom in Chinese higher education. The trend erases a steep drop in 2003–05 attributed to tightened visa procedures. http://bit.ly/cJfS6v

For the full postings and more, go to **news.sciencemag.org/scienceinsider**.

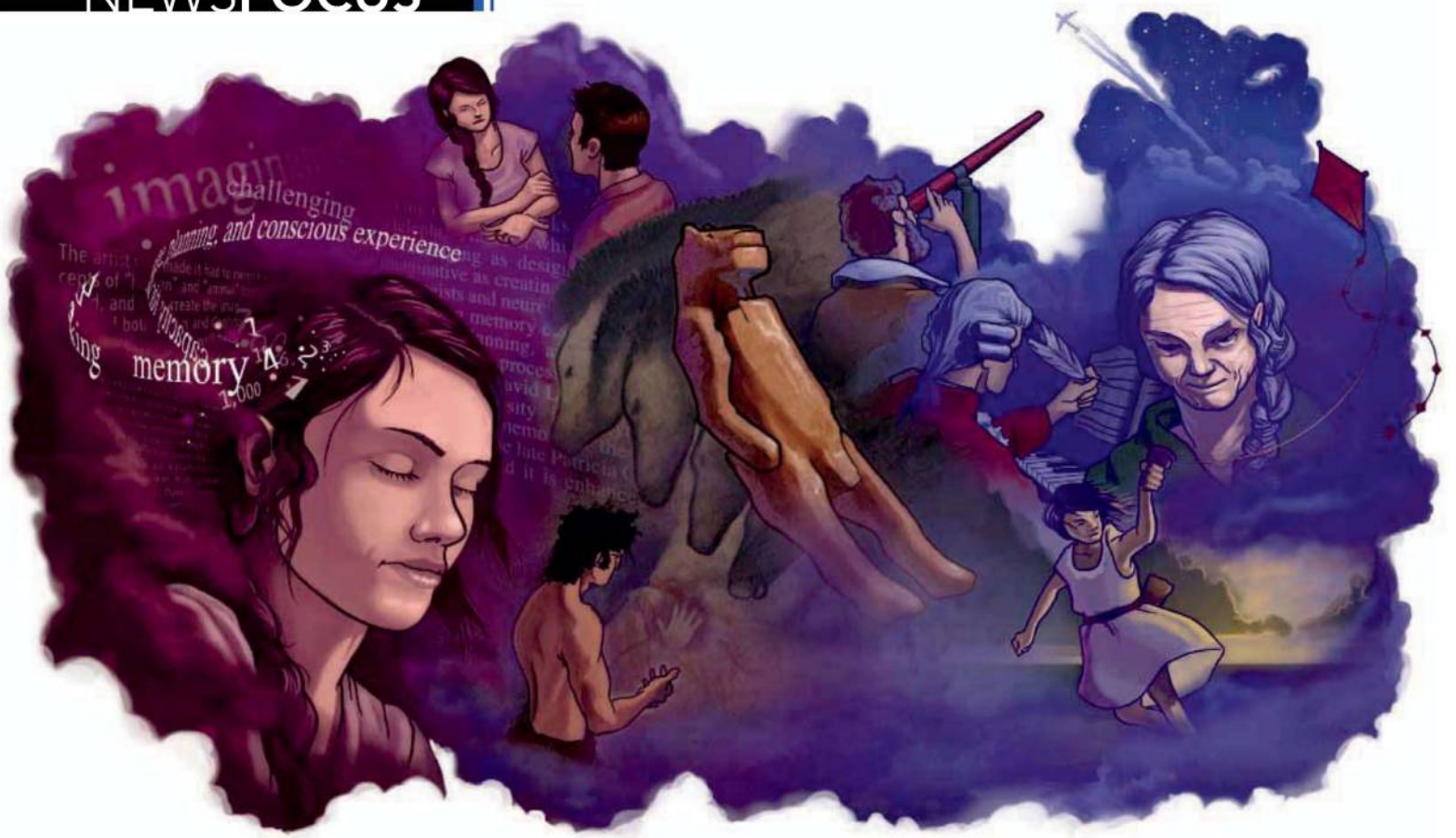

Did Working Memory Spark Creative Culture?

A provocative model suggests that a shift in what and how we remember may have been key to the evolution of human cognition

COLORADO SPRINGS, COLORADO—About 32,000 years ago, a prehistoric artist carved a special statuette from a mammoth tusk. Holding the abstract concepts of "human" and "animal" in his or her mind, the artist created an imaginary beast with the body of a human and the head of a lion. Archaeologists found the 28-centimeter-tall figurine in hundreds of pieces in the back of Germany's Hohlenstein-Stadel cave in 1939, and after World War II, they put the fragments back together, reconstructing the ancient artwork.

Today, archaeologists hail the "Lion Man" as one of the earliest unambiguous examples of artistic expression, a hallmark of modern human behavior. The figurine "has acquired an iconic status for modern archaeologists as profound as it must have been for the original artisan," wrote Thomas Wynn and Frederick Coolidge, both of the University of Colorado, Colorado Springs, in a paper last year. Wynn and Coolidge argue that the figurine's creation—as well as its subsequent reconstruction by archaeologists—is an excellent example of something unique to our species: an enhanced capacity to hold and manipulate information in one's conscious attention while carrying out specific tasks, an ability psychologists call working memory.

Right now you are using working memory as you read this story: You are holding the concept of the figurine, or its image from the illustration above, in your mind. As you go from sentence to sentence, you are also remembering the meaning of each bit of text. And you must pay active attention, shutting out extraneous thoughts such as how your grant application is doing.

We use our working memory for tasks as trivial as remembering a telephone number while we dial it, as technically challenging as designing an airplane, and as imaginative as creating works of art and music. Psychologists and neuroscientists consider working memory essential to the capacity for language, planning, and conscious experience. "Any symbolic processing, such as language, requires it," says David Linden, a psychologist at Bangor University in Gwynedd, U.K. Working memory is "the blackboard of the mind," as the late Patricia Goldman-Rakic of Yale University put it.

In the view of Wynn and Coolidge—an archaeologist and a psychologist who form an unusual scientific partnership—a stepwise increase in working memory capacity was central to the evolution of advanced human cognition. They argue that the final steps, consisting of one or more genetic mutations that led to "enhanced working memory," happened sometime after our species appeared nearly 200,000 years ago, and perhaps as recently as 40,000 years ago. With enhanced working memory, modern humans could do what their ancestors could not: express themselves in art and other symbolic behavior, speak in fully grammatical language, plan ahead, and make highly complex tools.

"The enhancement of working memory opened up a whole load of new possibilities

Online
sciencemag.org
Podcast interviews on this package of articles.

CREDIT: M. TWOMBLY/SCIENCE

Blackboard of the mind. Working memory is key to conscious thought.

for hominids," says anthropologist Dwight Read of the University of California, Los Angeles. "It was a qualitative shift."

However, others question how well the archaeological record supports Wynn and Coolidge's ideas. The pair argue that the final boost in working memory capacity came late in human evolution, whereas many archaeologists see the stirrings of complex behavior thousands of years earlier (see p. 164)—and some say, even in other species. "Enhanced working memory capacities can be observed in both modern humans and Neandertals," insists Anna Belfer-Cohen, an archaeologist at The Hebrew University of Jerusalem. "Working memory does not appear to be the major shift" in human evolution.

Despite the critics, Wynn and Coolidge's ideas are increasingly popping up in scientific journals. The pair "have made a really big splash," says Philip Barnard, a cognition researcher at the University of Cambridge in the U.K. This month, *Current Anthropology* devotes a special online supplement to the topic, and later in April, Wynn and Coolidge will update their ideas at a major meeting on the evolution of language in the Netherlands. The theory makes sense to many. "It is the most impressive, explicit, and scientifically based model" so far, says archaeologist Paul Mellars of the University of Cambridge.

Memorable pair. Thomas Wynn (*left*) and Frederick Coolidge hypothesize that working memory shaped human evolution.

Thanks for the memory

For as long as anyone can remember, researchers have been debating how many kinds of memory there are. In the late 19th century, American psychologist William James proposed two types of information storage: a temporary store that James called "the trailing edge of consciousness" and a more durable and even permanent store. His model was not immediately adopted, but by the 1960s, experiments with human subjects, including patients with amnesia or brain damage, had convinced many researchers that there are two types of memory: short-term and long-term.

It soon became clear that short-term memory was not just a passive, temporary storehouse. Experiments showed that retaining information in conscious memory required active "rehearsal" to keep it there, as we do when we repeat a telephone number in our minds until we have the chance to write it down. Temporary memory is a dynamic part of the conscious mind, engaged in all sorts of work, including processing and manipulating information. In 1974, psychologists Alan Baddeley and Graham Hitch of the University of York in the U.K. proposed a new model, replacing the concept of short-term memory with what they called working memory.

Baddeley and Hitch argued that working memory had three components: a "phonological loop," which stores and processes words, numbers, and sounds; a "visuospatial sketchpad," which stores and processes visual and spatial information; and a "central executive," which focuses the mind's attention on the information in the other two systems and controls how it is used. In 2000,

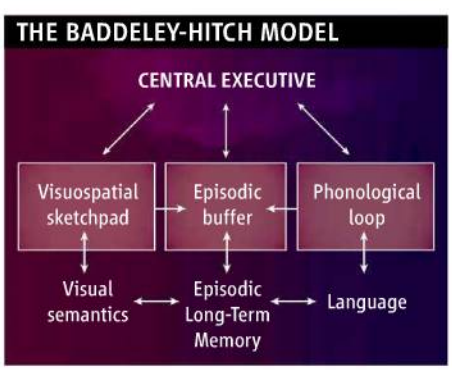

Memory modules. This view of working memory remains influential.

Baddeley added a fourth component, an "episodic buffer," which serves as an interface between the other three systems and long-term memory (see diagram, above).

Central to the model's experimental approach were so-called dual-task exercises, in which subjects had to do more than one memory-taxing thing at a time. Such experiments showed that some tasks interfere with each other: You memorize a list of words less efficiently when you are also reciting a series of numbers. But other tasks are apparently separate: You can remember the colors of items while reciting numbers.

This research convinced Baddeley, Hitch, and many others that words and numbers are stored in one kind of temporary memory buffer while visual information goes into another. Meanwhile, the central executive is thought to control the flow of information between working memory's temporary storage buffers, long-term memory, and other cognitive functions. Indeed, although the Baddeley model now has competitors (see sidebar, p. 162), most researchers agree that dynamic concepts of working memory, rather than passive storage, best explain sophisticated human cognition, which requires that we be masters and not slaves of our memories.

Working memory allows us to juggle the past and the present in our conscious minds, says Jackie Andrade, a psychologist at the University of Plymouth in the U.K., and so is critical to complex behavior. We can "aim for future goals rather than just being driven by our current goals or environment," she says. Or, as psychologist Nelson Cowan of the University of Missouri, Columbia, puts it, "Working memory holds the plan until we can execute it."

Wynn and Coolidge acknowledge that earlier hominins, and even apes, had enough working memory to carry out certain skilled tasks. The difference was one of degree, they say, and came in evolutionary stages. For example, the 1.8-million-year-old *Homo erectus*, creator of the first known bifacial tools, probably had more working memory than apes and australopithecines. The first big jump in working memory capacity, Wynn and Coolidge contend, came with the 650,000-year-old *H. heidelbergensis*, which made highly symmetrical hand axes—a talent that probably required holding a mental template of the tool in the mind while making it (*Science*, 6 February 2009, p. 709).

A meeting of minds

Wynn and Coolidge note that working memory has two key features that could make it subject to natural selection: It varies among individuals, and that variation may have a genetic basis. Numerous studies have found a close correlation between working memory capacity and performance in cognitive tasks such as language learning and reasoning ability. In a 2004 review, psychologist Randall Engle of the Georgia Institute of Technol-

CREDITS (TOP TO BOTTOM): EMILY WYNN; ADAPTED FROM ALAN BADDELEY

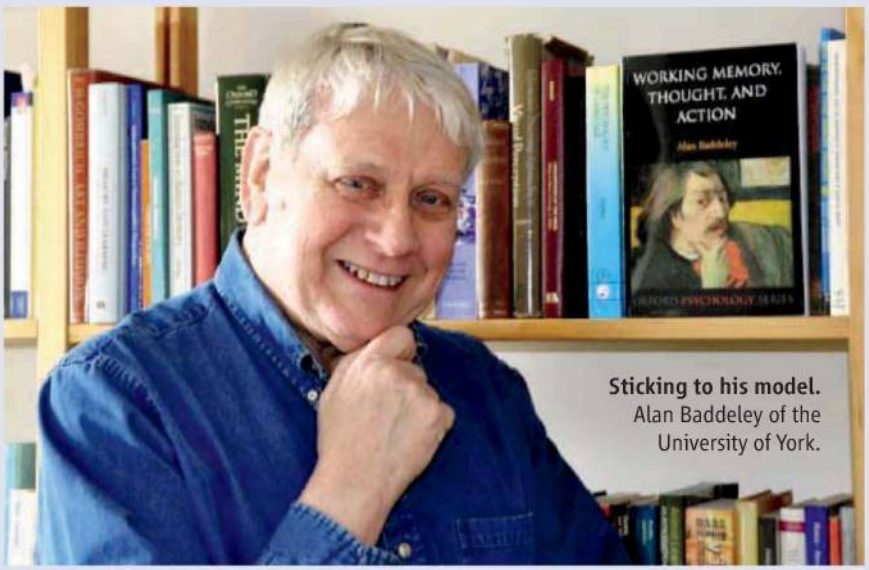

Sticking to his model. Alan Baddeley of the University of York.

Does 'Working Memory' Still Work?

The idea that a better working memory made *Homo sapiens* smarter than its ancestors is attracting attention from psychologists, archaeologists, and neuroscientists alike (see main text, p. 160). The architects of the hypothesis, Thomas Wynn and Frederick Coolidge of the University of Colorado, Colorado Springs, base their idea on a model of working memory proposed 35 years ago by two British psychologists. That model, devised by Alan Baddeley and Graham Hitch of the University of York in the United Kingdom, "was seminal" in memory research, says psychologist Randall Engle of the Georgia Institute of Technology in Atlanta. But now he and other researchers are challenging some of its basic tenets. "The Baddeley model has pretty stiff competition now" from alternative models, says psychologist Jackie Andrade of the University of Plymouth in the U.K.

Baddeley proposed that working memory includes separate, temporary storage areas for verbal and visual information, plus a central executive to direct information flow. Today, a key issue is whether our temporary memories are actually stored in buffers separate from long-term memory or if these simply represent "activated" parts of long-term memory.

The latter model is "more neurologically feasible," says psychologist Nelson Cowan of the University of Missouri, Columbia, who cites recent brain-imaging studies that he says contradict Baddeley's model. "The neural data don't support a buffer model of working memory," agrees Mark D'Esposito, a cognitive neuroscientist at the University of California, Berkeley, whose lab has done such experiments. Different parts of the brain are activated depending on what kind of working-memory task is being done, says D'Esposito, who concludes that "working memory" involves many different parts of the brain working together. "It doesn't appear that information is transferred to some other location, like RAM in a computer," he says.

The field is split, with many Europeans and psychologists tending to favor the Baddeley model, whereas many Americans and neuroscientists tend to favor activation models. "There are pretty much two traditions," says Andrade.

Baddeley finds the brain-imaging studies inconclusive. They "result in a veritable plum pudding of different areas activated by apparently similar tasks, whereas the [psychological and clinical] evidence has been broadly coherent and very fruitful over a 35-year span," he says. Psychologist David Linden of Bangor University in Gwynedd, U.K., also sees no reason to jettison the Baddeley model. He says working memory "is preserved in many patients who have severe amnesia and cannot encode new material into long-term memory. And it can deal with information that has no relevant representation in long-term memory, such as characters of an unknown language or novel sounds."

Although Wynn and Coolidge favor Baddeley's model, they say they are not wedded to it. "I don't think our approach stands or falls with the Baddeley model," says Wynn. Coolidge agrees: "Our puzzle for the future lies more in explaining what enhanced working memory did for humans rather than in strict lab tests of Baddeley's components." **–M.B.**

ogy in Atlanta and his co-workers identified nearly 40 cognitive tasks significantly correlated with working memory capacity. Some researchers have proposed that intelligence tests actually measure working memory capacity, although this is controversial. And a number of studies conclude that variances in working memory capacity, for example those linked to learning disabilities, could have a genetic component.

It was evidence for such genetic variation that first brought Coolidge and Wynn together. In 2000, Coolidge published a twin study suggesting a strong genetic correlation between attention deficit hyperactivity disorder and deficits in what researchers call "executive functions"—a range of mental abilities such as forming goals and planning ahead.

Coolidge, who had long been interested in archaeology, went to see Wynn, whom he then knew only casually. Wynn, known for analyzing the mental steps in hominin toolmaking, was attracted by Coolidge's suggestion that executive functions were key to modern human evolution.

In their first paper together in 2001, the pair focused solely on executive functions. But not long afterward, Wynn recalls, "Fred walked into my office and said, 'It's working memory.' " Coolidge had realized that there was considerable overlap between "executive functions" and the "central executive" in Baddeley's model. The best way to explore the evolution of modern human cognition, the pair decided, was to adopt the Baddeley model and see where it led them. "[It's] probably the most cited cognitive model of the past 30 years," Wynn says. "It gave us a theoretical model that had punch."

They scoured the archaeological record and began to spin out a series of papers contending that modern humans had greater working memory capacity than earlier hominins. For example, they argued in 2004 in the *Journal of Human Evolution* that Neandertals fell short mainly in areas such as complex hunting strategies and symbolic expression, which required enhanced working memory. They point out that for 200,000 years, Neandertal stone-tool technology, although skillful, changed little. And even when it did shift, it was "on a scale and at a rate that would appear to rule out conscious experimentation and creativity, the stuff of enhanced working memory," Wynn and Coolidge wrote.

The pair also cited the relative lack of evidence for Neandertal symbolic behavior, such as the elaborate burials and artistic expression typical of modern humans, as support for their conclusion. Neandertal cognition, they contended in another 2004

CREDIT: LINDSEY BOWES

paper, was like "modern human thinking" but with "a single piece missing": enhanced working memory.

Not everyone agrees with this evaluation of Neandertals, but Wynn and Coolidge see other examples of uniquely modern human behaviors that they think required enhanced working memory. Chief among them is the iconic Hohlenstein-Stadel figurine. "That is a beautiful archaeological example of their model," says archaeologist Lyn Wadley of the University of the Witwatersrand, Johannesburg, in South Africa. Wynn and Coolidge also cite research at Niah Cave in Borneo suggesting that about 40,000 years ago, modern humans deliberately set forest fires to nurture tubers and other edible plants and perhaps also trapped pigs. This "managed foraging" is evidence for advanced planning, they say.

The pair also sees enhanced working memory at work in the bone "tally sticks" found at sites in France and the Democratic Republic of the Congo. These notched objects date to 28,000 years ago or later and may have been "external memory devices" used to record something, according to work by archaeologist Francesco D'Errico of the University of Bordeaux in France. Wynn and Coolidge think that the sticks were used to perform calculations and perhaps to enhance working memory by transferring it to a physical object.

In choosing these examples, however—none of which date to earlier than 40,000 years ago—Wynn and Coolidge have bucked an increasing trend in archaeology. Many researchers now interpret artifacts such as 75,000-year-old beads and etched ochre at Blombos Cave in South Africa and 90,000-year-old beads at Qafzeh Cave in Israel as evidence that symbolic expression has much deeper evolutionary roots.

"They may have painted themselves into a corner by setting down a date of 40,000 years for modern cognition," Wadley says. Miriam Haidle, an archaeologist at the University of Tübingen in Germany, agrees. "Everything must start much earlier than they think," Haidle says. "Working memory was a neurological complex that slowly developed over at least 2 million years."

Wynn and Coolidge acknowledge that their model swims against the current tide of early claims for modern human behavior. But they argue that the Blombos artifacts may have represented only a simple sort of symbolism, such as that used to mark social identities, rather than the fully realized symbolic behavior typical of later modern humans. "We just think the late, jerky explanation requires fewer assumptions and caveats and takes the archaeological record seriously, instead of trying to explain it away," says Wynn.

What was that number? Chimpanzees are better than humans at some memory tasks.

Still, Wynn told *Science* that he is now "mostly convinced" by evidence, reported by Wadley last year, for the use of ochre adhesives to haft stone tools at the 70,000-year-old South African site of Sibudu, which suggests enhanced working memory. He and Coolidge say that the genetic mutation or mutations they propose may not have been as late as 40,000 years ago. They're open to other scenarios, such as that the cognitive advance was gradually manifested in the archaeological record, or that the genetic variants coding for enhanced working memory did not rise to high frequencies in human populations until more recently.

From past to future

While Wynn and Coolidge have focused their attention on relatively recent enhancements in working memory capacity, other researchers trace its evolution much further back in time—back to the split between humans and chimpanzees, about 5 million to 7 million years ago. In a 2008 paper in *Evolutionary Psychology*, UCLA's Read marshaled several lines of evidence suggesting that chimpanzees have much more limited working memory capacity than modern humans. He argued that the common ancestor of humans and chimps also had limited working memory capacity and limited ability to engage in what linguists call recursion, the embedding of phrases within each other, as in this sentence. Many researchers consider recursion the hallmark of modern human language.

However, primatologist Tetsuro Matsuzawa of Kyoto University in Japan claimed in 2007 that some young chimps are better than adult humans at a memory task using numbers flashed on a computer screen. "Seeing is believing," Matsuzawa told *Science*. "They are better than us in this memory test."

Read argues that this test measures a simpler form of passive photographic memory rather than full-fledged working memory. Wynn agrees that the chimp studies are not comparable with the dual-task experiments done with humans. "The tests included no distractions" to engage the central executive and explore the ability to focus attention on the task at hand, Wynn says.

Meanwhile, the working-memory concept continues to inspire others. Psychologists Thomas Suddendorf of the University of Queensland in Brisbane, Australia, and Michael Corballis of the University of Auckland in New Zealand think working memory is crucial to "mental time travel," the ability to harness memories of the past to imagine the future. They argue that this capacity was crucial to the evolution of language. Harvard University psychologist Daniel Schacter agrees. On the basis of brain-imaging studies and other research, Schacter and Donna Rose Addis of the University of Auckland have concluded that the same neural networks are implicated in both remembering the past and imagining the future and that both processes probably involve something like Baddeley's proposed episodic buffer. "Working memory is critically important for constructing simulations of future events," Schacter says.

Wynn and Coolidge, who routinely cite Schacter and Addis in their own papers, say that a jump in working memory capacity was also key to the construction of modern human symbolism and artistic expression, including the ability to imagine things that have never existed and never will, like the Lion Man. "We may have the exact timing wrong and the exact nature of the genetic events" wrong as well, Coolidge says. "But something happened that was less than gradual in the evolution of the human mind."

–MICHAEL BALTER

CREDITS: COURTESY OF TETSURO MATSUZAWA

ARCHAEOLOGY

Did Modern Humans Get Smart Or Just Get Together?

The first archaeological signs of art and symbolism may mark new heights of social interaction rather than a cognitive leap

When did humans start to do the things that make us human? The archaeological record is the obvious place to find out, but it presents a puzzle: About 40,000 years ago in Europe, when modern humans had moved into the continent, there was a burst of creativity expressed in everything from cave paintings to figurines to jewelry and complex tools. Some researchers have argued that this explosion of artistic material culture reflects a leap in human cognition—the point when we finally got smart enough to think symbolically and craft complex tools, perhaps because of an advance in working memory (see p. 160).

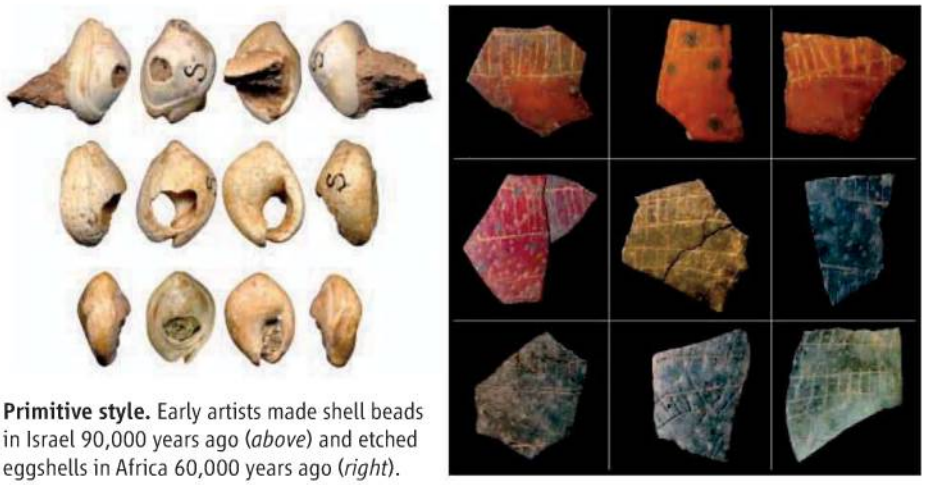

Primitive style. Early artists made shell beads in Israel 90,000 years ago (*above*) and etched eggshells in Africa 60,000 years ago (*right*).

But over the past decade, signs of such "modern" behavior have been found much earlier. Marine shell beads turn up in Israel about 90,000 years ago, then disappear. Chunks of red ochre with geometric scratchings and tiny shell beads pop up about 70,000 years ago or more in Africa and then vanish; etched ostrich eggshells then appear about 60,000 years ago. Complex behavior seems to flicker in and out of the record (*Science*, 6 February 2009, p. 709).

The pattern is "pretty hard to reconcile with a gene" that conferred a cognitive advance, says anthropologist Robert Boyd of the University of California, Los Angeles (UCLA). So several researchers, including Boyd and Stephen Shennan of University College London (UCL), have suggested another kind of explanation: demography. Perhaps our complex culture does not stem simply from individual cognition but from the shared knowledge we construct in groups, Shennan proposed in a talk at a recent high-level meeting on what makes humans unique.* In this view, complex culture requires a "cultural ratchet"—the cumulative effect of many people's contributions over time, each building on the other. (A recent computer tournament explored the power of such social learning compared with individual innovation; see p. 165.) If so, factors such as population size and structure may have helped to kindle, extinguish, and rekindle modern behavior.

This demography-based theory is an intriguing idea, but researchers have struggled to test it. At the meeting, one presenter backed the idea with simulations, and one with data.

Shennan presented modeling of demographic effects on culture, done with UCL colleagues Adam Powell and Mark Thomas. They simulated how culture would evolve in a population made up of small bands of humans, assuming that people could learn from others how to make a kayak or craft jewelry but that the learning process was not perfect. Larger groups had a higher probability of creating innovations that went beyond the previous best, so individuals in big groups, or who often traveled among groups, had a better chance of learning from an improved version.

In the simulations, bigger populations with more migration showed more cultural accumulation (*Science*, 5 June 2009, p. 1298). Populations that became smaller and more isolated actually lost culture. "We found that you could get stable, lasting differences between regions," Shennan said in his talk. He and colleagues compared their models with the archaeological record, using genetic data from living people to roughly estimate ancient population sizes. They found that the population densities during Europe's cultural flowering 40,000 or so years ago were reached in Africa about 100,000 years ago—not long before cultural complexity arose there.

Next came Boyd, who set out to test the model in the real world. He analyzed data from previously studied traditional societies on 10 islands in Oceania. Working with UCLA graduate student Michelle Kline, he compared the number and complexity of tools used to forage for marine resources on each island.

Boyd and Kline found a clear picture: Islands with bigger populations had more tools, whereas smaller populations had fewer tools. "The results are very strong," says Boyd. "Nothing else seems to matter at all." Shennan was enthusiastic about the data: "The predictions of the model were borne out in a modern situation where you can collect information on all the relevant variables," he says. "That doesn't happen all the time."

Translated into the past, this theory suggests that any cognitive leap happened perhaps 90,000 years ago or earlier and that bursts of complex culture may reflect bigger populations or more contact among groups. That may be true in Europe of 40,000 years ago, says archaeologist Francesco D'Errico of the University of Bordeaux in France, who thinks modern humans and Neandertals may have had similar cognitive abilities.

Conversely, if climate deteriorated and patches of habitat were farther apart, more isolated groups might lose culture. That happened on the island of Tasmania, where people lost the ability to craft bone tools and boats when they were isolated by rising sea levels about 10,000 years ago, Boyd notes.

At this point, says Shennan, theory and data "add up to a very strong alternative to the cognition model. Now we need more model development, testing, and data collection." But workshop co-organizer Curtis Marean of Arizona State University, Tempe, points out that cognition also plays a role, for example, influencing the rate of innovation in Shennan's models. "It's not just demography or cognition. We need to pull all of these together."

–ELIZABETH CULOTTA

*Human Uniqueness and Behavioral Modernity Workshop, Arizona State University, 20–22 February.

CREDIT (LEFT TO RIGHT): M. VANHAEREN *ET AL.*, *SCIENCE* **312**, 5781 (23 JUNE 2006); COURTESY OF PIERRE-JEAN TEXIER, DIEPKLOOF PROJECT

CREDIT: M. TWOMBLY/SCIENCE

CULTURAL EVOLUTION

Conquering by Copying

A computer tournament reveals the benefit of copying someone else's actions over solving a problem solo, a finding that has implications for cultural evolution

Lost in a jungle? Survival may depend on copying others or trial-and-error learning.

Suppose you find yourself in an unfamiliar environment where you don't know how to get food, avoid predators, or travel from A to B. Would you invest time working out what to do on your own, or observe other individuals and copy them? If you copy, who would you copy? The first individual you see? The most common behaviour? Do you always copy, or do so selectively?

What would you do?

With those provocative words, posted on a Web site and included in a flyer sent to colleagues and academic departments around the world in late 2007, Kevin Laland threw down the gauntlet on an international competition that he hoped would accelerate his academic field. Laland, an evolutionary biologist at the University of St. Andrews in the United Kingdom, is part of a consortium that has a €2 million grant to explore how human culture evolves. A crucial part of this issue is how people develop new behaviors. To probe this question, Laland and the rest of the consortium wanted to examine the relative importance of social learning, the acquisition of behaviors from watching other people, versus individual innovation.

The ability to learn from others is central to the evolution and persistence of culture, and it is viewed as part of the reason humans have come to dominate the planet. But, notes Laland, "it has proven quite tricky in a formal mathematical sense to link social learning to our success as a species."

Equally important, it hasn't been clear how people best learn socially. Sometimes individuals copy the behaviors of others seemingly at random; other times they appear to decide who to copy based on the level of prestige of the individual. "We find evidence of different rules, but it was frustrating because we didn't know which of these rules was the best," Laland says.

To address that question, the consortium decided to host a tournament, with a €10,000 prize, in which all comers would pit computer programs incorporating social-learning strategies against each other. "It was a gamble," Laland recalls. "My biggest fear was that nobody would participate."

The gamble paid off. More than 100 teams, including a few from high schools, competed—"far more than we even hoped for," says Laland. The analysis of the competition, reported on page 208, "addresses in a clearly new way some of the questions that have been nagging at the field of evolutionary social learning for more than 2 decades," says Luc-Alain Giraldeau, a behavioral ecologist at the University of Quebec, Montreal, in Canada.

A simple approach, from a surprising entry, won hands down. Most researchers had thought that a mix of learning on one's own and social learning would be the best strategy. Yet a pair of graduate students won the contest with a strategy heavily tilted toward imitation rather than innovation (see sidebar, p. 166). "The main take-home message is that it pays to imitate success, except when there is evidence that what has been successful recently is no longer working well," says Robert Axelrod of the University of Michigan, Ann Arbor.

The tournament's results, say some researchers, have implications for human cultural evolution. "It implies that our success as a species rests heavily on the right social and networking skills of knowing who, what, and when to copy," notes Samuel Bowles, an economist at the Santa Fe Institute.

Getting the game together

As strange as a face-off might seem for science, there's a powerful precedent for a tournament giving the study of human behavior a much-needed jolt. In the 1980s, Axelrod organized a competition to get a handle on why cooperation evolves. He challenged contestants to engage repeatedly in the prisoner's dilemma—in which two prisoners must choose between squealing on one another or cooperating in their refusal to talk to the police. "The strength of a tournament is that it provides the means to achieve insights that can be totally unexpected by both the contestants and even the designers of the tournament," says Axelrod.

In his contest, involving 28 entrants, a simple tit-for-tat strategy—cooperate if your fellow prisoner cooperates, otherwise don't—proved the most effective. The tournament "was enormously influential because before, not many people were studying the evolution of cooperation," says Laland, "It kick-started the field."

Laland felt the study of social learning would benefit from a similar boost. He tapped St. Andrews postdoctoral fellow Luke Rendell to design the tournament and recruited help from experts in social learning, cultural evolution, and game theory. Rendell's first task was to figure out a problem to be solved by contestants. The cooperation field had already accepted the prisoner's dilemma as relevant, but there was no such theoretical tool for assessing the adaptive value of social learning in a complex environment.

After much discussion, Laland's team decided to center the tournament on a learn-

Scheming. Daniel Cownden (*foreground*) and Timothy Lillicrap worked out a winning social-learning strategy.

A Winning Combination

The chance to spend 4 months designing a computer program to compete in a social-learning tournament (see main text, p. 165) immediately appealed to Timothy Lillicrap, a graduate student in computational neuroscience at Queen's University in Kingston, Canada. "So much time in science is spent getting half-answers to complicated questions, which often take decades to appreciate fully. The tournament was an opportunity to work on something with a hard and fast goal and a hard and fast answer," he recalls.

Lillicrap teamed up with Daniel Cownden, a fellow graduate student in mathematics, and together they obsessively spent hundreds of hours perfecting their social-learning strategy. Although they lacked experience in social-learning research, Lillicrap knew about figuring out the most efficient way to accomplish a task and estimating outcomes based on what known data is available, whereas Cownden understood evolutionary game theory. This mix of knowledge proved a winning combination, as their program easily beat about 100 others. "Certainly a reason for our success was the balance between Tim's concrete, computer science, 'code it and see' approach and my abstract, mathematical, 'hem and haw' approach," says Cownden.

Early on, the pair set up their own in-house competition according to the tournament's rules. The duo met weekly to face off with the latest iterations of their computer programs. The loser had to make the winner dessert but got to see the winner's program and crib from it if desired. They quickly homed in on potentially good approaches. "We were one of the few entries which noticed that it is virtually always better to observe others rather than gather information through innovation," says Lillicrap.

The two students created a player that had access to all the hidden variables, allowing it to "cheat" and make nearly perfect decisions. By recording how this superplayer worked the game, they obtained information needed to train a neural network that would underpin their final strategy. The cheater figured out, for example, how to evaluate whether to learn something that might be useful later on or just use a behavior already in its repertoire.

Cownden and Lillicrap called the strategy they entered "discountmachine" because it discounted less certain future rewards for more guaranteed immediate gains. That involved weighing how fast the environment will change—if it's changing fast, then past social learning gets outdated quickly—and how good, and reliable, the payoffs for an action were. Based on that information, discountmachine decides whether to do what it already knows how to do, getting an immediate reward, or whether to see what someone else is doing and learn from them, in the hope of getting what might be a bigger reward later.

Cownden and Lillicrap were definitely dark-horse candidates going into the contest. "We were quite surprised nobody from a social-learning lab had gone on to win," says Luke Rendell, an organizer of the tournament from the University of St. Andrews in the United Kingdom. "You have to take your hat off to them."

For Cownden, the tournament has made a big difference in his graduate studies. He wants to develop a better method for comparing the value of information with the value of actions in making decisions and plans to combine decision theory with evolutionary game theory to do so. In this way, he hopes to come up with a better way to approach problems such as that offered by the tournament. "My research goals were vague and unformed when I encountered the tournament. Now they are focused and clear." **–E.P.**

ing problem called the restless multiarmed bandit. The name is inspired by the "one-armed bandit"—the slot machine—in which pulling a lever sets off a game of chance. In the tournament's case, the multiple "arms" represent different abstract "behaviors"—100 possible ones in all, each associated with a different payoff. The challenge is to maximize one's payoff over the long run. "I often envisage it as being dropped onto a jungle island, where there are a number of possible ways of getting food," says Rendell. One might learn to gather fruit, hunt, fish, grub for bugs, dig out tubers, et cetera, with varying degrees of success.

In a new environment like a jungle, there are two ways to pick up a new skill: figure out what to do by trial and error or copy what others do after observing or interacting with them. Both learning approaches take time and may or may not lead to a good payoff. But eventually, one builds up a repertoire of useful behaviors.

Rendell created a computer program for running the multiarmed bandit problem under varying conditions. In each scenario, 100 individuals have three options every round: "observe," to learn a behavior by watching another individual; "innovate," to develop one of the behaviors on one's own; or "exploit," which is the equivalent of pulling one of the bandit's arms by engaging in one of the behaviors that have been acquired. Each round, only exploiters get points, so there is always a tradeoff between using an existing behavior and getting a payoff right away or learning a new, and potentially better, behavior that could earn points later.

The simulated individuals in Rendell's artificial world can follow different strategies programmed into them, such as observing more and innovating less, and each round some randomly "die." They are replaced, at times by copies of individuals with more effective learning strategies, as determined by earned points; the process approximates natural selection's survival of the fittest.

Rendell also made it so that he could vary the conditions between rounds. Learning from others might become more or less error-prone, for example. The payoff points associated with each behavior could also increase or decrease over the course of a simulation, adding another element to the changing environment. This twist introduces the possibility that the simulated individuals are acting on outdated information, which changes the dynamic between social learning and innovating.

Ready. Set. Go.

Designing, testing, and refining the tournament's rules took 18 months, and during that time no one in the consortium knew if it would attract entrants. To their relief, the interest was overwhelming; 104 entries from 16 countries

CREDIT: BRONWYN MCLEAN

and more than a dozen disciplines accepted the challenge, each providing a computer program encoding a strategy to guide the behavior of individuals in Rendell's tournament.

The first stage of the tournament, which took place in 2008, pitted pairs of strategies head to head, in more than 5000 contests. Each contest started with a simulation in which one strategy guided the actions of all 100 individuals for 100 rounds. Because of elements of chance built into the simulation—it might take one round or many to acquire a particular behavior by observing someone, for example—each individual accumulated a different point tally over that starting period. Then individuals whose actions are controlled by an opponent's program start to "invade," dropping into the "world" to replace some of the ones that "died." The two strategies would then battle for 10,000 rounds. Over that time, individuals accumulating more points reproduced more, representing an ever-greater proportion of the population. The strategy having the most individuals in the final 2500 rounds was declared the winner of that simulation. The overall winner in each head-to-head contest was determined by tallying 20 such simulations.

This first round, requiring more than 100,000 simulations, winnowed the field to 24 top learning strategies, which then further competed in a round-robin runoff to determine the top 10.

In early 2009, the second stage, the "melee," pitted all 10 finalists together in simulations. They played against each other under 15,000 scenarios, each with 10,000 rounds. The whole tournament was only able to be held thanks to more than 65,000 hours of computer time provided by the U.K. National Grid Service.

The winning team, two Canadian graduate students from outside the small world of social-learning research, was a shocker to many. "To be honest, I was quite surprised and annoyed. We really thought we had winning entries because we had run several tournaments using our own strategies before submitting the final versions," says Giraldeau.

The lack of formal training in social learning didn't prevent the winners from creating a strategy that depended more heavily on that process than others. "Very few other strategies realized that it *never* paid to innovate and that observation was the only choice," says Daniel Cownden, one of the two students from Queen's University in Kingston, Canada.

The pair's strategy was "exceptionally clever," says Robert Boyd, a biological anthropologist at the University of California, Los Angeles, who is a consortium member and an author of the tournament report. "In [an] environment where the world is changing, the best strategy is a lot of imitation."

Before the tournament, many researchers had considered imitation limited in value because one might unknowingly waste time copying an outdated or inappropriate behavior. The contest demonstrated that copying was a good approach because those being imitated had likely already decided on—and were enacting—the best strategy they could. "It's kind of parasitizing good ideas that other strategies are generating," says Laland. New, possibly better, behaviors still arise because copying is typically imperfect and errors in imitating a behavior at times yielded improvements.

Like father. Evolutionary biologist Kevin Laland being copied by his son, a tendency that has helped make humans so successful.

In general, the learning strategies that best succeeded in the tournament shared several features. They emphasized social learning but spent as much time as possible enacting known behaviors and earning payoff points. The results "say clearly that if you spend too much time learning, life will pass you by," says Rendell. Given the conditions set up in the tournament, devoting just 10% of one's time to learning proved to be optimal.

The competition also showed that it is important to assess changes in the environment, such as shifting payoffs for behaviors, and adjust accordingly, even in the middle of a run. Players benefited, too, if they could keep track of when something was learned, because in a changing environment older behaviors were more likely to become outdated.

Bowles suggests that the tournament's results will reorient thinking about what drives human progress. "Most people, when they think about where new ideas come from, think about some eccentric tinkering in a garage or some shy geek playing around with a computer. We think that's how progress gets made," he explains. "What this group of authors [is] suggesting is that this does go on, but what really is decisive is spreading these ideas."

Next step

Richard McElreath, an evolutionary ecologist at the University of California, Davis, agrees that the social-learning tournament was valuable, but he has some reservations. "Simulations and tournaments can be solidly criticized for being both difficult to interpret and potentially misleading," he says.

Consider the strategy ranked 95th in the tournament. Graduate students Shane Gero of Dalhousie University in Halifax and Marianne Marcoux of McGill University in Montreal, both in Canada, based their entry, "higherlearning," on the idea that the education of graduate students often depends on a lot of innovation and individual learning rather than social learning. In the tournament's simulations "being a graduate student was very maladaptive," Gero notes. In real-world academia, however, such behavior arguably does quite well.

Alan Rogers, an anthropologist at the University of Utah in Salt Lake City, suggests that the options in the tournament were also not as clear-cut as they appeared. He proposes that the very act of doing something, or exploiting, involves some subtle elements of individual learning that are not seen as learning per se.

Two more tournaments testing learning strategies are in the works. One will look at what happens when information flow is restricted: for example, when players can observe only a subset of the behaviors. In the other, the players will know something about the age and success rate of players whose behavior they can copy. Things like the perception of experience and prestige "may be very important in human culture," says Laland.

No matter what happens in any subsequent contests, this one's place in history seems assured. "This tournament will invigorate the field by attracting new scholars," says McElreath. "I expect it to become a classic." **–ELIZABETH PENNISI**

CREDIT: GILLIAN BROWN

LETTERS

edited by Jennifer Sills

Food Security: Population Controls

THE SPECIAL SECTION ON FOOD SECURITY (12 FEBRUARY, P. 797) PRESENTS VARIOUS TECHNOlogical fixes to address the problem of sustainably and equitably feeding the 9 billion humans now projected for 2050. However, population controls are not mentioned as a possible strategy. Suggestions for reducing demand are essentially limited to eating less meat and more insects, as well as establishing good governance and eliminating pervasive worldwide corruption. Why not make reduced world population a central part of the proposed mix of solutions for the future?

ARTHUR H. WESTING

Westing Associates in Environment, Security, and Education, Putney, VT 05346, USA. E-mail: westing@sover.net

Editor's Note: We received a number of thoughtful letters on this point. You can read them online at www.sciencemag.org/cgi/eletters/328/5975/169-b. **JENNIFER SILLS**

Food Security: Green Revolution Drawbacks

AS DISCUSSED IN THE SPECIAL SECTION ON FOOD Security (12 February, p. 797), the process of increasing food production and improving its quality to sustain population growth without compromising environmental safety has been called a global green revolution. Science and technology are supposed to play a key role in this revolution by enhancing crop efficiency and food quality, as well as developing alternative protein sources (*1*). A successful green revolution, however, will likely maintain or exacerbate the current rates of population growth, eventually leading to resource exhaustion. Scientists should think critically about the green revolution option, just as they would about any other scientific endeavor. A green revolution is only needed if the current global economy and mode of development must be maintained.

VALENTÍ RULL

Palynology and Paleoecology Laboratory, Botanical Institute of Barcelona, 08038 Barcelona, Spain. E-mail: vrull@ibb.csic.es

Reference

1. J. Beddington, *Phil. Trans. R. Soc. B* **365**, 61 (2010).

Food Security: Beyond Technology

THE AUTHORS OF THE SPECIAL SECTION ON Food Security (12 February, p. 797) make a plausible case that feeding a hungry world requires "rethinking agriculture." Unfortunately, the advocacy on display here implies that technological solutions—any technological solutions—are not only necessary but sufficient. This would be a serious mistake.

Those of us engaged "on the ground" in Africa and elsewhere know very well that the binding constraint on a viable food system is not deficient technology but the institutional (policy) and organizational (bureaucratic) incoherencies—touched on in the Perspective by G. Ejeta ("African green revolution needn't be a mirage," p. 831)—that combine to pervert incentives, render necessary inputs unavailable, defeat the best efforts of dedicated extension agents, and generally encourage individual farmers to retreat into autarchy.

We have nothing against promising technology. We remain, however, incorrigible realists when it comes to the inevitable optimism that offers up the latest technical solution to complex policy and organizational settings and circumstances.

DANIEL W. BROMLEY

Professor Emeritus, Department of Agricultural and Applied Economics, University of Wisconsin–Madison, Madison, WI 53706, USA. E-mail: dbromley@wisc.edu

Food Security: Crop Species Diversity

THE SPECIAL SECTION ON FOOD SECURITY (12 February, p. 797) did not consider the value of crop species diversity. It is agronomically, ecologically, nutritionally, and economically risky and unsustainable to rely almost exclusively on a handful of major crops to provide food for the world's projected 9 billion people by 2050. Indeed, this approach may have been partially responsible for the failure of the green revolution in much of Africa.

Calls for improvement of major crops (described in M. Tester and P. Langridge's

CREDIT: KRISTINA STEFANOVA/USAID

Letters to the Editor

Letters (~300 words) discuss material published in *Science* in the previous 3 months or issues of general interest. They can be submitted through the Web (www.submit2science.org) or by regular mail (1200 New York Ave., NW, Washington, DC 20005, USA). Letters are not acknowledged upon receipt, nor are authors generally consulted before publication. Whether published in full or in part, letters are subject to editing for clarity and space.

Review, "Breeding technologies to increase crop production in a changing world," p. 818), such as Africa's major staples (described in G. Ejeta's Perspective, "African green revolution needn't be a mirage," p. 831), should be extended to include locally important crops. Such crops generally are well adapted to local conditions, form the basis of local food systems, show remarkable resilience to environmental change, and frequently possess unique characteristics that are in demand on the global marketplace (*1*). Although the breeding infrastructure for such species is often severely underdeveloped and underfunded, breeding can be facilitated by linkages to closely related major crops (*2*). Strategies that aim to increase or sustain crop diversity in agricultural production systems have many benefits, including the maintenance of cultural practices and traditional knowledge, balanced nutrition, increased resilience to climate extremes, and exploitation of a broader array of environments for food production.

HANNES DEMPEWOLF,[1]* PAUL BORDONI,[2] LOREN H. RIESEBERG,[1] JOHANNES M. M. ENGELS[2]

[1]The Biodiversity Research Centre and Department of Botany, University of British Columbia, Vancouver, BC V6T 1Z4, Canada. [2]Bioversity International, 00057 Maccarese, Rome, Italy.

*To whom correspondence should be addressed. E-mail: handem@biodiversity.ubc.ca

References

1. R. L. Naylor *et al.*, *Food Pol.* **29**, 15 (2004).
2. R. J. Nelson *et al.*, *Crop Sci.* **44**, 1901 (2004).

Food Security: GM Crops Threaten Biodiversity

THE SPECIAL SECTION ON FOOD SECURITY (12 February, p. 797) appeared to strongly and uncritically support the application and development of genetically modified (GM) technologies and the reliance on agrochemicals. There was little appreciation of the conflicts that are likely to arise. Increased access to expensive nonrenewable inputs, along with increased public acceptance and trust of GM crops, could threaten biodiversity (*1*, *2*) and overall sustainability of agriculture. The articles should have acknowledged the success of non-GM alternatives, such as observed increases in yields resulting from low-input ecological practices on rainfed farms (*3*).

In their Review for the section ("Food security: The challenge of feeding 9 billion people," p. 812), H. C. J. Godfray *et al.* wrote, "we must avoid the temptation to further sac-

CORRECTIONS AND CLARIFICATIONS

Perspectives: "A test for geoengineering?" by A. Robock *et al.* (29 January, p. 530). In the third paragraph, the sentence "Some authors have argued that the effects of polar testing could be confined to the Arctic (*4*)" should read, "Some authors, in simulations designed to control Arctic climate, have confined radiative forcing to the Arctic (*4*)." In the fourth paragraph, the phrase "Even if insertion does indeed have to end up as planetwide" should read "Even if insertion does indeed have to end up affecting a large part of the planet...."

Association Affairs: "Reflections on: Our planet and its life, origins, and futures" by J. J. McCarthy (18 December 2009, p. 1646). In the second sentence of the Fig. 10 caption, the allowed emissions should have been referred to as gray, not blue.

Reports: "Imaging the interaction of the heliosphere with the interstellar medium from Saturn with Cassini" by S. M. Krimigis *et al.* (13 November 2009, p. 971). Because of a conversion error, on p. 973, first column, line 15, the expression ($B^2/2\mu_0 = 0.25$ pPa), and in Fig. 4 the label at lower right $P_B \sim 0.25$ pPa are both inconsistent with the value commonly assumed for the interstellar magnetic field (ISMF) of 0.25 nT (brought to the authors' attention by J. F. Cooper). The value of 0.25 nT for the ISMF corresponds to a pressure of 0.025 pPa. For the hot plasma pressure that was estimated (0.31 pPa) from the measurements to be balanced by the external ISMF, the external field would need to be ~0.9 nT.

rifice Earth's already hugely depleted biodiversity for easy gains in food production." By being held hostage to the agro-industrial "machine," we succumb to that temptation.

REYES TIRADO* AND PAUL JOHNSTON

Greenpeace Research Laboratories, School of Biosciences, University of Exeter, Exeter EX4 4RN, UK.

*To whom correspondence should be addressed. E-mail: r.tirado@exeter.ac.uk

References

1. E. J. Rosi-Marshall *et al.*, *Proc. Natl. Acad. Sci. U.S.A.* **104**, 16204 (2007).
2. J. Schmidt, C. Braun, L. Whitehouse, A. Hilbeck, *Arch. Environ. Contam. Toxicol.* **56**, 221 (2009).
3. J. N. Pretty, J. I. L. Morison, R. E. Hine, *Agric. Ecosys. Environ.* **95**, 217 (2003).

Food Security: Rigorous Regulation Required

WE AGREE WITH N. V. FEDOROFF *ET AL.* THAT the U.S. regulatory framework for agricultural biotechnology needs serious reexamination ("Radically rethinking agriculture for the 21st century," Perspectives, special section on Food Security, 12 February, p. 833). However, we disagree with their suggestion that regulators should relax oversight to facilitate biotechnology products' entry into the market. The existing framework is already too weak. For example, under current food laws, the Food and Drug Administration (FDA) does not require data, review it, and then use it to conclude that biotech plant foods are safe (*1*). Instead, the agency reviews studies submitted by product developers and issues letters that simply restate the developers' conclusions about the safety of their products [e.g., (*2*)]. Understanding that this cozy approach would be unacceptable for biotech food animals, FDA regulates them under stronger, but inappropriate, authority as drugs (*3*).

The authors are wrong to assert that genetically modified (GM) crops are safe because we've consumed them "without incident" for 15 years. First, no agency collects data to evaluate adverse incidents, and because GM foods aren't labeled, consumers experiencing problems would not know to report them as such. Second, the relative safety of the insect- and herbicide-resistant crops that dominate today says little about the safety of more complex traits the industry has promised for the future.

There are some benefits associated with GM crops, but the authors oversell their virtues. Insect-resistant crops have reduced insecticide use, but this is offset by the surge in herbicide use due to resistant weeds (*4*). GM corn and soy yields have indeed risen, but the increase is largely due to the success of classical breeding and other practices, not GM traits (*5*). Finally, further increases in no-till farming would have environmental payoffs, but recent research has called into question the extent of its carbon sequestration benefits (*6*–*8*).

We applaud the authors' recommendation to radically rethink the U.S. agriculture system, but it might be simpler than they suggest. Cover-cropping and four-crop rotations for commodity crops, for example, would enable farmers to reduce pesticide use and nitrogen fertilizer pollution [e.g., (*9*, *10*)] without ever encountering a federal regulator. Policymakers should prioritize increased research support to optimize such methods and provide incentives for farmers to adopt them.

MARGARET MELLON

Food and Environment Program Director, Union of Concerned Scientists, Washington, DC 20006, USA. E-mail: mmellon@ucsusa.org

References and Notes

1. U.S. Food and Drug Administration, "Consultation procedures under FDA's 1992 statement of policy: Foods derived from new plant varieties" (1997); www.fda.gov/Food/GuidanceComplianceRegulatoryInformation/GuidanceDocuments/Biotechnology/ucm096126.htm.
2. A letter from FDA to a biotechnology developer at the conclusion of a safety review includes the following: "Based on the safety and nutritional assessment that *Pioneer has conducted, it is our understanding that Pioneer has concluded* that the new soybean variety is not materially different in any respect relevant to food or feed safety compared to soybean varieties currently on the market and that the genetically engineered soybean does not raise issues that would require premarket review or approval by FDA" (emphasis added); www.fda.gov/Food/Biotechnology/Submissions/ucm155567.htm.
3. U.S. Food and Drug Administration, "Guidance for industry: Regulation of genetically engineered animals containing heritable recombinant DNA constructs, final guidance" (2009); www.fda.gov/downloads/AnimalVeterinary/GuidanceComplianceEnforcement/GuidanceforIndustry/UCM113903.pdf.
4. C. Benbrook, "Impacts of genetically engineered crops on pesticide use: The first thirteen years" (The Organic Center, Boulder, CO, 2009); www.organic-center.org/science.pest.php?action=view&report_id=159.
5. D. Gurian-Sherman, "Failure to yield: Evaluating the performance of genetically engineered crops" (Union of Concerned Scientists, Cambridge, MA, 2009); www.ucsusa.org/food_and_agriculture/science_and_impacts/science/failure-to-yield.html.
6. J. M. Baker *et al.*, *Agric. Ecosys. Environ.* **118**, 1 (2007).
7. H. Blanco-Canqui, R. Lal, *Soil Sci. Soc. Am. J.* **72**, 693 (2008).
8. V. Poirier *et al.*, *Soil Sci. Soc. Am. J.* **73**, 255 (2009).
9. M. Liebman *et al.*, *Agron. J.* **100**, 600 (2008).
10. C. Tonitto *et al.*, *Agric. Ecosys. Environ.* **112**, 58 (2005).

Food Security: Focus on Agriculture

THE REVIEW BY H. C. J. GODFRAY *ET AL.* (12 February, p. 812) and the rest of the special section on Food Security call for a multifaceted approach to future global food security. We would like to emphasize three agricultural issues that were lacking.

First, it is important to analyze yield as the result of genotype, environment, and management interactions. This type of analysis permits a nuanced understanding of the factor(s) that lie behind regional differences in yield gaps, especially between developed- and developing-country agriculture. These insights can then be used to apply more targeted research as needed.

Second, we must pursue the fastest route to improved yield. We have 30 to 40 years, and it can take 10 to 15 years to develop a food crop variety that can be cultivated extensively in farmers' fields. We have little time to experiment with totally new crop plants and need to work with currently available genetic material. Poor farmers in Africa will benefit sooner by having access to plentiful and inexpensive nitrogen and phosphorus fertilizer than by waiting for possible N-fixing cereal crops.

Third, there needs to be a focus on scenario-building exercises for agriculture—the kind used in the development of the Millennium Ecosystem Assessment and the IPCC reports. Major drivers such as regional or global agricultural markets should be analyzed against low or high impacts of environmental change (including climate) on agriculture. Such scenario analyses recognize that agriculture is more than just food production; this is a crucial perspective, given that 45% of the global population depends on agriculture for their livelihoods.

JOHN R. PORTER,[1]* ANDREW CHALLINOR,[2] FRANK EWERT,[3] PETE FALLOON,[4] TONY FISCHER,[5] PETER GREGORY,[6] MARTIN K. VAN ITTERSUM,[7] JØRGEN E. OLESEN,[8] KENNETH J. MOORE,[9] CYNTHIA ROSENZWEIG,[10] PETE SMITH[11]

[1]Department of Agriculture and Ecology, University of Copenhagen, 1870 Copenhagen, Denmark. [2]Institute for Climate and Atmospheric Science, University of Leeds, Leeds LS2 9JT, UK. [3]Institute of Crop Science and Resource Conservation, University of Bonn, Katzenburgweg 5, D-53115 Bonn, Germany. [4]Hadley Centre, FitzRoy Road, Exeter EX1 3PB, UK. [5]ATSE Crawford Fund, One Geils Court, Deakin, 2600 ACT, Australia. [6]Scottish Crop Research Institute, Invergowrie, Dundee DD2 5DA, Scotland, UK. [7]Plant Production Systems Group, Wageningen University, Droevendaalsesteeg 1, 6708 PB Wageningen, The Nether-

lands. [8]Department of Agroecology and Environment, University of Aarhus, Blichers Allé, DK-8830 Tjele, Denmark. [9]Department of Agronomy, Iowa State University, 2101 Agronomy Hall, Ames, IA 50011–1010, USA. [10]NASA Goddard Institute for Space Studies, 2880 Broadway, New York, NY 10025, USA. [11]Institute of Biological and Environmental Sciences, University of Aberdeen, Aberdeen AB24 3UU, Scotland, UK.

*To whom correspondence should be addressed. E-mail: jrp@life.ku.dk

Food Security: Fossil Fuels

THE SPECIAL SECTION ON FOOD SECURITY (12 February, p. 797) omitted two points. First, addressing the unmet need for voluntary, cost-effective family planning (*1*) deserves mention as a means for improving global food security in the coming decades. Second, any discussion of food security should address the dangerously heavy dependence of global agriculture on fossil fuels. Although several authors stressed the need for sustainability in agricultural systems, none even alluded to the virtual certainty that the peak of global oil production will occur before 2050. The rise in food prices in 2008 and the attendant civil unrest derived in part from the extreme rise in the costs of oil and of fertilizer. The potential for similar disruption in the future—possibly as soon as the global economy recovers—deserves serious consideration.

RICHARD E. WHITE[1]* AND RICHARD GROSSMAN[2]

[1]Sustainability Alliance of Southwest Colorado, Durango, CO 81302, USA. [2]Department of Biology, Fort Lewis College, Durango, CO 81301, USA.

*To whom correspondence should be addressed. E-mail: rwhite@gobrainstorm.net

Reference

1. S. Singh *et al.*, *Adding it Up: The Benefits of Investing in Sexual and Reproductive Health Care* (Alan Guttmacher Institute, New York, 2003).

Food Security: Perception Failures

THE SPECIAL SECTION ON FOOD SECURITY (12 February, p. 797) examines several obstacles to achieving global food security. One obstacle the section did not address is perception failure.

Perception failure poses an imminent danger to the advancement of science. Consumer resistance to genetically modified (GM) products affects trade relations and reduces private research and development on plant biotechnology (*1*). A case in point is the recent rejection of GM eggplant in India, detailed in the News of the Week story by P. Bagla in the same issue ("After acrimonious debate, India rejects GM eggplant," p. 767). GM technology is not new to India; *Bacillus thuringiensis* (Bt) cotton was first commercialized in India in 2002. Since then, about 5 million farmers have adopted the technology (*2*). Thus, negative experiences with GM crops cannot explain the rejection of Bt eggplant. Nor can regulation—India's highest biotechnology regulatory body, The Genetic Engineering Approval Committee, approved the Bt eggplant, deeming the technology safe (recounted in Bagla's News story). The major obstacle stemmed not from inadequate technology or strict regulations, but from the public's perception of the technology. Bridging the gap between science and society needs to be a high priority in order to put all currently available science to efficient use in addressing global food security concerns.

ARJUNAN SUBRAMANIAN,[1,2]*
KERRY KIRWAN,[1] DAVID PINK[2]

[1]Warwick Manufacturing Group, University of Warwick, Coventry CV4 7AL, UK. [2]Warwick HRI, University of Warwick, Coventry CV35 9EF, UK.

*To whom correspondence should be addressed. E-mail: s.arjunan@warwick.ac.uk

References

1. J. Huang, S. Rozelle, C. Pray, Q. Wang, *Science* **295**, 674 (2002).
2. C. James, *ISAAA Briefs* **39** (2008).

It's more than genetic analysis.
It's the unstoppable drive to know more.
To find answers. To be the first.

The power of sequencing. The speed of arrays.
Limitless applications harnessed with intensity
and implemented with imagination.

The intangible force that fuels the
dynamic Illumina Community.

That's

genetic energy™

www.illumina.com/geneticenergy

illumina®

SOCIAL SCIENCES

Steering Clear of State Control

Fredrik Barth

Through his studies of Southeast Asian societies, political scientist James Scott has had a wide influence on the social sciences. His previous studies have included analyses of peasant practices in confrontations between persons of unequal class positions (*1*) and of the modes of operation in modern bureaucracies (*2*). In *The Art of Not Being Governed*, he looks closely at the 80 million people who live in stateless societies in Southeast Asia and seeks to understand the means by which such societies persist.

Anthropologists have long recognized that the peoples of Southeast Asia can be sorted typologically into hill people and valley people, with little regard for their linguistic classifications. In the valleys, one finds palaces and temples, ancient religions as well as elaborate irrigated agriculture, high population densities, towns, and central government officials. In contrast, the hills contain vast numbers of stateless small communities (practicing nonliterate religions) and simple economies. People of the valleys generally see the inhabitants of the hills as historical and refer to them as "slaves"—whom they wish to exploit for labor and army services. The hill people would rather live their own lives.

The Art of Not Being Governed
An Anarchist History of Upland Southeast Asia

by James C. Scott

Yale University Press, New Haven, CT, 2009. 464 pp. $35, £20. ISBN 9780300152289. Agrarian Studies.

Both anthropologists and lay people often try to transform such typologies into conjectural histories and interpret the presence of hill people as evidence of relatively recent local developments, although we know that both types have been present together through a thousand years or more. Scott asks the more analytically useful question of how they have coexisted: what are the social strategies that the weaker parties have practiced so as to survive? Scott comments on the unilateral impositions by valley people of state taxation, tribute, and corveé labor as well as the mutual looting and other uses of force. The hill people, being the weaker side, practice withdrawal and flight, which leads to their territorial dispersal. He also notes the occurrence of innumerable rebellions in the hills, launched by inspired and visionary leaders. In short, the hill people's position cannot entail passivity and inaction. Instead, they may make use of strategies other than those of the members of states; their approach requires that we consider other arenas than those favored by the valley people.

Characteristically, Scott credits the upland tribes with purposeful action to maintain their valued independence. The disparity of power, however, perhaps makes their effort less evident to the historian's eyes. Indeed, flight and dispersal seem to be the most recurring consequences of the processes he identifies.

But there are other things going on that may affect the picture. Most of the mercenaries of local wars have always been low-status hill persons, who hold positions of authority in the armies of the valleys but not in their own tribal society. More pervasively, many of the hill people also occupy positions in larger social systems, which achieve considerable scale and surely some importance: Patrilineal descent among the hill people places all persons in patrilineal clans. Marriages link persons in matrilateral and affinal relations of peculiar structure and with hierarchical significance. Gifts are required when certain affinal relations meet unexpectedly, and a failure to give causes great embarrassment. These gifts are differentiated and symbolic of the reciprocal relationships.

Another hierarchy of positions among hill people is associated with formal "feasts of merit," which involve massive distributions of wealth linked to life stages and reputation. Such festivities are variously elaborated in different tribal groups. I do not know how they may play into the picture that Scott offers. But nor do I know that they are not relevant to shaping the forms of political organization. To find out, we need to consider further details of ethnography, despite the vast amount of material the author already presents.

Indeed, even with the many comparisons that Scott presents throughout his text, his conclusions seem weakened because of a failure of comparative method. Although *The Art of Not Being Governed* encompasses an extensive range of details and observations, uninformed readers will be in no position to assimilate and make systematic use of them. Besides the study's complex topics, I felt overwhelmed by a spate of brief comparisons and one-liners about much of the world—from Cossacks, European Jews, and Middle Eastern nomads to Latin Americans. For any two features of the world, there are at least two interesting similarities and two interesting differences. If we are to draw useful conclusions, we need features to be systematized and the connections among them to be illuminated. I hope the very interesting material Scott discusses will be further pursued and pruned, so that a more illuminating picture can emerge.

References

1. J. C. Scott, *Weapons of the Weak: Everyday Forms of Peasant Resistance* (Yale Univ. Press, New Haven, CT, 1985).
2. J. C. Scott, *Seeing Like a State: How Certain Schemes to Improve the Human Condition Have Failed* (Yale Univ. Press, New Haven, CT, 1998).
3. F. Garnier, *Voyage d'exploration en Indo-Chine: effectué pendant les anneés 1866, 1867, et 1868* (Hachette, Paris, 1873).

10.1126/science.1187817

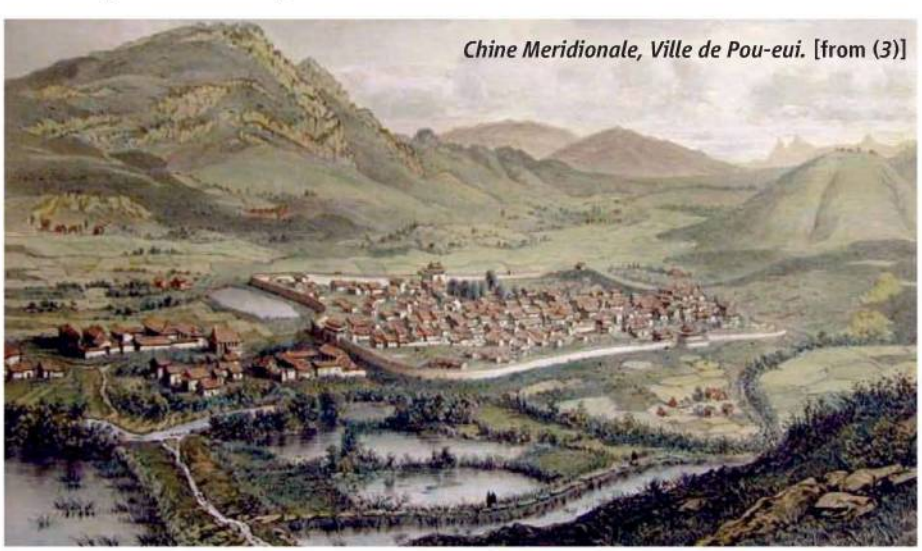

Chine Meridionale, Ville de Pou-eui. **[from (*3*)]**

CREDIT: COURTESY YALE UNIVERSITY PRESS

The reviewer is at the Department of Social Anthropology, University of Oslo, Postboks 1091 Blindern, 0317 Oslo, Norway. E-mail: swatsult@gmail.com

Les prix

CANADA GAIRDNER Awards

The Gairdner Foundation is pleased to announce the recipients of the 2010 awards

The Canada Gairdner Awards, considered among the most prestigious in biomedical science, are given in 3 categories; International Awards (for outstanding discoveries/contributions to medical science), the Global Health Award (for scientific advances contributing to health in the developing world) and the Wightman Award (for leadership in Canadian medicine).

William G. Kaelin Jr. M.D., Dana-Farber/ Harvard Cancer Center, Boston, MA

For identification of molecular mechanisms of oxygen sensing in the cell

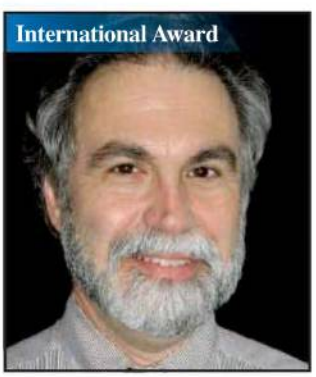

Gregg L. Semenza M.D., Ph.D., The Johns Hopkins Institute for Cell Engineering, Baltimore, MD

For identification of molecular mechanisms of oxygen sensing in the cell

Peter J. Ratcliffe M.D., University of Oxford, Oxford

For identification of molecular mechanisms of oxygen sensing in the cell

William A. Catterall Ph.D., Department of Pharmacology, University of Washington, Seattle, WA

For discovery of the voltage-gated sodium channel and calcium channel proteins and their function and regulation

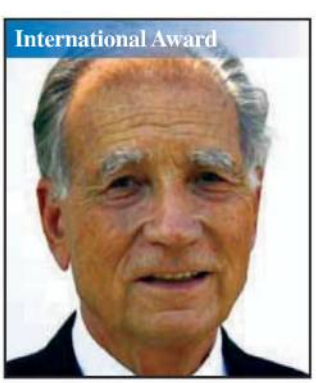

Pierre Chambon M.D., Institut de Génétique et de Biologie Moléculaire et Cellulaire, Strasbourg

For the elucidation of mechanisms of transcription in animal cells and fundamental contributions to the field of nuclear receptors

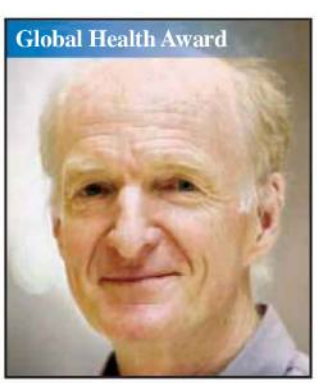

Nicholas White, M.D. D.Sc., University of Oxford and Mahidol University, Faculty of Tropical Medicine, Bangkok

For clinical studies on the effectiveness of artemesinins in the treatment of malaria and elucidating the basis for the use of ACT to prevent resistance

Calvin Stiller C.M., O.Ont., M.D., Professor Emeritus, University of Western Ontario and Chair, Ontario Institute for Cancer Research

For his pioneering work in transplantation and diabetes, and as a remarkable entrepreneur and builder of private and public institutions in Canada

Supported nationally by:

CIHR IRSC

The awards will be presented in Toronto, Canada on October 28, 2010

www.gairdner.org

This announcement is supported by:

Ontario

AMGEN 50 YEARS

ECOLOGY

The Barometer of Life

A broader taxonomic base to threatened species assessments will enable better conservation and policy decisions.

S. N. Stuart,[1]* E. O. Wilson,[2] J. A. McNeely,[3] R. A. Mittermeier,[4] J. P. Rodríguez[5]

On 11 January 2010, the United Nations inaugurated the International Year of Biodiversity in Berlin. This initiative is timely, because the environmental movement suffers from an imbalance between its sense of urgency and its intensity of activity. Center stage is now occupied by concerns for the physical environment—in particular, climate change, pollution, and depletion of nonrenewable resources. However, if the living world is to be kept in anything approaching a sustainable condition that can adapt to changes, then politicians, government officials, scientists, and the public will need to give biodiversity the urgent attention that they are starting to give to the physical environment.

About 1.9 million species (*1*) have been discovered and given scientific names (*2*), though the actual number may exceed 10 million (*3*). Bacteria and archeans could comprise tens of millions species—once taxonomic units are precisely defined. Knowledge about species and extinction rates remains very poor, and species disappear before we know they existed. We propose that, as scientists are better able to assess the conservation status of the species that compose an ecosystem, the more they will understand the health of that ecosystem. It is time to accelerate taxonomy and scientific natural history, two of the most vital but neglected disciplines of biology (*4*, *5*).

The Encyclopedia of Life (EOL), a powerful initiative (*5*), is now fully operational and working toward its goal of documenting every known species. Essential though the EOL is, it needs to be complemented by another project, the "Barometer of Life." This initiative would need to unite taxonomists, biogeographers, ecologists, conservationists, and amateur naturalists in a coordinated exploration of global biodiversity, with an emphasis on identifying which species are threatened. While the EOL will provide a Web page on every species, the barometer would compile conservation-related data on distributions, threats, and assessments of extinction risk on a subset of species broadly representative of biodiversity as a whole. The logical platform for this barometer is *The Red List of Threatened Species* (*6*) of the International Union for Conservation of Nature (IUCN), which, for over 45 years, has published information on the status and trends of species. The IUCN Red List began by focusing on selected species, but it now covers entire taxonomic classes. It provided the first global picture of vertebrate diversity—a measure of the magnitude, geography and type of threats among several taxonomic groups, and a baseline from which to measure changes in status of species (*7*, *8*). The IUCN Red List includes assessments of all species of mammals, birds, amphibians, freshwater crabs, reef-building corals, cycads, and conifers (*8*). More than 250 national red lists for various taxonomic groups have been developed in >100 countries (*9*).

However, the Red List is biased toward higher vertebrates. The vast majority of species—including most plants, invertebrates, and lower vertebrates, and almost all fungi—are still grossly underrepresented. A more finely tuned barometer is within reach by expanding the taxonomic base of the Red List to make it much more representative of the diversity of life. We anticipate that a representative barometer will need to monitor the status of 160,000 species (see table, above), roughly three times the almost 48,000 species currently on the Red List. The target number of species to be assessed is still provisional. Some groups (e.g., nematodes and sponges) are so poorly known that it would be hard to include them in the barometer at this time.

A representative barometer would provide a solid basis for informing decisions globally, for example, on conservation planning, resource allocation, environmental impact assessments, monitoring biodiversity trends (through the IUCN Red List Index) (*7*, *8*), and enabling countries to develop national-level biodiversity indicators (*10*).

For the Red List to reach its full potential as the Barometer of Life, a substantial increase in the magnitude of the current effort will be required. About U.S.$4 million is spent annually to maintain and enhance the IUCN Red List (*11*), in addition to voluntary contributions of thousands of biologists worldwide. The total cost of achieving the broader taxonomic base is on the order of U.S.$60 million. The barometer would, from an economic perspective, be one of the best investments for the good of humanity.

SPECIES AND PROJECTED COSTS FOR A BAROMETER OF LIFE

Major taxonomic grouping	Described species*	Species assessed on IUCN Red List by 2009†	FOR THE BAROMETER: Provisional target number of species	FOR THE BAROMETER: Estimated cost to complete (US$)
Chordates	64,788	27,882	61,635	16,000,000
Invertebrates	1,359,365	7,615	45,344	20,000,000
Plants	310,129	12,151	38,521	17,000,000
Fungi and others	165,305	18	14,500	7,000,000
	1,899,587	**47,666**	**160,000**	**60,000,000**

*Data on the number of described species taken from (*1*). †Data on the number of assessed species from www.iucnredlist.org.

[1]International Union for Conservation of Nature (IUCN) Species Survival Commission, 1196 Gland, Switzerland; United Nations Environmental Programme World Conservation Monitoring Centre, Al Ain Wildlife Park and Resort, Al Ain, United Arab Emirates; and Department of Biology and Biochemistry, University of Bath, Bath BA2 7AY, UK. [2]Museum of Comparative Zoology, Harvard University, Cambridge, MA 02138, USA. [3]IUCN, 1196 Gland, Switzerland. [4]Conservation International, Arlington, VA 22202, USA. [5]Centro de Ecología, Instituto Venezolano de Investigaciones Científicas, Apartado 20632, Caracas 1020-A, Venezuela, and Provita, Apartado 47552, Caracas 1041-A, Venezuela.

*Author for correspondence. E-mail: simon.stuart@iucn.org

References and Notes

1. A. D. Chapman, *Numbers of Living Species in Australia and the World* (Australian Biological Resources Study, Canberra, Australia, ed. 2, 2009).
2. F. A. Bisby *et al.*, *Catalogue of Life: 2009 Annual Checklist* (Species 2000 and Integrated Taxonomic Integration System, 2009); www.catalogueoflife.org/info_about_col.php.
3. G. M. Mace *et al.*, in *Millennium Ecosystem Assessment: Ecosystems and Human Well-Being*, vol. 1, *Current State and Trends*, R. Hassan, R. Scholes, N. Ash, Eds. (Island Press, Washington, DC, 2005), pp. 77–122.
4. Q. D. Wheeler, P. H. Raven, E. O. Wilson, *Science* **303**, 285 (2004).
5. E. O. Wilson, *Trends Ecol. Evol.* **18**, 77 (2003).
6. The IUCN Red List of Threatened Species, www.iucnredlist.org/.
7. A. S. L. Rodrigues, J. D. Pilgrim, J. F. Lamoreux, M. Hoffmann, T. M. Brooks, *Trends Ecol. Evol.* **21**, 71 (2006).
8. J.-C. Vié, C. Hilton-Taylor, S. N. Stuart, Eds., *Wildlife in a Changing World: An Analysis of The 2008 IUCN Red List of Threatened Species* (IUCN, Gland, Switzerland, 2009).
9. T. J. Zamin *et al.*, *Conserv. Biol.*, in press.
10. J. P. Rodríguez, *Endanger. Species Res.* **6**, 193 (2008).
11. J.-C. Vié, personal communication.
12. We thank T. Brooks and A. Rodrigues for helpful comments on earlier drafts, and A. Angulo and C. Hilton-Taylor for answering questions.

10.1126/science.1188606

Gordon Research Conferences

frontiers of science

Session II (June-September) 2010: New Conferences and Gordon Research Seminars (GRS)

*Several **new** Gordon Research Conferences will be held throughout the remainder of 2010. Conferences will also be held for the first time at Davidson College in North Carolina (pictured). **A list of upcoming NEW meetings appears below**. For a complete list of meetings, locations, programs (and more), please visit our web site at **www.grc.org**.*

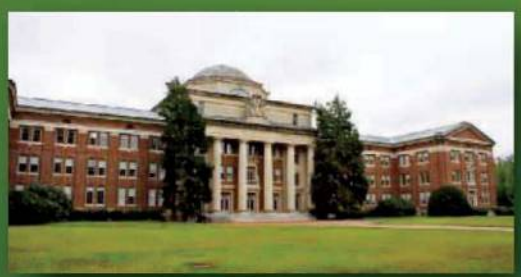

Auditory System
Jun 13-18, 2010

Biointerface Science
Sep 5-10, 2010

Crystal Engineering
Jun 6-11, 2010

Intrinsically Disordered Proteins
Jul 11-16, 2010

Natural Gas Hydrate Systems
Jun 6-11, 2010

Neurobiology of Cognition
Aug 1-6, 2010

Noble Metal Nanoparticles
Jun 20-25, 2010

Nox Family NADPH Oxidases
Jun 6-11, 2010

Oceans & Human Health
Jun 13-18, 2010

Plasmonics
Jun 13-18, 2010

Single Molecule Approaches to Biology
Jun 27 - Jul 2, 2010

Thiol-Based Redox Regulation & Signaling
May 9-14, 2010

Transglutaminases in Human Disease Processes
Jul 18-23, 2010

Gordon Research Seminars

*The Gordon Research Seminar Program (GRS) is a series of highly successful and unique opportunities for young researchers to share in the GRC experience. Each seminar is held in conjunction with a related Gordon Research Conference and begins the weekend immediately prior to the GRC. **A list of upcoming GRSs appears below**:*

Aging, Biology of (GRS)*
Aug 21-22, 2010

Auditory System (GRS)
Jun 12-13, 2010

Barriers of the CNS (GRS)*
Jun 19-20, 2010

Bioanalytical Sensors (GRS)
Jun 19-20, 2010

Bioelectrochemistry (GRS)*
Jul 10-11, 2010

Corrosion - Aqueous (GRS)
Jul 24-25, 2010

Flow & Transport in Permeable Media (GRS)*
Jul 10-11, 2010

Hemostasis (GRS)*
Jul 24-25, 2010

Industrial Ecology (GRS)*
Jul 10-11, 2010

Inorganic Chemistry (GRS)
Jun 19-20, 2010

Meiosis (GRS)*
Jun 12-13, 2010

Membranes: Materials & Processes (GRS)
Jul 24-25, 2010

Microbial Toxins & Pathogenicity (GRS)
Jul 10-11, 2010

Mitochondria & Chloroplasts (GRS)
Jul 10-11, 2010

Oceans & Human Health (GRS)
Jun 12-13, 2010

Organometallic Chemistry (GRS)
Jul 10-11, 2010

Plasma Processing Science (GRS)*
Jul 10-11, 2010

Plasmonics (GRS)*
Jun 12-13, 2010

Signaling by Adhesion Receptors (GRS)
Jul 10-11, 2010

Signal Transduction by Engineered Extracellular Matrices (GRS)*
Jun 26-27, 2010

** The Kenan Institute for Engineering, Technology & Science generously provided seed money to all new Gordon Research Seminars in 2010.*

*visit **www.grc.org** for more information*

MEDICINE

The Microbes Made Me Eat It

Susceptibility to obesity is influenced by the interaction between microbes and immune system function in our digestive system.

Darleen A. Sandoval and Randy J. Seeley

We share our bodies with a huge array of microorganisms. Many of these live in the intestine and number in the trillions (*1*). On page 228 in this issue, Vijay-Kumar *et al.* (*2*) show that the interaction between our immune system and these gut microbes plays an important role in the metabolic diseases that plague developed countries, with profound implications for the rise in obesity and what can be done about it.

There are few proven hypotheses regarding the cause of obesity, type 2 diabetes, and cardiovascular disease. One possibility is that gut microbes contribute to these conditions—referred to collectively as metabolic syndrome—by regulating immune function. Because of its large surface area and exposure to diverse microbes and the food we eat, the gastrointestinal tract is a unique interface between the external and internal environment. This positions the gastrointestinal tract to play a predominant role in immunity.

Although the human body depends on bacteria in the gut for normal functioning, bacteria in other locations may cause infections that must be targeted by the immune system. One component of this response is Toll-like receptors that are expressed by certain immune cells. These receptors recognize the flagella of bacteria and activate the immune system. Obesity is associated with an increase in immune system activity and this may contribute to a range of other symptoms associated with obesity, including elevated risk for cardiovascular disease and type 2 diabetes (*3*).

Vijay-Kumar *et al.* show that mice lacking Toll-like receptor 5 (expressed by intestinal cells, as well) were obese and had many characteristics of metabolic syndrome, all of which were exacerbated when the mice were put on a high-fat diet. It should not be surprising that manipulation of the immune system might result in such an outcome given the importance of inflammation to the metabolic syndrome. However, by crossing these mice with mouse strains lacking other key components of immune system signaling, the authors found that this phenotype did not change. Metabolic syndrome therefore was not the result of direct interaction between the Toll-like receptor and these other immune system molecules. So if not the immune system, what could account for the resulting metabolic syndrome?

When Vijay-Kumar *et al.* treated the obese mice with antibiotics to kill their microbes, they reversed the metabolic syndrome. Additionally, by transferring bacteria from the gut of obese mice to that of mice that were depleted of gut bacteria, they could recapitulate the metabolic syndrome of the obese mice. Thus, the gut microbiota in the obese mice was both necessary and sufficient for the resulting obesity.

This isn't the first time that researchers have linked gut microbes to our waistlines. Earlier studies (*4*, *5*) found that obese humans and obese mice had different bacteria in their gastrointestinal tracts than lean individuals. They concluded that in obese individuals, the mix of gut microbes could extract a small amount of calories from what would normally be undigested food, and that these calories contributed to weight gain. However, the hypothesis implies that in starvation,

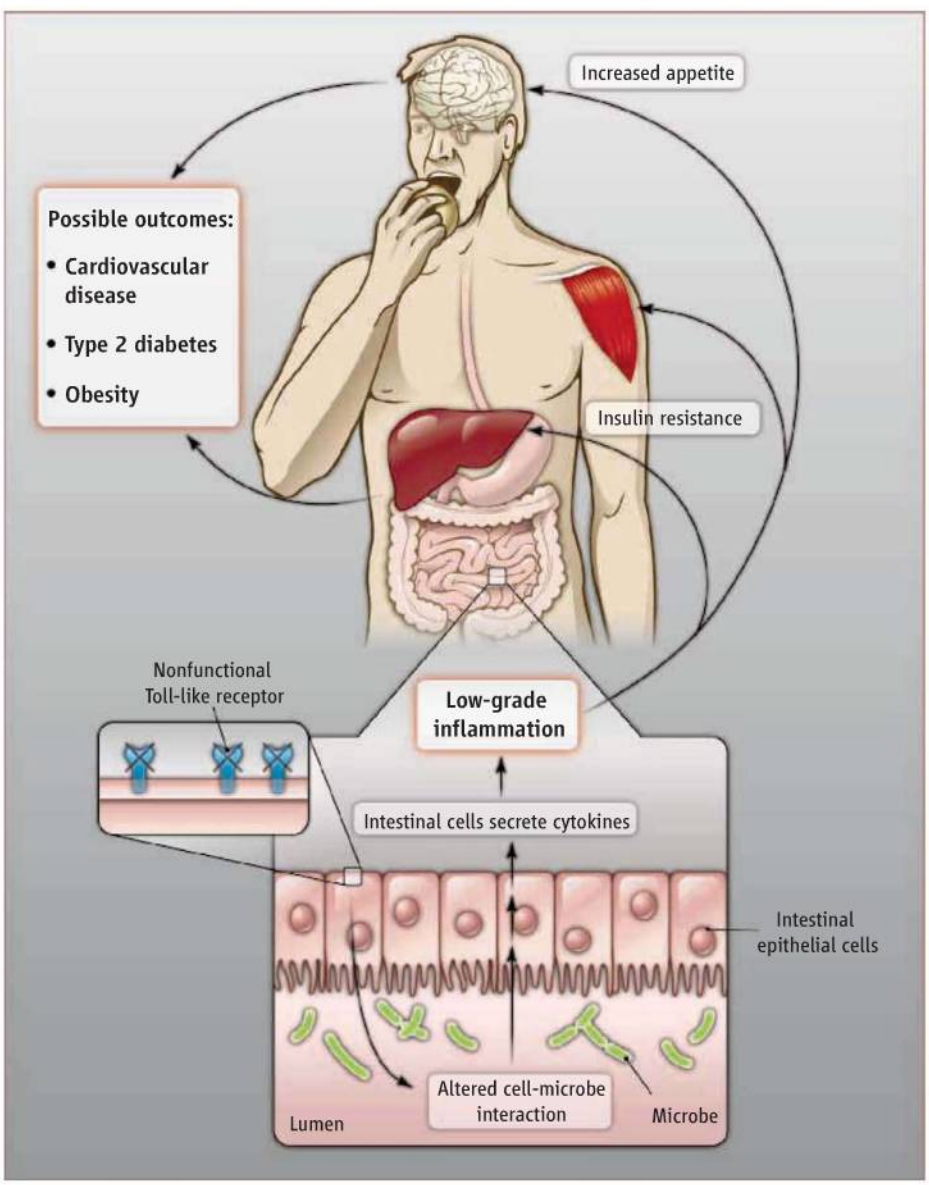

CREDIT: Y. GREENMAN/SCIENCE

Microbes and obesity? The absence of Toll-like receptor 5 in mice alters the gut microbiota, causing increased food intake, insulin resistance, and obesity. Is this true for humans?

Metabolic Diseases Institute and Department of Internal Medicine, University of Cincinnati, Cincinnati, OH 45237, USA. E-mail: randy.seeley@uc.edu

when the need to extract calories from food increases, our gut bacteria would actually become less efficient. Moreover, our bodies sense calories, and it is unclear why animals would not adjust to greater caloric extraction by eating less food.

Vijay-Kumar *et al.* paint a different picture of how gut bacteria might contribute to obesity. Rather than delivering additional calories to its host, gut bacteria interact with physiological processes that control multiple aspects of metabolism. Importantly, what regulates this interaction is the immune system, through activity of a Toll-like receptor. Thus, it may be that part of how the human immune system influences metabolic disease is via regulating gut microbes; this, in turn, might regulate other aspects of our immune system, including the production of proinflammatory cytokines (see the figure).

The study by Vijay-Kumar *et al.* falls under a growing set of theories that obesity is the result of infection. Whereas this work focuses on a potential role for bacteria, others have speculated that specific viral infections can lead to increased body weight (*6*). Although the thought of obese individuals as "contagious" adds many negative connotations to a group that already suffers enormous discrimination, the idea that some gut bacteria contribute to susceptibility to obesity means that we may be able to reverse this trend by targeting the key microbes. These insights may allow us to identify new strategies to prevent obesity by manipulating immune system–gut microbiota interactions through drugs, the food we eat, or probiotics.

References

1. S. R. Gill *et al.*, *Science* **312**, 1355 (2006).
2. M. Vijay-Kumar *et al.*, *Science* **328**, 228 (2010); published online 4 March 2010 (10.1126/science.1179721).
3. H. Xu *et al.*, *Invest* **112**, 1821 (2003).
4. R. E. Ley, D. A. Peterson, J. I. Gordon, *Cell* **124**, 837 (2006).
5. P. J. Turnbaugh *et al.*, *Nature* **444**, 1027 (2006).
6. N. V. Dhurandhar, *Drug News Perspect.* **17**, 307 (2004).

10.1126/science.1188876

MATERIALS SCIENCE

Holding On by a Hard-Shell Thread

The byssal threads that secure mussels onto surfaces have a hard coating created by iron cross-links of proteins rich in L-dopa.

Phillip B. Messersmith

Mussels anchor to surfaces in turbulent aqueous environments with a remarkable acellular tissue, the byssus, or "beard." The threadlike byssal attachments are strong yet highly extensible, and have a thin cuticle coat that is harder than the core of the thread itself. On page 216 of this issue, Harrington *et al.* (*1*) present results that show how the chemistry of byssal thread cuticle may impart these distinctive mechanical properties.

The major cuticular protein in mussels, called mfp-1 (mussel foot protein 1), contains 10 to 15 mol % of the catecholic amino acid 3,4-dihydroxyphenyl-L-alanine (dopa). The core proteins of the threads are collagen-like and contain very little dopa. The mussel employs a truly elegant approach to byssal thread fabrication (see the figure). In a series of events that are reminiscent of industrial approaches to polymer injection molding, the mussel injects liquid protein solution onto the substrate surface and into a groove along the length of the foot. The protein solidifies in a short period of time. Detachment of the foot reveals the newly formed thread and adhesive plaque. The mussel then repeats this process many times to secure its attachment to the substrate.

The mussel relies on the durability of the byssus for its survival. The byssal threads have very robust mechanical properties, and have been shown to have self-healing capacity (*2*). Harrington *et al.* focused on the mechanochemistry of the byssal thread cuticle. Earlier studies of byssal threads revealed the cuticle to be about five times as stiff as the core and enriched in iron and calcium, but otherwise free of detectable inorganic mineral phases (*3*, *4*). Catechols are known to have a high affinity for transition metals, including iron, and iron ions can bind either two or three dopa molecules to form bis- and tris-complexes, respectively (*5*).

The possibility of iron complexation by dopa, together with evidence for colocalization of mfp-1 and iron in the thread cuticle, has led to speculation of a mechanical role for dopa-iron complexes (*4*). However, direct chemical and spectroscopic evidence for the localization of dopa-iron complexes in byssal thread cuticle has been lacking. Harrington *et al.* filled this gap and established a framework for understanding the possible mechanical function of dopa-iron coordination in the mussel byssal thread cuticle. The authors used in situ confocal Raman spectroscopy on slices of byssal thread tissue to demonstrate the existence of dopa-iron complexes within the thread cuticle. The submicrometer resolution

Making strong attachments. A still image is shown of a mussel attached to a surface. The attachment process is revealed in movie S1. As the foot detaches from the surface, it leaves behind an intact byssal thread and adhesive pad.

Departments of Biomedical Engineering, Materials Science and Engineering, Chemical and Biological Engineering, Chemistry of Life Processes Institute, and Institute for Bionanotechnology in Medicine, Northwestern University, Evanston, IL 60208, USA. E-mail: philm@northwestern.edu

of the technique allowed detection of higher dopa-iron content within cuticular granules as opposed to the continuous cuticular matrix.

An earlier observation that cuticle hardness is reduced by ~50% upon chelation of iron by EDTA (*3*), along with the observation by Harrington *et al.* of a disappearance of Raman spectroscopic signal of dopa-iron, suggested a connection between dopa-iron complexes and mechanical properties (*3*). The authors propose a model whereby dopa-iron complexation contributes both hardness and extensibility to the thread cuticle. Additional detailed experiments will likely be necessary to further elucidate the chemomechanical basis for these properties. However, single-molecule experiments have demonstrated substantial bond-rupture forces between dopa and metal oxide surfaces (*6*). These results, together with the successful use of catechols as anchors for grafting molecules onto metal oxide surfaces (*7*–*11*), leave little doubt that dopa-metal coordination interactions of the type spectroscopically detected by Harrington *et al.* can impart mechanical stabilization.

Evidence is accumulating for metal coordination as a biological strategy for fabricating mechanically competent organic tissues in which there is little or no inorganic mineral present. For example, in the case of the hard load-bearing jaws of polychaetes, a type of annelid worm, coordination complexes between histidine and copper or zinc are suggested to play an important role in mechanical performance of the tissue (*12*). By contrast, in the dopa-iron complexes of the byssal thread cuticle, metal coordination occurs entirely through catechol.

Metal coordination bonds acting as cross-links in polymer and protein systems are expected to behave quite differently under applied force than covalent cross-links do. For example, coordination bonds can be considered sacrificial, in that they can break under an applied load, but then re-form when the load is withdrawn. It will be interesting to see if this molecular behavior proves to be the underlying basis of the macroscopic observations of self-healing in byssal threads. Synthetic materials scientists exploiting dopa-iron complexes will likely be inspired by this study. Indeed, one report exists of self-assembly and stabilization of collagen-like peptides mediated by catechol-iron interactions (*13*).

References

1. M. J. Harrington, A. Masic, N. Holten-Andersen, J. H. Waite, P. Fratzl, *Science* **328**, 216 (2010); published online 4 March 2010 (10.1126/science.1181044).
2. E. Carrington, J. M. Gosline, *Am. Malacol. Bull.* **18**, 135 (2004).
3. N. Holten-Andersen, G. E. Fantner, S. Hohlbauch, J. H. Waite, F. W. Zok, *Nat. Mater.* **6**, 669 (2007).
4. N. Holten-Andersen *et al.*, *Langmuir* **25**, 3323 (2009).
5. S. W. Taylor, D. B. Chase, M. H. Emptage, M. J. Nelson, J. H. Waite, *Inorg. Chem.* **35**, 7572 (1996).
6. H. Lee, N. F. Scherer, P. B. Messersmith, *Proc. Natl. Acad. Sci. U.S.A.* **103**, 12999 (2006).
7. J. L. Dalsin, B.-H. Hu, B. P. Lee, P. B. Messersmith, *J. Am. Chem. Soc.* **125**, 4253 (2003).
8. T. Paunesku *et al.*, *Nat. Mater.* **2**, 343 (2003).
9. A. R. Statz, R. J. Meagher, A. E. Barron, P. B. Messersmith, *J. Am. Chem. Soc.* **127**, 7972 (2005).
10. C. Xu *et al.*, *J. Am. Chem. Soc.* **126**, 9938 (2004).
11. S. Zuercher *et al.*, *J. Am. Chem. Soc.* **128**, 1064 (2006).
12. C. C. Broomell *et al.*, *J. R. Soc. Interface* **4**, 19 (2007).
13. W. Cai *et al.*, *J. Am. Chem. Soc.* **126**, 15030 (2004).

Supporting Online Material

www.sciencemag.org/cgi/content/full/328/5975/180/DC1
Movie S1

10.1126/science.1187598

GEOPHYSICS

Central Chile Finally Breaks

It has been known for 10 years that the site of the Maule mega-earthquake of 27 February 2010 was fully locked and ready to break.

Raul Madariaga[1], Marianne Métois[1], Christophe Vigny[1], Jaime Campos[2]

Chile is the site of some of the largest earthquakes in the world: On average, a magnitude 8 earthquake occurs there every 10 years or so. These earthquakes take place in the subduction zone, either as interplate ruptures at the interface between the South American and Nazca plates or as intraplate events within the subducted Nazca plate. A few times in every century, massive plate-interface earthquakes break several hundred kilometers in a single shock. This is what happened on 27 February 2010, when a major earthquake (magnitude 8.8) occurred in the Maule and Biobío regions in central Chile (see the first figure). This region had last experienced a major subduction earthquake in 1835, when Darwin (*1*) visited the area as part of his voyage on the Beagle. His description of the earthquake inspired many seismologists and historians of Chilean earthquakes (*2*, *3*).

In the early 1970s, Kelleher proposed that Chilean earthquakes occurred on "gaps" left from previous large events (*4*). At the time, the Maule region was not identified as a gap, because a very large earthquake (magnitude 7.8) had occurred there on 25 January 1939 (*5*); the deadliest event in Chile to date, it claimed some 20,000 lives (*3*). In the 1990s, seismologists found that the 1939 earthquake was not a subduction earthquake but the largest intraplate event ever recorded in Chile (*6*–*9*).

Once the region between Concepción and Constitución in Chile was identified as seismic gap, a group of Chilean and European researchers decided to take a closer look into the area (*10*). They discovered that the plate interface was completely locked (coupled), so that stress was building up at the fastest possible speed. Interpretation of the geodetic data obtained by several groups (*11*–*16*) showed that coupling along the Chilean subduction zone changes widely from south to north but is largest in the most ancient gaps.

In the second figure, we show the plate coupling in the area of the Maule earthquake derived from all available GPS data. The red areas

Tsunami damage. Shortly after the Maule mega-earthquake, a tsunami hit nearby coastal areas, such as the village of Penco (near Concepción), shown here.

CREDIT: JONNE RORIZ/AGÊNCIA ESTADO/AE (AGENCIA ESTADO VIA AP IMAGES)

[1]Laboratoire de Géologie et LIA Montessus de Ballore, CNRS and Ecole Normale Supérieure, 75231 Paris Cedex 05, France. [2]LIA Montessus de Ballore, Departamento de Geofisica, FCFM, Universidad de Chile, Santiago, Chile. E-mail: madariag@geologie.ens.fr

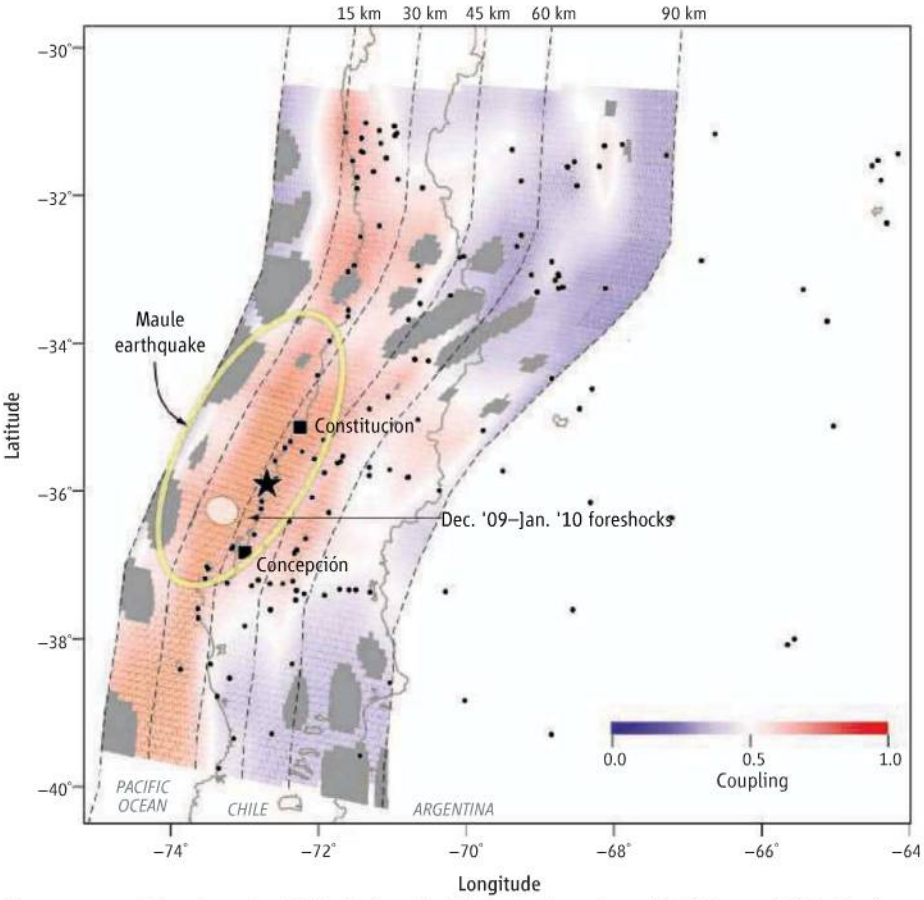

Stress accumulation in central Chile before the Maule earthquake on 27 February 2010. The figure shows the degree of coupling (or locking) of the plate interface between the Nazca and South American plates. The dark red areas coincide very well with the rupture zone (yellow ellipse). Dots are the GPS sites used to generate the image. The large black star is the epicentre of the earthquake. The small ellipse is the area where foreshocks were observed from December 2009 to January 2010.

of the plate interface are those where the two plates have been completely locked since at least 2000. A detailed seismic study of the area was unfortunately not possible because its seismicity was weak and very few seismometers recorded it. According to earthquake catalogs, only 10 earthquakes of magnitude greater than 5 occurred in the Maule and Biobío regions in the 10-year lapse before 29 December 2009. On that date, a series of events started to break the elliptical zone plotted in the figure, less than 30 km from the future epicenter of the Maule earthquake.

The Maule earthquake caught Chile without a seismic network capable of recording large earthquakes. A few accelerometers in Chile and Argentina recorded the earthquake; this is the first mega-earthquake for which digital strong motion data from near the source is available. Geodetic data of the main event are more abundant: The earthquake took place inside campaign GPS networks deployed by several groups (*13*–*16*). A continuously recording GPS receiver in Constitución recorded a peak oceanward displacement of more than 4 m. Because of the lack of a continuously recording strong-motion network, the Chilean government had no reliable information about the earthquake and could not prepare for the tsunami that hit the coastal cities near the earthquake less than an hour after the main shock (see the first figure). There was no earthquake-proof communication network, hampering the emergency response.

Despite its magnitude, the Maule shock had an official toll of fewer than 500 victims—a small number compared to several recent events. The reason is the good performance of modern earthquake-resistant building designs and the rapid reaction of the population that escaped from the tsunami in spite of the hesitation of authorities. At the epicenter, the earthquake produced horizontal ground accelerations of up to 6 m/s^2 (that is, about 60% of the acceleration of gravity, the unit used by earthquake engineers), but accelerations were lower in the more populated central Valley of Chile. These peak accelerations are within the earthquake design requirements of the Chilean seismic code. Well-built structures sustained some heavy damage, but very few collapsed, in sharp contrast to some doomsday scenarios disseminated a few years ago by geographers in the Chilean press.

Studies farther north along the Chilean coast show that a similar stressing of the plate interface is occurring between the Mejillones Peninsula and the boundary between Chile and Peru. This region, known as the Tarapacá gap, last had major earthquakes in 1868 and 1877, with magnitudes close to 8.7 (*2*–*5*). Chilean, European, and American researchers have deployed a network of seismic and geodetic instruments in Northern Chile. The Tarapacá region is showing signs of renewed activity: A large earthquake of magnitude 7.8 occurred in November 2007 at the southern end of the gap, and since last year, the city of Iquique has experienced several magnitude 6 events. It is urgent that the data from this network is processed in real time in Chile to provide early warning when the next large earthquake strikes in the next few decades.

The main lesson from the Maule earthquake is that the sites of rare catastrophic events can be identified in advance, but it remains impossible to predict when these events will occur (*17*). Mega-earthquakes are rare events that require a long-term public policy of enforcement of building regulations. In Chile, buildings resisted well, but communication networks failed. Tsunami alarm could also work if the appropriate instruments—continuous accelerometers like those of northern Chile—are used together with an earthquake-proof communication network in order to compute almost-real-time location and magnitudes in Chile.

References

1. C. Darwin, *Journal of Researches into the Natural History* (John Murray, London, 1845); available at darwin-online.org.uk/EditorialIntroductions/Freeman_JournalofResearches.html
2. F. Montessus de Ballore, *Historia Sismica de los Andes Meridionales* (Cervantes, Santiago, 1911–1916).
3. C. Lomnitz, *Geofis. Panamericana* **1**, 151 (1971).
4. J. A. Kelleher, *J. Geophys. Res.* **77**, 2087 (1972).
5. S. P. Nishenko, *J. Geophys. Res.* **90**, 3589 (1985).
6. S. Barrientos, *Seismol. Res. Lett.* **61**, 43 (1990).
7. J. Campos, E. Kausel, *Seismol. Res. Lett.* **61**, 1 (1990).
8. R. Madariaga, *Fis. Tierra* **10**, 221 (1998).
9. S. Beck *et al.*, *J. S. Am. Earth Sci.* **11**, 115 (1998).
10. J. Campos *et al.*, *Phys. Earth Planet Inter.* **132**, 177 (2002).
11. J. Klotz *et al.*, *Earth Planet. Sci. Lett.* **193**, 437 (2001).
12. J. C. Ruegg *et al.*, *Geophys. Res. Lett.* **29**, 1517 (2002).
13. B. A. Brooks *et al.*, *Geochem. Geophys. Geosyst.* **4**, 1085 (2003).
14. M. Moreno *et al.*, *Geochem. Geophys. Geosyst.* **9**, Q12024 (2008).
15. J. C. Ruegg *et al.*, *Phys. Earth Planet Inter.* **175**, 78 (2009).
16. C. Vigny *et al.*, *Phys. Earth Planet Inter.* **175**, 86 (2009).
17. S. Hough, *Predicting the Unpredictable* (Princeton Univ. Press, Princeton, NJ, 2010).

10.1126/science.1189197

MATERIALS SCIENCE

Probing the Nanoscale

Probes that can now measure a variety of nanomechanical properties provide opportunities for new science and devices.

Robert F. Cook

Measurement probes to determine nanomechanical properties are confirming long-held beliefs, revealing new phenomena, and enabling commercialization of devices based on micro- and nano-electromechanical systems (MEMS and NEMS). The resistance of materials and structures to the complete range of deformation modes—reversible, irreversible, and time-dependent—can now be measured with great accuracy, precision, and spatial resolution.

As most devices are designed to perform mechanically in an elastic (reversible) manner, the mechanical property of greatest importance is the elastic modulus. The technique that provides the greatest spatial resolution is contact resonance atomic force microscopy (CR-AFM). Changes in the resonance frequencies of an AFM cantilever probe are measured as the probe tip is brought into contact with a surface; the contact stiffens the cantilever response, increasing the cantilever resonance frequencies. Knowledge of the cantilever dynamics and contact mechanics of the tip-surface interface allows the modulus of the contacted material to be determined. Contact radii of 2 to 3 nm are generated by means of probe tips of 20- to 40-nm radius and controlled contact loads in the 100 nN range, providing the ability to map the stiffness (and hence the modulus) with better than 10-nm spatial resolution. This system was used to map the elastic modulus of a nanocrystalline gold film (*1*) and confirmed directly the long-held belief that, as they are less dense, grain boundary regions are more compliant than grains, up to a factor of two smaller in modulus in some cases. Such measurements are critical in predicting the response of nanomaterials to stress, especially nanograined polycrystals, because they contain a much greater proportion of grain boundary material than their macrograined counterparts and are thus more compliant (see the figure, panel A).

CR-AFM was also used to measure the elastic moduli of zinc oxide (*2*) and tellurium nanowires (NWs) (*3*) and revealed new mechanical phenomena intrinsic to the nanoscale. NWs with radii greater than about 100 nm exhibited moduli comparable to bulk material. However, NWs with radii less than 100 nm exhibited dramatically enhanced moduli. The change in the NW properties is opposite to that for grain boundaries: Surface tension effects lead to a rearrangement of atomic positions and greater atomic densities at surfaces and thus lead to a stiffer shell of surface material surrounding a NW core of bulk-like material. As the NW radius decreases, the ratio of shell/core material increases, leading to stiffening. For NWs smaller than a critical radius, the bulk core disappears, the NW is all "shell," and the modulus is invariant (*3*) (see the figure, panel B).

Other mechanical properties define limits on the loading that a device can withstand and still perform. The technique that provides the greatest resolution for measurement of material resistance to (irreversible) plastic deformation is instrumented indentation testing, or nanoindentation. Here, the load and displacement of a hard, stiff probe, typically a pyramidal diamond with a 50-nm tip radius, are measured as the probe contacts a surface. For very small indentation contacts on metals, the deformation is elastic and yield—the onset of plastic deformation—is quantized, as irreversible deformation is associated with the nucleation or motion of individual dislocations. Such quantized yield is discernible as an abrupt displacement of the indenter into the surface of the material at a fixed load, a "pop-in" event. Nanoindentation measurements, combined with AFM of the real shape of the indenting probe and finite element analyses of the indentation stress field, were used to measure the single-crystal shear yield stress of tungsten (*4*). The loads required for such irreversible events were in the 100 μN range, generating contact radii of about 30 nm; both much greater than those for the purely elastic responses sensed in CR-AFM.

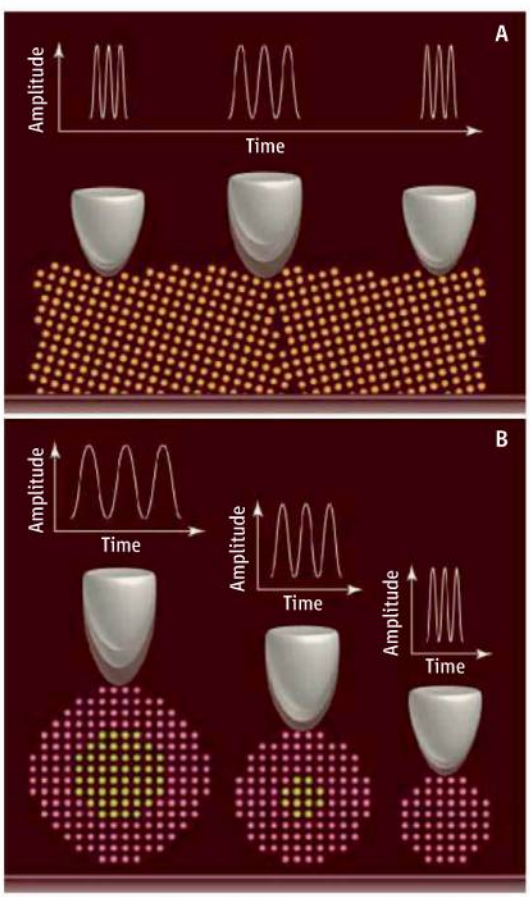

Material probes. The oscillation frequency of an AFM probe is altered as it encounters materials with different structure and stiffness. (**A**) The frequency decreases as the probe is scanned over disordered and less dense grain boundary regions, confirming directly that grain boundaries are more compliant than grains. (**B**) The frequency increases as the probe contacts nanowires of decreasing radii, indicating that surface effects lead to a stiffer, denser shell surrounding a bulk-like core. Nanowires smaller than a critical radius are all surface-affected shell.

Nanoindentation techniques have also been developed to measure viscoelastic (time-dependent) properties. The response of the indenter during fixed-load or fixed-displacement is measured as a function of time. Such methods have been used to determine the viscoelastic properties of polyurethane (*5*) using a spherical indenter and thence to predict the time-dependent responses over different time scales and indenter geometries. Flat-punch indentation measurements of the amplitude and phase of the probe displacement for an oscillating contact load were used to predict the time-dependent nanoindentation response of polyvinylchloride (*6*). Conical indentation models can describe and predict the time-dependent and irreversible viscous-elastic-plastic properties of glassy polymers (*7*) such as polymethylmethacrylate.

Although enormous progress has been made in the past 20 years in nanomechanical probing, two challenges remain, at either end of the

Nanomechanical Properties Group, National Institute of Standards and Technology, Gaithersburg, MD 20899, USA. E-mail: robert.cook@nist.gov

materials spectrum. The first challenge is brittle materials and fracture. Although nanoindentation techniques with acute probes can generate cracks at small length scales (*8*), and the mechanics of acute indentation have been identified and analyzed (*9*), postindentation observation of cracks is required to determine toughness. The methodology has been demonstrated on nanoporous dielectric films with crack lengths as short as 300 nm in 500-nm thick films (*8*, *9*). A method that determined fracture properties in situ—for example derived from the indentation pop-in associated with crack nucleation—would be an obvious advantage in improving the reliability and thus commercialization of MEMS and NEMS devices.

The second challenge is biological and other gel-like materials that contain an appreciable fluid phase. In these systems, flow through a porous elastic or viscoelastic matrix determines the time-dependent deformation properties. Probe-based techniques, rooted in poroelastic mechanics, have been used to characterize the behavior of hydrogels (*10*). Such measurements are also able to determine the permeability of the matrix to the fluid and indicate reduced permeability at the nanoscale in bone (*11*). Development of nanomechanical probes for poroelastic systems would enable rapid development of artificial tissues and biomedical devices.

The primary focus of the Feynman lecture "There's Plenty of Room at the Bottom" (*12*) was fabrication of nanoscale devices, although the important differences between mechanical properties at the nanoscale and those of bulk materials were mentioned as critical in designing and operating such devices. This need is now being met as nanomechanical probes can determine elastic, plastic, viscous, and fracture properties of materials and structures with nanoscale spatial resolution. Such probes are enabling bounds to be placed on the length scales at which materials behave as the bulk and revealing exciting new phenomena when these bounds are exceeded.

References

1. G. Stan *et al.*, *Nanotechnology* **19**, 235701 (2008).
2. G. Stan *et al.*, *Nano Lett.* **7**, 3691 (2007).
3. G. Stan *et al.*, *Appl. Phys. Lett.* **92**, 241908 (2008).
4. L. Ma *et al.*, *J. Mater. Res.* **24**, 1059 (2009).
5. M. L. Oyen, *Philos. Mag.* **86**, 5625 (2006).
6. E. G. Herbert *et al.*, *J. Mater. Res.* **24**, 626 (2009).
7. M. L. Oyen *et al.*, *J. Mater. Res.* **18**, 139 (2003).
8. D. J. Morris *et al.*, *J. Mater. Res.* **23**, 2429 (2008).
9. D. J. Morris *et al.*, *J. Mater. Res.* **23**, 2443 (2008).
10. M. Galli *et al.*, *J. Mater. Res.* **24**, 973 (2009).
11. M. L. Oyen *et al.*, *J. Mater. Res.* **23**, 1307 (2008).
12. R. P. Feynman, *Eng. Sci.* **23**, 22 (1960).

10.1126/science.1186023

MEDICINE

Poisonous Contacts

The therapeutic effect of arsenic on promyelocytic leukemia depends on direct binding of the compound to the causative oncogenic protein.

Scott C. Kogan

In the 1939 play *Arsenic and Old Lace*, the main character discovers many secrets about his family, including that his aunts are serial killers who murder lonely old men by serving them elderberry wine poisoned with arsenic. In addition to its use as a lethal poison, arsenic has been used since ancient times to treat human illnesses, including infectious diseases and malignancies (*1*). The remarkable story of arsenic as a modern medical treatment continues, and on page 240 of this issue (*2*), Zhang *et al*. add to our understanding of how its therapeutic effects have made acute promyelocytic leukemia "curable," with survival rates of ~90% (*3*).

Until recently, the use of arsenic in modern Western medicine was limited to treating parasitic infection. This began to change when in 1992 a group from Harbin, China, reported using a traditional Chinese medicine, "Ai-ling 1," to successfully treat patients with promyelocytic leukemia (*4*). The active ingredient in Ai-ling 1 was shown to be arsenic trioxide, which induced remissions in patients with promyelocytic leukemia, including those who had relapsed after other prior therapy (*5*, *6*).

Acute promyelocytic leukemia is one subtype of acute myeloid leukemia. It is characterized in nearly all cases by a recurrent reciprocal translocation between chromosomes 15 and 17, involving the gene encoding the retinoic acid receptor alpha (*RARA*) which is fused to the promyelocytic leukemia gene (*PML*) (see the figure). The leukemic cells of promyelocytic leukemia are morphologically distinctive (they exhibit numerous primary granules) because of their growth arrest at the promyelocyte stage of a differentiation process that produces mature neutrophils. The PML-RARα fusion protein represses transcription at multiple sites in the genome. In combination with other events, often including an activated FLT3 tyrosine kinase, PML-RARα blocks myeloid differentiation. However, retinoic acid induces differentiation of the leukemic promyelocytes, and both retinoic acid and arsenic trioxide together cause degradation of PML-RARα protein, a key event in their ability to eliminate the leukemia (*7*). Current treatment protocols for promyelocytic leukemia include combining both agents (*3*).

The discovery of arsenic therapy for promyelocytic leukemia was made empirically, but was quickly found to be a gene-targeted therapy. Arsenic causes the degradation of normal PML, a protein important for regulating growth and programmed cell death (apoptosis), as well as the destruction of the PML-RARα fusion protein. Arsenic also induces modification of PML-RARα with the molecules SUMO and ubiquitin, the transfer of PML-RARα to an insoluble nuclear matrix, and the degradation of both PML and PML-RARα (*8*–*12*). How arsenic exerts these effects has not been clear. Arsenic trioxide binds to thiol groups and thereby can inhibit protein phosphatases. This promoted the hypothesis that arsenic trioxide increases the phosphorylation of PML at a site that stimulates SUMOylation and subsequent degradation. Surprisingly, Zhang *et al*. show that arsenic works not through binding and inhibiting a phosphatase, but by direct binding to thiol groups within PML itself.

Zhang *et al*. used a combination of immunofluorescent localization within cells, cellular fractionation, mass spectrometry, nuclear magnetic resonance, near-ultraviolet and x-ray spectroscopy, and circular dichroism to examine the interactions of PML with arsenic. Their results show a direct interaction of arsenic with PML, including through cysteines located in PML zinc fingers (structural motifs that coordinate zinc) within the RING and B2 domains of the protein. The interaction of arsenic (instead of zinc) with zinc fingers induced subtle changes in the structure of the fingers, and these changes were associated with oligomerization of PML proteins. The exact molecular mechanisms by which arsenic triggers this oligomerization, as well as

Laboratory Medicine, University of California San Francisco Cancer Center, CA 94143–0100, USA. E-mail: scott.kogan@ucsf.edu

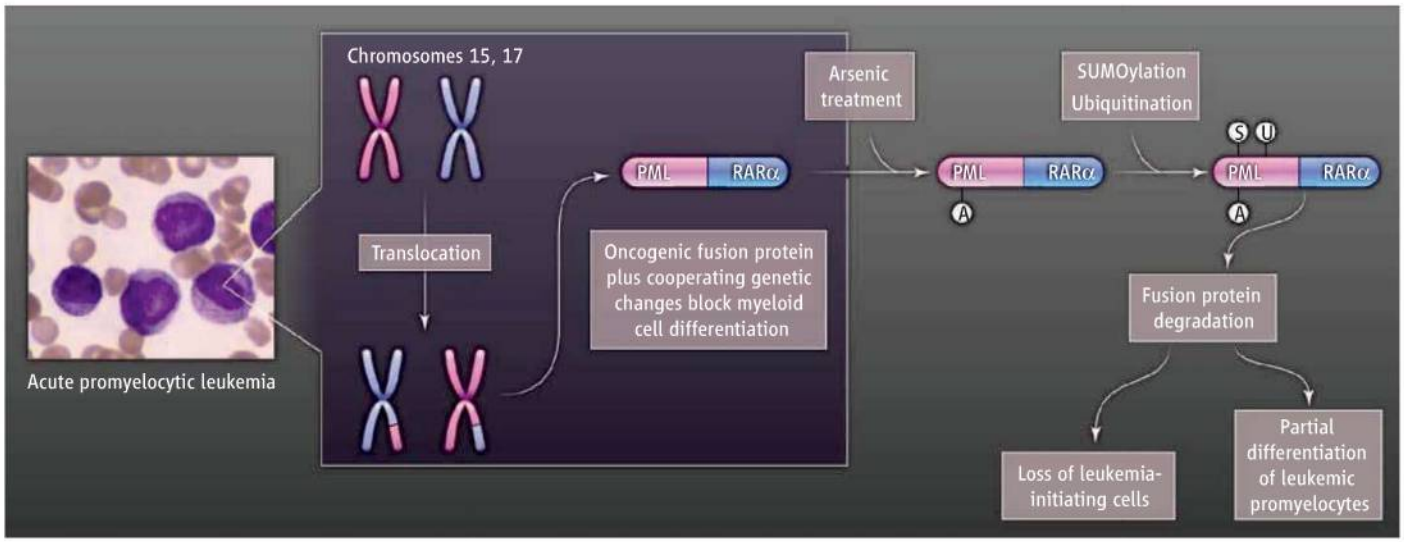

Arsenic therapy. Acute promyelocytic leukemia arises from a translocation that produces the fusion protein PML-RARα. Arsenic binds to PML-RARα, stimulating its SUMOylation, ubiquitination, and degradation. This allows partial differentiation of leukemic promyelocytes and eliminates leukemia-initiating cells.

stimulates the recruitment of the SUMOylation and ubiquitination complexes to PML proteins, remain to be elucidated.

Of note, Zhang *et al.* demonstrate that mutations of cysteine to alanine within either of two zinc fingers of the RING domain in PML decreased arsenic binding, and consequently, abrogated the ability of arsenic to induce degradation of PML. These data indicate that binding to more than one site within PML cooperatively contributes to arsenic's therapeutic effect. It will be of interest to assess whether point mutations can prevent arsenic-induced degradation without disrupting the function of normal PML or the oncogenic effects of PML-RARα.

Understanding the molecular mechanisms underlying promyelocytic leukemia is of great interest, but it remains to be seen whether the findings of Zhang *et al.* will have broader clinical importance. Arsenic-induced degradation of PML might be useful for treating other human malignancies. Recent data suggest that PML degradation might eliminate the cells from which chronic leukemias relapse after therapy (*13*), and implicate the importance of PML for the oncogenic effects of mutant p53 protein, a change seen in many human cancers (*14*). Despite disappointing clinical results with arsenic to date, perhaps proper case selection and combination therapy with arsenic will lead to improved outcomes for treating not only promyelocytic leukemia but other human malignancies as well. If so, an ancient medicine, revived through careful clinical and biological studies in modern times, will have an even greater impact on human health.

References and Notes

1. J. Zhu *et al.*, *Nat. Rev. Cancer* **2**, 705 (2002).
2. X.-W. Zhang *et al.*, *Science* **328**, 240 (2010).
3. J. Hu *et al.*, *Proc. Natl. Acad. Sci. U.S.A.* **106**, 3342 (2009).
4. H. Sun *et al.*, *Chin. J. Integrat. Tradit. Chin. West. Med.* **12**, 1701 (1992).
5. P. Zhang *et al.*, *Chin. J. Hematol.* **17**, 58 (1996).
6. Z. Shen *et al.*, *Blood* **89**, 3354 (1997).
7. R. Nasr *et al.*, *Nat. Med.* **14**, 1333 (2008).
8. J. Zhu *et al.*, *Proc. Natl. Acad. Sci. U.S.A.* **94**, 3978 (1997).
9. S. Muller, M. Matunis, A. Dejean, *EMBO J.* **17**, 61 (1998).
10. W. Shao *et al.*, *J. Natl. Cancer Inst.* **90**, 124 (1998).
11. V. Lallemand-Breitenbach *et al.*, *J. Exp. Med.* **193**, 1361 (2001).
12. M. H. Tatham *et al.*, *Nat. Cell Biol.* **10**, 538 (2008).
13. K. Ito *et al.*, *Nature* **453**, 1072 (2008).
14. S. Haupt *et al.*, *Cancer Res.* **69**, 4818 (2009).

10.1126/science.1189198

MATERIALS SCIENCE

Graphene Spreads the Heat

Can graphite monolayers outcompete traditional heat-spreading materials in electronic devices?

Ravi Prasher

The reliability and speed of electronic and optoelectronic devices strongly depend on temperature (*1*, *2*). Materials with very high thermal conductivities are required to spread the heat generated locally in such devices (*2*). Bulk copper, which is widely used as heat spreader in computers, has a thermal conductivity of ~400 W m^{-1} K^{-1} at room temperature, but copper thin films, used as electrical interconnects, can have lower thermal conductivity (below 250 W m^{-1} K^{-1}) (*3*). The search is thus on for materials with thermal conductivities higher than that of copper. On page 213 of this issue, Seol *et al.* (*4*) report that single monolayers of graphite (graphene) in contact with silicon dioxide (SiO_2) has a thermal conductivity of ~600 W m^{-1} K^{-1}.

Pure-carbon materials such as diamond, graphite, and carbon nanotubes have very high thermal conductivities, because the strong covalent bonding between carbon atoms results in a large phonon (lattice vibration) contribution to the thermal conductivity. Recently, graphene has attracted much attention due to its unique properties (*5*), such as very high intrinsic charge carrier mobility. Yin *et al.* have reported the fabrication of 100-GHz graphene-based transistors (*6*).

For future applications, it will be crucial to understand heat generation and dissipation from graphene-based devices. Previous measurements (*7*, *8*) on single monolayers of single-wall carbon nanotubes and graphene were performed in suspended form (see the figure, panel A), where the thermal conductivity was very high due to the strong covalent

Intel Corporation, 5000 West Chandler Boulevard, Chandler, AZ 85226, USA. E-mail: ravi.s.prasher@intel.com

CREDIT: C. BICKEL/*SCIENCE*

bonds between the carbon atoms. Suspended graphene has a thermal conductivity of 5000 W m^{-1} K^{-1} at room temperature (*7*)—about 2.5 times as large as that of diamond, which has the highest thermal conductivity among natural materials.

However, in most practical applications—such as composites for thermal interface materials (*9*) or heat spreaders in devices (*10*)—single-layer materials will be bound to a much thicker bulk material, such as SiO_2 or a polymer, typically through weak van der Waals forces. How do these weak contacts affect thermal transport in the monolayers?

To address this question, Seol *et al.* first attached a graphene layer to an SiO_2 surface through a process known as mechanical exfoliation (*11*) and measured the thermal conductance of the combined structure. They then etched away the graphene layer and measured the thermal conductance of only the SiO_2 layer. The difference between the two values gave them the conductance of the graphene layer, from which the thermal conductivity of the graphene layer was extracted. At room temperature, the thermal conductivity of the supported graphene layer is ~600 W m^{-1} K^{-1}, an order of magnitude lower than that of suspended graphene. However, this is still higher than the thermal conductivities of bulk or thin-film copper (*3*). When Klemens (*12*) first envisioned this type of experiment, he predicted a decrease in the thermal conductivity of graphene in contact with a substrate, even before single-layer graphene exfoliation was first demonstrated (*11*).

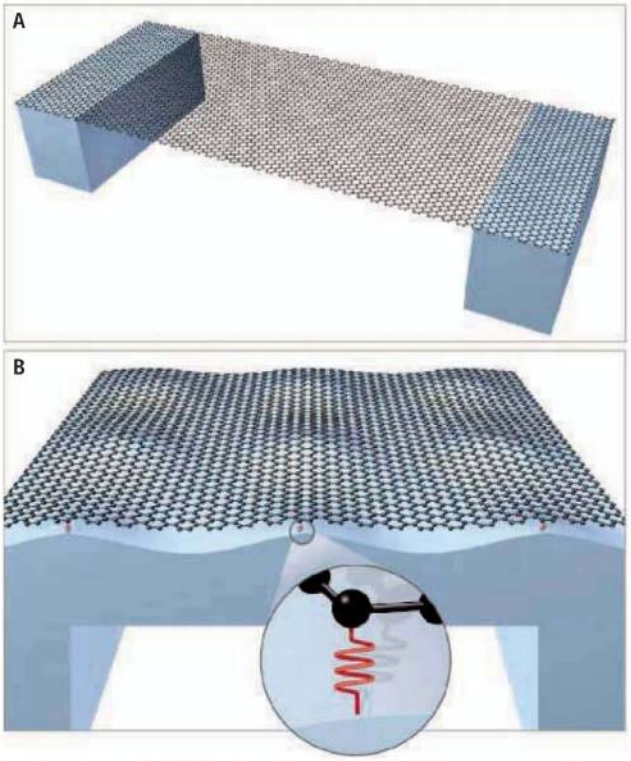

Lending support. (**A**) Previous thermal conductivity measurements were performed on suspended graphene. (**B**) Seol *et al.* instead studied graphene supported on a substrate. The graphene layer does not conform to the nanoscale roughness of the substrate; rather, it makes contact on the summits of the rough surface, interacting with the substrate through van der Waals forces (red springs).

In bulk carbon materials such as diamond, three acoustic phonon modes contribute substantially to the thermal conductivity: one longitudinal (LA) and two transverse (TA) modes. For LA modes, the atomic vibration is in the direction of the wave propagation, whereas for TA modes, it is perpendicular to the wave-propagation direction. For both modes, the phonon frequency is proportional to the wave vector (inverse of wavelength), that is, the phonon dispersion is linear. In large-diameter single-wall carbon nanotubes, there are also three phonon modes, but one of them is a flexural (ZA) mode with a quadratic phonon dispersion. Similarly, in graphene, the third mode is flexural.

Thermal conductivity is given by the product of specific heat, mean phonon scattering time, and the square of phonon group velocity integrated over the whole phonon frequency range. In suspended graphene, the contribution of the ZA mode was thought to be negligible (*13*), because the group velocity of the ZA mode is smaller than the group velocity of the LA and TA modes. Starting with this assumption for suspended graphene and then applying the van der Waals forces for supported graphene, Seol *et al.* could not explain their experimental data on supported graphene both in magnitude and trend.

To explain their data over the entire temperature range, Seol *et al.* performed a revised calculation for suspended graphene. They show that the ZA mode contributes substantially to the thermal conductivity of suspended graphene, for two reasons: First, the specific heat for the ZA mode is higher than that of the LA and TA mode for temperatures up to ~360 K, because the maximum frequency of ZA mode is smaller than that of the LA and TA modes. Second, the mean scattering time of the ZA mode is much larger than that of the LA and TA modes. Because of these two effects, the ZA mode can contribute as much as 77% at 300 K and 86% at 100 K of the calculated thermal conductivity for suspended graphene. In the case of supported graphene, the van der Waals interactions between graphene and the substrate (see the figure, panel B) reduce the contribution of the ZA mode (*4*): At room temperature, the ZA mode contributes only 25% to the thermal conductivity in supported graphene, compared to 77% in suspended graphene.

To explain their results, Seol *et al.* propose that ZA mode phonons leak into the substrate through the van der Waals springs that connect the graphene to the substrate (see the figure, panel B). The force constant of the ZA mode is much larger than that of the LA and TA modes. Larger force constant means tighter coupling with the substrate, leading to more leaking of ZA modes compared to the LA and TA modes. Leaking of phonons into the substrate was also predicted by Klemens (*12*). To explain their data, Seol *et al.* also assume—based on scanning probe microscopy studies (*14*)—that the graphene does not conform completely to the surface (see the figure, panel B).

What makes this study remarkable is that it combines thermal, structural, and mechanical phenomena into one theoretical framework. This is a crucial first step toward explaining the thermal conductivity of supported graphene. However, many questions remain. For example, the large thermal contact resistance of carbon nanotubes has severely limited their use as a high-thermal-conductivity material. Can graphene overcome this limitation due to its flat structure? Future studies should also investigate what will happen to the in-plane thermal conductivity and contact resistance if the graphene completely conforms to the surface or is embedded in a bulk material, or if the interactions with the substrate are stronger, for example, in contact with metals.

References

1. A. Majumdar, *Nat. Nanotechnol.* **4**, 214 (2009).
2. R. Mahajan *et al.*, *Proc. IEEE* **94**, 1476 (2006).
3. Y. Yang *et al.*, *Appl. Phys. Lett.* **84**, 3121 (2004).
4. J. H. Seol *et al.*, *Science* **328**, 213 (2010).
5. A. K. Geim, *Science* **324**, 1530 (2009).
6. Y.-M. Lin *et al.*, *Science* **327**, 662 (2010).
7. A. A. Balandin *et al.*, *Nano Lett.* **8**, 902 (2008).
8. C. Yu *et al.*, *Nano Lett.* **5**, 1842 (2005).
9. R. Prasher, *Proc. IEEE* **94**, 1571 (2006).
10. A. A Balandin, Better computing through CPU cooling, *IEEE Spectrum*, October 2009, http://spectrum.ieee.org/semiconductors/materials/better-computing-through-cpu-cooling/0
11. K. S. Novoselov *et al.*, *Science* **306**, 666 (2004).
12. P. G. Klemens, *Int. J. Thermophys* **22**, 265 (2001).
13. D. L. Nika *et al.*, *Appl. Phys. Lett.* **94**, 203103 (2009).
14. V. Geringer *et al.*, *Phys. Rev. Lett.* **102**, 076102 (2009).

10.1126/science.1188998

Four-Dimensional Electron Microscopy

Ahmed H. Zewail

The discovery of the electron over a century ago and the realization of its dual character have given birth to one of the two most powerful imaging instruments: the electron microscope. The electron microscope's ability to resolve three-dimensional (3D) structures on the atomic scale is continuing to affect different fields, including materials science and biology. In this Review, we highlight recent developments and inventions made by introducing the fourth dimension of time in electron microscopy. Today, ultrafast electron microscopy (4D UEM) enables a resolution that is 10 orders of magnitude better than that of conventional microscopes, which are limited by the video-camera rate of recording. After presenting the central concept involved, that of single-electron stroboscopic imaging, we discuss prototypical applications, which include the visualization of complex structures when unfolding on different length and time scales. The developed UEM variant techniques are several, and here we illucidate convergent-beam and near-field imaging, as well as tomography and scanning-pulse microscopy. We conclude with current explorations in imaging of nanomaterials and biostructures and an outlook on possible future directions in space-time, 4D electron microscopy.

The microscope and the telescope are arguably among the most powerful human-made instruments. To our vision, they have brought the very small and the very far away. Robert Hooke, for his *Micrographia*, chose the subtitle *Some Physiological Descriptions of Minute Bodies Made by Magnifying Glasses with Observations and Inquiries Thereupon* (*1*). These words were made in reference to the traditional optical microscope, for which the spatial resolution is limited by the wavelength of light; centuries later, major advances by new variant techniques have resulted in the crossing of such a limit (*2*–*4*). The transmission electron microscope (TEM), since its invention in the 1930s (*5*), has provided wavelengths on the picometer scale, taking the field of imaging beyond the "minutes" of Hooke's 17th-century *Micrographia*: It has become possible to image atoms in real space, reaching resolutions below 0.1 nm. The scope of applications (*6*) spans essentially all of the physical sciences and includes biology. Until recently, the structures determined in these studies were time-averaged over seconds of recording.

To reach the ultrashort time resolution of atomic motions (*7*), and at the same time maintain the high spatial resolution, a different approach from that of the millisecond-limited TEM or the nanosecond high-speed imaging method had to be conceived. In conventional microscopes, the electrons are produced by heating the source or by field emission, resulting in randomly distributed bursts of a continuous electron beam. Photoelectron emission from a cathode can provide ultrashort pulses of electrons for time-resolved diffraction, as discussed below and detailed elsewhere (*8*); but for imaging, the use of a large number of electrons in a pulse imposes limits on the temporal and spatial resolutions of the microscope. This is because repulsion between electrons prevents the attainment of high spatiotemporal resolutions, and it is not feasible to image the ultrafast elementary dynamics of a complex transformation. The challenge was then in obtaining the high spatial resolution of conventional electron microscopy (EM) but simultaneously enabling the temporal resolution of atomic-scale motions.

In this Review, we discuss the development of four-dimensional ultrafast electron microscopy (4D UEM) (*9*–*11*) and summarize applications (*12*) that illustrate the potential of the approach. In UEM space-time domains (Fig. 1), images are obtained stroboscopically with single-electron coherent packets. Under such a condition, electron repulsion is absent, permitting real-space imaging, Fourier-space diffraction, and energy-space electron spectroscopy with high spatiotemporal resolutions. The time resolution becomes limited only by the laser pulse width and energy width of the packets, the camera rate of recording becomes irrelevant for the temporal resolution, and the delay between pulses can be controlled to allow for the cooling of the specimen and/or repetitiveness of the specimen's exposure. The applications given here are selected to display phenomena of different length and time scales, from atomic motions in structural dynamics, to phase transitions, to membrane mechanical drumming. We also discuss single-pulse and single-particle imaging, using convergent-beam UEM, and include the recent developments of techniques for nanomaterials and biological structures. To begin, it is instructive to discuss the concepts involved in 4D microscopy imaging.

Physical Biology Center for Ultrafast Science & Technology, California Institute of Technology, Pasadena, CA 91125, USA. E-mail: zewail@caltech.edu

Single-Electron Imaging: Space and Time

Since its original use in viewing rotating objects, a stroboscope (*strobos* from the Greek word for "whirling" and *scope* from the Greek for "look at") can produce, with appropriately chosen pulses of light, a well-resolved image of a moving object, such as a bullet or a falling apple. Thus, the pulse duration plays the same role as the opening of a camera shutter. The time duration required to observe, with high definition, transformations in which atoms move at speeds of the order of 1 km/s is in the femtosecond domain, and although laser light pulses can capture atoms in motion (*7*), they cannot, for complex structures, image the positions of all atoms in space because of the limitation imposed by their relatively long wavelength. Accelerated electrons, however, waive such a restriction.

The concept of single-electron imaging is based on the premise that trajectories of coherent and timed single-electron packets can provide an image that is equivalent to that obtained by using many electrons in conventional microscopes. Unlike the random electron distribution of con-

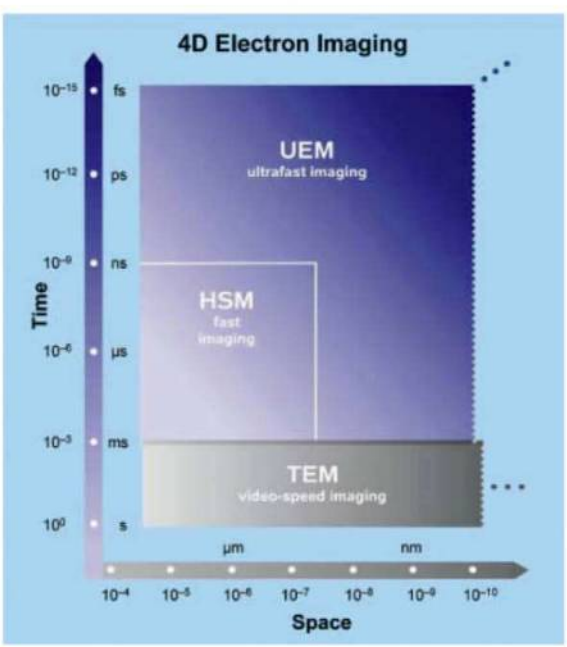

Fig. 1. 4D electron imaging. The resolution boundaries of ultrafast imaging are compared with those achieved in conventional TEM, limited by the speed of video camera, and, in high-speed microscopy (HSM), defined by the rectangle shown. The spatiotemporal scales of UEM achieved to date are outlined with possible future extensions. The approaches of single-electron and single-pulse imaging are fundamentally different because of the limiting problem of space-charge described in the text.

ventional microscopes, in UEM, the packets are timed with femtosecond precision, and each electron has a unique coherence volume (Fig. 2). Each electron with de Broglie's "pilot waves" (*13*) is (transversely) coherent over the object length scale to be imaged, with a longitudinal coherence length that depends on the electron's velocity; on the detector, the electron produces a "click," behaving as a classical particle. When a sufficient number of such clicks is accumulated stroboscopically, the whole image emerges. In other words, "each electron interferes only with itself." In the microscope, the electron pulse that produces the image is termed the probe pulse, and in ultrafast imaging with a train of such pulses, the number of frames in a movie could be higher than 10^{12} per second; as such, this stop-motion photography constitutes a real-time movie of the process.

To visualize the motion, the molecule or material must be launched on its path by using a femtosecond initiation optical pulse, called the clocking or pump pulse, thus establishing a temporal reference point (time zero) for the changes that occur in the motion. By sending the clocking pulse along an adjustable optical path, we can precisely fix each probe frame on the time axis: Knowing the speed of light, a typical optical path accuracy of 1 μm corresponds to absolute timing of the snapshots of 3.3 fs. Because the clocking pulse is controlled to precede each electron pulse, the time axis is defined by the separation between them and is no longer limited by the response of the video detector in the microscope. Lastly, to synchronize the motion of many independent atoms or molecules so that all of them have reached a similar point in the course of their structural evolution, the relative timing of clocking and probe pulses must be of femtosecond precision, and the launch configuration must be defined to sub-angstrom resolution.

In imaging with electrons (fermions), unlike with photons (bosons), we must also consider consequences of the Pauli exclusion principle. The maximum number of electrons that can be packed into a state (or a cell of phase space) is two, one for each spin; in contrast, billions of photons can be condensed in a state of the laser radiation. This characteristic of electrons represents a fundamental difference in what is termed the "degeneracy," or the mean number of electrons per cell in phase space. Typically it is about 10^{-4} to 10^{-6}, but it is possible in UEM to increase the degeneracy by orders of magnitude, a feature that could be exploited for studies in quantum electron optics (*12*). We note here that the definition of a "single electron packet" is reserved for the case when each timed packet contains one, or a small number, of electrons such that the Coulombic repulsion is effectively absent.

The temporal (longitudinal) coherence length of the packet is simply given by $l_{tc} = v_e \cdot (h/\Delta E)$, with the width ΔE being determined by the energy of the photoelectrons relative to the work function of the cathode, v_e is the electron velocity,

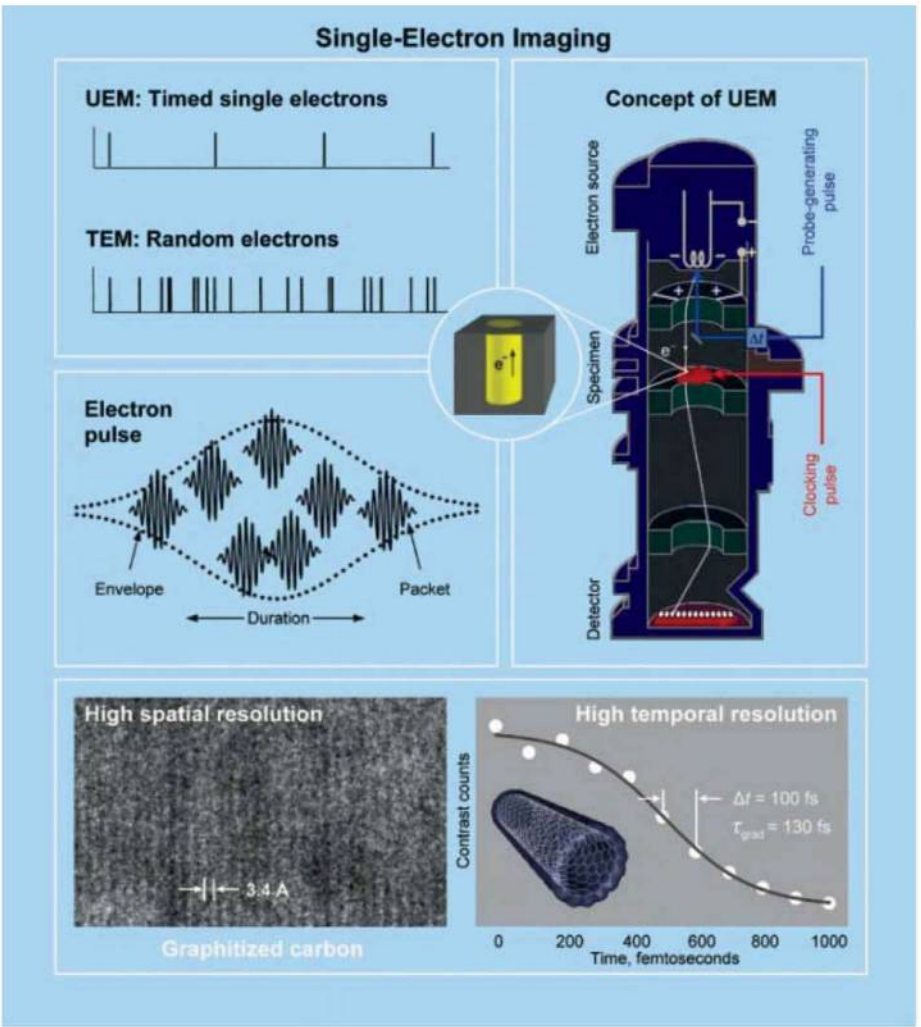

Fig. 2. Conceptual and experimental realization of single-electron imaging. Shown are schematics of timed single-electron packets (UEM) and random electrons (conventional TEM) used in imaging (upper left). Also depicted is the electron-pulse envelope together with individual electron packets (center left). A single-electron trajectory is schematized in the microscope together with an illustration of what is meant by a coherence volume (upper right; see text). The bottom panel displays a high-resolution UEM image of graphitized carbon with lattice-plane separations of 3.4 Å (left), and a temporal profile obtained from the images of evanescent fields in carbon nanotubes; the time steps are of 100-fs duration, and the rate of change is given by the gradient (τ_{grad} = 130 fs), which is determined by the materials response and pulse widths involved (see the section on near-field UEM and Fig. 5). The experimental data are from (*10*, *46*).

and h is Planck's constant. The spatial (transverse) coherence length (l_{sc}) is a measure of the beam coherence and is given by $h/\Delta P_T$, where ΔP_T is the transverse momentum spread; it can be expressed in terms of the source angular deviation (α) at the specimen, $l_{sc} = \lambda_e/\alpha$, by simply dividing both the numerator and denominator of $h/\Delta P_T$ by the longitudinal momentum value. The coherence volume of each cell becomes

$$V_c(\text{cell}) \equiv \Delta x \Delta y \Delta z = l_{tc}(\text{longitudinal}) \times l_{sc}^2(\text{transverse}) \quad (1)$$

The value of l_{tc} can be estimated from knowing the energy width ΔE, and l_{sc} for a simple geometry becomes the product of the de Broglie wavelength (λ_e) and the ratio of the distance (L) to the specimen from the source and the source's width (w), $l_{sc} \approx \lambda_e(L/w)$. For λ_e of 2.5079 pm (200 keV UEM), this gives a coherence volume of about 10^6 nm^3, assuming the simple geometry mentioned. For a real microscope, electron trajectory calculations predict a range of 10^3 to 10^6 nm^3, depending on the number of electrons and the angular spread. The issues of cell volume and brightness of the source are important when considering the prerequisites of high-resolution imaging, through the so-called contrast transfer function, and for the regimes of noninteractive electron statistics. Figure 2 summarizes the key concepts involved in single-electron microscopy, together

with a typical high-resolution image and a temporal profile obtained in UEM.

The Ultrafast Electron Microscope

At the California Institute of Technology (Caltech), three UEM microscopes are in operation; one at a maximum voltage of 120 kV, the second at 200 kV, and the third with high-brightness, pulse-scanning capabilities. Upon the initiation of the structural change of the specimen by heating, or through electronic excitation by the ultrashort clocking pulse, a series of frames for real-space images, and similarly for diffraction patterns or electron energy-loss spectra (EELS), is obtained. In the single-electron mode of operation, which affords studies of reversible processes or repeatable exposures, the train of strobing electron pulses is used to build up the image. By contrast, in the single-pulse mode, each recorded frame is created with only one pulse of 10^5 to 10^6 electrons. By simply flipping two mirrors, one has the freedom to operate the apparatus in either single-electron or single-pulse mode.

The first high-resolution images were obtained in UEM-2 (Fig. 2). Frames of real-space images taken for graphitized carbon display the separations of atomic planes at 3.4 Å. For these carbon-family materials, the temporal response, acquired with EELS, was recorded on the femtosecond time scale, and so were their diffraction patterns in Fourier space (see below). Besides the electron-energy resolution, the apparatus can operate in the scanning transmission (STEM) mode, and with the variants of convergent-beam and near-field UEM imaging, as shown below.

Unlike measurements obtained from the whole of the specimen, microscopy images from a 2000- × 2000-pixel charge-coupled device (CCD) camera provide up to 4 million simultaneous observations, each attributable to a single, independent location on the specimen (subject to point-spread function limitations). As a result, the spatiotemporal changes, frame by frame, can be observed for all specimen points at once, which is the analog of parallel processing, without the spatial averaging. The power of selected-area (pixels) image dynamics was demonstrated in a study of gold following in situ femtosecond heating, at a rate higher than 10^{12} K/s, of the nanometer-thick single crystal (*10*).

Diffraction in Fourier Space: A Prelude

Historically, the discovery of electron diffraction was first made for materials (*14*, *15*) and then, within a few years, for gaseous molecules (*16*). With photoelectric methods, the time resolution in diffraction was advanced, first using 100-ps electron pulses and later with pulses in the 10-ps range; for a review of the early work by Mourou, Elsayed-Ali, and others, see (*17*). With diffraction, the challenge became in clocking structural changes with higher time resolution, and especially in the gas phase for isolated chemical reactions.

At Caltech, by using different generations of instruments (*8*), our research has focused on ultrafast structural dynamics in different phases (*17*, *18*). Experiments have included the following: isolated chemical reactions (*19*, *20*), structural phase transitions (*21*, *22*), molecular interfaces on hydrophobic and hydrophilic substrates (*23*–*25*), and nanowires of optoelectronic materials (*26*). In the groups of Miller, Cao, and Ruan (*27*–*29*), most of the work has been devoted to nonthermal melting and phonon dynamics and to nanoparticles. Typically, in such diffraction studies, the electron pulse contains thousands of electrons, but for subpicosecond electron dynamics (*30*, *31*), 100 or fewer electrons are used and with a novel geometry for the compensation of group-velocity mismatch between light and electron pulses (*22*). Care had to be taken to discern the effect of "surface charging," especially at high fluences (*12*).

Imaging in the Millisecond and Nanosecond Regimes

In conventional microscopes with a field-emission gun (FEG) or cathode heating, processes occurring on seconds or longer time scales are easily accessible. With fast CCD cameras, this scale can reach the millisecond time range. One of the most impressive examples comes from the study of relatively slow catalytic reactions and materials imperfections (*32*). It is difficult in EM to operate the instrument in such a manner as to allow for gas-solid and liquid-solid interactions, because the mean free path of the electrons becomes infinitesimal under these conditions. Gai and Boyes (*32*), in their environmental TEM, achieved atomic spatial resolution in the imaging of nanoparticles participating in catalytic turnover (Fig. 3), and they illustrated how such reactions can be temperature-resolved and time-resolved, at milliseconds and longer times. Similarly, nanoparticles shape change at elevated temperatures, and other phenomena related to materials imperfections can be examined.

With faster detectors, it is possible to reach the submillisecond range, however, not beyond the known response of electronics. Photoelectrons, which were invoked in the diffraction studies discussed above, provide the means to reach much higher time resolution, assuming that the photoelectrons generated by an optical pulse do not suffer from temporal and spatial losses of resolution during the journey to the specimen and on to the detector. Bostanjoglo and co-workers (*33*), in a series of seminal investigations of melting and ablation in thin metal films, obtained nanosecond temporal resolution and micrometer (and later submicrometer) spatial resolution using single pulses. Originally, they detected on a fast oscilloscope the total electron current in the bright field, after the sample had been pumped by a nanosecond laser pulse, obtaining low-resolution patterns. Later, however, with nanosecond electron pulses and deflection plates after the specimen, they obtained with somewhat better spatial resolution two or three images (deflected to different regions of the CCD) for the irreversible process under examination. Hence, the resolution was limited by the nanosecond pulses in the space-charge regime and by the electronics used for the electron beam deflection, which was used to overcome the slow detector response. Figure 3 displays typical frames that were taken with this high-speed recording method (see Fig. 1) in the Berlin laboratory.

In these studies of metal films exposed to high-fluence pulses of 7 to 30 J/cm^2, the focus was on the investigation of surface evaporation, boiling, and gas bubble formation. The images cannot provide structural information because of their low resolution, and for this reason, they invoked diffraction, as in the study of the phase change of crystalline titanium (*34*). Subsequent work at the Lawrence Livermore National Laboratory (LLNL) has further improved the spatial resolution and provided, from a large amount of nanosecond electron diffraction data, the transition time for titanium phase change; the resolution in images can reach tens of nanometers with nanosecond pulses. More recently, the LLNL group extended the high-speed nanosecond recording, in what is referred to as dynamic TEM, into another domain of investigation (*35*), namely the monitoring of reaction fronts in multilayer foils by initiating the reaction (with a light pulse) at one spot on the specimen and observing the front movement with the electron pulse at a distant location (Fig. 3).

These studies are valuable for nanosecond-limited irreversible processes, as discussed below. For them, the spatiotemporal resolution is determined by the fundamental space-charge effect, which was the central issue resolved by single-electron imaging.

4D UEM: Applications and Variants

Breaking the barrier into ultrafast temporal and high spatial resolutions provides the opportunity to explore new applications and to discover new phenomena. A paradigm case of UEM exploration, which illustrates the methodology, is that of the quasi-2D graphite studied in specimens of nanoscale. Graphite is unusual for many reasons, especially for its structure-phase connection to graphene and diamond. For this case, we shall consider below the progression in length and time scales, from those that characterize atomic motions to the macroscopic behavior when emergent function, such as drumming, becomes evident in 4D imaging (Fig. 4).

Prototypical Case: Graphite in 4D Space

Atomic motions. When the layered structure of graphite is subjected to a shock, the structure distorts, and ablation to form graphene (individual sheets of hexagonal sp^2-bonded carbons) may result from its instability. To elucidate the dynamics, a series of images and diffraction patterns were obtained at different times. The Bragg diffraction

shows changes in the position, intensity, and width of the peaks. These changes mirror the dynamics of the atomic positions of the crystal structure, because any increase or decrease in lattice spacings results in changes in diffraction characteristics. The patterns, when analyzed, reveal an initial lattice distortion (in the first 1 to 2 ps) followed by an expansion along the *c* axis of graphite, that is, the axis perpendicular to the carbon-atom planes. The maximum observed expansion of the lattice in 7 ps corresponds to ~1.25% of the *c* axis equilibrium value, 6.7 Å, which is beyond any thermal value, because such a change would correspond to a temperature jump of more than 1500 K. This conclusion is supported by the magnitude of the observed change, which scales correctly with the order of diffraction in both the intensity and the position of Bragg spots (*12*). Theory attributes the formation of graphene from graphite to these compression-expansion dynamics, and they are consistent with recent optical and surface studies of graphite (*12*, *29*, *36*–*38*).

Acoustic resonances and elasticity. On longer time and length scales, following the femtosecond pulse of heating stress, a strain propagates in the nanomaterial, and the strobing electron packets can then be used to probe the elastic modulation that occurs at the speed of sound. In other words, the initial atomic movements transform into acoustic waves of different frequencies and shapes (modes), and, depending on energy, some persist for picoseconds and beyond. This gives rise to an oscillatory (resonance) behavior in both the images obtained in real space and the diffraction patterns recorded in reciprocal space. The coherent resonance has two important features: the frequency and the decay of the amplitude. The latter gives the thickness inhomogeneity of the specimen, which, for the graphite studied, was found to be ±2 nm.

The resonance frequency (Fig. 4) directly relates to the force holding the layers (elasticity) and thickness of the material, in the same way a musical tone will. From these real-time experiments, the stress-strain profile, characterized by Young's modulus, was determined at the nanoscale. These hitherto-unobserved, very-high-frequency resonances (30-GHz range) are unique to the nanoscale dimensions of graphite. The speed of sound in nanographite along the longitudinal (*c* axis) direction is determined to be 4.0×10^5 cm/s, giving Young's modulus of 36.0 GPa. The period observed in the image is the same as that for the diffraction, indicating a direct correlation between the local atomic structure and the macroscopic elastic behavior. Selected-area imaging dynamics played a critical role, because different regions have temporally different amplitudes and phases across the image (*10*, *39*). These observations raise the following question: At what nanoscale would the continuum bulk material model break down?

Membrane mechanical drumming. At even longer time and length scales, new features came into focus in real-space imaging of graphite (*39*). The images displayed the vibrations of mechanical drumming. Upon the impulsive heating at time zero, the image changes considerably with a transition from a chaotic-looking behavior at early times, to quasiperiodicity at intermediate times, and on to a well-defined resonance oscillation emerging at longer times (Fig. 4). In other words, the motion collapses into a final resonance, in this case with a frequency of 1.08 MHz after several microseconds. The behavior is reminiscent of nonlinear couplings between modes of oscillations, but it may also reflect differences in the lifetimes of the modes excited in the nanosites. From this resonance of mechanical drumming of the whole plate, the in-plane (carbon sheets) Young's modulus was obtained, with a value of 0.94 TPa. This value is different by more than an order of magnitude from the *c* axis value, reflecting the strong in-plane chemical bonding and anisotropic behavior.

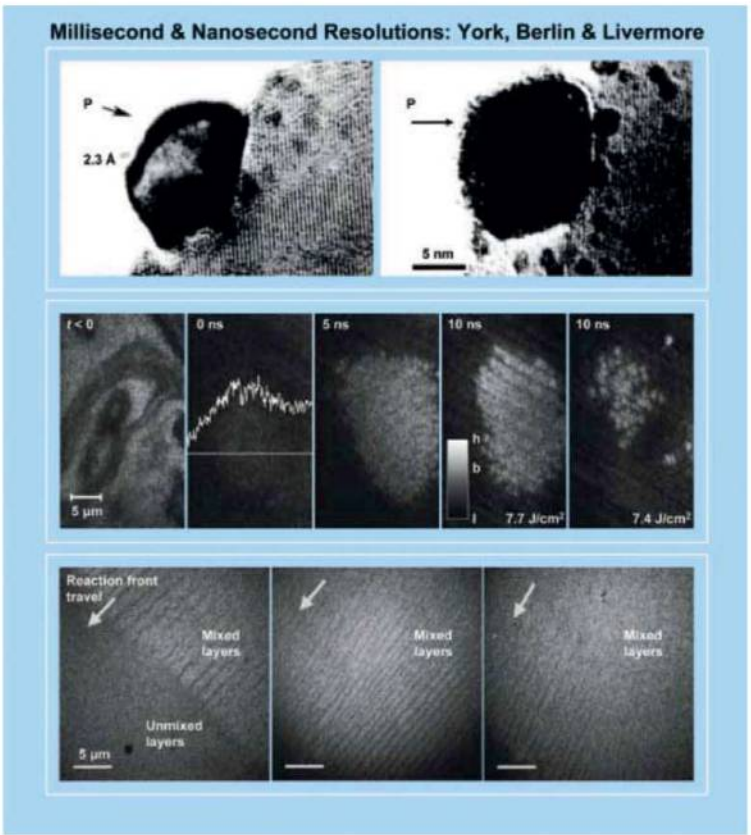

Fig. 3. Millisecond and nanosecond imaging by the groups at York, Berlin, and Livermore. Displayed at the top is the work from the group of Gai (*32*). Shown are in situ atomic-resolution environmental TEM images of Pt/titania catalyst activated in hydrogen at 300°C, with the atomic planes resolved (2.3 Å) in the Pt particle (P). The same particle is shown at 450°C, also in hydrogen, demonstrating the growth of Ti-oxide overlayer and development of Pt clusters. Such an experiment can be ramped at 30 frames per second. The middle panel depicts single shots of explosion in a nickel film acquired with nanosecond resolution. The pattern at time $t = 0$ indicates the intensity change across the line shown with the bar (at $t < 0$) giving the micrometer scale. At $t = 10$ ns, the bar reflects the change in the transmitted intensity of initial liquid (l), bubbles (b), and final hole (h). The fluence is very high (~8 J/cm^2). This panel is adapted from (*55*) of the Berlin group. In the lower panel, shown is the resolution of a reaction front on the microsecond time scale, displaying a transient behavior in the mixed layers. This panel is adapted from the work at LLNL (*35*).

Chemical bonding and FEELS. In the above applications, the electrons interact elastically with matter, that is, with no loss of their energies. However, it is also possible to record EELS due to inelastic interactions, and when they are femtosecond-resolved (FEELS), we can obtain 3D maps of time-energy-amplitude for the characterization of binding during materials change of valency and phase. In UEM with FEELS, we obtained these 3D plots for graphite, recording frames' changes in 100 fs and for electron energy loss from 0 to 50 eV (Fig. 4). Because in this energy range the electron spectrum displays binding characteristics of the π and σ electrons and of bulk and surface atoms, the change in amplitudes of scattering and energy positions in FEELS is telling of bonding changes with time, following the impulsive energy stress. The dynamics reveal a striking correlation between the compression and expansion of layers on the sub-picometer scale for surface and bulk atoms and the direction of change from sp^2 (2D-graphene) to sp^3 (3D-diamond) electronic hybridization (*11*). Recent scanning tunneling microscopy (STM) investigation (*37*) has revealed domains of these sp^3-type structures in femtosecond (not nanosecond) irradiated graphite, which is consistent with our FEELS observations. A perspective on this 10–orders of magnitude

improvement in EELS was recently published by Thomas (*40*).

Functional Nanomechanical Systems: Cantilevers

UEM can also be used to study in situ structural transformations of a material during a function. The change is directly visualized in the variation of the properties of the material itself. As such, the method can be used to optimize and discover new micro- and nanoelectromechanical systems (MEMS and NEMS). Whereas current methods of detection provide insights into the movements of nanoscale structures, direct real-space and -time visualization of modes of oscillations at frequencies pitched in the ultrasonic range (that is, kilohertz to gigahertz) was not possible. Here, we highlight one prototypical study of cantilevers made of nano(micro)crystals of Cu-TCNQ, a quasi-1D semiconductor (*41*).

In UEM, the static structures were determined from a tomographic-like tilt series of images, whereas the in situ temporal evolution was established using the stroboscopic electron packets. A movie of the 3D motions of cantilevers was produced from frames of the optomechanical expansions, which were triggered by the charge transfer from the TCNQ radical anion ($TCNQ^-$) to copper (Cu^+). The expansions are colossal, reaching the micrometer scale, and the observed resonance oscillations are of two types, longitudinal and transverse, with resonance Q factors that make them persist for up to 1 ms. From them, we obtained Young's elastic modulus (2 GPa), the force (600 μN), and the potential energy (200 pJ) stored. The mechanical function is robust, at least for 100 continuous pulse cycles (~10^{11} oscillations for the recorded frames), with no apparent damage or plasticity. Of the initial optical energy, a minimum of 1% is converted into mechanical motion, but in fact it could reach 10% or more. Nanoscale cantilevers, which were studied similarly, displayed resonance modes of much higher frequencies (*41*).

Irreversible Phase Transitions and Crystallization

For transformations that are irreversible in nature, we explored two types of phase transitions: nucleation and crystallization in silicon and martensitic structural changes in iron. With a single-electron pulse, the process is followed in situ in the microscope, and structural changes are visualized in the images and diffraction patterns. The embryonic stages of crystallization, when observed in real time, elucidate two types of processes involved in the transition from amorphous to crystalline structure in silicon: one that occurs at early times (nanoseconds) and involves a nondiffusive motion, and another one that takes place on a significantly longer time scale (microseconds) (*42*).

The other irreversible phase transition studied with single-pulse imaging is that of the para(ferro)magnetic transformation in iron, from body-centered to face-centered cubic crystal structure. For this transformation, the intermediate(s) involved were arrested in time, and the temporal behavior provides the following time scales for the processes: first, a nanosecond nucleation from incoherent but collective energy-barrier crossing motions of atoms; and second, a barrierless phase growth on the picosecond time scale for nanometer domains (*43*). As mentioned above, such phase changes in titanium (*34*, *44*), silicon (*42*), iron (*43*), and other materials (*12*) can be resolved using single-pulse imaging on the nanosecond and longer time scale.

Variant Techniques: Convergent-Beam, Near-Field, and Tomographic UEM

To study single particles (sites) of nanoscale with UEM, we recently developed 4D nanodiffraction imaging of structural dynamics with convergent electron (pulsed) beams (*45*). Instead of using a parallel electron-beam illumination with a single-electron wave vector, a convergent beam (CB) with a span of incident wave vectors is focused on the specimen. This method of CB-

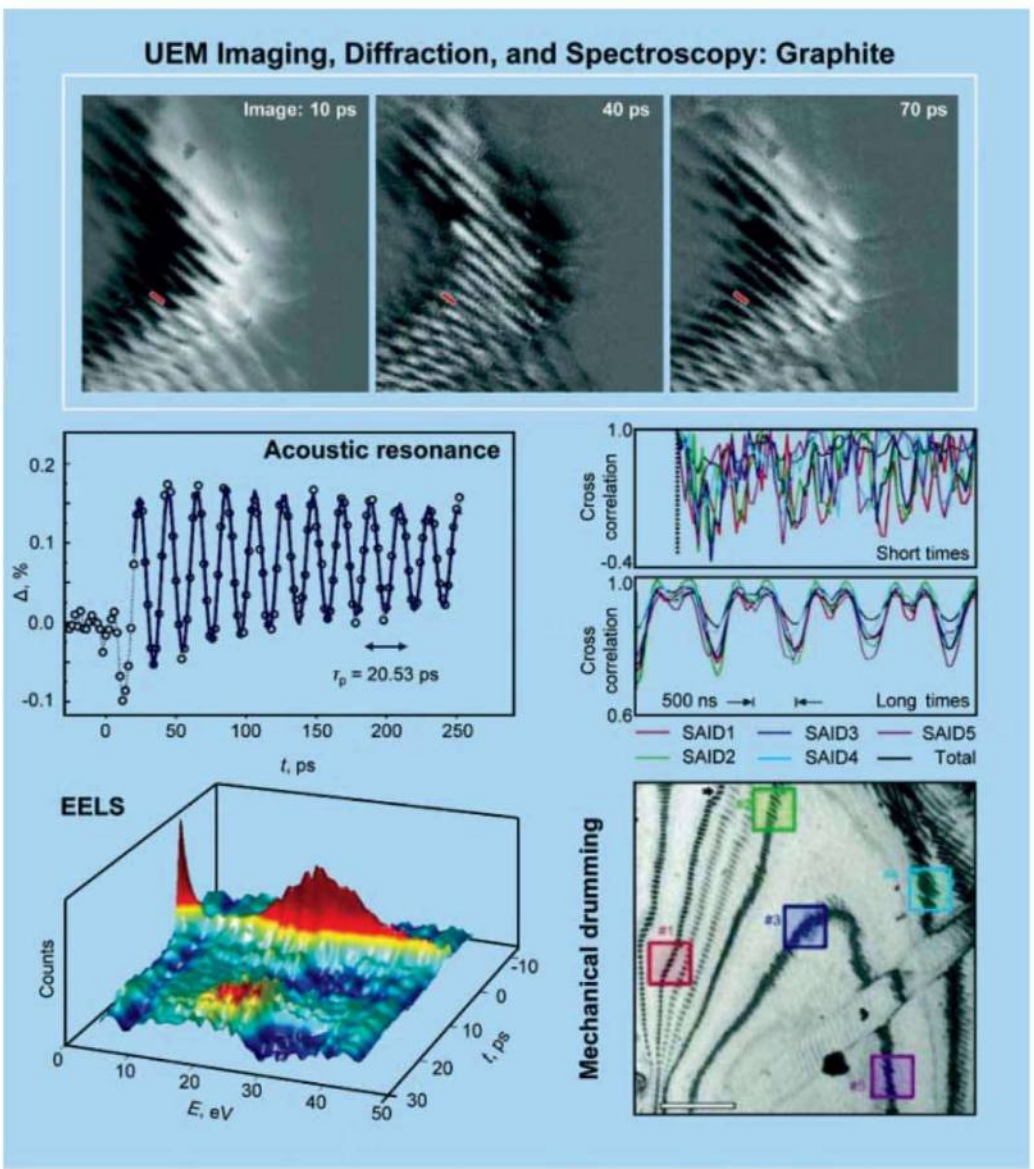

Fig. 4. UEM imaging, diffraction, and spectroscopy of graphite: a prototypical case study. Shown are three frames for the change in the image with time (upper panel), the observed acoustic resonance (center left), the FEELS contour map (lower left), and the drumming resonance observed at longer times (lower right and center right). The selected area image dynamics (SAID) display the observed local resonances. See text and (*10*, *11*, *39*, *56*); the values discussed in the text for resonance frequencies, Young's moduli, and the speed of sound are given in (*56*).

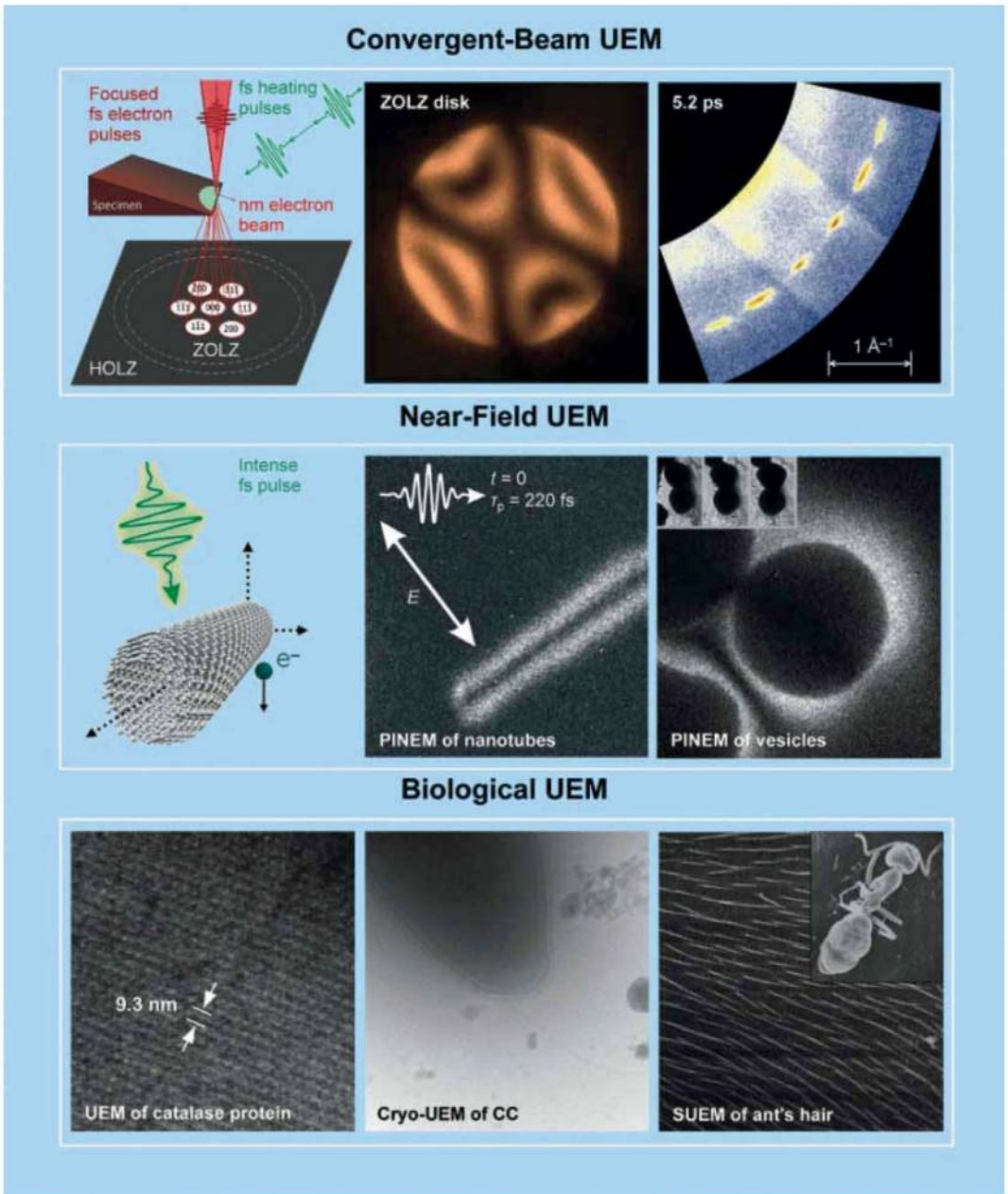

Fig. 5. Convergent-beam, near-field, and biological UEM imaging. The upper panel displays concepts pertinent to CB-UEM together with a typical zero-order Laue zone disk and a nanodiffraction frame taken at 5.2 ps. By following the individual spots in the ring as a function of time, the dynamics of the probed nanoarea of the specimen are obtained [see (*45*)]. Shown in the middle panel is the concept pertinent to PINEM together with the image of a carbon nanotube as obtained using perpendicularly polarized photons. The image was obtained at time $t = 0$ with femtosecond resolution [see (*46*, *47*)]. Also shown (on the right) is the application of PINEM to visualize a protein shell of a liquid-filled vesicle; the inset depicts three tomographic frames showing the spherical shape of the vesicle as seen from different angles. The protein shell "lights up" at $t = 0$ and dims in 200 fs. In the bottom panel, displayed are catalase protein crystal (with the lattice-plane separations of 9.3 nm), bio-UEM micrographs of *Caulobacter crescentus* (CC; the image obtained by cryomicroscopy), and a scanning UEM image of ant's hair. See text.

UEM affords determination of 3D structures with high precision for local areas, reaching below one unit cell. For silicon, the observed structural dynamics (rate of 0.14 ps^{-1}), the temperatures (rate of 10^{14} K/s), and the amplitudes of atomic vibrations (up to 0.084 Å) are all for the local site (10 to 300 nm) probed, not for the bulk material (Fig. 5). We anticipate a broad range of applications of CB-UEM and its variants, especially for structural dynamics of single particles and heterogeneous assemblies.

Another variant UEM technique is 4D tomography, in which the electron pulses, for a given beam focus and at a fixed time delay, give rise to images for a whole series of tilt angles, as recently demonstrated by O.-H. Kwon in this laboratory. When this process is repeated for a sequence of time delays on the femtosecond and nanosecond timescales, a 4D tomograph is constructed. The obtained tomographs constitute a movie that displays the motions of the nanoobject, all visualized at once. This 4D tomography was demonstrated first for carbon nanowire structures, and in Fig. 5, an example is given for a biological structure at three representative angles and at time zero, as obtained by D. Flannigan and B. Barwick of this laboratory.

In general, photons in UEM are used to initiate a change (clocking) for the study of structural or morphological dynamics, but before these structural and morphological changes occur, electronic distributions are altered, with the dynamical changes being on the femtosecond and shorter time scale. It is possible to exploit strong interactions between photons and electrons to open up a new avenue in UEM investigations. Recently, we reported the development of photon-induced near-field EM (PINEM) (*46*) for the probing of interfacial evanescent and ephemeral fields in nanostructures. Only when the field is induced and probed on the ultrashort time scale would it be visualized and controlled for applications in imaging and spectroscopy. In contrast to FEELS, in PINEM we observe gain, instead of loss, of electron energy with, remarkably, 10 or more photons being absorbed by the electron. Such phenomena of energy gain, as electrons and photons team up (*47*), are observed only in the presence of the nanostructure, and they display unique spatial, temporal, and polarization properties of the nanomaterials and biological structures studied (Figs. 2 and 5, and below).

Future Outlook

The tabletop electron microscope is arguably the most powerful scientific instrument because of its three major domains: real-space imaging, Fourier-space diffraction, and energy-space spectroscopy. The scope of applications is wide-ranging, from materials and mineralogy to nanoscience and

biology. Because of the powerful focusing capabilities of electrons, structures can be determined for local (sub)nanosites, and not averaged over micrometers of specimens' dimensions, which, as in x-ray crystallography, would provide higher precision. Whereas optical imaging, which is essential in mapping live cells, locates particles' positions, electron imaging resolves the structures down to the atomic scale.

The integration of the fourth dimension—time—should now transform static imaging into the realm of dynamics in both space and time, and the opportunities are numerous. With environmental high-resolution imaging, it should be possible to study materials and biological systems at controlled conditions, and with circulating fluid cells (*48*), the issue of specimen recovery becomes irrelevant. The advent of near-field and convergent-beam UEM variants opens the door for applications in nanoscale plasmonics and photonics and for studies of heterogeneous processes, such as those involved in the catalytic properties of nanoparticles or in phase transitions. Moreover, the discovery of the photon-induced near-field (PIN) effect, with multiple quanta of energy exchange, may lead into nonlinear electron spectroscopy at the atomic scale, and with recent developments in attosecond optical pulse generation by Krausz, Corkum, and others (*49*), we may soon make possible, with UEM, the imaging of matter's electron dynamics (*50*).

Our first entry into bioimaging resulted in a proof-of-principle UEM visualization of a stained rat cell (amplitude contrast) and, with cryotechniques, the membrane structure of cells in vitreous ice (phase contrast). Proteins were also imaged in real space (Fig. 5). More recently, UEM-3 was developed using a FEG of high brightness and coherence, and with the scanning of the electron probe pulse, we were able to image biological specimens and materials surfaces, as demonstrated by D.-S. Yang and O. Mohammed of this laboratory (see Fig. 5). Using near-field UEM, it was also possible to "light up" the field of a "dark" protein shell forming a liquid-filled vesicle (Fig. 5). The enhanced imaging, by the PIN effect, disappears in a few hundreds of femtoseconds. The potential of recording femtosecond (or longer) time-scale dynamics and arresting specimens' movements, which should result in much sharper images, represent exciting directions of research. Lastly, we have found, based on theoretical studies by M. Lin of this laboratory, that there exist some criteria for taking advantage of the regularity of pulsed dosing, and this concept is now being tested experimentally for the control of energy redistribution and heat dissipation, and hence radiation damage, in bio-UEM.

From a historical perspective, the progress in this field has been made over a century of developments. The discovery of the electron (J. J. Thomson) and its wave character (L. de Broglie) laid the foundation for 2D electron microscopy (M. Knoll and E. Ruska) in the 1930s. Three decades later, 3D image reconstruction from a single projection (D. J. DeRosier, A. Klug, and R. A. Crowther) and from a tilt series (R. G. Hart and others) was achieved, and since then, numerous advances in nanotomography and holography (P. Midgley, D. Muller, C. Colliex, A. Tonomura, and others) have been made [see (*12*)]. The transition to ultrafast electron imaging was accomplished during the past decade, and with the arsenal of variant techniques available, 4D electron microscopy has the potential to decipher the fundamental forces behind the function of complex structures, physical and biological.

References and Notes

1. R. Hooke, *Micrographia* (Royal Society, London, 1665).
2. S. W. Hell, *Science* **316**, 1153 (2007).
3. B. Huang, M. Bates, X. Zhuang, *Annu. Rev. Biochem.* **78**, 993 (2009).
4. W. Min *et al.*, *Nature* **461**, 1105 (2009).
5. M. Knoll, E. Ruska, *Z. Phys.* **78**, 318 (1932).
6. P. W. Hawkes, J. C. H. Spence, Eds., *Science of Microscopy* (Springer, New York, 2007).
7. A. H. Zewail, in *Les Prix Nobel: The Nobel Prizes 1999*, T. Frängsmyr, Ed. (Almqvist & Wiksell, Stockholm, 2000), p. 110.
8. A. H. Zewail, *Annu. Rev. Phys. Chem.* **57**, 65 (2006).
9. A. H. Zewail, V. A. Lobastov, U.S. Patent 7,154,091 (2006).
10. B. Barwick, H. S. Park, O.-H. Kwon, J. S. Baskin, A. H. Zewail, *Science* **322**, 1227 (2008).
11. F. Carbone, O.-H. Kwon, A. H. Zewail, *Science* **325**, 181 (2009).
12. A. H. Zewail, J. M. Thomas, *4D Electron Microscopy: Imaging in Space and Time* (Imperial College Press, London, 2010).
13. T. Folger, *Science* **324**, 1512 (2009).
14. C. Davisson, L. H. Germer, *Phys. Rev.* **30**, 705 (1927).
15. G. P. Thomson, A. Reid, *Nature* **119**, 890 (1927).
16. H. Mark, R. Wierl, *Naturwiss* **18**, 205 (1930).
17. R. Srinivasan, V. A. Lobastov, C.-Y. Ruan, A. H. Zewail, *Helv. Chim. Acta* **86**, 1761 (2003).
18. D. Shorokhov, A. H. Zewail, *J. Am. Chem. Soc.* **131**, 17998 (2009).
19. H. Ihee *et al.*, *Science* **291**, 458 (2001).
20. R. Srinivasan, J. S. Feenstra, S. T. Park, S. Xu, A. H. Zewail, *Science* **307**, 558 (2005).
21. N. Gedik, D.-S. Yang, G. Logvenov, I. Bozovic, A. H. Zewail, *Science* **316**, 425 (2007).
22. P. Baum, D.-S. Yang, A. H. Zewail, *Science* **318**, 788 (2007).
23. C.-Y. Ruan, V. A. Lobastov, F. Vigliotti, S. Chen, A. H. Zewail, *Science* **304**, 80 (2004).
24. D.-S. Yang, A. H. Zewail, *Proc. Natl. Acad. Sci. U.S.A.* **106**, 4122 (2009).
25. S. Chen, M. T. Seidel, A. H. Zewail, *Angew. Chem. Int. Ed.* **45**, 5154 (2006).
26. D.-S. Yang, C. Lao, A. H. Zewail, *Science* **321**, 1660 (2008).
27. B. J. Siwick, J. R. Dwyer, R. E. Jordan, R. J. D. Miller, *Science* **302**, 1382 (2003).
28. H. Park, X. Wang, S. Nie, R. Clinite, J. Cao, *Phys. Rev. B* **72**, 100301 (2005).
29. R. K. Raman *et al.*, *Phys. Rev. Lett.* **101**, 077401 (2008).
30. M. Y. Shchelev, *Quantum Electron.* **37**, 927 (2007).
31. A. Gahlmann, S. T. Park, A. H. Zewail, *Phys. Chem. Chem. Phys.* **10**, 2894 (2008).
32. P. L. Gai, E. D. Boyes, *Electron Microscopy in Heterogeneous Catalysis* (IOP Publishing, Bristol, UK, 2003).
33. O. Bostanjoglo, *Adv. Imaging Electron Phys.* **121**, 1 (2002).
34. H. Kleinschmidt, A. Ziegler, G. H. Campbell, J. D. Colvin, O. Bostanjoglo, *J. Appl. Phys.* **98**, 054313 (2005).
35. J. S. Kim *et al.*, *Science* **321**, 1472 (2008).
36. K. Ishioka *et al.*, *Phys. Rev. B* **77**, 121402 (2008).
37. J. Kanasaki, E. Inami, K. Tanimura, H. Ohnishi, K. Nasu, *Phys. Rev. Lett.* **102**, 087402 (2009).
38. H. Yan *et al.*, *Phys. Rev. B* **80**, 121403 (2009).
39. O.-H. Kwon, B. Barwick, H. S. Park, J. S. Baskin, A. H. Zewail, *Nano Lett.* **8**, 3557 (2008).
40. J. M. Thomas, *Angew. Chem. Int. Ed.* **48**, 8824 (2009).
41. D. J. Flannigan, P. C. Samartzis, A. Yurtsever, A. H. Zewail, *Nano Lett.* **9**, 875 (2009).
42. O.-H. Kwon, B. Barwick, H. S. Park, J. S. Baskin, A. H. Zewail, *Proc. Natl. Acad. Sci. U.S.A.* **105**, 8519 (2008).
43. H. S. Park, O.-H. Kwon, J. S. Baskin, B. Barwick, A. H. Zewail, *Nano Lett.* **9**, 3954 (2009).
44. T. LaGrange, G. H. Campbell, P. E. A. Turchi, W. E. King, *Acta Mater.* **55**, 5211 (2007).
45. A. Yurtsever, A. H. Zewail, *Science* **326**, 708 (2009).
46. B. Barwick, D. J. Flannigan, A. H. Zewail, *Nature* **462**, 902 (2009).
47. F. J. García de Abajo, *Nature* **462**, 861 (2009).
48. N. de Jonge, D. B. Peckys, G. J. Kremers, D. W. Piston, *Proc. Natl. Acad. Sci. U.S.A.* **106**, 2159 (2009).
49. F. Krausz, M. Ivanov, *Rev. Mod. Phys.* **81**, 163 (2009).
50. P. Baum, A. H. Zewail, *Chem. Phys.* **366**, 2 (2009).
51. K. D. M. Harris, J. M. Thomas, *Cryst. Growth Des.* **5**, 2124 (2005).
52. J. M. Thomas, *Angew. Chem. Int. Ed.* **44**, 5563 (2005).
53. J. M. Thomas, *Angew. Chem. Int. Ed.* **43**, 2606 (2004).
54. J. M. Thomas, *Nature* **351**, 694 (1991).
55. H. Dömer, O. Bostanjoglo, *Appl. Surf. Sci.* **208–209**, 442 (2003).
56. H. S. Park, J. S. Baskin, B. Barwick, O.-H. Kwon, A. H. Zewail, *Ultramicroscopy* **110**, 7 (2009).

57. In the course of developments at the Center for Ultrafast Science and Technology (UST), I have enjoyed the scholarly discussions with and enthusiasm of J. M. Thomas of Cambridge University, the fruit of which resulted in his overview articles (*40*, *51*–*54*) and our joint monograph (*12*) on 4D EM. The dedication and hard work of members of the UST Center made possible the story told here. I particularly wish to acknowledge the effort of D. Shorokhov in helpful discussion and in manuscript preparation. This research was carried out with support from NSF and the Air Force Office of Scientific Research in the Physical Biology Center for UST supported at Caltech by the Gordon and Betty Moore Foundation.

10.1126/science.1166135

Congratulations

to the 2010 AAAS Student Poster Competition Winners

AAAS announces the winners of the 2010 Student Poster Competition that took place at the AAAS Annual Meeting in San Diego, 18-22 February. Their work in a variety of fields displayed originality and understanding that set them apart from their colleagues. First-place winners receive cash prizes thanks to the generous support of Subaru of America, Inc.

BRAIN AND BEHAVIOR

Winner: Nicholas Olivas, University of California, Irvine
High Resolution Imaging and Precise Evaluations of Hippocampal Circuit Organization and Dynamics

Honorable Mention: Chelsea Ruller, San Diego State University
Coxsackievirus B3 Infection Affects Neurogenesis and Hinders Normal Brain Development

CELLULAR AND MOLECULAR BIOLOGY

Winner (tie): Molly Burke, University of California, Irvine
Genomic Analysis of Adaptive Differentiation in Laboratory-Selected Populations of Drosophila melanogaster

Winner (tie): Emuejevoke Olokpa, Olivia Dziadek, and Mahjabeen Khan, Baylor College of Medicine
A Novel Xenograft Model Identifies Centrosome Pathways as Therapeutic Targets for Uterine Leiomyosarcoma

DEVELOPMENTAL BIOLOGY, PHYSIOLOGY, AND IMMUNOLOGY

Winner: Lamar Blackwell, University of California, Irvine
An Investigation into the ERK Phosphorylation (de) Cycle Via in vitro *Kinase Assays*

Honorable Mention: Lauren Imbornoni and Fatma Hanif, Arizona State University
Impact of Inspired Oxygen Concentration on Cerebral Blood Flow in Univentricular Circulation

ENVIRONMENT AND ECOLOGY

Winner: Christine Goedhart, University of California, Irvine
Linkages Between Community Composition and Plant Physiological Traits Along a Depth to Watertable Gradient in Owens Valley, California

Honorable Mention: Gouri Shankar Mishra, University of California, Davis
Life Cycle Analysis of Alternative Transportation Fuels: A Case Study Approach

Full abstracts can be viewed at
www.aaas.org/meetings.

MATH, TECHNOLOGY, AND ENGINEERING

Winner: Jose Rios, Arizona State University
Self-Assembled Nanostructures Based on Combinations of Poly(ethylene glycol) and Polyphenols

Honorable Mention: Rotem Ben-Shachar, University of California, Los Angeles
A Mathematical Model of Food Intake Effects on Human Serum Leptin

MEDICINE AND PUBLIC HEALTH

Winner: Ashley Masters, Midland College
Inducing Triclosan Resistance

Honorable Mention: Joanne Osburn, California State University, East Bay
Re-Evaluating the Florida Dentist Case with a New Statistical Framework

PHYSICAL SCIENCES

Winner: Samuel Penwell, University of Wisconsin, Madison, and Clara Druzgalski, University California, Irvine
Thin Film Graphene for Transparent Electrodes

Honorable Mention: Andrew Ault, University of California, San Diego
Investigations into the Chemically-Resolved Optical Properties of Transported Asian Outflow Particles at Gosan, Korea

SOCIAL SCIENCES

Winner: Sébastien Casault, University of Ottawa
Putting a Price on It: Using Real Options To Encourage R&D Investments

Honorable Mention: Allyn Knox and Bethany Cutts, Arizona State University
Peer Influence on Student Water Use Practices

Sign up at www.aaas.org/meetings to receive announcements about the 2011 AAAS Annual Meeting 17-21 February. The Poster Submission site opens 20 July 2010.

The Student Poster Competition recognizes the individual research efforts of undergraduate- and graduate-level students who are enrolled in a degree program. Posters are judged at the meeting. Winners in each category receive a cash award and framed certificate. Postdocs are not eligible.

AAAS
ADVANCING SCIENCE, SERVING SOCIETY

Australopithecus sediba: A New Species of *Homo*-Like Australopith from South Africa

Lee R. Berger,[1,2]* Darryl J. de Ruiter,[3,1] Steven E. Churchill,[4,1] Peter Schmid,[5,1] Kristian J. Carlson,[1,6] Paul H. G. M. Dirks,[2,7] Job M. Kibii[1]

Despite a rich African Plio-Pleistocene hominin fossil record, the ancestry of *Homo* and its relation to earlier australopithecines remain unresolved. Here we report on two partial skeletons with an age of 1.95 to 1.78 million years. The fossils were encased in cave deposits at the Malapa site in South Africa. The skeletons were found close together and are directly associated with craniodental remains. Together they represent a new species of *Australopithecus* that is probably descended from *Australopithecus africanus*. Combined craniodental and postcranial evidence demonstrates that this new species shares more derived features with early *Homo* than any other australopith species and thus might help reveal the ancestor of that genus.

The origin of the genus *Homo* is widely debated, with several candidate ancestors being proposed in the genus *Australopithecus* (*1*–*3*) or perhaps *Kenyanthropus* (*4*). The earliest occurrence of fossils attributed to *Homo* (*H.* aff. *H. habilis*) at 2.33 million years ago (Ma) in Ethiopia (*5*) makes it temporally antecedent to all other known species of the genus *Homo*. Within early *Homo*, the hypodigms and phylogenetic relationships between *H. habilis* and another early species, *H. rudolfensis*, remain unresolved (*6*–*8*), and the placement of these species within *Homo* has been challenged (*9*). *H. habilis* is generally thought to be the ancestor of *H. erectus* (*10*–*13*), although this might be questioned on the basis of the considerable temporal overlap that existed between them (*14*). The identity of the direct ancestor of the genus *Homo*, and thus its link to earlier *Australopithecus*, remains controversial. Here we describe two recently discovered, directly associated, partially articulated *Australopithecus* skeletons from the Malapa site in South Africa, which allow us to investigate several competing hypotheses regarding the ancestry of *Homo*. These skeletons cannot be accommodated within any existing fossil taxon; thus, we establish a new species, *Australopithecus sediba*, on the basis of a combination of primitive and derived characters of the cranium and postcranium.

The following is a description of *Au. sediba*: Order Primates Linnaeus 1758; suborder Anthropoidea Mivart 1864; superfamily Hominoidea Gray 1825; family Hominidae Gray 1825; genus *Australopithecus* DART 1925; species *Australopithecus sediba* sp. nov.

Etymology. The word *sediba* means "fountain" or "wellspring" in the seSotho language.

Holotype and paratype. Malapa Hominin 1 (MH1) is a juvenile individual represented by a partial cranium, fragmented mandible, and partial postcranial skeleton that we designate as the species holotype [Figs. 1 and 2, supporting online material (SOM) text S1, figs. S1 and S2, and table S1]. The first hominin specimen recovered from Malapa was the right clavicle of MH1 (UW88-1), discovered by Matthew Berger on 15 August 2008. MH2 is an adult individual represented by isolated maxillary teeth, a partial mandible, and partial postcranial skeleton that we designate as the species paratype. Although MH1 is a juvenile, the second molars are already erupted and in occlusion. Using either a human or an ape model, this indicates that MH1 had probably attained at least 95% of adult brain size (*15*). Although additional growth would have occurred in the skull and skeleton of this individual, we judge that it would not have appreciably altered the morphology on which this diagnosis is based.

Locality. The two *Au. sediba* type skeletons were recovered from the Malapa site (meaning "homestead" in seSotho), situated roughly 15 km NNE of the well-known sites of Sterkfontein, Swartkrans, and Kromdraai in Gauteng Province, South Africa. Detailed information regarding geology and dating of the site is in (*16*).

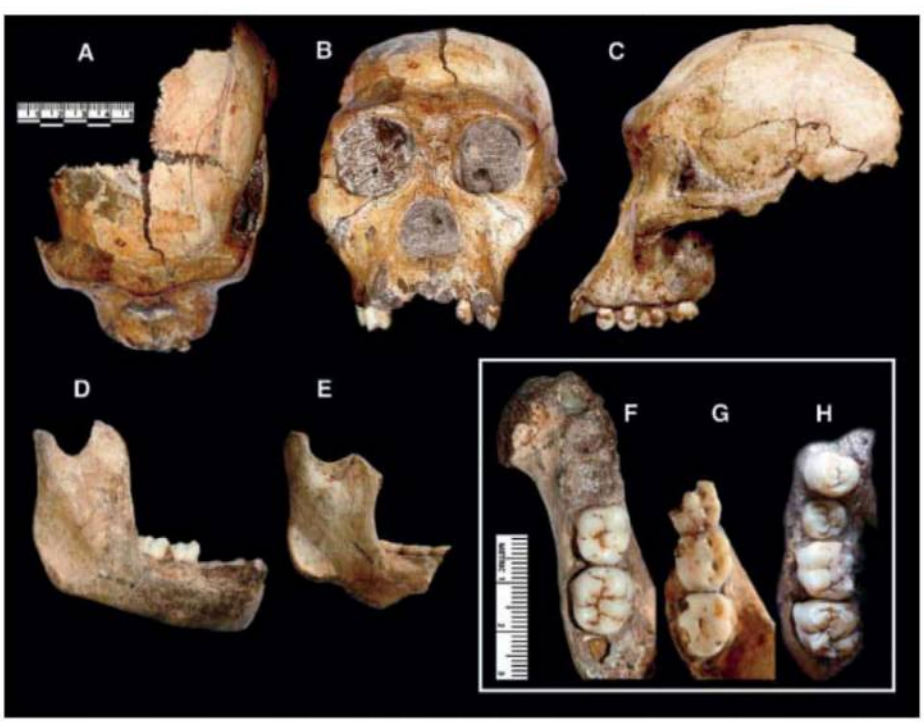

Fig. 1. Craniodental elements of *Au. sediba*. UW88-50 (MH1) juvenile cranium in (**A**) superior, (**B**) frontal, and (**C**) left lateral views. (**D**) UW88-8 (MH1) juvenile mandible in right lateral view, (**E**) UW88-54 (MH2) adult mandible in right lateral view, (**F**) UW88-8 mandible in occlusal view, (**G**) UW 88-54 mandible in occlusal view, and (**H**) UW 88-50 right maxilla in occlusal view (scale bars are in centimeters).

[1]Institute for Human Evolution, University of the Witwatersrand, Private Bag 3, Wits 2050, South Africa. [2]School of Geosciences, University of the Witwatersrand, Private Bag 3, Wits 2050, South Africa. [3]Department of Anthropology, Texas A&M University, College Station, TX 77843, USA. [4]Department of Evolutionary Anthropology, Box 90383, Duke University, Durham, NC 27708, USA. [5]Anthropological Institute and Museum, University of Zürich, Winterthurerstrasse 190, CH-8057 Zürich, Switzerland. [6]Department of Anthropology, Indiana University, Bloomington, IN 47405, USA. [7]School of Earth and Environmental Sciences, James Cook University, Townsville, Queensland 4811, Australia.

*To whom correspondence should be addressed. E-mail: profleeberger@yahoo.com

Diagnosis. *Au. sediba* can be distinguished from other species of *Australopithecus* by a combination of characters presented in Table 1; comparative cranial measures are presented in Table 2. A number of derived characters separate *Au. sediba* from the older chronospecies *Au. anamensis* and *Au. afarensis*. *Au. sediba* exhibits neither the extreme megadontia, extensive cranial cresting, nor facial prognathism of *Au. garhi*. The suite of derived features characterizing *Au. aethiopicus*, *Au. boisei*, and *Au. robustus*, in particular the pronounced cranial muscle markings, derived facial morphology, mandibular corpus robusticity, and postcanine megadontia, are absent in *Au. sediba*. The closest morphological comparison for *Au. sediba* is *Au. africanus*, as these taxa share numerous similarities in the cranial vault, facial skeleton, mandible, and teeth (Table 1). Nevertheless, *Au. sediba* can be readily differentiated from *Au. africanus* on both craniodental and postcranial evidence. Among the more notable differences, we observe that although the cranium is small, the vault is relatively transversely expanded with vertically oriented parietal walls and widely spaced temporal lines; the face lacks the pronounced, flaring zygomatics of *Au. africanus*; the arrangement of the supraorbital torus, nasoalveolar region, infraorbital region, and zygomatics result in a derived facial mask; the mandibular symphysis is vertically oriented with a slight bony chin and a weak post-incisive planum; and the teeth are differentiated by the weakly defined buccal grooves of the maxillary premolars, the weakly developed median lingual ridge of the mandibular canine, and the small absolute size of the postcanine dentition. These exact differences also align *Au. sediba* with the genus *Homo* (see SOM text S2 for hypodigms used in this study). However, we consider *Au. sediba* to be more appropriately positioned within *Australopithecus*, based on the following craniodental features: small cranial capacity, pronounced glabelar region, patent premaxillary suture, moderate canine jugum with canine fossa, small anterior nasal spine, steeply inclined zygomaticoalveolar crest, high masseter origin, moderate development of the mesial marginal ridge of the maxillary central incisor, and relatively closely spaced premolar and molar cusps.

Postcranially, *Au. sediba* is similar to other australopiths in its small body size, its relatively long upper limbs with large joint surfaces, and the retention of apparently primitive characteristics in the upper and lower limbs (table S2). *Au. sediba* differs from other australopiths, but shares with *Homo* a number of derived features of the os coxa, including increased buttressing of the ilium and expansion of its posterior portion, relative reduction in the distance between the sacroiliac and hip joints, and reduction of distance from the acetabulum to the ischial tuberosity. These synapomorphies with *Homo* anticipate the reorganization of the pelvis and lower limb in *H. erectus* and possibly the emergence of more energetically efficient walking and running in that taxon (*17*). As with the associated cranial remains, the postcranium of *Au. sediba* is defined not by the presence of autapomorphic features but by a unique combination of primitive and derived traits.

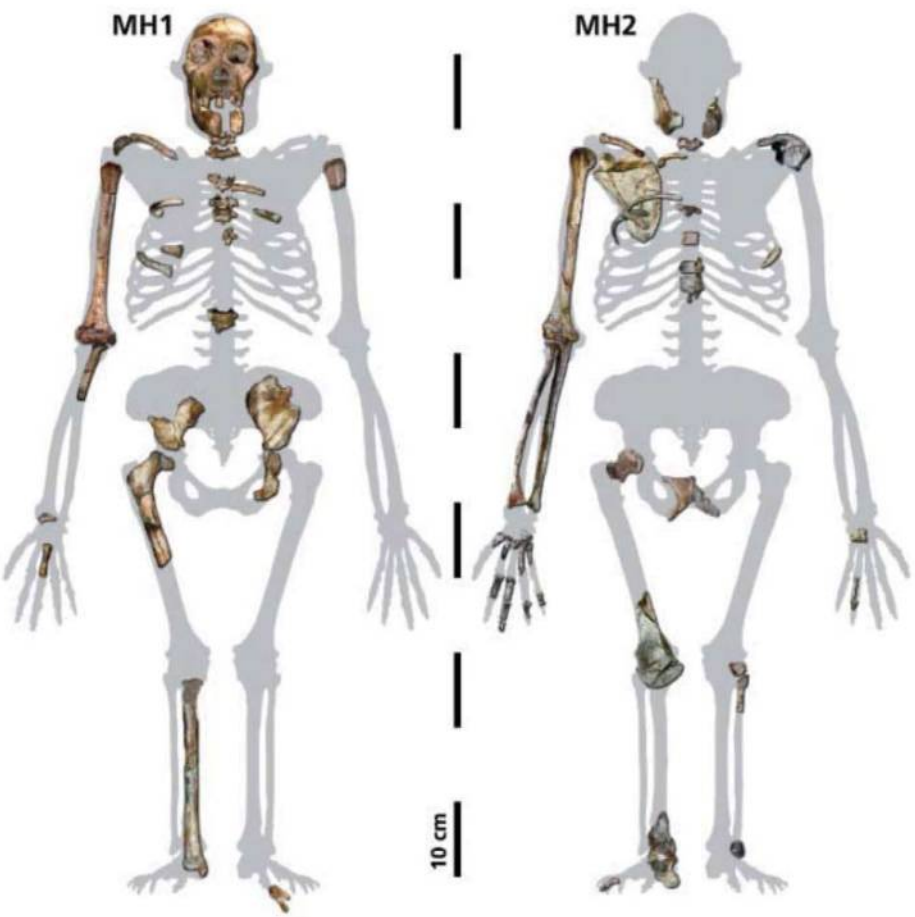

Fig. 2. Associated skeletal elements of MH1 (**left**) and MH2 (**right**), in approximate anatomical position, superimposed over an illustration of an idealized *Au. africanus* skeleton (with some adjustment for differences in body proportions). The proximal right tibia of MH1 has been reconstructed from a natural cast of the proximal metaphysis.

Cranium. The cranium is fragmented and slightly distorted. The minimum cranial capacity of MH1 is estimated at 420 cm^3 (SOM text S4). The vault is ovoid, with transversely expanded, vertically oriented parietal walls. The widely spaced temporal lines do not approach the midline. Postorbital constriction is slight. The weakly arched supraorbital torus is moderately developed and laterally extended, with sharply angled lateral corners and a weakly defined supratoral sulcus. A robust glabelar region is evident, with only a faint depression of the supraorbital torus at the midline. The frontal process of the zygomatic faces primarily laterally and is expanded medially but not laterally. The zygomatic prominence does not show anterolateral expansion. The zygomatics are weakly flared laterally, resulting in an uninterrupted frontal profile of the facial mask that is squared superiorly and tapered inferiorly. The zygomaticoalveolar crests are long, straight, and steeply inclined, resulting in a high masseter origin. The root of the zygomatic begins at the anterior margin of M^1. The nasal bones are widened superiorly, become narrowest about one-third of the way down, and flare to their widest extent at their inferior margin. The nasal bones are elevated as a prominent ridge at the internasal suture, with an increasingly anterior projection inferiorly. The bone surface of the maxilla retreats gently away from the nasal aperture laterally, resulting in an everted margin of the superolateral portion of the aperture relative to the infraorbital region. The inferolateral portion of the nasal aperture becomes bluntly rounded. The infraorbital region is slightly convex (*18*) and is oriented at an approximately right angle to the alveolar plane. There is a trace of a premaxillary suture near the superolateral margin of the nasal aperture. Prominent canine juga delineate moderately developed canine fossae. Anterior pillars are absent. The inferior margin of the nasal aperture is marked by a stepped nasal sill and a small but distinct anterior nasal spine. The subnasal region is straight in the coronal plane and only weakly projecting relative

Table 1. List of characters used to diagnose *Au. sediba*. These characters are commonly used in hominin phylogenetic studies (*11, 38–40*) or have been recorded as diagnostic for various hominin taxa in the past (*3*, *10*, *36*). Recognizing the potential pitfalls of performing a cladistic analysis on possibly interdependent characters of uncertain valence, we produced a cladogram from the data in this table as a test of the phylogenetic position of *Au. sediba* (fig. S3). Our most parsimonious cladogram places *Au. sediba* at the stem of the *Homo* clade. Numbers in parentheses in the first column refer to measures presented in Table 2; descriptions of these character states are provided in SOM text S3. Abbreviations are as follows: A-M, anteromedial; costa supr., costa supraorbitalis; intermed., intermediate; lat., lateral; med., medial; mesognath., mesognathic; mod., moderately; MMR, mesial marginal ridge; orthogn., orthognathic; procumb., procumbent; proj., projecting; TMJ, temperomandibular joint.

Characters	*Au. afarensis*	*Au. garhi*	*Au. africanus*	*Au. sediba*	*H. habilis*	*H. rudolfensis*	*H. erectus*	*Au. aethiopicus*	*Au. boisei*	*Au. robustus*
Vault										
Cranial capacity (1)	Small	Small	Small	Small	Intermed.	Large	Large	Small	Small	Small
A-M incursion of temporal lines on frontal bone (9)	Strong	Moderate	Moderate	Weak	Weak	Weak	Weak	Strong	Strong	Strong
Position of temporal lines on parietal bones	Crest	Crest	Variable	Wide	Variable	Wide	Wide	Crest	Crest	Crest
Compound temporal nuchal crest (males)	Extensive	?	Absent	Absent	Variable	Absent	Absent	Extensive	Variable	Absent
Postorbital constriction (5)	Marked	Moderate	Moderate	Slight	Moderate	Moderate	Slight	Marked	Marked	Marked
Pneumatization of temporal squama	Extensive	?	Extensive	Reduced	Reduced	Reduced	Reduced	Extensive	Variable	Reduced
Facial hafting	Low	Low	Low	Low	Low	Low	Low	High	High	High
Frontal trigon	Present	Present	Absent	Absent	Absent	Absent	Absent	Present	Present	Present
Supraglenoid gutter width	Narrow	?	Narrow	Narrow	Narrow	Narrow	Narrow	Wide	Wide	Wide
Horizontal distance between TMJ and M2/M3 (6)	Long	?	Long	Short	Short	Long	Short	Long	Long	Long
Parietal transverse expansion/tuber	Absent	Absent	Absent	Present	Present	Present	Present	Absent	Absent	Absent
Facial skeleton										
Supraorbital expression	Costa supr.	Costa supr.	Intermed.	Torus	Torus	Intermed.	Torus	Costa supr.	Costa supr.	Costa supr.
Supraorbital contour	Less arched	Less arched	Variable	Arched	Arched	Arched	Arched	Less arched	Variable	Arched
Glabellar region forms as prominent block	No	No	Variable	Yes	No	Variable	No	No	Yes	Yes
Lat. half of infraorbital margin blunt and protruding	No	?	No	No	No	No	No	Yes	No	Yes
Zygomatic arch relative to inferior orbital margin	Above	?	Level	Level	Level	?	Level	Above	Above	Above
Convexity/concavity of infraorbital region	?	?	Convex	Convex	Concave	Concave	Convex	Concave	Concave	Concave
Nasal bone projection above frontomaxillary suture	Expanded	?	Variable	No	No	No	No	Tapered	Expanded	Expanded
Inferior width of projecting nasal bone (25)	Wide	?	Variable	Wide	Variable	Narrow	Wide	Not proj.	Not proj.	Not proj.
Infraorbital foramen height (32)	High	?	Variable	High	High	?	High	Low	Low	Low

continued on next page

Characters	*Au. afarensis*	*Au. garhi*	*Au. africanus*	*Au. sediba*	*H. habilis*	*H. rudolfensis*	*H. erectus*	*Au. aethiopicus*	*Au. boisei*	*Au. robustus*
Canine juga prominence/anterior pillars	Prominent	Prominent	Variable	Prominent	Variable	Weak	Weak	Weak	Weak	Pillars
Patency of premaxillary suture	Obliterated	?	Occasional	Trace	Obliterated	Obliterated	Obliterated	Obliterated	Obliterated	Occasional
Inferolateral nasal aperture margin	Sharp	Sharp	Variable	Blunt	Variable	Sharp	Blunt	Blunt	Variable	Blunt
Eversion of superior nasal aperture margin	?	?	None	Slight	Slight	Slight	Slight	Slight	Variable	None
Nasoalveolar triangular frame/gutter	Triangular	?	Triangular	Triangular	Triangular	Triangular	Triangular	Gutter	Gutter	Gutter
Nasal cavity entrance	Stepped	Stepped	Stepped	Stepped	Variable	Stepped	Stepped	Smooth	Smooth	Smooth
Nasoalveolar clivus contour in coronal plane	Convex	Convex	Straight	Straight	Straight	Straight	Straight	Concave	Concave	Concave
Subnasal projection (38)	Marked	Marked	Variable	Weak	Variable	Weak	Weak	Marked	Moderate	Moderate
Canine fossa	Present	Present	Present	Present	Present	Absent	Absent	Absent	Absent	Absent
Maxillary fossula	Absent	Absent	Absent	Absent	Absent	Absent	Absent	Absent	Absent	Present
Incisor procumbency	Procumb.	Procumb.	Variable	Vertical	Variable	Vertical	Vertical	Vertical	Vertical	Vertical
Anterior nasal spine rel. to nasal aperture	Absent	?	Anterior	Anterior	Anterior	?	Enlarged	Posterior	Posterior	Posterior
Expansion of frontal process of zygomatic bone	Med. and lat.	?	Med. and lat.	Medial	Medial	Medial	Medial	Med. and lat.	Med. and lat.	Med. and lat.
Angular indentation of lateral orbital margin	?	?	Indented	Curved	Curved	Curved	Curved	?	Curved	Curved
Zygomatic prominence development	Prominent	?	Prominent	Slight	Slight	?	Slight	Prominent	Prominent	Prominent
Lateral flaring of zygomatic arches	Marked	?	Marked	Slight	Slight	Slight	Slight	Marked	Marked	Marked
Outline of superior facial mask	Tapered	?	Tapered	Squared	Squared	Squared	Squared	Tapered	Tapered	Tapered
Zygomaticoalveolar crest/malar notch	Straight	?	Straight	Straight	Notch	Notch	Notch	Straight	Straight	Straight
Infraorbital plate angle relative to alveolar plane	Obtuse	?	Obtuse	Right	Right	Right	Right	Obtuse	Obtuse	Obtuse
Zygomaticomaxillary steps and fossae present	No	?	No	No	No	No	No	No	No	Yes
Height of masseter origin (35)	Low	Low	High	High	Low	Low	Low	High	High	High
Malar thickness (31)	Thin	?	Thin	Thin	Thin	?	Thin	Thick	Thick	Thick
Projection of zygomatics relative to nasal bones	Posterior	Posterior	Variable	Posterior	Posterior	Level	Posterior	Anterior	Anterior	Anterior
Facial prognathism (7) (sellion-prosthion angle)	Prognathic	Prognathic	Variable	Mesognath.	Mesognath.	Mesognath.	Orthogn.	Prognathic	Mesognath.	Mesognath.
Masseteric position relative to sellion	Anterior	?	Posterior	Posterior	Posterior	?	Posterior	Anterior	Anterior	Anterior
Lateral anterior facial contour	Bipartite	Bipartite	Variable	Straight	Variable	Straight	Straight	Straight	Straight	Straight

Characters	*Au. afarensis*	*Au. garhi*	*Au. africanus*	*Au. sediba*	*H. habilis*	*H. rudolfensis*	*H. erectus*	*Au. aethiopicus*	*Au. boisei*	*Au. robustus*
Palate										
Protrustion of incisors beyond bi-canine line	Yes	Yes	Yes	Yes	Yes	No	Yes	No	No	No
Anterior palatal depth	Shallow	Shallow	Deep	Deep	Variable	Deep	Variable	Shallow	Deep	Shallow
Dental arcade shape	Rectangle	Rectangle	Variable	Parabolic	Parabolic	Parabolic	Parabolic	Rectangle	Parabolic	Parabolic
Maxillary I2/C diastema	Present	Present	Absent	Absent	Variable	Absent	Absent	Absent	Absent	Absent
Mandible										
Orientation of mandibular symphysis	Receding	?	Receding	Vertical	Vertical	Vertical	Vertical	Vertical	Vertical	Vertical
Bony chin (*mentum osseum*)	Absent	?	Slight	Slight	Slight	Slight	Slight	Slight	Slight	Slight
Direction of mental foramen opening	Variable	?	Variable	Lateral	Lateral	Lateral	Lateral	Lateral	Lateral	Lateral
Post-incisive planum	Prominent	?	Prominent	Weak	Prominent	Weak	Weak	Prominent	Prominent	Prominent
Torus marginalis and marginal tubercles	Prominent	?	Moderate	Moderate	Moderate	Prominent	Prominent	?	Prominent	Prominent
Mandibular corpus cross-sectional area at M_1 (50)	Small	?	Small	Small	Small	Variable	Small	Large	Large	Large
Teeth										
Incisor-to-postcanine ratio (maxillary) (60)	Large	Moderate	Moderate	Moderate	Moderate	Moderate	Large	?	Small	Small
Canine-to-postcanine ratio (maxillary/mandibular) (61, 62)	Large	Large	Large	Large	Large	Large	Large	?	Small	Small
Postcanine crown area (maxillary/mandibular) (57, 59)	Moderate	Large	Large	Moderate	Moderate	Large	Small	Large	Large	Large
Maxillary I^1: MMR development, lingual face	Moderate	?	Moderate	Moderate	Weak	Weak	Weak	?	Moderate	Moderate
Maxillary C: development of lingual ridges	Marked	Marked	Marked	Weak	Weak	Marked	Marked	?	Marked	Weak
Maxillary premolar molarization	None	Minor	Minor	None	Minor	Minor	None	Marked	Marked	Marked
Maxillary premolars: buccal grooves	Marked	Marked	Marked	Weak	Weak	Marked	Weak	?	Weak	Weak
Median lingual ridge of mandibular canine	Prom.	?	Prom.	Weak	Weak	Weak	Weak	?	Weak	Weak
Mandibular P_3 root number	2	?	2	2	1	2	1	?	2	2
Protoconid/metaconid more mesial cusp (molars)	Equal	?	Equal	Protoconid	Protoconid	Protoconid	Protoconid	?	Equal	Equal
Peak of enamel forms between roots of molars	No	?	Yes	Yes	No	No	No	?	No	Yes
Relative enamel thickness	Thick	Thick	Thick	Thick	Thick	Thick	Thick	Hyper	Hyper	Hyper
Positions of apices of lingual (LC) and buccal (BC) cusps of premolars and molars relative to occlusal margin	LC at margin, BC slightly lingual	LC at margin, BC slightly lingual	LC slightly buccal, BC moderately lingual	LC slightly buccal, BC moderately lingual	LC at margin, BC slightly lingual	LC at margin, BC slightly lingual	LC at margin, BC slightly lingual	LC mod. buccal, BC strongly lingual	LC mod. buccal, BC strongly lingual	LC mod. buccal, BC strongly lingual

Table 2. Craniodental measurements for early hominins in Africa. *Au. sediba* is represented by MH1. Unless otherwise defined, measurements are based on (*6*). Some measures were unavailable for specimens of *Au. afarensis* and *Au. garhi*, in which case the character states in Table 1 were estimated. Several character states in Table 1 are recorded as variable, although only species average values are presented here. Measurements are in millimeters unless otherwise indicated. Descriptions of character states presented in Table 1 that are based on measurements from this table are provided in SOM text S3. Abbreviations are as follows: br, bregma; ek, ectoconchion; ekm, ectomolare; fmt, frontomolare temporale; ft, frontotemporale; g, glabella; mf, maxillofrontale; n, nasion; ns, nasospinale; or, orbitale; po, porion; pr, prosthion; rhi, rhinion; zm, zygomaxillare; zy, zygion; zyo, zygoorbitale.

Item	Measurement description in (*6*)	Measurement	*Au. afarensis*	*Au. africanus*	*Au. sediba*	*H. habilis*	*H. rudolfensis*	*H. erectus*	*Au. aethiopicus*	*Au. boisei*	*Au. robustus*
1		Cranial capacity (cm^3)	415	442	420	631	751	900	419	515	530
2	9	Maximum parietal breadth	90	99	100	103	114	126	94	99	100
3	11	Bi-porionic breadth (po-po)	126	99	104	104	127	121	125	116	—
4		Postorbital constriction (narrowest point behind the orbits)	77	69	73	76	85	89	65	64	73
5		Postorbital constriction index (4/14 × 100)	66	71	85	70	72	80	65	61	68
6		Horizontal distance between TMJ and M^2/M^3	83	61	45	51	58	57	94	82	81
7		Facial prognathism (sellion-prosthion angle)	63	61	65	65	68	72	41	66	69
8	75	Infratemporal fossa depth	–	31	21	27	–	37	51	50	36
9	8	Minimum frontal breadth (ft-ft)	40	54	70	66	72	76	33	36	35
10	17	Glabella to bregma (g-br)	101	80	75	83	86	103	–	87	–
11		Frontal chord (n-br)	–	84	74	80	93	99	–	84	–
12	62	Supraorbital torus vertical thickness	–	8	8	8	10	12	10	12	9
13	43	Superior facial height (n-pr)	87	78	68	68	90	76	99	100	80
14	49	Superior facial breadth (fmt-fmt)	117	97	86	100	117	107	100	108	107
15	50	Bi-orbital breadth (ek-ek)	89	84	78	89	100	99	101	93	82
16	52	Bizygomatic breadth (zy-zy)	157	126	102	117	–	135	153	165	143
17		Zygomatic breadth index (14/16 × 100)	75	74	84	85	–	84	–	65	74
18	53	Bimaxillary breadth (zm-zm)	–	103	84	97	113	105	126	119	106
19	55	Interorbital breadth (mf-mf)	18	19	20	27	24	25	23	24	24
20	56	Orbital breadth (mf-ek)	38	36	31	33	39	39	36	37	33
21	57	Orbital height (perpendicular to 20)	34	32	31	31	33	36	41	33	30
22	71	Nasal bridge length (n-rhi)	–	27	26	18	20	18	35	30	28
23	73	Nasal bridge breadth superior	–	5	8	8	8	13	12	14	11
24		Nasal bridge breadth at anterior lacrimal crests	–	11	5	10	–	24	19	11	–
25	74	Nasal bridge breadth inferior	–	11	13	11	10	18	11	7	8
26		Nasal bridge height (nasion subtense at anterior lacrimal crests)	–	4	9	8	–	9	4	5	–
27	69	Nasal height (n-ns)	58	50	49	45	57	52	72	64	54
28	70	Nasal aperture height (rhi-ns)	29	26	22	28	39	30	38	35	24
29	68	Maximum nasal aperture width	23	23	26	25	27	32	30	31	25
30		Orbitoalveolar height (or-alveolar plane)	55	53	44	47	59	51	53	69	57
31	60	Malar thickness	14	13	13	8	–	12	20	18	18
32		Infraorbital foramen height (to inferior orbital margin)	–	12	15	15	14	16	30	25	26
33		Prosthion to zygomaxillare (pr-zm)	–	67	57	55	69	67	80	82	71
34		Prosthion to zygoorbitale (pr-zyo)	–	60	50	57	75	70	73	81	69
35		Masseter origin height index (33/34 × 100)	–	112	104	96	92	96	110	101	103
36	47	Subnasale to prosthion (horizontal projection)	28	23	13	19	17	16	23	27	26
37	48	Subnasal to prosthion (vertical projection)	15	21	17	18	30	21	12	25	22
38		Subnasale projection index (36/37 × 100)	187	108	76	106	57	79	192	108	122
39	94	Incisor alveolar length	–	13	16	15	14	16	15	15	13
40	96	Premolar alveolar length	–	15	18	16	16	13	21	22	17

continued on next page

Item	Measurement description in (6)	Measurement	*Au. afarensis*	*Au. africanus*	*Au. sediba*	*H. habilis*	*H. rudolfensis*	*H. erectus*	*Au. aethiopicus*	*Au. boisei*	*Au. robustus*
41	98	Intercanine distance	26	30	30	30	33	31	–	29	27
42	88	Palate breadth (ekm-ekm)	68	64	63	70	80	66	83	82	67
43	141	Mandibular symphysis height	39	38	32	27	36	34	–	47	42
44	142	Mandibular symphysis depth	60	20	19	19	24	19	–	28	25
45	147	Mandibular corpus height at P_4	34	33	28	30	38	30	–	42	38
46	148	Mandibular corpus depth at P_4	19	21	18	20	22	19	–	28	24
47	149	Cross-sectional area at P_4 (calculated as an ellipse)	511	558	382	427	653	458	–	910	709
48	150	Mandibular corpus height at M_1	33	32	28	29	36	30	35	41	37
49	151	Mandibular corpus depth at M_1	19	21	18	20	23	20	26	28	26
50	152	Cross-sectional area at M_1 (calculated as an ellipse)	488	532	396	421	667	469	715	913	759
51	154	Mandibular corpus height at M_2	31	31	25	31	36	30	–	41	35
52	155	Mandibular corpus depth at M_2	22	25	22	23	26	21	–	31	28
53	156	Cross-sectional area at M_2 (calculated as an ellipse)	536	612	436	537	745	504	–	980	770
54	162	Height of mental foramen relative to alveolar margin	20	19	13	13	17	13	–	20	20
55		Maxillary incisor crown area (I^1+I^2)	143	135	109	132	137	136	–	117	109
56		Maxillary canine crown area	107	104	79	95	118	96	–	76	79
57		Maxillary postcanine crown area	713	868	731	755	829	617	–	1012	941
58		Mandibular canine crown area	87	95	68	83	–	79	–	72	61
59		Mandibular molar crown area	550	651	536	565	668	466	–	781	678
60		Maxillary incisor to postcanine ratio	20.0	15.6	14.9	17.4	16.6	22.1	–	11.5	11.6
61		Maxillary canine to postcanine ratio	15.0	11.9	10.8	12.6	14.2	15.5	–	7.5	8.4
62		Mandibular canine to molar ratio	15.8	14.6	12.7	14.6	–	16.7	–	9.2	9.0

to the facial plane. The face is mesognathic. The palate is consistently deep along its entire extent, with a parabolic dental arcade.

Mandible. Descriptions apply to the more complete juvenile (MH1) mandible unless otherwise stated. The nearly vertical mandibular symphysis presents a weak lateral tubercle, resulting in a slight mental trigone, and a weak mandibular incurvation results in a slight *mentum osseum*. The post-incisive planum is weakly developed and almost vertical. Both mandibular corpora are relatively gracile, with a low height along the alveolar margin. The extramolar sulcus is relatively narrow in both mandibles. In MH1, a moderate lateral prominence displays its greatest protrusion at the mesial extent of M_2, with a marked decrease in robusticity to P_4; in MH2 the moderate lateral prominence shows its greatest protrusion at M_3, with a marked decrease in robusticity to M_2. The alveolar prominence is moderately deep with a notable medial projection posteriorly. The anterior and posterior subalveolar fossae are continuous. The ramus of MH1 is tall and narrow, with nearly parallel, vertically oriented anterior and posterior borders; the ramus of MH2 is relatively broader, with nonparallel anterior and posterior borders (fig. S2). The mandibular notch is relatively deep and narrow in MH1 and more open in MH2. The coronoid extends farther superiorly than the condyle. The condyle is mediolaterally broad and anteroposteriorly narrow. The endocondyloid buttress is absent in MH1, whereas in MH2 a weak endocondyloid buttress approaches the condyle without reaching it.

Dental size and proportions. The dentition of the juvenile (MH1) is relatively small, whereas preserved molars of the adult (MH2) are even smaller (Fig. 3 and fig. S4). For MH1, the maxillary central incisor is distinguishable only from the reduced incisors of *Au. robustus*. The maxillary canine is narrower than all canines of *Au. africanus* except TM 1512, whereas the mandibular canine falls well below the range of *Au. africanus*. Premolars and molars are at the lower end of the *Au. africanus* range and within that of *H. habilis–H. rudolfensis* and *H. erectus*. Molar dimensions of the adult individual (MH2) are smaller than those of *Au. africanus*, are at or below the range of those of *H. habilis–H. rudolfensis*, and are within the range of those of *H. erectus*. *Au. sediba* mirrors the *Au. africanus* pattern of maxillary molars that increase slightly in size posteriorly, though it differs in that the molars tend to be considerably larger in the latter taxon. Conversely, the *Au. sediba* pattern varies slightly from that seen in specimens KNM-ER 1813, OH 13, and OH 65 and *H. erectus*, wherein the molars increase from M^1 to M^2 but then decrease to M^3. In broad terms, the teeth of *Au. sediba* are similar in size to teeth of specimens assigned to *Homo* but share the closely spaced cusp apices seen in *Australopithecus*.

Postcranium. Preserved postcranial remains of *Au. sediba* (table S1) denote small-bodied

hominins that retain an australopith pattern of long upper limbs, a high brachial index, and relatively large upper limb joint surfaces (table S2). In addition to these aspects of limb and joint proportions, numerous other features in the upper limb are shared with sibling species of *Australopithecus* (to the exclusion of later *Homo*), including a scapula with a cranially oriented glenoid fossa and a strongly developed axillary border; a prominent conoid tubercle on the clavicle, with a pronounced angular margin; low proximal-to-distal humeral articular proportions; a distal humerus with a marked crest for the brachioradialis muscle, a large and deep olecranon fossa with a septal aperture, and a marked trochlear/capitular keel (*19*); an ulna with a pronounced flexor carpi ulnaris tubercle; and long, robust, and curved manual phalanges that preserve strong attachment sites for the flexor digitorum superficialis muscle.

Numerous features of the hip, knee, and ankle indicate that *Au. sediba* was a habitual biped. In terms of size and morphology, the proximal and distal articular ends of the femur and tibia fall within the range of variation of specimens attributed to *Au. africanus*. However, several derived features in the pelvis link the Malapa specimens with later *Homo*. In the os coxa (Fig. 4), *Au. sediba* shares with *Homo* a pronounced acetabulocristal buttress; a more posterior position of the cristal tubercle; a superoinferiorly extended posterior iliac blade, with an expanded retroauricular area; a sigmoid-shaped anterior inferior iliac spine; a reduced lever arm for weight transfer between the auricular surface and the acetabulum; an enlarged and rugose iliofemoral ligament attachment area; a tall and thin pubic symphyseal face; and a relatively short ischium with a deep and narrow tuberoacetabular sulcus. These features are present in taxonomically unassigned postcranial remains from Koobi Fora (KNM-ER 3228) and Olduvai Gorge (OH 28), which have been argued to represent early *Homo* (*20*), as well as in early *Homo erectus* (*21*). An os coxa from Swartkrans (SK 3155) has been considered by some to also represent early *Homo* (*22*) but can be seen to possess the australopith pattern in most of these features. In addition, *Au. sediba* shares with later *Homo* the human-like pattern of low humeral-to-femoral diaphyseal strength ratios, in contrast to the ape-like pattern seen in the *H. habilis* specimen OH 62 (table S2).

Although aspects of the pelvis are derived, the foot skeleton is more primitive overall, sharing with other australopiths a flat talar trochlea articular surface with medial and lateral margins with equal radii of curvature, and a short, stout, and medially twisted talar neck with a high horizontal angle and a low neck torsion angle

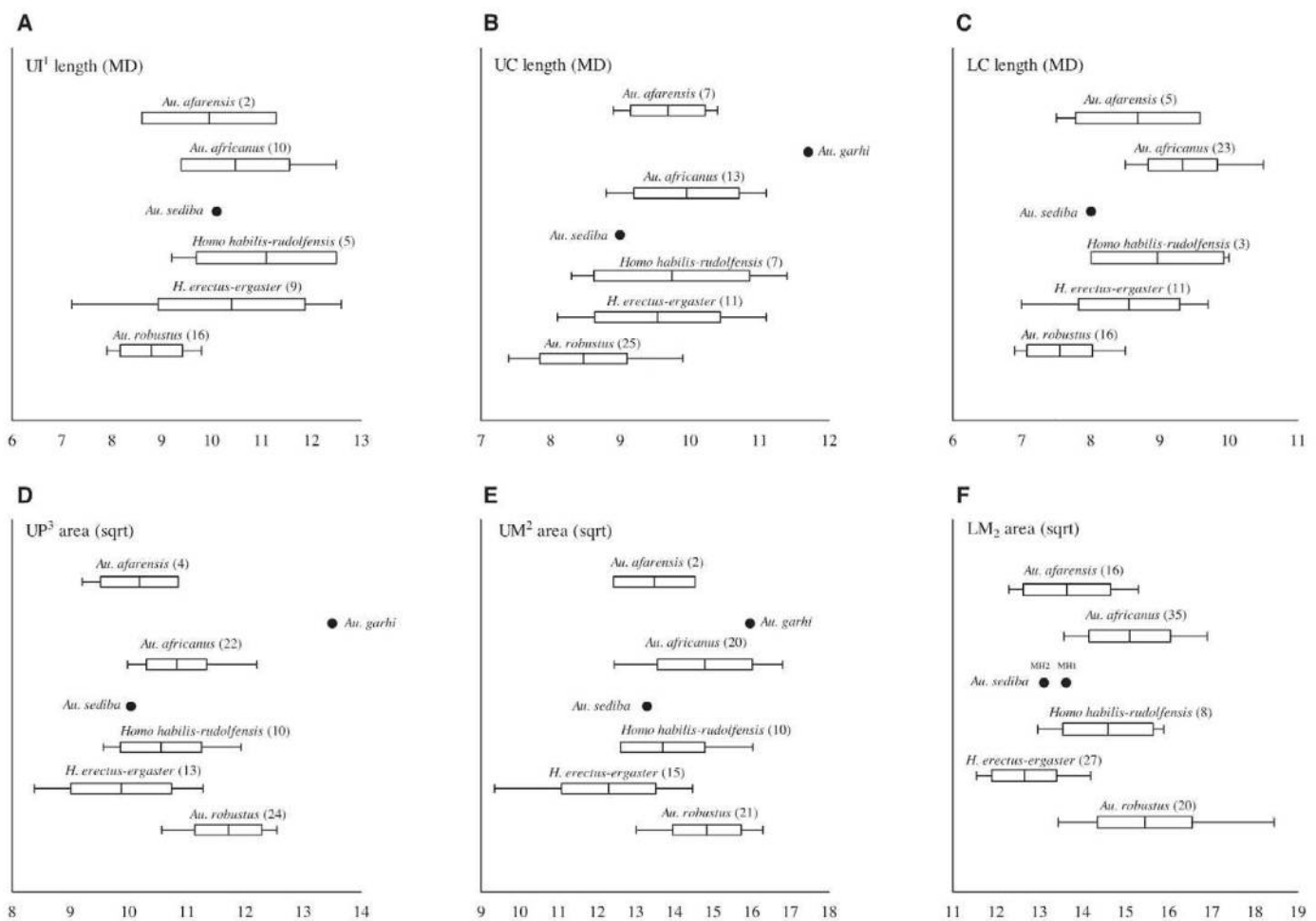

Fig. 3. Dental size of a selection of *Au. sediba* teeth compared to other early hominin taxa; see fig. S4 for additional teeth. Dental measurements were taken as described by Wood (*6*). Owing to small sample sizes, *H. habilis* and *H. rudolfensis* were combined. (**A**) Upper central incisor mesiodistal (MD) length. (**B**) Upper canine MD length. (**C**) Lower canine MD length. (**D**) Square root of calculated [MD × BL (BL, buccolingual)] upper third premolar area. (**E**) Square root of calculated (MD × BL) upper second molar area. (**F**) Square root of calculated (MD × BL) lower second molar area. Measures were taken on original specimens by D.J.D. for *Au. africanus*, *Au. robustus*, and *Au. sediba*. Measurements for *Au. afarensis*, *H. habilis*, *H. rudolfensis*, and *H. erectus* are from (*6*). P^4 is not fully erupted on the right side of MH1, therefore measures of the maxillary postcanine dentition are presented for the left side only. Dental metrics for *Au. sediba* are as follows (MD, BL, in millimeters): Maxillary: MH1: RI1 10.1, 6.9; LI2 7.7 (damaged), 5.1; RC 9.0, 8.8; LP3 9.0, 11.2; LP4 9.2, 12.1; LM1 12.9, 12.0; LM2 12.9, 13.7; LM3 13.3, 14.1; MH2: RM3 11.3, 12.9. Mandibular: MH1: LC 8.0, 8.5; RM1 12.5, 11.6; RM2 14.4, 12.9; RM3 14.9, 13.8; MH2: RM1 11.8, 11.1; RM2 14.1, 12.2; RM3 14.2, 12.7; LM3 14.1, 12.5.

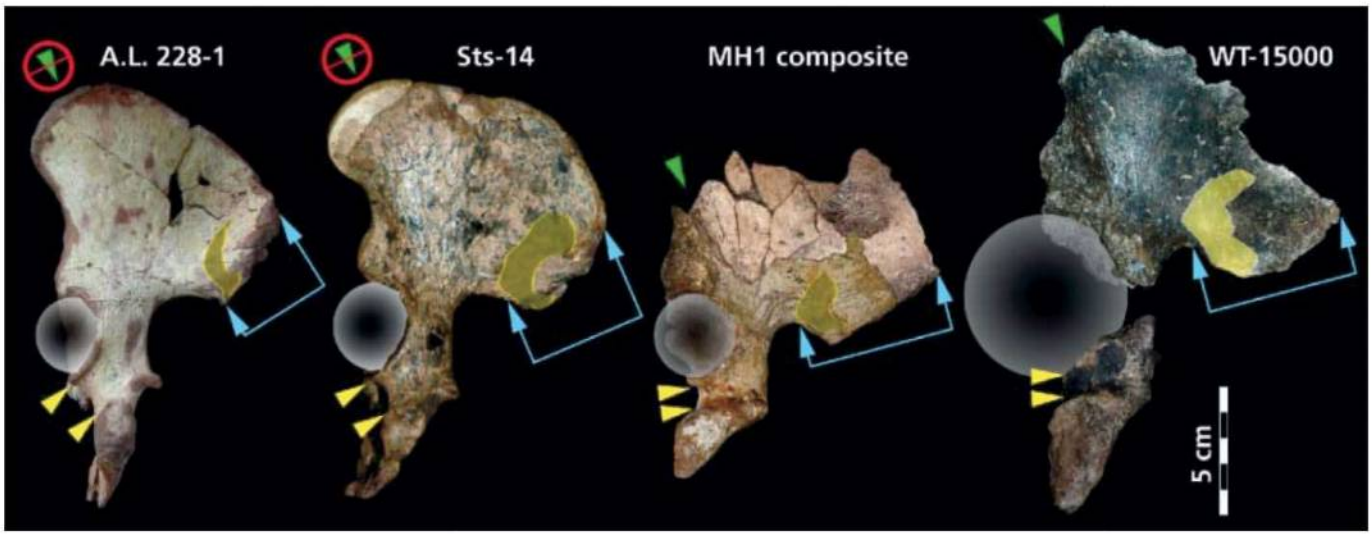

Fig. 4. Representative ossa coxae, in lateral view, from left to right, of *Au. afarensis* (AL 288-1), *Au. africanus* (Sts 14), *Au. sediba* (MH1), and *H. erectus* (KNM-WT 15000). The specimens are oriented so that the iliac blades all lie in the plane of the photograph (which thus leads to differences between specimens in the orientation of the acetabula and ischial tuberosities). MH1 possesses derived, *Homo*-like morphology compared to other australopithecines, including a relative reduction in the weight transfer distance from the sacroiliac (yellow) to hip (circle) joints; expansion of the retroauricular surface of the ilium (blue arrows) (determined by striking a line from the center of the sphere representing the femoral head to the most distant point on the posterior ilium; the superior arrow marks the terminus of this line, and the inferior arrow marks the intersection of this line with the most anterior point on the auricular face); narrowing of the tuberoacetabular sulcus (delimited by yellow arrows); and pronouncement of the acetabulocristal (green arrows) and acetabulosacral buttresses.

(table S2 and fig. S5). The calcaneus is markedly primitive in its overall morphology: the bone is strongly angled along the proximodistal axis, with the point of maximum inflexion occurring at an enlarged peroneal trochlea; the lateral plantar tubercle is lacking; the calcaneal axis is set about 45° to the transverse plane; and the calcaneocuboid facet is vertically set and lacks an expanded posterior projection for the beak of the cuboid (*23*).

Discussion. The age and overall morphology of *Au. sediba* imply that it is most likely descended from *Au. africanus*, and appears more derived toward *Homo* than do *Au. afarensis*, *Au. garhi*, and *Au. africanus*. Elsewhere in South Africa, the Sterkfontein cranium Stw 53, dated to 2.0 to 1.5 Ma, is generally considered to represent either *H. habilis* (*10*, *24*, *25*) or perhaps an undiagnosed form of early *Homo* (*26*). It played an important role in the assignment of OH 62 to *H. habilis* (*27*). However, the derived craniodental morphology of *Au. sediba* casts doubt on the attribution of Stw 53 to early *Homo* [see also (*28*)]: Stw 53 appears to be more primitive than MH1 in retaining closely spaced temporal lines; marked postorbital constriction; a weakly developed supraorbital torus; narrow, nonprojecting nasal bones; anterior pillars; marked nasoalveolar prognathism; medial and lateral expansion of the frontal process of the zygomatic bone; and laterally flared zygomatics. If Stw 53 instead represents *Au. africanus*, the assignment of OH 62 to *H. habilis* becomes tenuous. Attribution of the partial skeleton KNM-ER 3735 to *H. habilis* was tentatively based, in part, on a favorable comparison with OH 62 and on the hypothesis that there were no other contemporaneous non-robust australopith species to which it could be assigned in East Africa (*29*). As a result, the interpretation of KNM-ER 3735 as *H. habilis* also becomes uncertain.

The phylogenetic significance of the co-occurrence of derived postcranial features in *Au. sediba*, *H. erectus*, and a sample of isolated fossils generally referred to *Homo* sp. indet. (table S2) is not clear: The latter might represent early *H. erectus*, it might sample the postcranium of *H. rudolfensis* (which would then imply an evolutionary pathway from *Au. sediba* to *H. rudolfensis* to *H. erectus*), or it might represent the postcranium of *H. habilis* [which would suggest that OH 62 and KNM-ER 3735 (two specimens with ostensibly more primitive postcranial skeletons) do not belong in this taxon]. If the latter possibility holds, it could suggest a phylogenetic sequence from *Au. sediba* to *H. habilis* to *H. erectus*. Conversely, although the overall postcranial morphology of *Au. sediba* is similar to that of other australopiths, a number of derived features of the os coxa align the Malapa hominins with later *Homo* (*H. erectus*) to the exclusion of other australopiths. Additionally, *Au. sediba* shares a small number of cranial traits with *H. erectus* that are not exhibited in the *H. habilis–H. rudolfensis* hypodigm, including slight postorbital constriction and convexity of the infraorbital region (*18*). Following on this, MH1 compares favorably with SK 847 (*H. erectus*) in the development of the supraorbital torus, nasal bones, infraorbital region, frontal process of the zygomatic, and subnasal projection. However, MH1 differs from SK 847 in its relatively smaller size, the robust glabelar region, the weakly developed supratoral sulcus, the steeply inclined zygomaticoalveolar crests with a high masseter origin, and the moderate canine juga, all features aligning MH1 with *Australopithecus*. It is thus not possible to establish the precise phylogenetic position of *Au. sediba* in relation to the various species assigned to early *Homo*. We can conclude that combined craniodental and postcranial evidence demonstrates that this new species shares more derived features with early *Homo* than does any other known australopith species (Table 1 and table S2) and thus represents a candidate ancestor for the genus, or a sister group to a close ancestor that persisted for some time after the first appearance of *Homo*.

The discovery of a <1.95-million-year-old (*16*) australopith that is potentially ancestral to *Homo* is seemingly at odds with the recovery of older fossils attributed to the latter genus (*5*) or of approximately contemporaneous fossils attributable to *H. erectus* (*6*, *30*). However, it is unlikely that Malapa represents either the earliest or the latest temporal appearance of *Au. sediba*, nor does it encompass the geographical expanse that the species once occupied. We hypothesize that *Au. sediba* was derived via cladogenesis from *Au. africanus* (≈3.0 to 2.4 Ma), a taxon whose first and last appearance dates are also uncertain (*31*). The possibility that *Au. sediba* split from *Au. africanus* before the earliest appearance of *Homo* cannot be discounted.

Although the skull and skeleton of *Au. sediba* do evince derived features shared with early *Homo*, the overall body plan is that of a hominin at an australopith adaptive grade. This supports the argument, based on endocranial volume and craniodental morphology, that this species is most parsimoniously attributed to the genus *Australopithecus*. The Malapa specimens dem-

onstrate that the evolutionary transition from a small-bodied and perhaps more arboreal-adapted hominin (such as *Au. africanus*) to a larger-bodied, possibly full-striding terrestrial biped (such as *H. erectus*) occurred in a mosaic fashion. Changes in functionally important aspects of pelvic morphology, including a reduction of the sacroacetabular weight-bearing load arm and enhanced acetabulosacral buttressing (reflecting enhancement of the hip extensor mechanism), enlargement of the iliofemoral ligament attachment (reflecting a shift in position of the line of transfer of weight to behind the center of rotation of the hip joint), enlargement of the acetabulocristal buttress (denoting enhancement of an alternating pelvic tilt mechanism), and reduction of the distance from the acetabulum to the ischial tuberosity (reflecting a reduction in the moment arm of the hamstring muscles) (*20*, *32*) occurred within the context of an otherwise australopith body plan, and seemingly before an increase in hominin encephalization [in contrast to the argument in (*33*)]. Relative humeral and femoral diaphyseal strength measures (table S2) also suggest that habitual locomotor patterns in *Au. sediba* involved a more modern human-like mechanical load-sharing than that seen in the *H. habilis* specimen OH 62 (*34*, *35*). Mosaic evolutionary changes are mirrored in craniodental morphology, because the increasingly wide spacing of the temporal lines and reduction in postorbital constriction that characterize *Homo* first appeared in an australopith and before significant cranial expansion. Moreover, dental reduction, particularly in the postcanine dentition, preceded the cuspal rearrangement (wide spacing of postcanine tooth cusps) that marks early *Homo*.

The pattern of dental eruption and epiphyseal fusion exhibited by MH1 indicates that its age at death was 12 to 13 years by human standards, whereas in MH2 the advanced degree of occlusal attrition and epiphyseal closure indicates that it had reached full adulthood (SOM text S1). Although juvenile, MH1 exhibits pronounced development of the supraorbital region and canine juga, eversion of the gonial angle of the mandible, and large rugose muscle scars in the skeleton, all indicating that this was a male individual. And, although fully adult, the mandible and skeleton of MH2 are smaller than in MH1, which, combined with the less rugose muscle scars and the shape of the pubic body of the os coxa, suggests that MH2 was a female. In terms of dental dimensions, MH1 has mandibular molar occlusal surface areas that are 10.7% (M_1) and 8.1% (M_2) larger than those of MH2. Dimorphism in the postcranial skeleton likewise is not great, though the juvenile status of MH1 tends to confound efforts to assess adult body size. The diameter of the proximal epiphysis for the femoral head of MH1 (29.8 mm) is approximately 9.1% smaller than the superoinferior diameter of MH2's femoral head (32.7 mm). It is likely that MH1 would have experienced some appositional increase in joint size before maturity, thus this disparity would probably have decreased somewhat. The distal humeral epiphysis of MH1 is fully fused and its articular breadth (35.3 mm) is only marginally larger than that of MH2 (35.2 mm). Thus, although the dentition and postcranial skeleton are at odds in the degree of apparent size differences, the overall level of dimorphism, if these sex attributions are correct, appears slight in the Malapa hominins and was probably similar to that evinced by modern humans.

References and Notes

1. R. A. Dart, *Nature* **115**, 195 (1925).
2. D. C. Johanson, T. D. White, *Science* **203**, 321 (1979).
3. B. Asfaw *et al.*, *Science* **284**, 629 (1999).
4. M. G. Leakey *et al.*, *Nature* **410**, 433 (2001).
5. W. H. Kimbel, D. C. Johanson, Y. Rak, *Am. J. Phys. Anthropol.* **103**, 235 (1997).
6. B. Wood, *Koobi Fora Research Project, Volume 4: Hominid Cranial Remains* (Clarendon Press, Oxford, 1991).
7. G. P. Rightmire, *Am. J. Phys. Anthropol.* **90**, 1 (1993).
8. R. J. Blumenschine *et al.*, *Science* **299**, 1217 (2003).
9. B. Wood, M. Collard, *Science* **284**, 65 (1999).
10. P. V. Tobias, *Olduvai Gorge Volume 4: The Skulls, Endocasts and Teeth of* Homo habilis (Cambridge Univ. Press, Cambridge, 1991).
11. D. S. Strait, F. E. Grine, *J. Hum. Evol.* **47**, 399 (2004).
12. D. E. Lieberman, *Nature* **410**, 419 (2001).
13. The *H. erectus* hypodigm includes African specimens that are referred to the taxon *H. ergaster* by some. Unless otherwise stated, we collectively refer to *H. habilis*, *H. rudolfensis*, *H. erectus*, and *H. ergaster* materials as "early *Homo*."
14. F. Spoor *et al.*, *Nature* **448**, 688 (2007).
15. P. V. Tobias, *The Brain in Hominid Evolution* (Columbia Univ. Press, New York, 1971).
16. P. H. G. M. Dirks *et al.*, *Science* **328**, 205 (2010).
17. D. M. Bramble, D. E. Lieberman, *Nature* **432**, 345 (2004).
18. Rak (*36*) describes a feature in the infraorbital region of *Au. boisei* that he refers to as a nasomaxillary basin: a concave depression that is surrounded by a more elevated topography. We see a similar concavity in the infraorbital region of specimens of *H. habilis–H. rudolfensis* (KNM-ER 1470, KNM-ER 1805, KNM-ER 1813, and OH 24), although it is not clear whether they represent homologous structures. In specimens of *Au. africanus, Au. sediba*, and *H. erectus*, we recognize a slight convexity in this area.
19. Some humeri that are probably best attributed to *Australopithecus* lack marked development of the trochlear/capitular keel [or "lateral crest": see (*37*)], and thus the absence of a marked crest does not reliably differentiate *Australopithecus* from *Homo*. However, although some specimens of early *Homo* (such as KNM-WT 15000) have crests that are more strongly developed than those of modern humans, none exhibit the marked crests of the australopiths. Thus, the marked crest seen in the Malapa humeri can be seen to be shared with *Australopithecus* rather than *Homo*.
20. M. D. Rose, *Am. J. Phys. Anthropol.* **63**, 371 (1984).
21. A. Walker, C. B. Ruff, in *The Nariokotome* Homo erectus *Skeleton*, A. Walker, R. E. F. Leakey, Eds. (Harvard Univ. Press, Cambridge, MA, 1993), pp. 221–233.
22. C. K. Brain, E. S. Vrba, J. T. Robinson, *Ann. Transv. Mus.* **29**, 55 (1974).
23. L. C. Aiello, C. Dean, *An Introduction to Human Evolutionary Anatomy* (Academic Press, London, 1990).
24. A. R. Hughes, P. V. Tobias, *Nature* **265**, 310 (1977).
25. D. Curnoe, P. V. Tobias, *J. Hum. Evol.* **50**, 36 (2006).
26. F. E. Grine, W. L. Jungers, J. Schultz, *J. Hum. Evol.* **30**, 189 (1996).
27. D. C. Johanson *et al.*, *Nature* **327**, 205 (1987).
28. R. J. Clarke, *S. Afr. J. Sci.* **104**, 443 (2008).
29. R. E. F. Leakey, A. Walker, C. V. Ward, H. M. Grausz, in *Hominidae*, G. Giacobini, Ed. (Jaca Books, Milano, Italy, 1989), pp. 167–173.
30. L. Gabunia, A. Vekua, *Nature* **373**, 509 (1995).
31. T. D. White, in *Paleoclimate and Evolution with Emphasis on Human Origins*, E. S. Vrba, G. H. Denton, T. C. Partridge, L. H. Burckle, Eds. (Yale Univ. Press, New Haven, CT, 1995), pp. 369–384.
32. J. T. Stern Jr., R. L. Susman, *Am. J. Phys. Anthropol.* **60**, 279 (1983).
33. C. O. Lovejoy, *Gait Posture* **21**, 113 (2005).
34. C. Ruff, *Am. J. Phys. Anthropol.* **138**, 90 (2009).
35. It is possible that the more *Homo*-like humeral-to-femoral diaphyseal strength ratios in *Au. sediba* reflect a relative reinforcement of the femoral diaphysis in the context of femoral elongation (resulting in longer bending-moment arms) without a change in locomotor behavior. At present, we are unable to directly assess the absolute and relative length of the femur in *Au. sediba*.
36. Y. Rak, *The Australopithecine Face* (Academic Press, New York, 1983).
37. M. R. Lague, W. L. Jungers, *Am. J. Phys. Anthropol.* **101**, 401 (1996).
38. R. R. Skelton, H. M. McHenry, *J. Hum. Evol.* **23**, 309 (1992).
39. M. Collard, B. Wood, *Proc. Natl. Acad. Sci. U.S.A.* **97**, 5003 (2000).
40. H. F. Smith, F. E. Grine, *J. Hum. Evol.* **54**, 684 (2008).

41. We thank the South African Heritage Resources Agency for the permits to work at the Malapa site; the Nash family for granting access to the Malapa site and continued support of research on their reserve; the South African Department of Science and Technology, the South African National Research Foundation, the Institute for Human Evolution, the Palaeontological Scientific Trust, the Andrew W. Mellon Foundation, the AfricaArray Program, the U.S. Diplomatic Mission to South Africa, and Sir Richard Branson for funding; the University of the Witwatersrand's Schools of Geosciences and Anatomical Sciences and the Bernard Price Institute for Palaeontology for support and facilities; the Gauteng Government, Gauteng Department of Agriculture, Conservation and Environment and the Cradle of Humankind Management Authority; E. Mbua, P. Kiura, V. Iminjili, and the National Museums of Kenya for access to comparative specimens; Optech and Optron; Duke University; the Ray A. Rothrock Fellowship of Texas A&M University; and the University of Zurich 2009 Field School. Numerous individuals have been involved in the ongoing preparation and excavation of these fossils, including C. Dube, B. Eloff, C. Kemp, M. Kgasi, M. Languza, J. Malaza, G. Mokoma, P. Mukanela, T. Nemvhundi, M. Ngcamphalala, S. Jirah, S. Tshabalala, and C. Yates. Other individuals who have given significant support to this project include B. de Klerk, C. Steininger, B. Kuhn, L. Pollarolo, B. Zipfel, J. Kretzen, D. Conforti, J. McCaffery, C. Dlamini, H. Visser, R. McCrae-Samuel, B. Nkosi, B. Louw, L. Backwell, F. Thackeray, and M. Peltier. T. Stidham helped construct the cladogram in fig. S3. J. Smilg facilitated computed tomography scanning of the specimens. R. Clarke and F. Kirera provided valuable discussions on these and other hominin fossils in Africa.

Supporting Online Material

www.sciencemag.org/cgi/content/full/328/5975/195/DC1
SOM Text 1 to 4
Figs. S1 to S5
Tables S1 and S2
References

19 November 2009; accepted 26 February 2010
10.1126/science.1184944

Geological Setting and Age of *Australopithecus sediba* from Southern Africa

Paul H. G. M. Dirks,[1,2]* Job M. Kibii,[3] Brian F. Kuhn,[3] Christine Steininger,[3,2] Steven E. Churchill,[4,3] Jan D. Kramers,[2,5,6] Robyn Pickering,[7] Daniel L. Farber,[8,9] Anne-Sophie Mériaux,[10] Andy I. R. Herries,[11,12] Geoffrey C. P. King,[13] Lee R. Berger[3,2]

We describe the geological, geochronological, geomorphological, and faunal context of the Malapa site and the fossils of *Australopithecus sediba*. The hominins occur with a macrofauna assemblage that existed in Africa between 2.36 and 1.50 million years ago (Ma). The fossils are encased in water-laid, clastic sediments that were deposited along the lower parts of what is now a deeply eroded cave system, immediately above a flowstone layer with a U-Pb date of 2.026 ± 0.021 Ma. The flowstone has a reversed paleomagnetic signature and the overlying hominin-bearing sediments are of normal polarity, indicating deposition during the 1.95- to 1.78-Ma Olduvai Subchron. The two hominin specimens were buried together in a single debris flow that lithified soon after deposition in a phreatic environment inaccessible to scavengers.

Two hominin fossils assigned to *Australopithecus sediba* (*1*) were found in deposits in Malapa cave (Fig. 1). This newly discovered site is one of several Plio-Pleistocene cave deposits in the Cradle of Humankind World Heritage Site (South Africa) that host hominin fossils and associated faunal and archaeological remains, including Sterkfontein, Swartkrans, Kromdraai, and Coopers (*2*–*8*). The fossiliferous deposits in these caves formed in broadly similar ways, mostly as debris cone accumulations beneath vertical cave openings (*6*–*11*). Clastic sedimentation alternated with periods of erosion (*7*) or flowstone formation (*11*), producing unconformities representing time markers between caves. Here we describe the geological, geochronological, geomorphological, and faunal context of the Malapa site and the fossils of *Au. sediba* (*1*).

Malapa cave formed in stromatolite-rich dolomite of the late Archaean [2.64 to 2.50 billion years ago (Ga)] Malmani Subgroup (*12*, *13*), which is subdivided into five formations (from base to top: the Oaktree, Monte Christo, Lyttelton, Eccles, and Frisco formations) (*13*, *14*). Malapa cave is located 15 km north-northeast of Sterkfontein, in the steep-sided valley of the spring-fed Grootvleispruit. It is situated at the north end of a line of north-south–trending caves that are stratigraphically bound to the top 40 m of the 155-m-thick Lyttelton Formation, in layered dolomite that dips 8° to 13° to the north-northwest, an angle 2° to 5° shallower than the slope of the valley where the caves are exposed (Fig. 1).

Caves near Malapa define a 500-m-long and 100-m-wide network of interconnected openings along chert-filled fractures (Fig. 1). In the immediate vicinity of Malapa (elevation: 1442 m above mean sea level), erosion remnants of cave deposits form shallow depressions. Caves farther upslope are progressively deeper and preserve interconnected subterranean caverns that reach a vertical depth of 25 to 30 m. The cave system closes above an elevation of ~1490 m, directly below the sheared upper contact of the Lyttelton formation (Fig. 1). These trends, combined with valley slope and bedding orientation, suggest that Malapa lies near the base of an originally >30-m-deep, strata-bound and fracture-controlled cave system eroded by valley incision.

Malapa cave formed at the intersection of a north-northeast and a north-northwest fracture, with hominin remains occurring in a 3.5-m-deep excavation (3.3 m by 4.4 m in size) centered on the north-northwest fracture. Minor limestone mining took place at Malapa in the early 20th century, exposing in situ hominin material. The cave deposits comprise five distinct sedimentary facies called, from base to top, A to E. Facies A–B occur below a central flowstone sheet (Fig. 2 and fig. S1). The fossils of *Au. sediba* (*1*) are in facies D, with additional hominin remains in facies E (Fig. 2).

Facies A consists of dark-colored, moderately sorted, coarse-grained clastic sediment, with abun-

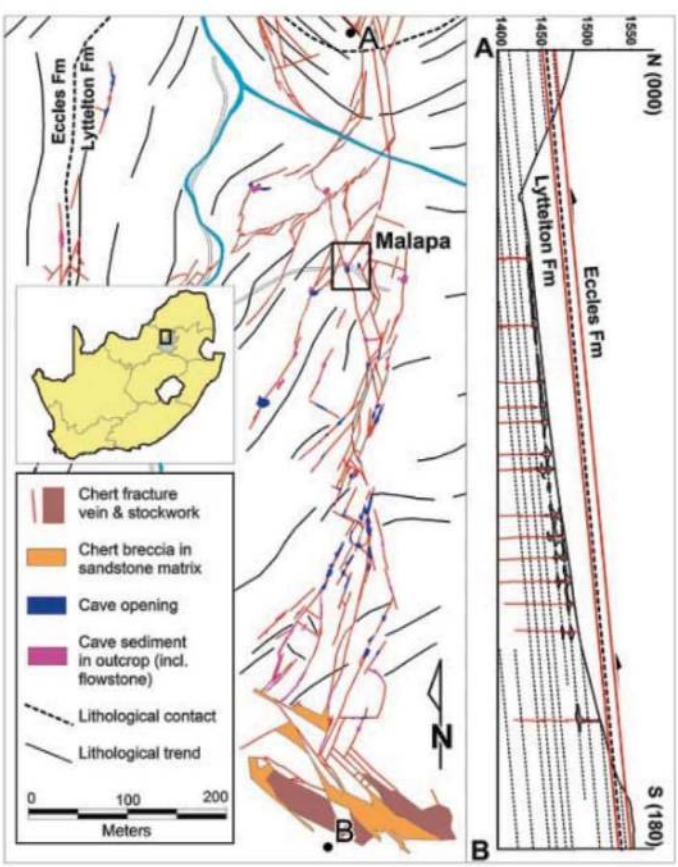

Fig. 1. Location of the Malapa site in the valley of the Grootvleispruit, showing the principal geological controls on cave formation. Malapa is positioned along a complex fracture system in the most deeply eroded parts of a 500-m-long cave system as illustrated by section A-B.

[1]School of Earth and Environmental Sciences, James Cook University, Townsville, QLD 4811, Australia. [2]School of Geosciences, University of the Witwatersrand, Johannesburg, Private Bag 3, Wits 2050, South Africa. [3]Institute for Human Evolution, University of the Witwatersrand, Johannesburg, Private Bag 3, Wits 2050, South Africa. [4]Department of Evolutionary Anthropology, Box 90383, Duke University, Durham, NC 27708, USA. [5]Institute of Geological Sciences, University of Bern, Baltzerstrasse 3, 3012 Bern, Switzerland. [6]Department of Geology, University of Johannesburg, Auckland Park 2006, South Africa. [7]School of Earth Sciences, University of Melbourne, VIC 3010, Australia. [8]Center for Accelerator Mass Spectrometry, Lawrence Livermore National Laboratory, Livermore, CA 94550, USA. [9]Department of Earth and Planetary Sciences, University of California, Santa Cruz, Santa Cruz, CA 95064, USA. [10]School of Geography, Politics and Sociology, Newcastle University, Claremont Road, Newcastle upon Tyne NE1 7RU, UK. [11]UNSW Archaeomagnetism Laboratory, School of Medical Sciences, University of New South Wales, Sydney, NSW 2052, Australia. [12]Geomagnetism Laboratory, Oliver Lodge, Department of Earth and Ocean Science, University of Liverpool, L69 3BX, UK. [13]Laboratoire Tectonique, Institut de Physique du Globe Paris, 4 Place Jussieu, 75252 Paris, France.

*To whom correspondence should be addressed. E-mail: paul.dirks@jcu.edu.au

dant rounded grains (0.5 to 6 mm) of chert, quartz, dolomite, iron oxide–coated grains or ooids, bone fragments and peloids, and little feldspar and mica schist. The openly packed framework grains are embedded in blocky sparite. Bedding is defined by normal and inverse grading, and a weak preferred orientation of rock and bone fragments. The coarsest-grained parts of facies A occur toward the center of the unit defining a shallow central channel.

Facies B consists of peloidal grainstone alternating with clastic sandstone. The grainstone contains >50% rounded peloids and lesser amounts of bone fragments and clastic grains (mostly quartz), many iron oxide–coated, to form an open framework cemented with blocky sparite. Fenestrae with sparry calcite are common along horizontal bedding planes. Peloids (0.4 to 1 mm) consist of fine-grained (0.02 to 0.10 mm) angular quartz grains in a micaceous mud and sparite matrix. Sandstone rich in bone fragments and rounded iron oxide–coated grains forms layers preserving grading (coarsening and fining upward) and grain imbrication. Small stalagmite bosses growing on a grainstone substrate, and isolated limestone blocks (<40 cm), are incorporated in facies B.

After deposition, facies A and B were eroded and covered by a flowstone carapace that dips moderately to the north-northeast, indicating north-directed water flow along the cave axis. The flowstone contains intercalations of fossil-bearing, detrital sandstone. A milky quartz vein surrounded by an alteration halo of iron oxide and clay intruded facies A–B, but does not appear to intrude the flowstone (Fig. 2).

Facies C is identical to the peloidal grainstone units in facies B. It is preserved as a 5- to 30-cm-thick erosion remnant that drapes over the flowstone in the northwest corner of the pit (Fig. 2). Subrounded fragments of quartz, limestone, and shale, many iron oxide–coated, as well as bone fragments, occur toward the top of the layer, and fenestrae are common.

Facies D overlies flowstone in the center and east of the pit and sits unconformably on facies C in the west. This massive, up to 1.5-m-thick, light-colored unit contains abundant, well-preserved macro- and micromammal fossils, including the remains of two skeletons of *Au. sediba* (*1*) and articulated remains of *Equus* sp. (Fig. 2). The poorly sorted, coarse-grained sandstone is cemented by blocky sparite, which displays isopachous (radial outward) overgrowths in larger pore spaces. Framework grains are mostly 0.5 to 2.5 mm in size and consist of quartz, chert, dolomite, peloids, and, less commonly, iron oxide–coated grains, ooids, shale, and feldspar (microcline). Rounding varies from well-rounded ooids to angular vein-quartz crystals. Angular limestone blocks (<50 cm) and flowstone fragments (<5 cm) occur throughout facies D. Peloids are common, but peloidal boundaries are diffuse, and groups of peloids are fused in irregular patches. The hominin skeletons are in close spatial association, separated by no more than 40 cm vertically (Fig. 2). The recovered remains of the juvenile occur in close association (*1*) toward the top of facies D, and the partly articulated remains of the adult (*1*) occur near the base.

Facies E consists of calcareous sandstone, similar to facies D, but darker colored and finer grained, with a higher degree of sorting and rounding, and preserving 4- to 15-cm-scale horizontal layering. The basal layer of facies E consists of well-sorted, coarse-grained sandstone dominated by 0.6- to 1.5-mm-large iron oxide–coated chert and quartz grains and aggregates of peloids. The layer preserves northwest-dipping laminations, indicating directional water flow. Horizontal layering in facies E is defined by grain-size variations (coarsening and fining upward), mud partings, thin (<1 mm) flowstone drapes, and orientated bone fragments. Fossil bone is abundant, but less well preserved than bone in facies D, with solution damage and partial fragmentation suggesting exposure to standing or flowing water before final burial and cementation (*15*).

The rocks of facies A–E were water-laid with all sandstone units displaying loose packing of framework grains indicating little postdepositional compaction (*16*). Abundant fenestrae in facies B and C reflect trapped gas possibly formed from the decay of organic matter (*16*, *17*). The abundant peloids are interpreted as fecal remains (*16*, *17*) or soil micropeds (*11*, *18*). Coalescence of peloids in facies D and E reflects mechanical

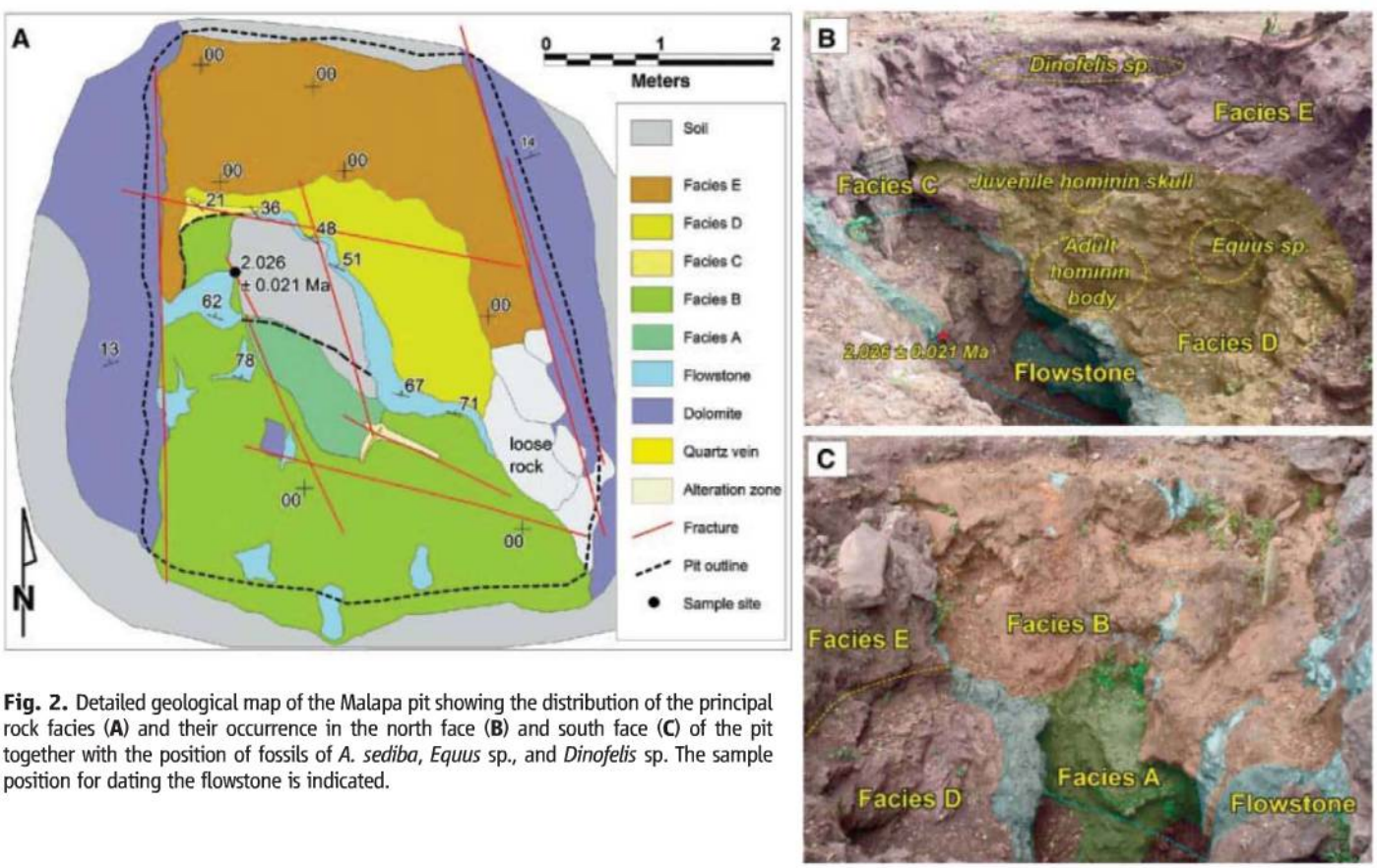

Fig. 2. Detailed geological map of the Malapa pit showing the distribution of the principal rock facies (**A**) and their occurrence in the north face (**B**) and south face (**C**) of the pit together with the position of fossils of *A. sediba*, *Equus* sp., and *Dinofelis* sp. The sample position for dating the flowstone is indicated.

reworking of unconsolidated peloids deposited in a water-logged environment. The homogeneous sandstone of facies D contains allochtonous material (chert, shale and feldspar grains, bone fragments) mixed with cave-derived sediment and coarse blocks, suggesting deposition as a single debris flow that carried partially articulated (i.e., only partially decomposed) hominins with it. The superb preservation and state of articulation of fossil material (*1*) indicate rapid deposition, limited transport distance, and laminar flow conditions consistent with debris flows (*17*, *19*). The presence of isopachous sparite indicates that cementation occurred soon after deposition in a phreatic environment (*16*). After the debris flow, the cave filled with horizontally layered clastic deposits (facies E) dominated by autochtonous sediment with sedimentary structures indicating north-directed water flow that weakened and strengthened from time to time, carrying with it bone fragments and partially articulated faunal remains. Absence of carnivore damage in the fossil assemblage indicates that scavengers had no access to the cave.

We collected 209 nonhominin fossil specimens from facies D–E, of which 25 specimens have been identified to at least the genus level (Table 1). Representatives of the extant species *Felis silvestris* and *Parahyaena brunnea*, as well as *Lycaon* sp., *Tragelaphus* cf. *strepsiceros*, and *Equus* sp., have their earliest recorded appearance in Africa at ~2.36 million years ago (Ma) (*20*–*22*). The extinct felid *Megantereon whitei* collected from facies E has a last recorded appearance in Africa at ~1.5 Ma (*23*). These ages thus bracket the depositional age of the fossil hominins.

The flowstone underlying facies C and D was dated independently at two separate laboratories (Bern and Melbourne) by slightly different U-Pb techniques (*8*, *24*) (SOM Text S1). Dates were obtained from thin, U-bearing (0.7 parts per million) seams near the base of a flowstone sheet (figs. S1 and S2) stratigraphically 20 cm below the adult hominin skeleton (Fig. 2), but separated from the skeleton by an erosional surface along the top of the flowstone. The dates of 2.024 ± 0.062 Ma (Bern) and 2.026 ± 0.021 Ma (Melbourne) are identical within error and provide a maximum age limit for the hominin remains (table S1 and fig. S3).

To further constrain the age of deposition of the fossils, we took samples for paleomagnetic analysis from across the flowstone layer and the overlying sedimentary facies (SOM Text S2, table S3, and figs. S1, S4, and S5). The flowstone mainly preserves reverse polarity, but near its base, a normal polarity excursion occurs that is interpreted as the Huckleberry Ridge Subchron at 2.06 ± 0.04 Ma (*25*). The sediments of facies C, D, and E above the flowstone record normal polarity that is interpreted as the beginning of the 1.95- to 1.78-Ma Olduvai Subchron (*26*).

To constrain the level of erosion and original depth of the cave system, we collected samples for cosmogenic ^{10}Be analysis from two sites (SOM Text S3, table S4, and fig. S6) to bracket the minimum and maximum erosion rates Malapa experienced: (i) the plateau 650 m south and 82 m above Malapa (TNHL08) equated to the African Erosion Surface (*5*) that is thought to have experienced low erosion rates (<10 m) over the past tens of millions of years, and (ii) the gently northwest-dipping bedrock channel of the Grootvleispruit, 3400 m west-northwest and 85 m below Malapa (LH08). Samples from TNHL08 give consistent values for the long-term erosion rate of the surface of ~3 to 5 m per million years (My) with a mean of 3.6 ± 1.1 m/My (table S5). These rates are more than an order of magnitude higher than are common in ancient relic landscapes (*27*–*29*) and indicate that over the past ~2 million years, at least ~8 m of overburden was removed from Malapa. To constrain the downcutting rate of the river into shale overlying the Malmani Subgroup, and thus the rate of valley formation, we collected bedrock samples from LH08 from a chert layer forming a dip slope and the stream channel (SOM Text S3 and fig. S7). A linear fit to data collected from ~1 to 6 m above the active channel spans a time frame of 10^5 years and yields a river incision rate of 53 ± 9 m/My (fig. S8). This suggests that erosion rates at Malapa are significantly greater than those measured on the plateau, indicating that Malapa cave was tens of meters deep when the *Hominin* fossils were deposited.

As a taphonomic hypothesis, we suggest that at the time of burial of the hominins, the complex cave system near Malapa had opened along deep vertical shafts that operated as death traps to animals on the surface (Fig. 3). In addition to being inconspicuous drops into which animals accidentally wandered, the cave openings may have been loci of animal activity, enhancing their operation as natural traps. Animals might have been attracted to the smell of water coming from the shaft, and carnivores might have been attracted to the smell of decomposing bodies. These factors could have operated to accumulate a diverse assemblage of carcasses in the chamber below, away from carnivore activity. The sediments imply that subsequent high-volume water inflow, perhaps the result of a large storm, caused a

Table 1. Nonhominin faunal material recovered from Malapa with estimates of minimum numbers of individuals (MNI) and number of identified specimens (NISP).

Order	Family	Tribe	Genus and species	MNI	NISP
Carnivora	Felidae		*Dinofelis* sp.	1	2
			Megantereon whitei	1	1
			Felis silvestris	1	1
	Hyaenidae		*Parahyaena brunnea*	2	8
	Canidae		*Lycaon* sp.	1	1
	Herpestidae		*Atilax mesotes**	1	1
			Mungos sp.	1	1
Perissodactyla	Equidae		*Equus* sp.	1	1
Artiodactyla	Suidae		*Suidae* Indet.	1	1
	Bovidae	Neotragini	*Oreotragus* sp.	1	1
		Alcelaphini	*Megalotragus* sp.	1	1
			Large-sized alcelaphine	1	1
		Tragelaphini	*Tragelaphus* cf. *scriptus*	1	1
			Tragelaphus cf. *strepsiceros*	1	1
Lagomorpha	Leporidae		*Lepus* sp.	1	3
Total				16	25

*Considered by some to be *Herpestes mesotes*.

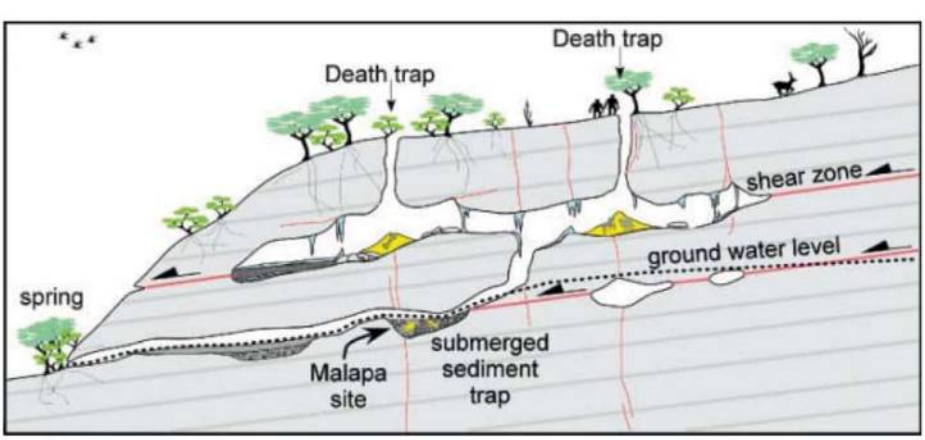

Fig. 3. Cartoon illustrating how two hominins might have become trapped and buried in alluvial sediments at the bottom of a Pliocene cave.

debris flow that carried the still partially articulated bodies deeper into the cave, to deposit them along a subterranean stream (Fig. 3).

References and Notes

1. L. R. Berger *et al.*, *Science* **328**, 195 (2010).
2. R. Broom, J. T. Robinson, *Nature* **164**, 322 (1949).
3. A. R. Hughes, P. V. Tobias, *Nature* **265**, 310 (1977).
4. R. Clarke, *S. Afr. J. Sci.* **94**, 460 (1998).
5. T. C. Partridge, in *The Cenozoic of Southern Africa*, T. C. Partridge, R. R. Maud, Eds. (Oxford Univ. Press, New York, 2000), pp. 100–125.
6. T. C. Partridge, D. E. Granger, M. W. Caffee, R. J. Clarke, *Science* **300**, 607 (2003).
7. C. K. Brain, in *Swartkrans: A Cave's Chronicle of Early Man*, C. K. Brain, Ed. (Monogr. 8, Transvaal Museum, Pretoria, ed. 2, 2004).
8. D. J. de Ruiter *et al.*, *J. Hum. Evol.* **56**, 497 (2009).
9. T. C. Partridge, *Nature* **275**, 282 (1978).
10. C. K. Brain, in *Palaeoclimate and Evolution, with Emphasis on Human Origins*, E. S. Vrba, Ed. (New Haven, 1995), pp. 385–424.
11. R. Pickering *et al.*, *J. Hum. Evol.* **53**, 602 (2007).
12. D. McB. Martin, C. W. Clendennin, B. Krapez, N. J. McNaughton, *J. Geol. Soc. London* **155**, 311 (1998).
13. P. G. Eriksson *et al.*, in *The Geology of South Africa*, M. R. Johnson, C. R. Anhaeusser, R. J. Thomas, Eds. (Geological Society of South Africa, Johannesburg, 2006), pp. 237–260.
14. K. A. Eriksson, J. F. Truswell, *Trans. Geol. Soc. S. Afr.* **77**, 211 (1974).
15. C. K. Brain, *The Hunters or the Hunted? An Introduction to African Cave Taphonomy* (Univ. of Chicago Press, Chicago, 1981).
16. H. Blatt *et al.*, *Petrology: Igneous, Sedimentary and Metamorphic* (Freeman, New York, ed. 3, 2006).
17. M. E. Tucker, *Sedimentary Petrology* (Blackwell, Oxford, ed. 2, 1991).
18. G. J. Retallack, *Soils of the Past: An Introduction to Palaeopedeology* (Harper Collins, London, 1990).
19. P. Coussot, M. Meunier, *Earth Sci. Rev.* **40**, 209 (1996).
20. L. R. Berger, R. Lacruz, D. J. De Ruiter, *Am. J. Phys. Anthropol.* **119**, 192 (2002).
21. J. P. Brugal, H. Roche, M. Kibunjia, *C. R. Palevol.* **2**, 675 (2003).
22. F. H. Brown, I. McDougall, I. Davies, R. Maier, in *Ancestors: The Hard Evidence*, E. Delson, Ed. (Liss, New York, 1985), pp. 82–90.
23. M. E. Lewis, L. Werdelin, in *Hominin Environments in the East African Pliocene: An Assessment of the Faunal Evidence*, R. Bobe, Z. Alemseged, A. K. Behrensmeyer, Eds. (Springer, Netherlands, 2007), pp. 77–105.
24. J. D. Woodhead *et al.*, *Quat. Geochronol.* **1**, 208 (2006).
25. M. A. Lanphere, D. E. Champion, R. L. Christiansen, G. A. Izett, *GSA Bull.* **114**, 559 (2002).
26. J. G. Ogg, A. G. Smith, in *A Geologic Time Scale 2004*, F. Gradstein, J. G. Ogg, A. G. Smith, Eds. (Cambridge Univ. Press, Cambridge, UK, 2004), pp. 63–86.
27. K. Nishiizumi, M. W. Caffee, R. C. Finkel, G. Brimhall, T. Mote, *Earth Planet. Sci. Lett.* **237**, 499 (2005).
28. S. R. Hall, D. L. Farber, L. Audin, R. C. Finkel, A. S. Meriaux, *Tectonophysics* **459**, 186 (2008).
29. A. Matmon *et al.*, *Geol. Soc. Am. Bull.* **121**, 688 (2009).

30. We thank the South African Heritage Resource Agency for allowing work on the Malapa site; the Nash family for granting access to the Malapa site and continued support; the Palaeontological Scientific Trust (PAST), the Institute for Human Evolution, University of the Witwatersrand and the School of Geosciences, University of the Witwatersrand, for funding; and the University of the Witwatersrand's Schools of Geosciences and Anatomical Sciences and the Bernard Price Institute for Palaeontology for support and facilities. Further support was provided by AfricaArray (P.H.G.M.D.), the France-SA, !Khure Africa project (G.C.P.K., D.L.F., A.-S.M.), and LLNL GEO-CAMS and the US-NSF EAR-0345895 (D.L.F.). R.P. is supported by a Swiss National Science Foundation Post-Doctoral Grant and gratefully acknowledges J. Woodhead, A. Grieg, and the team at Melbourne University. A.I.R.H. was funded through a UNSW Faculty of Medicine research grant and ARC Discovery Grant DP0877603 and acknowledges the support of the Liverpool University Geomagnetism Laboratory staff. Contributions to mapping and sample preparation by G. Charlesworth and Z. Jinnah are kindly acknowledged.

Supporting Online Material

www.sciencemag.org/cgi/content/full/328/5975/205/DC1
SOM Text S1 to S3
Figs. S1 to S8
Tables S1 to S4
References

19 November 2009; accepted 26 February 2010
10.1126/science.1184950

Why Copy Others? Insights from the Social Learning Strategies Tournament

L. Rendell,[1]* R. Boyd,[2] D. Cownden,[3] M. Enquist,[4,5] K. Eriksson,[5,6] M. W. Feldman,[7] L. Fogarty,[1] S. Ghirlanda,[5,8] T. Lillicrap,[9] K. N. Laland[1]*

Social learning (learning through observation or interaction with other individuals) is widespread in nature and is central to the remarkable success of humanity, yet it remains unclear why copying is profitable and how to copy most effectively. To address these questions, we organized a computer tournament in which entrants submitted strategies specifying how to use social learning and its asocial alternative (for example, trial-and-error learning) to acquire adaptive behavior in a complex environment. Most current theory predicts the emergence of mixed strategies that rely on some combination of the two types of learning. In the tournament, however, strategies that relied heavily on social learning were found to be remarkably successful, even when asocial information was no more costly than social information. Social learning proved advantageous because individuals frequently demonstrated the highest-payoff behavior in their repertoire, inadvertently filtering information for copiers. The winning strategy (discountmachine) relied nearly exclusively on social learning and weighted information according to the time since acquisition.

Human culture is widely thought to underlie the extraordinary demographic success of our species, manifest in virtually every terrestrial habitat (*1*, *2*). Cultural processes facilitate the spread of adaptive knowledge, accumulated over generations, allowing individuals to acquire vital life skills. One of the foundations of culture is social learning, learning influenced by observation or interaction with other individuals (*3*), which occurs widely in various forms across the animal kingdom (*4*). Yet it remains something of a mystery why individuals profit by copying others and how best to do this.

At first sight, social learning appears advantageous because it allows individuals to avoid the costs, in terms of effort and risk, of trial-and-error learning. However, social learning can also cost time and effort, and theoretical work reveals that it can be error-prone, leading individuals to acquire inappropriate or outdated information in nonuniform and changing environments (*5*–*11*). Current theory suggests that to avoid these errors individuals should be selective in when and how they use social learning, so as to balance its advantages against the risks inherent in its indiscriminate use (*9*). Accordingly, natural selection is expected to have favored social learning strategies, psychological mechanisms that specify when individuals copy and from whom they learn (*12*, *13*).

These issues lie at the interface of multiple academic fields, spanning the sciences, social sciences and humanities, from artificial intelligence to zoology (*5*, *14*–*18*). Formal theoretical analyses [e.g., (*2*, *5*–*9*, *11*–*13*, *19*)] and experimental studies (*20*, *21*) have explored a small number of plausible learning strategies. Although insightful, this work has focused on simple rules that can be studied with analytical methods and can only explore a tiny subset of strategies. For a more authoritative understanding of when to acquire information from others and how best to do so, the relative merits of a large number of alternative social learning strategies must be assessed. To address this, we organized a computer tournament in which strategies competed in a complex and changing simulation environment. €10,000 was offered as first prize. The organization of similar tournaments by Robert Axelrod in the 1980s proved an extremely effective means for

[1]Centre for Social Learning and Cognitive Evolution, School of Biology, University of St. Andrews, Queen's Terrace, St. Andrews, Fife KY16 9TS, UK. [2]Department of Anthropology, University of California, Los Angeles, CA 90095, USA. [3]Department of Mathematics and Statistics, Queen's University, Jeffery Hall, University Avenue, Kingston, Ontario K7L 3N6, Canada. [4]Department of Zoology, Stockholm University, 11691 Stockholm, Sweden. [5]Centre for the Study of Cultural Evolution, Stockholm University, 11691 Stockholm, Sweden. [6]School of Education, Culture, and Communication, Mälardalen University, 72123 Västerås, Sweden. [7]Department of Biological Sciences, Stanford University, Stanford, CA 94305, USA. [8]Department of Psychology, University of Bologna, 40127 Bologna, Italy. [9]Centre for Neuroscience Studies, Queen's University, 18 Stuart Street, Kingston, Ontario K7L 3N6, Canada.

*To whom correspondence should be addressed. E-mail: ler4@st-andrews.ac.uk (L.R.); knl1@st-andrews.ac.uk (K.N.L.)

investigating the evolution of cooperation and is widely credited with invigorating that field (*22*).

The tournament. The simulated environment for our tournament was a "multiarmed bandit" (*18*), analogous to the "one-armed bandit" slot machine but with multiple "arms." In the tournament, the bandit had 100 arms, each representing a different behavior and each with a distinct payoff drawn independently from an exponential distribution. Furthermore, we posited a temporally varying environment realized by changing the payoffs with a probability, p_c, per behavior per simulation round, with new payoffs drawn from the same distribution. The possibility of acquiring outdated information is seen as a crucial weakness of social learning [e.g., (*6*)].

Entered strategies had to specify how individual agents in a finite population choose between three possible moves in each round, namely Innovate, Observe, and Exploit. Innovate represented asocial learning, that is, individual learning stemming solely through direct interaction with the environment, for example, through trial and error. An Innovate move always returned accurate information about the payoff of a randomly selected behavior previously unknown to the agent. Observe represented any form of social learning or copying through which an agent could acquire a behavior performed by another individual, whether by observation of or interaction with that individual (*3*). An Observe move returned noisy information about the behavior and payoff currently being demonstrated in the population by one or more other agents playing Exploit. Playing Observe could return no behavior if none was demonstrated or if a behavior that was already in the agent's repertoire is observed and always occurred with error, such that the wrong behavior or wrong payoff could be acquired. The probabilities of these errors occurring and the number of agents observed were parameters we varied. Lastly, Exploit represented the performance of a behavior from the agent's repertoire, equivalent to pulling one of the multiarmed bandit's levers. Agents could only obtain a payoff by playing Exploit.

Evolutionary dynamics were realized by a death-birth process (*23*). Agents died with a constant probability of 1/50 per round and were replaced by the offspring of another agent. The probability that an agent was chosen to reproduce was proportional to its mean lifetime payoff, calculated as its summed payoff from playing Exploit divided by the number of simulation rounds that it had been alive. The obtained payoffs thus directly affected an agent's fitness. Offspring inherited their parent's strategy unless mutation occurred, in which case the offspring was given a strategy randomly chosen from the others playing in that simulation. We recorded the average frequency of each strategy in the population over the last 2500 rounds of each 10,000-round simulation and gave each strategy a score that was the mean of these values over the simulations in which it participated.

Axelrod's cooperation tournaments were based on a widely accepted theoretical framework for the study of cooperation: the Prisoner's Dilemma. Although there is no such currently established framework for social learning research, multiarmed bandits have been widely deployed to study learning across biology, economics, artificial intelligence research, and computer science [e.g., (*18*, *24*–*28*)] because they mimic a common problem faced by individuals who must make decisions about how to allocate their time in order to maximize their payoffs. Multiarmed bandits capture the essence of many difficult problems in the real world, for instance, where there are many possible actions, only a few of which yield a high payoff; where it is possible to learn asocially or through observation of others; where copying error occurs; and where the environment changes. When the payoffs of a multiarmed bandit change over time as in our tournament, the bandit is termed "restless," and the framework has the advantage of proving extremely difficult, perhaps impossible, to optimize analytically [e.g., (*29*)]. Thus, we could be confident that our tournament would be a genuine challenge for all entrants.

In all other respects, we attempted to keep the model structure as simple as possible to maintain breadth of applicability and ease of understanding and to attract the maximum number of participants. We balanced this simplicity with the inclusion of three features that we considered critical, namely, individual memories (to facilitate learning); a degree of error associated with social learning (the existence of which nearly all the current literature agrees on); and replicator dynamics with mutation, to allow an evolutionary process. We used a common currency for costs (time) and made each possible move cost the same to

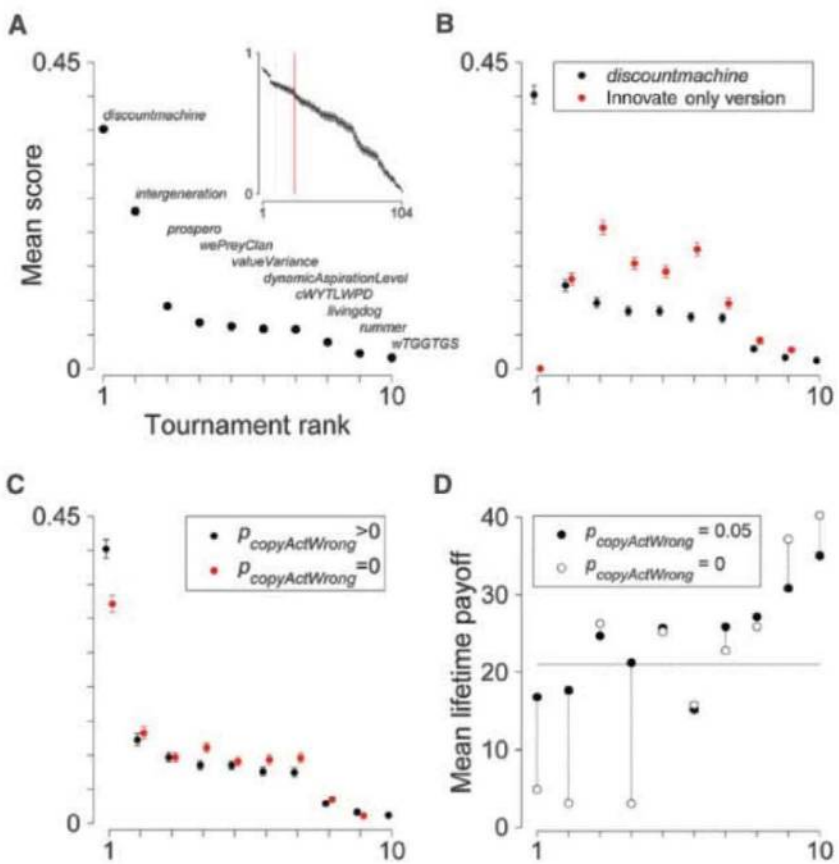

Fig. 1. Performance of entered strategies. (**A**) Ranked overall strategy scores in the final stage of the tournament (cWYTLWPD indicates copyWhenYoungThenLearnWhen-PayoffsDrop; wTGGTGS, whenTheGoingGetsToughGetScrounging). Scores are averaged over all final stage simulations. (Inset) Scores for all 104 entered strategies. Dotted black line indicates the 10 highest scoring strategies; solid red line indicates the 24 strategies entered into further pairwise conditions. Error bars are ± SEM but mostly not visible because all SEMs < 0.004. (**B**) Ranked scores from those final-stage simulations in which conditions were chosen at random (*33*), and under the same conditions but with the tournament winner, discountmachine, recoded to learn only with Innovate and never Observe (red). (**C**) As in (B) but comparing original results with $p_{copyActWrong}$ fixed at 0 (red). (**D**) Average individual fitness, measured as mean lifetime payoff, in populations containing only single strategies for each of the final-stage contestants, ranked by tournament placing. Data are average values from the last quarter of single simulations, which were run under the same conditions as the first stage of the tournament and also under the same conditions except with $p_{copyActWrong} = 0$. The horizontal dashed line represents the mean lifetime payoff of individuals when all strategies are played together under the same conditions. Strategies relying exclusively on social learning are those ranked 1, 2, and 4.

minimize structural assumptions about learning costs. The agents in our simulations could not identify or communicate directly with each other, an assumption that precluded the deployment of some model-based strategies present in the cultural evolution literature [e.g., prestige bias (*30*)]. Nonetheless, we reasoned that the simplicity, accessibility, and generality of the proposed tournament structure outweighed the benefits of further complexity.

Analyses. We received 104 entries, most, although not all (*31*), from academics across a wide range of disciplines and from all over the world. The tournament was run in two stages. Strategies first competed in pairwise round-robin contests, taking turns to invade or to resist invasion by another strategy under a single set of conditions (*32*). The 10 best performers progressed to a second stage, where all 10 strategies competed simultaneously in melee contests over a range of simulation conditions (*33*). Scores in the first stage ranged from 0.02 to 0.89 (with a theoretical maximum of 1), indicating considerable variation in strategy effectiveness (Fig. 1A).

Statistical analysis indicates that much of this variation is explained by the extent to which strategies used social learning, more social learning being associated with higher payoffs. We examined the factors that made strategies successful by using linear multiple regression and model selection by using Akaike's information criterion (AIC) (*33*). The best-fit model contained five predictors (Table 1). Two predictors had effect sizes more than twice the magnitude of the others: the proportion of those learning moves that were Observe and the variance in the number of rounds before a strategy first played Exploit. The proportion of learning moves dedicated to Observe had a strong positive effect on a strategy's score (Fig. 2A). Although Innovate cost no more than Observe, the best strategies relied almost entirely on social learning; that is, when learning, they almost exclusively chose Observe rather than Innovate. The proportion of moves that involved learning of any kind had a negative effect, indicating that it was detrimental to invest too much time in learning because payoffs came only through Exploit. The data reveal an unexpectedly low optimum proportion of time spent learning (Fig. 2C).

The timing of (either form of) learning also emerged as a crucial factor. Strategies with a high variance in the number of rounds spent learning before the agent first played Exploit, caused by occasionally waiting too long before beginning to exploit, tended to do poorly (Fig. 2B). Conversely, strategies that engaged in longer bouts of exploiting between learning moves tended to do significantly better (Fig. 2D). Successful strategies were able to target their learning to coincide with periods when average population payoffs dropped, indicating a change in the environment that had rendered a behavior less profitable (Fig. 2E). This pattern was observable statistically as the lagged correlation between the time series of average payoff and the proportion of learning moves in the population. We calculated Pearson correlation coefficients between the average payoff at simulation round t and the proportion of learning moves at round $t + \Delta$, with $0 < \Delta < 10{,}000$. Accurate targeting of learning to periods where payoffs are dropping produces large negative correlation coefficients for small Δ. We compared the correlations for populations containing the 10 strategies that progressed to the final stage with the correlations from simulations run with strategies ranked 78 to 88 in the first stage of the tournament (i.e., markedly less-successful strategies). For the final-stage strategies, the strongest negative correlations were always found with lags of less than three ($\Delta < 3$) and were significantly stronger than the strongest correlations found for the less-successful strategies [two-sample t test, $P < 0.0001$ (fig. S9)]. Successful strategies

Table 1. Parameters of the AIC best-fit model predicting strategy scores in the first, pairwise, tournament stage. Adjusted $R^2 = 0.76$. Dash entry indicates not applicable.

Predictor	Effect size (β weight)	β	SE	t	$p(>\|t\|)$
(Intercept)	–	0.32	0.06	5.43	<0.0001
Proportion of learning that is Observe	0.42	0.43	0.06	7.15	<0.0001
Variance in rounds to first Exploit*	−0.42	−0.06	0.01	−6.62	<0.0001
Proportion of learning moves	−0.17	−0.34	0.12	−2.79	0.0063
Average rounds between learning moves	0.16	0.01	<0.01	3.09	0.0026
Estimate p_c? (yes = 1, no = 0)	−0.07	−0.04	0.03	−1.47	0.1452

*We used the natural log of this predictor to give a better linear relationship.

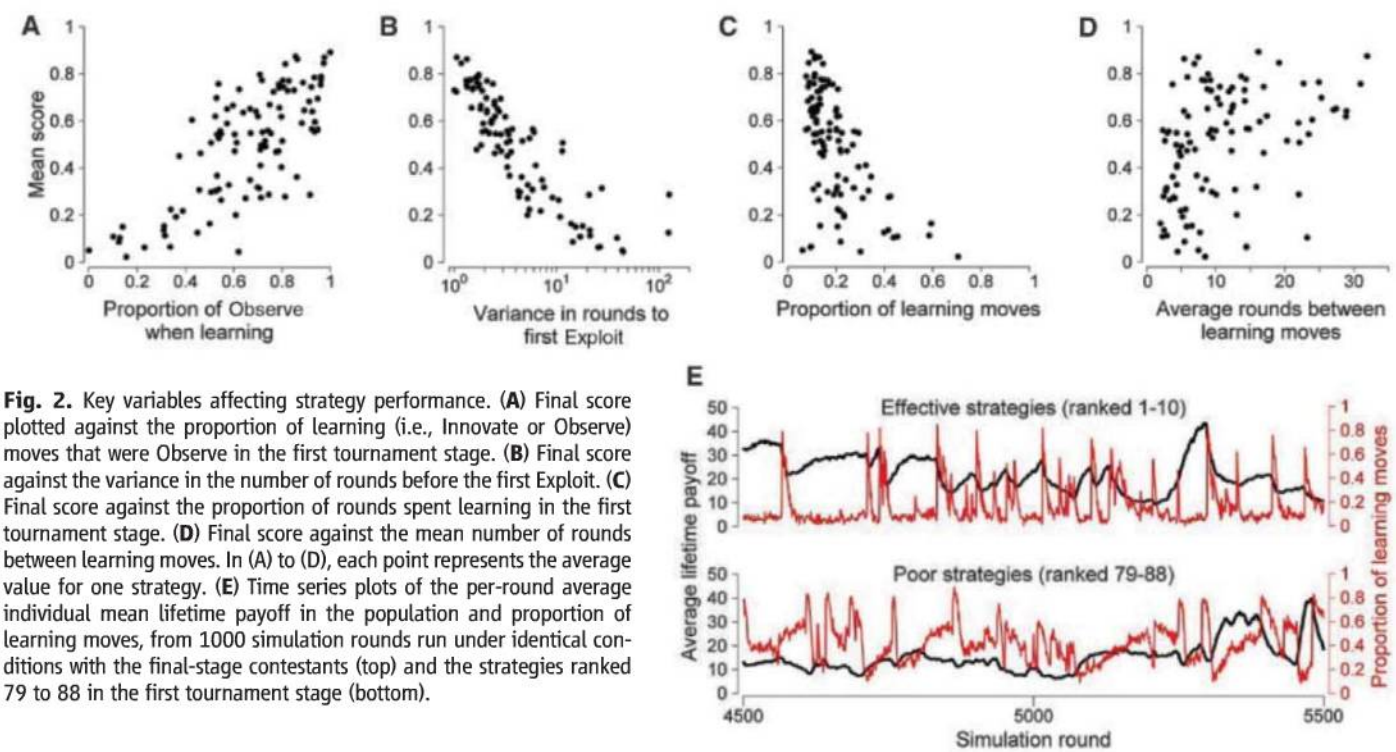

Fig. 2. Key variables affecting strategy performance. (**A**) Final score plotted against the proportion of learning (i.e., Innovate or Observe) moves that were Observe in the first tournament stage. (**B**) Final score against the variance in the number of rounds before the first Exploit. (**C**) Final score against the proportion of rounds spent learning in the first tournament stage. (**D**) Final score against the mean number of rounds between learning moves. In (A) to (D), each point represents the average value for one strategy. (**E**) Time series plots of the per-round average individual mean lifetime payoff in the population and proportion of learning moves, from 1000 simulation rounds run under identical conditions with the final-stage contestants (top) and the strategies ranked 79 to 88 in the first tournament stage (bottom).

targeted learning to periods when it was likely to be most valuable (i.e., when the environment changed) but otherwise minimized learning, allowing them both to improve their payoffs through learning and to maintain high rates of exploiting (Table 1). The issue of when to break off exploiting current knowledge in order to invest in further knowledge gain, the exploitation/exploration tradeoff, had not been incorporated into previous theory in this field, and our tournament introduces this dimension into the domain of understanding social learning.

The strategy discountmachine (*34*) emerged as a convincing winner (Fig. 1A) in the second stage of the tournament, which pitted the 10 best performers in the first stage against each other in simultaneous competition under a range of conditions (it was also the winner of the pairwise phase). Strikingly, both discountmachine and the runner-up, intergeneration, relied nearly exclusively on Observe as their means to learn (Fig. 3, C and D), and at least 50% of the learning of all of the second-stage strategies was Observe. Although all second-stage strategies increased their amount of learning as the rate of environmental change increased, the best performers capped the level of learning to a maximum to maintain payoffs (Fig. 3A). The winning strategy stood out by spreading learning more evenly across agent life spans than any other second-stage strategy (Fig. 3B). It did this by, uniquely among the finalists, using a proxy of geometric discounting to estimate expected future payoffs from either learning or playing Exploit.

Winning strategies also relied more heavily on recently acquired than older information. The top two strategies shared the following expression for estimating the expected payoff ($w_{expected}$) of a known behavior:

$$w_{exp} = w(1 - p_{est})^i + \overline{w}_{est}\left(1 - (1 - p_{est})^i\right) \quad (1)$$

where w is the current payoff held in the agent's memory and acquired i rounds ago, $\overline{w}_{est}$ is the estimated mean payoff for all behavior, and p_{est} is an estimate of p_c, the probability of payoff change. This expression weighs expected payoffs increasingly toward an estimated mean as the time since information was last obtained increases. Given the uncertain and potentially conflicting nature of information obtained through social learning, the winning strategy used a further weighing based on its estimate of p_c, discounting older social information more severely in more variable environments than in relatively constant ones. No other strategies in the melee round evaluated payoffs in this way.

In the melee round, simulations were run to explore the effects of varying the rate of environmental change (p_c); the probability and scale of errors associated with social learning; and the relative costs of the two forms of learning, the last achieved by increasing the number of other agents sampled when playing Observe (social learning being cheap when multiple individuals are observed). We found the tournament results to be unexpectedly robust to variation in these factors (Fig. 4). The first- and second-place strategies switched rank in some conditions, namely when the environment was more stable (Fig. 4A) and when social learning was cheap relative to asocial learning [i.e., the number of agents sampled by Observe was high (Fig. 4D)]. Increasing the probability and the magnitude of errors associated with social learning made nearly no difference to the strategy rankings (Fig. 4, B and C); even at extreme values, strategies heavily reliant on social learning thrived (fig. S11). This implies that social learning is of widespread utility even when it provides no in-

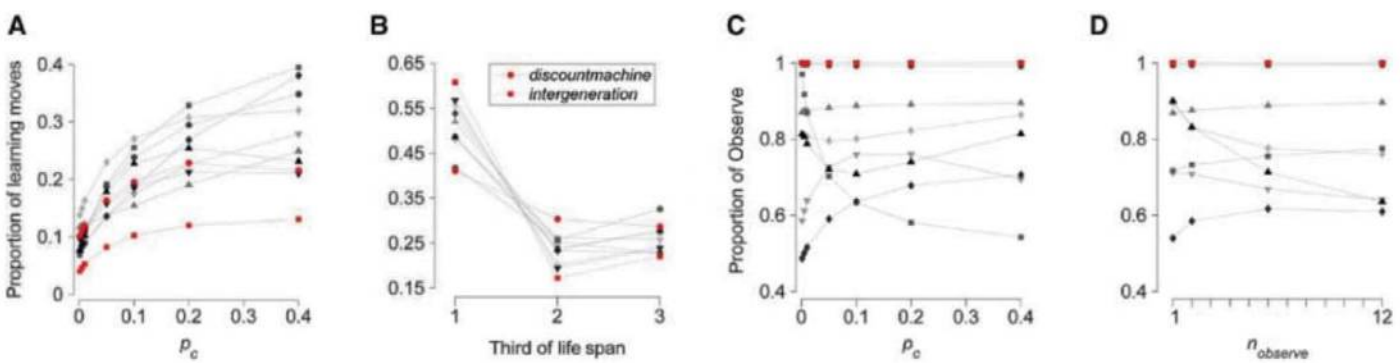

Fig. 3. Why the winner won. Error bars are ± SEM but mostly not visible because all SEMs < 0.003. (**A**) Proportion and (**B**) timing of learning moves in the final tournament stage. First and second place strategies are highlighted; the rank of the other strategies is indicated by shading, with darker shading indicating higher rank. (**C** and **D**) Variation in the proportion of learning moves that were Observe with (C) variation in the rate of environmental change (p_c) and (D) the number of agents sampled when playing Observe ($n_{observe}$), in the final tournament stage.

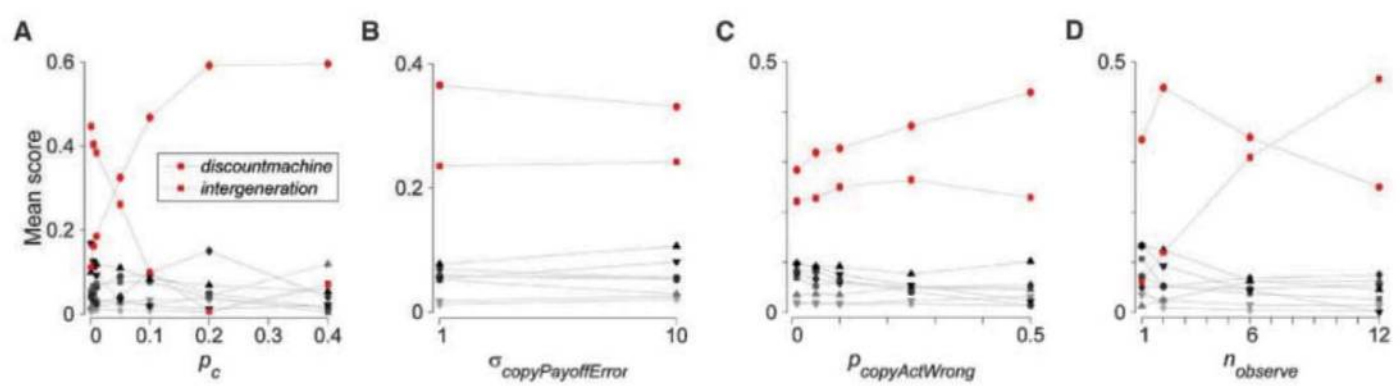

Fig. 4. Social learning dominates irrespective of cost across a broad range of conditions. Plots show mean strategy scores (±variance) across systematic melee conditions with respect to (**A**) variation in the rate of environmental change (p_c), (**B**) $\sigma_{copyPayoffError}$, the standard deviation of a normally distributed error applied to payoffs returned by Observe, (**C**) $p_{copyActWrong}$, the probability that Observe returned a behavior selected, at random from those not actually observed, and (**D**) the number of other agents sampled when playing Observe ($n_{observe}$). First and second place strategies are highlighted; the rank of the other strategies is indicated by shading with darker shading indicating higher rank. Error bars are ± SEM but mostly not visible because all SEMs < 0.01.

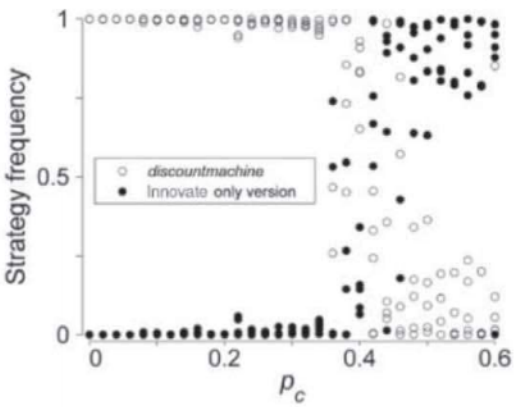

Fig. 5. Results of a series of simulations in which the tournament winner played against a version of itself altered to learn only by Innovate. The rate of environmental change (p_c) was systematically varied. Five simulations were run at each level of p_c. Other parameters were fixed at $n_{observe} = 1$, $p_{copyActWrong} = 0.05$, and $\sigma_{payoffError} = 1$.

formation about payoffs. Nor does this utility rest on our assumption that copying errors can introduce new behaviors (fig. S13). These are surprising results, given that the error-prone nature of social learning is widely thought to be a weakness of this form of learning, whereas the ability to copy multiple models rapidly or preferentially copy high-payoff behavior are regarded as strengths (*1*). Strategies relying heavily on social learning did best irrespective of the number of individuals sampled by Observe (Fig. 4D). These findings are particularly unexpected in the light of previous theoretical analyses (*5*–*8*, *10*, *11*, *13*), virtually all of which have posited some structural cost to asocial learning and errors in social learning.

Previous theory also suggests that reliance on social learning should not necessarily raise the average fitness of individuals in a population (*6*, *7*, *10*) and may even depress it (*35*). However, this was not the case for the strategies successful enough to make the second stage; in this second round, average individual fitness in mixed-strategy populations was positively correlated with the proportion of learning in the population that was social [$r = 0.16$, $P = 0.02$ (fig. S9)]. In contrast, for poorly performing strategies the relationship between average individual fitness and the rate of social learning was strongly negative ($r = -0.71$, $P < 0.001$; fig. S9). This highlights the importance of the strategic use of social learning in raising the average fitness in a population (*5*, *12*, *19*).

Strategies that did well were not, however, those that maximized average individual fitness when fixed in a population. Instead, we found a strong inverse relationship between the mean fitness of individuals in populations containing only one strategy and that strategy's performance in the tournament (Fig. 1D). Furthermore, the mean lifetime payoff in the population when all strategies competed together under the same conditions was lower than the levels achieved by lower-ranking strategies when playing alone. This illustrates the parasitic effect of strategies that rely heavily on Observe (e.g., discountmachine, intergeneration, wePreyClan, and dynamicAspirationLevel; ranked 1, 2, 4, and 6; all played Observe on at least 95% of learning moves). From this we can conclude that strategies using a mixture of social and asocial learning are vulnerable to invasion by those using social learning alone, which may result in a population with lower mean fitness. An established rule in ecology specifies that, among competitors for a resource, the dominant competitor will be the species that can persist at the lowest resource level (*36*). Recent theory suggests an equivalent rule may apply when alternative social learning strategies compete in a population: The strategy that eventually dominates will be the one that can persist with the lowest frequency of asocial learning (*13*). Our findings are consistent with this hypothesis.

Discussion. The most important outcome of the tournament is the remarkable success of strategies that rely heavily on copying when learning in spite of the absence of a structural cost to asocial learning, an observation evocative of human culture. This outcome was not anticipated by the tournament organizers, nor by the committee of experts established to oversee the tournament, nor, judging by the high variance in reliance on social learning (Fig. 2A), by most of the tournament entrants. Although the outcome is in some respects consistent with models that used simpler environmental conditions and in which individual learning is inherently costly relative to social learning (*5*), in our tournament the environment was complex and there was no inherent fitness cost to asocial learning. Indeed, there turned out to be a considerable cost to social learning because it failed to introduce new behavior into an agent's repertoire in 53% of all the Observe moves in the first tournament phase, overwhelmingly because agents observed behaviors they already knew. Nonetheless, social learning proved advantageous because other agents were rational in demonstrating the behavior in their repertoire with the highest payoff, thereby making adaptive information available for others to copy. This is confirmed by modified simulations wherein social learners could not benefit from this filtering process and in which social learning performed poorly (fig. S12). Under any random payoff distribution, if one observes an agent using the best of several behaviors that it knows about, then the expected payoff of this behavior is much higher than the average payoff of all behaviors, which is the expected return for innovating. Previous theory has proposed that individuals should critically evaluate which form of learning to adopt in order to ensure that social learning is only used adaptively (*11*), but a conclusion from our tournament is that this may not be necessary. Provided the copied individuals themselves have selected the best behavior to perform from at least two possible options, social learning will be adaptive. We suspect that this is the reason why copying is widespread in the animal kingdom.

That social learning was critical to the success of the winning strategy is shown by the results of running the random conditions portion of the second tournament stage with a version of discountmachine recoded to learn only by Innovate: it placed last (Fig. 1B). We also found that discountmachine dominated its recoded cousin across a large portion of the plausible parameters space with respect to environmental change (Fig. 5), with payoffs needing to change with 50% probability per round before the Innovate-only version could gain a foothold. This is another way that our tournament challenges existing theory, which predicts that evolution will inevitably lead to a stable equilibrium where both social and asocial learning persist in a population [e.g., (*6*)].

It is important to note that, although our tournament may offer greater realism than past analytical theory, the simulation framework remains a simplification of the real world where, for instance, model-based biases and direct interactions between individuals (*15*) operate. It remains to be established to what extent our results will hold if these are introduced in future tournaments, where the specific strategies that prospered here may not do so well. Nonetheless, the basic generality of the multiarmed bandit problem we posed lends confidence that the insights derived from the tournament may be quite general.

The tournament also draws attention to the importance of social learning errors as a source of adaptive behavioral diversity. In our tournament, there was a probability, $p_{copyActWrong}$, that a social learner acquired a randomly selected behavior rather than the observed behavior. Modeling social learning errors in this way means new behavior can enter the population without explicit innovation. The importance of these errors is illustrated by the fact that strategies relying exclusively on social learning were unable to maintain high individual fitness when $p_{copyActWrong} = 0$ (Fig. 1D). This does not mean that the success of the winning strategy depended on the condition $p_{copyActWrong} > 0$; in the presence of other strategies providing the necessary innovations, discountmachine and intergeneration maintain their respective first and second places when $p_{copyActWrong} = 0$ (Fig. 1C). Other models have highlighted copying errors as potentially important in human cultural evolution (*37*), but the extent to which adaptive innovations actually come about through such

errors is an important empirical question ripe for investigation.

The ability to evaluate current information on the basis of its age and to judge how valuable that information might be in the future, given knowledge of rates of environmental change, is also highlighted by the tournament. There is limited empirical evidence that animals are able to discount information on the basis of the time since it was acquired (*38*), but little doubt that humans are capable of such computation. Our tournament suggests that the adaptive use of social learning could be critically linked to such cognitive abilities. There are obvious parallels with the largely open question of mental time travel, the ability to project current conditions into the future, in nonhumans (*39*), raising the hypothesis that this cognitive ability could be one factor behind the gulf between human culture and any nonhuman counterpart. A critical next step will be to evaluate experimentally to what extent human behavior mirrors that of the tournament strategies [e.g., (*40*)]. By drawing attention to the importance of adaptive filtering by the copied individual and temporal discounting by the copier, the tournament helps to explain both why social learning is common in nature and why human beings happen to be so good at it.

References and Notes

1. P. J. Richerson, R. Boyd, *Not by Genes Alone* (Univ. of Chicago Press, Chicago, 2005).
2. L. L. Cavalli-Sforza, M. W. Feldman, *Cultural Transmission and Evolution: A Quantitative Approach* (Princeton Univ. Press, Princeton, NJ, 1981).
3. C. M. Heyes, *Biol. Rev. Camb. Philos. Soc.* **69**, 207 (1994).
4. W. Hoppitt, K. N. Laland, *Adv. Stud. Behav.* **38**, 105 (2008).
5. R. Boyd, P. J. Richerson, *Culture and the Evolutionary Process* (Univ. of Chicago Press, Chicago, 1985).
6. A. Rogers, *Am. Anthropol.* **90**, 819 (1988).
7. M. W. Feldman, K. Aoki, J. Kumm, *Anthropol. Sci.* **104**, 209 (1996).
8. T. Kameda, D. Nakanishi, *Evol. Hum. Behav.* **23**, 373 (2002).
9. L.-A. Giraldeau, T. J. Valone, J. J. Templeton, *Philos. Trans. R. Soc. London Ser. B* **357**, 1559 (2002).
10. J. Y. Wakano, K. Aoki, M. W. Feldman, *Theor. Popul. Biol.* **66**, 249 (2004).
11. M. Enquist, K. Eriksson, S. Ghirlanda, *Am. Anthropol.* **109**, 727 (2007).
12. K. N. Laland, *Learn. Behav.* **32**, 4 (2004).
13. J. Kendal, L.-A. Giraldeau, K. Laland, *J. Theor. Biol.* **260**, 210 (2009).
14. E. Danchin, L.-A. Giraldeau, T. J. Valone, R. H. Wagner, *Science* **305**, 487 (2004).
15. J. Apesteguia, S. Huck, J. Oechssler, *J. Econ. Theory* **136**, 217 (2007).
16. H. Whitehead, L. Rendell, R. W. Osborne, B. Würsig, *Biol. Conserv.* **120**, 427 (2004).
17. K. Dautenhahn, C. L. Nehaniv, Eds., *Imitation in Animals and Artifacts* (MIT Press, London, 2002).
18. K. H. Schlag, *J. Econ. Theory* **78**, 130 (1998).
19. J. Henrich, R. McElreath, *Evol. Anthropol.* **12**, 123 (2003).
20. J. R. Kendal, L. Rendell, T. W. Pike, K. N. Laland, *Behav. Ecol.* **20**, 238 (2009).
21. B. G. Galef Jr., *Adv. Stud. Behav.* **39**, 117 (2009).
22. R. Axelrod, W. D. Hamilton, *Science* **211**, 1390 (1981).
23. M. A. Nowak, *Evolutionary Dynamics: Exploring the Equations of Life* (Harvard Univ. Press, Cambridge, MA, 2006).
24. D. E. Koulouriotis, A. Xanthopoulos, *Appl. Math. Comput.* **196**, 913 (2008).
25. R. Gross *et al.*, *J. R. Soc. Interface* **5**, 1193 (2008).
26. D. Bergemann, J. Valimaki, *Econometrica* **64**, 1125 (1996).
27. J. Niño-Mora, *Top (Madr.)* **15**, 161 (2007).
28. P. Auer, N. Cesa-Bianchi, P. Fischer, *Mach. Learn.* **47**, 235 (2002).
29. C. H. Papadimitriou, J. N. Tsitsiklis, *Math. Oper. Res.* **24**, 293 (1999).
30. J. Henrich, F. J. Gil-White, *Evol. Hum. Behav.* **22**, 165 (2001).
31. Three strategies were entered by high school students, and one of these (whenTheGoingGetsToughGetScrounging, submitted by Ralph Barton and Joshua Borin of Westminster School in the United Kingdom) achieved notable success by ranking 10th overall.
32. These conditions were $p_c = 0.01$, $n_{observe} = 1$ (the number of agents sampled when playing Observe), $p_{copyActWrong} = 0.05$ (the probability that Observe returned a behavior selected, at random, from those not actually observed), $\sigma_{payoffError} = 1$ (the standard deviation of a normally distributed error applied to observed payoffs); and we also ran more pairwise contests under several other conditions with the top 24 performing strategies to ensure that progression to the second stage was not solely dependent on these particular parameter values.
33. A full description of the simulation procedures and statistical analyses is available on *Science* Online.
34. This strategy was entered by Daniel Cownden and Timothy Lillicrap, who were subsequently invited to be authors on this paper.
35. L. Rendell, L. Fogarty, K. N. Laland, *Evolution* **64**, 534 (2010).
36. D. Tilman, *Resource Competition and Community Structure* (Princeton Univ. Press, Princeton, NJ, 1982).
37. J. Henrich, R. Boyd, *J. Cogn. Cult.* **2**, 87 (2002).
38. Y. van Bergen, I. Coolen, K. N. Laland, *Proc. Biol. Sci.* **271**, 957 (2004).
39. T. Suddendorf, M. C. Corballis, *Behav. Brain Sci.* **30**, 299, discussion 313 (2007).
40. M. J. Salganik, P. S. Dodds, D. J. Watts, *Science* **311**, 854 (2006).

41. The authors acknowledge the use of the U.K. National Grid Service (www.grid-support.ac.uk) in carrying out this work. We thank all those who entered the tournament for contributing to its success. We are also very grateful to R. Axelrod for providing advice and support with regard to the tournament design. This research was supported by the CULTAPTATION project (European Commission contract FP6–2004-NESTPATH-043434).

Supporting Online Material

www.sciencemag.org/cgi/content/full/328/5975/208/DC1
Materials and Methods
SOM Text
Figs. S1 to S13
Tables S1 to S5
References
Appendices A to C

16 November 2009; accepted 22 February 2010
10.1126/science.1184719

Two-Dimensional Phonon Transport in Supported Graphene

Jae Hun Seol,[1] Insun Jo,[2] Arden L. Moore,[1] Lucas Lindsay,[3,4] Zachary H. Aitken,[5] Michael T. Pettes,[1] Xuesong Li,[1,6] Zhen Yao,[2] Rui Huang,[5] David Broido,[3] Natalio Mingo,[7] Rodney S. Ruoff,[1,6] Li Shi[1,6]*

The reported thermal conductivity (κ) of suspended graphene, 3000 to 5000 watts per meter per kelvin, exceeds that of diamond and graphite. Thus, graphene can be useful in solving heat dissipation problems such as those in nanoelectronics. However, contact with a substrate could affect the thermal transport properties of graphene. Here, we show experimentally that κ of monolayer graphene exfoliated on a silicon dioxide support is still as high as about 600 watts per meter per kelvin near room temperature, exceeding those of metals such as copper. It is lower than that of suspended graphene because of phonons leaking across the graphene-support interface and strong interface-scattering of flexural modes, which make a large contribution to κ in suspended graphene according to a theoretical calculation.

Since graphene was first exfoliated from graphite and studied on dielectric substrates in 2004 (*1*), the monatomic layer of carbon atoms has attracted great interest for electronic applications because of superior charge mobility (*2*) and mechanical strength (*3*), as well as its compatibility with existing planar silicon devices. Other carbon allotropes, including diamond (*4*), graphite (*5*), and carbon nanotubes (CNTs) (*6*–*8*), have the highest thermal conductivity (κ) values reported because the strong bonding of the light carbon atoms results in a large phonon contribution to κ despite a much smaller electronic component. For similar reasons, graphene is

[1]Department of Mechanical Engineering, The University of Texas at Austin, Austin, TX 78712, USA. [2]Department of Physics, The University of Texas at Austin, Austin, TX 78712, USA. [3]Department of Physics, Boston College, Chestnut Hill, MA 02467, USA. [4]Department of Physics, Computer Science, and Engineering, Christopher Newport University, Newport News, VA 23606, USA. [5]Department of Aerospace Engineering and Engineering Mechanics, The University of Texas at Austin, Austin, TX 78712, USA. [6]Texas Materials Institute, The University of Texas at Austin, Austin, TX 78712, USA. [7]Laboratoire d'Innovation pour les Technologies des Energies Nouvelles et les Nanomatériaux, Commissariat à l'Énergie Atomique Grenoble, 17 rue des Martyrs, 38054 Grenoble, France.

*To whom correspondence should be addressed. E-mail: lishi@mail.utexas.edu

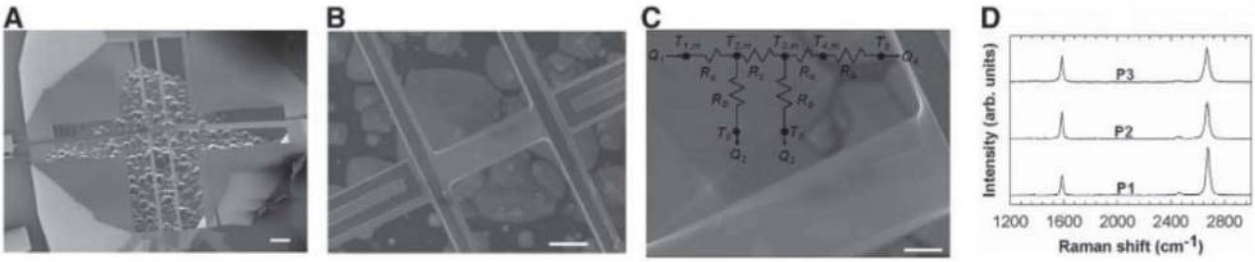

Fig. 1. Graphene sample G2. (**A** to **C**) SEM images of the suspended device, the central beam, and the folded edge of the SLG ribbon near the right electrode. The inset in (C) is a thermal circuit of the measurement device, where R_o is the thermal resistance of the SiO_2 joint between two adjacent RT lines. The scale bar is 10, 3, and 1 μm in (A), (B), and (C), respectively. (**D**) Raman spectra obtained from G2 immediately after the thermal measurement. The spectra (e.g., P1) obtained near the left end of the SLG indicates a monolayer sample, whereas those (such as P2 and P3) taken at the center and near the right electrode show a broadened 2D peak (centered at 2700 cm^{-1}) and a decreased 2D peak to G peak (centered at 1580 cm^{-1}) ratio because the folded-edge region of the SLG has a signal similar to that of bilayer graphene.

expected to possess a much higher κ than the silicon active layers and copper interconnects in current-generation electronic devices. This potential enhancement may provide a solution to the increasingly severe heat dissipation problem in nanoelectronics, which is caused by increased power density as well as reduced κ of electronic materials with decreasing feature sizes (*9*, *10*).

Although electronic transport in graphene has been investigated extensively, there have been few studies on the thermal transport because of experimental challenges. Recently, the room-temperature κ of a suspended single-layer graphene (SLG) flake has been reported from a Raman measurement (*11*). The obtained values, 3000 to 5000 W m^{-1} K^{-1}, exceed those of diamond (*4*) and graphite (*5*). However, because of the limited temperature (*T*) sensitivity of the Raman technique, this study has not yielded the $\kappa - T$ relation that is important for understanding the intriguing two-dimensional (2D) behavior of phonons in SLG. Furthermore, SLG is usually supported on a dielectric substrate for device applications. The charge mobility in SLG supported on silicon dioxide (SiO_2) is suppressed by about 10 times compared with clean suspended SLG because of scattering by substrate phonons and impurities (*12*). The effect of substrate interaction on thermal transport, however, has not been elucidated so far.

Here, we report thermal transport measurements on SLG supported on amorphous SiO_2, which represents the most commonly used device configuration. Despite phonon-substrate scattering, we find that the room-temperature κ of the supported SLG approaches about 600 W m^{-1} K^{-1}, considerably higher than the κ values of common thin-film electronic materials (*9*, *10*). In addition, using full quantum mechanical calculations of the three-phonon scattering processes, we find a large κ contribution from the flexural (ZA) modes in suspended SLG. The measured $\kappa - T$ relation can be explained by large suppression of the ZA contribution in the supported SLG.

We made thermal measurements on three SLG flakes exfoliated onto SiO_2 using the device shown in Fig. 1, A to C (*13*). The patterned SLG of 1.5 to 3.2 μm in width (*W*) and 9.5 to 12.5 μm in length (*L*) covers the surface of a ~300-nm-thick SiO_2 beam, the two ends of which are connected to four Au/Cr resistance thermometer (RT) lines on suspended SiO_2 beams. The two straight inner RT lines cover the two ends of the SLG, which does not contact the two outer U-shaped RT lines.

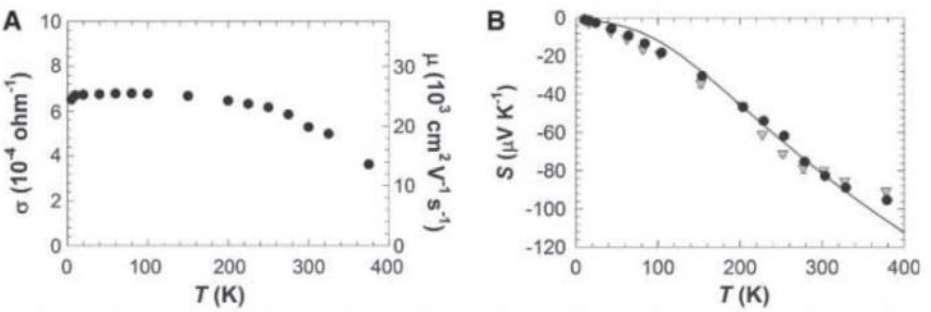

Fig. 2. (**A**) Measured two-probe electrical conductivity (σ) and extracted electron mobility (μ) of G2 as a function of temperature. (**B**) Measured Seebeck coefficients as a function of temperature for G1 (triangles) and G2 (circles). The error bars reported in this work include both bias and random uncertainties, the latter of which are determined based on three to nine measurements.

The SLG samples were characterized with Raman spectroscopy and scanning electron microscopy (SEM) (*13*). Sample 1 (G1) consists of a 3.2-μm-wide ribbon and a 1.5-μm-wide ribbon in parallel. Although a portion of one edge of the 2.4-μm-wide sample 2 (G2) is folded near one electrode (Fig. 1C), the two edges of the 2.4-μm-wide sample 3 (G3) appear to be straight. In addition, the obtained Raman spectra show that G1, G2 (Fig. 1D), and G3 are monolayers with no indication of the D band associated with defects (*14*).

The two-probe electrical resistance (*R*) at room temperature was measured to be 160, 7, and 5400 kilohm for G1, G2, and G3, respectively. The much lower two-probe *R* of G2 is indicative of smaller contact resistance and a cleaner electrode-graphene interface than for the other two samples. For G2 (Fig. 2A), the two-probe, 2D electrical conductivity, $\sigma \equiv L/WR$, shows a *T* dependence similar to that reported for oxide-supported SLG (*12*).

We measured the Seebeck coefficient (*S*) of the SLG by electrically heating one outer U-shaped RT line (RT 1). Because of a linear temperature profile between the midpoint and the ends of the other three RT lines (RT 2, 3, and 4 in order of increasing distance from RT 1, respectively), the highest temperature rise at the midpoint ($\Delta T_{j,m}$) is twice the average rise ($\overline{\Delta T_j}$) of each of the three lines (*13*), i.e., $\Delta T_{j,m} \equiv T_{j,m} - T_0 = 2\overline{\Delta T_j}; j = 2,3,4$, where T_0 is the substrate temperature. Using the thermal circuit in Fig. 1C and averaging the parabolic temperature profile of RT 1, we derive (*13*)

$$\Delta T_{1,m} = \frac{3}{2}\overline{\Delta T_1} - \frac{1}{2}(\overline{\Delta T_2} + \overline{\Delta T_3} + \overline{\Delta T_4}) \quad (1)$$

where $\overline{\Delta T_j}$ is obtained from the measured four-probe electrical resistance of each RT line. The measurement yields $S = V_{23}/(\Delta T_{2,m} - \Delta T_{3,m})$, where V_{23} is the thermovoltage between the two inner electrodes.

The obtained room-temperature *S* values of G1 and G2 (Fig. 2B) are –79.7 ± 0.6 and –82.7 ± 0.2 μV K^{-1}, respectively, which suggests that the Fermi energy (E_F) is in the conduction band. We fit the experimental $S-T$ curve using a theoretical model (*15*) for oxide-supported SLG where screened charged impurity scattering dominates electron transport. For G2, the best fit to the measured *S* is given by $E_F = 0.049$ eV (*13*). The electron concentration is obtained as $n = (E_F/\hbar v_F)^2/\pi = 1.7 \times 10^{11}$ cm^{-2}, where $\hbar$ is the reduced Planck's constant, and $v_F = 1 \times 10^6$ m/s is the Fermi velocity in SLG. Based on $\mu = \sigma/ne$, with *e* being the elemental charge, a μ value of

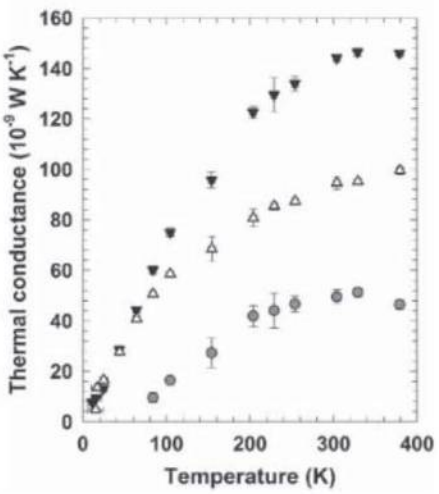

Fig. 3. Measured thermal conductance of G2 before (solid downward triangles) and after (unfilled upward triangles) the SLG was etched, with the difference being the contribution from the SLG (circles).

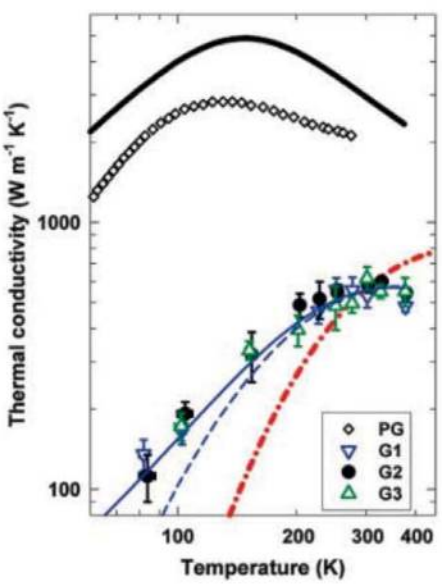

Fig. 4. Measured thermal conductivity of G1, G2, and G3 together with the highest reported values of PG (*5*), the BTE calculation results of suspended SLG (black solid line) and supported SLG with $K_{LATA} = 0$ and $K_{ZA} = 0.73$ N/m (blue solid line) or $K_{LATA} = K_{ZA} = 0.46$ N/m (blue dashed line), the RTA calculation result (red dashed-dotted line) for supported SLG with $K_{LATA} = 0.8$ N/m. Specular edges are assumed in the calculations. For supported SLG, $s = d = 30$ nm, and the calculation results are insensitive to edge specularity and can be reproduced with decreased d/s and increased K_{ZA} for the same K_{LATA}/K_{ZA}.

~20,000 cm^2/Vs (Fig. 2A) is obtained, comparable to the highest electron mobility values reported for oxide-supported SLG (*12*, *16*), thus suggesting similar sample quality.

For the κ measurement, the thermal resistance of each RT line including the SiO_2 beam is the same and was obtained as (*13*)

$$R_b = 2\frac{\Delta T_{1,m} + \Delta T_{2,m} + \Delta T_{3,m} + \Delta T_{4,m}}{Q} \quad (2)$$

where Q is the electrical heating in RT 1. The thermal resistance of the central beam is found from the thermal circuit as

$$R_s = R_b \frac{\Delta T_{2,m} - \Delta T_{3,m}}{\Delta T_{3,m} + \Delta T_{4,m}} \quad (3)$$

and was several orders of magnitude higher than the calculated interface thermal resistance between the SLG and the electrode or the SiO_2 (*13*). The thermal conductance ($G \equiv 1/R_s$) of the central beam was measured before and after the SLG was etched away in oxygen plasma. The measured G after etching was considerably smaller than that before etching for T above 80 K, below which the difference decreases to near the measurement uncertainty (Fig. 3). The difference in G before and after the etching is attributed to the thermal conductance of the SLG, G_g. We follow the convention to obtain $\kappa = G_g L/Wt$, where we use the interlayer spacing in graphite as the SLG thickness, $t = 0.335$ nm. The results are similar for the three samples (Fig. 4). For G2, the room-temperature κ of 579 ± 34 W m^{-1} K^{-1} is about a factor of 3.4 lower than the highest reported basal-plane value of pyrolytic graphite (PG) (*5*). The appearance of the peak κ position at a much higher $T \approx 300$ K in the supported SLG than $T \approx 140$ K in the PG suggests that phonon scattering is dominated by substrate interaction and umklapp scattering at below and above 300 K, respectively.

Interestingly, Klemens (*17*) had envisioned the feasibility of our thermal measurements several years before SLG was first exfoliated onto SiO_2 (*1*). He suggested that phonons leaking from supported SLG into the substrate would suppress the contribution of low-frequency phonons and reduce κ by 20 to 50%. In SLG, the longitudinal (LA) and in-plane transverse (TA) acoustic branches are linear, whereas the out-of-plane ZA branch shows a quadratic dependence of the frequency (ω) on the wave vector. The contribution to κ from the ZA branch would be negligible based on a relaxation time approximation (RTA) model (*18*) because of the small group velocity and large umklapp scattering rate (τ_u^{-1}) calculated from an expression derived by Klemens and Pedraza (*19*).

In addition to a long wavelength approximation and the assumptions of a linear branch and high T, Klemens and Pedraza cautioned that the greatest uncertainty in their τ_u^{-1} expression stems from the inaccuracy of the assumed three-phonon scattering phase space that was not explicitly calculated (*19*). To address this problem, we carried out full quantum mechanical calculations of both normal and umklapp three-phonon scattering processes in SLG throughout the Brillouin zone (*13*). Through the calculations of the three-phonon matrix elements, we obtain a selection rule for three-phonon scattering, which requires that an even number of ZA phonons be involved in each process as a consequence of the reflection symmetry in flat 2D SLG (*13*). We note that this selection rule was not used in a recent calculation (*20*), whereas an analogous selection rule has been found for electron-ZA phonon scattering in SLG (*21*). This selection rule strongly restricts the phase space for umklapp scattering of ZA phonons in flat SLG. We also find that this selection rule applies in large-radius single-walled CNTs whose curvature is comparable to that of ripples that can form in SLG. We have incorporated this selection rule in an exact numerical solution of the linearized phonon Boltzmann transport equation (BTE) for SLG. Our BTE approach is similar to that used recently for nanotubes (*22*). We find that the ZA modes can contribute as much as 77% and 86% of the total calculated κ at 300 K and 100 K, respectively, for a 10-μm-long suspended SLG with specular edges and 1.1% C^{13} isotopic impurities (*13*). The calculated κ for the suspended SLG is about a factor of 5 and 1.5 higher than the measured κ of the supported SLG and the PG, respectively, at $T \approx 300$ K (Fig. 4).

Scanning probe microscopy measurements have found that SLG exfoliated on SiO_2 is partially conformal to the surface roughness (*23*) and partly suspended between hills on the surface (*24*). These experiments consistently obtained a substrate-induced correlation length in SLG of ~30 nm, which gives a measure of the average center-to-center separation (s) between adjacent hills in intimate contact with the SLG. Perturbation theory yields an approximate expression for the scattering rate due to phonon leakage back and forth across the contact patches as $\tau_{sub,j}^{-1} \propto \rho_j(\omega) K_j^2/\omega^2$, where $\rho_j(\omega)$ depends on the phonon density of states, and K_j is the average van der Waals (vdW) interatomic force constant between the SLG and the SiO_2 support for polarization j = ZA, TA, or LA (*13*). A similar frequency dependence has been obtained for phonon transmission across a vdW interface between two half spaces (*25*). In our case, the expression accounts for parallel momentum not being conserved due to the amorphous structure of the SiO_2 support. The obtained $\tau_{sub,j}^{-1}$ increases with the diameter (d) of the contact patches and the d to s ratio (*13*).

Based on the interlayer vdW energy $\Gamma_0 \approx 0.1$ J/m^2 in graphite and the measured average SLG-SiO_2 separation $h_0 \approx 0.42$ nm reported in (*23*), we calculate $K_{ZA} = 27 S_a \Gamma_0 / h_0^2 \approx 0.4$ N/m, where S_a is the area occupied by one carbon atom in graphene (*13*). The interface force constant K_{LATA} for the in-plane LA and TA modes is generally smaller than K_{ZA} (*26*), especially for an amorphous substrate. At the upper limit of $K_{LATA} = K_{ZA} = 0.46$ N/m and $d = s = 30$ nm, the BTE model obtains a κ value close to the measured value at 300 K, and yields a large ZA contribution (*13*). However, the calculated κ increases

signal (Fig. 3B). To further verify that the distribution of dopa-metal signal stems from variation in sample composition and not topography or thickness, a depth scan (in the *z* plane) was performed across a region in which the granules were particularly well-resolved, confirming that granules are regions of high intrinsic signal intensity (Fig. 3C). Analysis of the region within the highlighted box in Fig. 3C indicates that the maximum granule and minimum matrix intensities of the integrated catechol-metal peak differ by a factor of ~2 to 3.

From these data, we infer that the granules contain a higher dopa-metal cross-link density than the surrounding matrix. By extension, a reasonable prediction would be that the mechanical behavior of the granules differs from that of the matrix. Previous atomic force microscopy (AFM)–based studies have shown that during elongation of *M. galloprovincialis* cuticle, the granule aspect ratio increases up to ~30% in proportion to cuticle strain, indicating that the matrix and granules behave essentially as a single phase (*16*). However, above ~30% strain the granules essentially stop deforming, shifting further strain to the surrounding matrix (*16*). Microcrack formation is consequently observed in the cuticle, but not within the granules (*16*). Furthermore, by returning stretched threads (50% strain) to their initial length and then immediately measuring aspect ratios, we observed that whereas granule elongation is instantaneously reversible, recovery from microcracks is not (Fig. 3D and fig. S3). Cuticle microcracking qualitatively resembles the large-scale cavitation observed in synthetic nanocomposites in which hard inclusions are embedded in a softer polymer (*27*), suggesting that past 30% strain granules behave more stiffly and are less compliant than the matrix.

Several findings of this study point toward a key role of metal cross-links within the cuticle polymer: (i) Cuticle cohesion is based on the presence of dopa-metal cross-links. (ii) The non-covalent and reversible nature of this bonding structure, evident from EDTA and $FeCl_3$ recovery experiments, demonstrates its inherent versatility as compared with that of covalent cross-links (Fig. 2C). (iii) In light of previous nanoindentation-based studies (*13*), the results of EDTA treatment strongly support the role that dopa-iron cross-linking plays in modulating cuticle mechanical properties. And (iv), granules were shown to have a higher relative resonance signal than the matrix, which is indicative of a higher density of dopa-metal–based cross-linking within the granules.

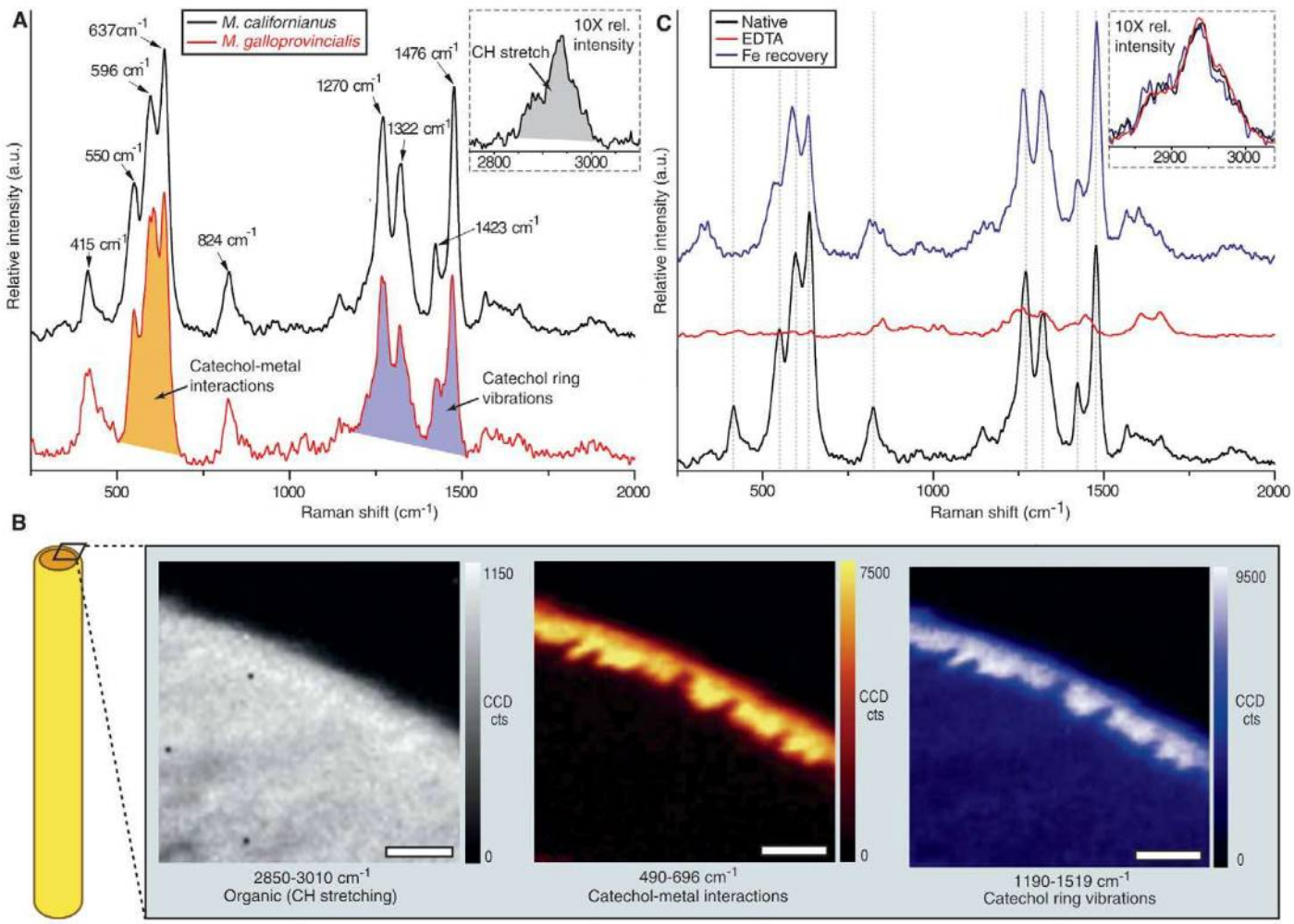

Fig. 2. Raman spectroscopy of byssus cuticles. (**A**) Resonance Raman spectra from *M. californianus* and *M. galloprovincialis* cuticles. The cuticle spectra correspond closely to spectra of mefp-1 and Fe^{3+} in vitro (*23*). Despite differences in cuticle morphology and mfp-1 sequence in the two species, the spectra are barely distinguishable. (Inset) The nonresonance peak for aliphatic CH stretching from *M. californianus* cuticle magnified 10× the relative intensity. According to the assignments, the most prominent peaks can be attributed to the interaction of metal with the catecholic oxygens and to the vibrations of the carbon bonds in the catechol ring, respectively. (**B**) 2D Raman imaging of the same transverse *M. californianus* thread section integrated over three different wave-number ranges as indicated. Organic material is uniformly distributed; however, dopa-Fe^{3+} resonance is confined to the outer coating. Scale bars, 5 μm. (**C**) Resonance Raman spectra of thread cuticles from *M. californianus* in the native state, after EDTA treatment, and after re-exposure to Fe in a depleted thread. The nearly complete loss of resonance peaks after EDTA treatment is reversed by a nearly complete restoration by means of incubation in 1 mM $FeCl_3$ (pH3.2). The three spectra were normalized to the area under the aliphatic CH peak [2850 to 3010 cm^{-1} (inset)].

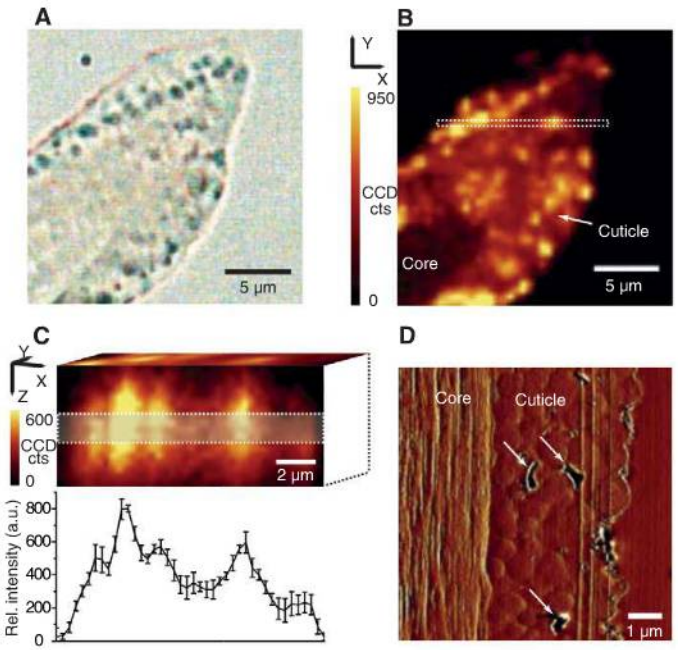

Fig. 3. High-resolution Raman imaging of byssus cuticle. (**A**) Light micrograph of a thin section (~3 μm) of *M. galloprovincialis* proximal cuticle with granules evident as dark spots (100× oil immersion). (**B**) 2D Raman image of (A) integrated for the Fe-catechol peak (490 to 696 cm^{-1}) reveals that granules have higher intensity than matrix. (**C**) Raman depth scan along trajectory (dashed box) in (B) further accentuates the strong difference in the Raman resonance signal between the granules and the matrix. The elongated shape of the granules in the *z* axis is an artifact resulting from the vertical resolution limit of the confocal Raman microscope. The relative intensity (mean ± SD) at each point along the *x* axis averaged over the height (*z* axis) of the highlighted box is plotted below the scan. (**D**) AFM amplitude image of a relaxed thread (recovered after 50% strain) showing the recovered shape of the granules and widespread cuticle microcracking (white arrows).

Although amino acid–metal complexes, particularly those involving dopa or histidine as ligands, are less than half as strong as covalent bonds, they are reversibly breakable through hundreds of cycles (*7*, *9*). Two different mechanical roles have been attributed to these cross-links in biological structures. First, in several damage-tolerant biological structures, low densities of metal complexes are believed to function as reversible sacrificial bonds. For instance, the collagenous core of byssal threads, which exhibits remarkable toughness and self-healing, is stabilized by histidine-metal complexes as opposed to typical collagen cross-linking chemistry (*4*). Similarly, spider silk infiltrated with transition metal ions acquires a substantial increase in toughness, probably because of the formation of coordination complexes (*5*). Second, in contrast to this proposed sacrificial role, the high density of histidine-zinc complexes in the jaws of marine worms (*Nereis* sp.) is adapted to fashion a lightweight material as hard as dentin in the absence of a mineral phase (*1*).

Conceivably, the byssus cuticle combines both of these cross-linking strategies to achieve its unique blend of hardness and extensibility. Consider a view of the cuticle as a continuous network of loosely folded mfp-1 chains with

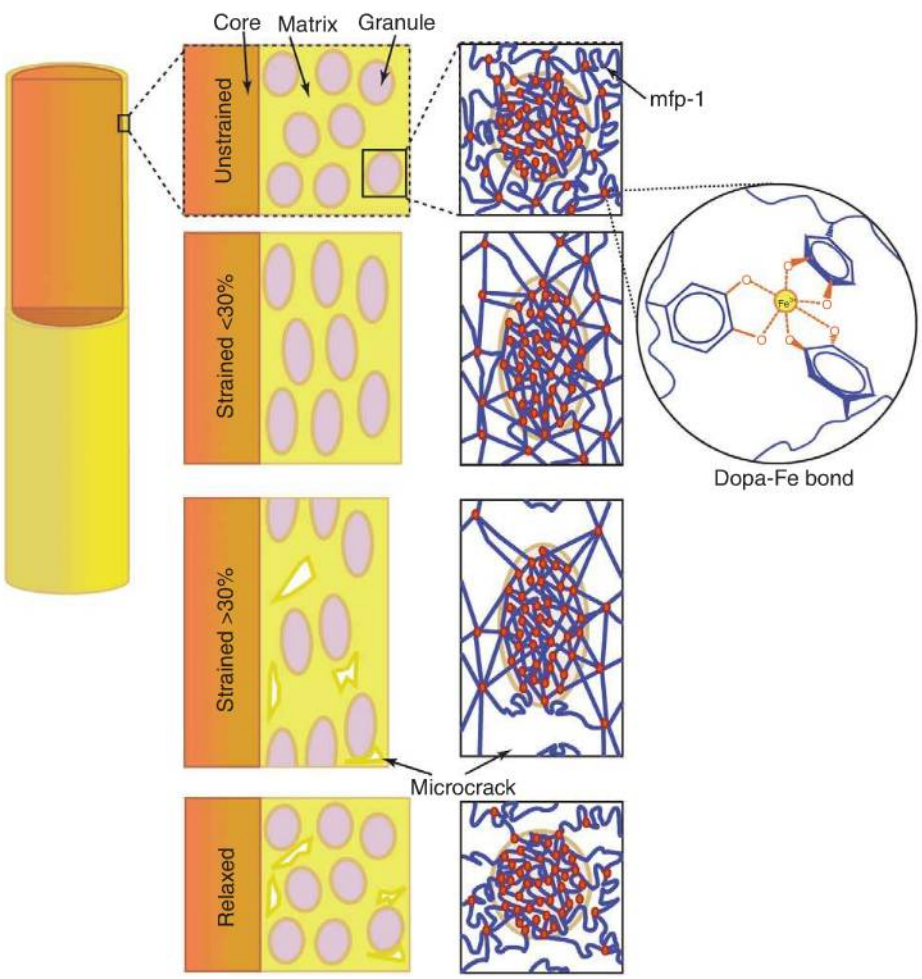

Fig. 4. Basic model illustrating the cohesive role of dopa-Fe complexes in the byssus cuticle. Granules contain a higher cross-link density than matrix. When the cuticle is stretched to less than 30% strain, the randomly coiled mfp-1 chains begin to unravel, and the granule and matrix deform equivalently. However, when stretched beyond 30% strain mfp-1 chains are largely unraveled, and microcracks form outside the granules because of the difference in cross-link density. When relaxed, the granule returns to its initial shape, whereas microcracks do not exhibit immediate recovery.

with T at a steeper rate than the measurement result (Fig. 4). In comparison, at the lower limit of $K_{LATA} = 0$, $K_{ZA} = 0.73$ N/m, and $s = d = 30$ nm, the BTE solution obtains a $\kappa - T$ curve in good agreement with the measurement (Fig. 4). In this case, the ZA contribution to κ becomes smaller than the corresponding TA and LA contributions (*13*), which are reduced only by the suppression of the ZA + ZA → LA or TA mode conversions because of leakage of ZA phonons.

In 2D and at the low T limit, if the scattering rate τ_j^{-1} is proportional to ω^{α}, the κ contribution is proportional to $T^{2-\alpha}$ for j = TA, LA, or ZA polarization. For $K_{LATA} = K_{ZA} = 0.46$ N/m, τ_j^{-1} of all the three polarizations is dominated by $\tau_{sub,j}^{-1}$, for which the α exponent is negative and results in an increased κ with T. In comparison, for $K_{LATA} = 0$ and $K_{ZA} = 0.73$ N/m, boundary scattering with $\alpha = 0$ and isotope and umklapp scatterings with positive α exponents play an increased role for the dominant in-plane polarizations at low and intermediate T, respectively, so that the calculated $\kappa - T$ slope in this T range is relatively small, in agreement with the measured data. On the other hand, we have also fit the measured κ at 300 K by including substrate scattering of $K_{LATA} = 0.8$ N/m in the RTA model (*18*) that neglects the ZA contribution (*13*). The as-calculated κ increases with T at a much more rapid rate than both the BTE results and the experimental data (Fig. 4), because of the negative α exponent of the dominant substrate scattering rate for the LA and TA phonons and the high zone-boundary frequencies of these two branches.

The theoretical analysis suggests that the ZA contribution to κ is large in suspended SLG and that the measured $\kappa - T$ relation can be explained by much stronger substrate scattering of ZA phonons than LA and TA phonons. Although the strong ZA scattering can be caused by the expected behavior of $K_{ZA} > K_{LATA}$, another possibility is that umklapp scattering of ZA phonons can be enhanced by the substrate interaction, which breaks the reflection symmetry. Indeed, our calculations show that the ZA contribution is reduced in suspended bilayer graphene because of interlayer interactions. Although future theoretical work is needed to clarify this issue, our experimental results clearly show that graphene exfoliated on SiO_2 still conducts heat rather efficiently despite phonon-substrate interaction. However, the substrate effect could be quite different for few-layer graphene or SLG grown by thermal decomposition (*27*) or chemical vapor deposition (*28*, *29*) on other substrates because of different interface interactions. These intriguing questions are expected to stimulate further experimental and theoretical investigations of phonon transport in suspended, supported, and embedded graphene.

References and Notes

1. K. S. Novoselov *et al.*, *Science* **306**, 666 (2004).
2. K. I. Bolotin *et al.*, *Solid State Commun.* **146**, 351 (2008).
3. C. Lee, X. Wei, J. W. Kysar, J. Hone, *Science* **321**, 385 (2008).
4. G. A. Slack, *J. Appl. Phys.* **35**, 3460 (1964).
5. G. A. Slack, *Phys. Rev.* **127**, 694 (1962).
6. P. Kim, L. Shi, A. Majumdar, P. L. McEuen, *Phys. Rev. Lett.* **87**, 215502 (2001).
7. C. Yu, L. Shi, Z. Yao, D. Li, A. Majumdar, *Nano Lett.* **5**, 1842 (2005).
8. E. Pop *et al.*, *Phys. Rev. Lett.* **95**, 155505 (2005).
9. Y. S. Ju, K. E. Goodson, *Appl. Phys. Lett.* **74**, 3005 (1999).
10. Y. Yang, W. Liu, M. Asheghi, *Appl. Phys. Lett.* **84**, 3121 (2004).
11. A. A. Balandin *et al.*, *Nano Lett.* **8**, 902 (2008).
12. J. H. Chen, C. Jang, S. Xiao, M. Ishigami, M. S. Fuhrer, *Nat. Nanotechnol.* **3**, 206 (2008).
13. Materials and methods are available as supporting materials on *Science* Online.
14. L. M. Malard, M. A. Pimenta, G. Dresselhaus, M. S. Dresselhaus, *Phys. Rep.* **473**, 51 (2009).
15. E. H. Hwang, E. Rossi, S. Das Sarma, *Phys. Rev. B* **80**, 235415 (2009).
16. Y.-W. Tan *et al.*, *Phys. Rev. Lett.* **99**, 246803 (2007).
17. P. G. Klemens, *Int. J. Thermophys.* **22**, 265 (2001).
18. D. L. Nika, S. Ghosh, E. P. Pokatilov, A. A. Balandin, *Appl. Phys. Lett.* **94**, 203103 (2009).
19. P. G. Klemens, D. F. Pedraza, *Carbon* **32**, 735 (1994).
20. D. L. Nika, E. P. Pokatilov, A. S. Askerov, A. A. Balandin, *Phys. Rev. B* **79**, 155413 (2009).
21. E. Mariani, F. von Oppen, *Phys. Rev. Lett.* **100**, 076801 (2008).
22. L. Lindsay, D. A. Broido, N. Mingo, *Phys. Rev. B* **80**, 125407 (2009).
23. M. Ishigami, J. H. Chen, W. G. Cullen, M. S. Fuhrer, E. D. Williams, *Nano Lett.* **7**, 1643 (2007).
24. V. Geringer *et al.*, *Phys. Rev. Lett.* **102**, 076102 (2009).
25. R. Prasher, *Appl. Phys. Lett.* **94**, 041905 (2009).
26. M. T. Dove, *Introduction to Lattice Dynamics, Cambridge Topics in Mineral Physics and Chemistry 4* (Cambridge Univ. Press, Cambridge, New York, 1993), pp. 29–32.
27. C. Berger *et al.*, *J. Phys. Chem. B* **108**, 19912 (2004).
28. K. S. Kim *et al.*, *Nature* **457**, 706 (2009).
29. X. Li *et al.*, *Science* **324**, 1312 (2009).

30. This work is supported in part by National Science Foundation awards CBET-0553649 and 0933454 (J.H.S. and L.S.), CBET 0651381 (D.A.B. and L.L.), 0651310 (N.M.), and CMMI-0926851 (Z.H.A. and R.H.); Office of Naval Research award N00014-08-1-1168 (A.L.M. and L.S.); Department of Energy Office of Science award DE-FG02-07ER46377(M.T.P. and L.S.); and The University of Texas at Austin (R.S.R.).

Supporting Online Material

www.sciencemag.org/cgi/content/full/328/5975/213/DC1
SOM Text
Figs. S1 to S11
References

30 October 2009; accepted 24 February 2010
10.1126/science.1184014

Iron-Clad Fibers: A Metal-Based Biological Strategy for Hard Flexible Coatings

Matthew J. Harrington,[1]*† Admir Masic,[1]† Niels Holten-Andersen,[2,3] J. Herbert Waite,[2,4] Peter Fratzl[1]

The extensible byssal threads of marine mussels are shielded from abrasion in wave-swept habitats by an outer cuticle that is largely proteinaceous and approximately fivefold harder than the thread core. Threads from several species exhibit granular cuticles containing a protein that is rich in the catecholic amino acid 3,4-dihydroxyphenylalanine (dopa) as well as inorganic ions, notably Fe^{3+}. Granular cuticles exhibit a remarkable combination of high hardness and high extensibility. We explored byssus cuticle chemistry by means of in situ resonance Raman spectroscopy and demonstrated that the cuticle is a polymeric scaffold stabilized by catecholato-iron chelate complexes having an unusual clustered distribution. Consistent with byssal cuticle chemistry and mechanics, we present a model in which dense cross-linking in the granules provides hardness, whereas the less cross-linked matrix provides extensibility.

Metal complexation in biological and bioengineered load-bearing structures is emerging as a versatile cross-linking strategy for assembling and mechanically reinforcing polymeric materials (*1*–*6*). Coordination complexes form cross-links when two or more ligands each donate a nonbonding electron pair to empty orbitals in a transition metal ion. Because of their high stability and rates of formation (*7*–*9*), coordination-based cross-links have been proposed to endow certain biological structures with a number of desirable material properties, including triggered self-assembly, increased toughness, self-repair, adhesion, high hardness in the absence of mineralization, and mechanical tunability (*1*–*4*, *7*). Spectroscopic evidence for the presence of coordination complexes in these various materials is often quite compelling (*10*, *11*), and the loss of material stiffness and hardness upon metal removal is strongly suggestive of a cross-linking role (*1*, *2*, *12*, *13*). Precise localization of coordination complexes in situ has remained elusive but is essential in

[1]Department of Biomaterials, Max Planck Institute for Colloids and Interfaces, Potsdam 14424, Germany. [2]Biomolecular Science and Engineering, University of California, Santa Barbara (UCSB), Santa Barbara, CA 93106, USA. [3]Department of Chemistry, University of Chicago, Chicago, IL 60637, USA. [4]Department of Molecular, Cellular, and Developmental Biology, UCSB, Santa Barbara, CA 93106, USA.

*To whom correspondence should be addressed. E-mail: Matt.Harrington@mpikg.mpg.de
†These authors contributed equally to this work.

defining structure-function relations. Here, we report on the precise localization of metal-protein complexes in mussel byssus by use of Raman microscopy.

The byssus, a shock-absorbing fibrous holdfast made by marine mussels (Fig. 1A), is a treasure trove of metal-polymer complexes, making it a suitable model system for investigating the load-bearing properties of metal coordination cross-links (*3*, *4*, *10*, *13*). Mussels use the byssus, a bundle of 50 to 100 individual threads that are extensible up to >100% strain, to fasten themselves to accessible surfaces of the rocky seashore (Fig. 1A) (*14*). Threads are formed one at a time by a secretion of soluble precursors (primarily protein) into a narrow groove of the thread-forming organ known as the foot. After assembly of the fibrous interior, a 2- to 5–μm-thick protective cuticle is applied as a separate secretion (Fig. 1, B and C) (*15*). Mechanically, the cuticle exhibits a hardness four- to fivefold higher than the fibrous core while maintaining, depending on the species, a breaking strain as high as 100% (Fig. 1B) (*16*, *17*). High cuticle failure strains are correlated with the presence of interspersed granules (Fig. 1C) that hinder crack propagation at high strains via the formation of numerous dispersed microcracks within the continuous intergranular matrix (*16*, *17*). Traditional engineering coatings with comparable hardness fail catastrophically long before reaching such strains.

Mussel foot protein 1 (mfp-1) is the only protein known to be present in the cuticle and is characterized by a high isoelectric point (pI) (~10), minimal secondary structure, and on average 10 to 15 mole percent (mol %) of a posttranslational modification of tyrosine known as 3,4-dihydroxyphenylalanine (dopa) (*18*–*20*). Mfp-1 consists largely of a tandemly repeated decapeptide $x_1Lys_2x_3x_4Tyr_5x_6x_7x_8Tyr_9Lys_{10}$, in which $Lys_{2,10}$ and $Tyr_{5,9}$ are completely conserved and the differential hydroxylation of tyrosine to dopa leads to the accumulation of two mfp-1 populations: (i) one with dopa limited to Tyr_9 and (ii) another with dopa at both Tyr_5 and Tyr_9 (*21*). The inorganic cuticle component, which comprises ~1% of the dry weight, includes metal ions, particularly iron and calcium, but mineralization is absent (*13*). The colocalization of Fe and dopa in the cuticle combined with the unusually high stability of catecholato-Fe^{3+} complexes has led to the proposition that dopa-Fe complexes provide cross-links between mfp-1 chains (Fig. 1D) (*10*, *13*, *22*–*24*). Taylor *et al.* (*23*) demonstrated the ability of mfp-1 to bind Fe^{3+} ions via dopa ligands in vitro using resonance Raman spectroscopy; however, dopa-metal cross-links have not been detected within the cuticle. We investigated the presence and distribution of dopa-dependent metal coordination within the cuticle in situ by exploiting the sub-micrometer resolution of confocal Raman spectroscopy. Results offer revealing insights into the spatial organization of dopa-Fe complexes in the cuticle and support an integral role of metal coordination chemistry in mechanical performance.

The resonance Raman spectra of *Mytilus californianus* and *M. galloprovincialis* thread cuticles are nearly identical (Fig. 2A) despite slight differences in the primary sequence of their respective mfp-1s and the average granule size (*M. californianus*, 200 ± 80 nm; *M. galloprovincialis*, 750 ± 200 nm) (*17*). Nearly all peaks can be attributed to the resonance enhanced interaction of iron (or a related transition-metal ion) with the catecholic moiety of dopa (Fig. 2A and table S1) (*23*, *25*). The peaks at 550, 596, and 637 cm^{-1} are assigned specifically to bidentate chelation of the metal ion by the phenolic oxygens of dopa and will be used throughout as an indicator of the presence of dopa-metal complexation (*26*). The peak at 415 cm^{-1} did not appear in previous in vitro spectra of mfp-1–Fe^{3+} solutions and therefore could not be confidently assigned (*23*); however, possible assignments based on similar chemical systems, particularly didopa cross-linking, are discussed in the supporting online material (SOM) text (table S2). The resonance Raman spectra are stable and persist in cuticles even after 15 days in raw seawater (fig. S1). There were no observable changes in the spectra of the cuticle during or after tensile strains of 100% (SOM text).

The specific enhancement of resonance peaks allows us to localize sites of dopa-metal coordination within the thread. Raman spectroscopic imaging was performed on freshly cut transverse cross-sections of *M. californianus* threads, and peak distribution maps were generated by the integration of the intensity of specific assigned peaks (Fig. 2B). The region corresponding to aliphatic CH vibrations, which is not resonance-dependent, is evenly distributed between the coating and core of the thread, indicating a constant distribution of organic material. In contrast, resonance peaks from catechol-metal interactions and catechol ring vibrations are localized exclusively within the outer cuticle of the thread (Fig. 2B).

It has been previously observed that EDTA depletes iron and calcium ions in the cuticle and results in a ~50% reduction in hardness of the material (*13*). Consistent with this observation, Raman spectra from EDTA-treated thread cuticles show a nearly complete loss of the metal-associated resonance peaks (Fig. 2C). When EDTA-treated threads are then soaked in a 1-mM solution of $FeCl_3$ for 1 hour, catechol-metal resonance is largely recovered; spectral differences between native and treated cuticles are minor (Fig. 2C). The most striking difference is the disappearance of the 415 cm^{-1} peak and the appearance of a group of peaks centered around 330 cm^{-1}. Treatment with $FeCl_3$ alone was sufficient to regenerate spectra; inclusion of $CaCl_2$ in the solution was not necessary.

Mytilus byssus cuticle is not a homogenous structure; rather, it resembles a particle-reinforced composite (Fig. 1C). To further investigate dopa-metal complex distribution within the composite cuticle, microtomed thin sections of *M. galloprovincialis* threads were prepared and imaged with Raman spectroscopy. Light microscopy of cuticle sections (with thicknesses of ~3 μm) revealed a dark granular consistency (Fig. 3A). A two-dimensional (2D) Raman image of the same region integrated for the catechol-metal resonance peak shows that the granular inclusions seen in Fig. 3A appear as regions of high signal intensity and that the matrix shows a weak but measurable

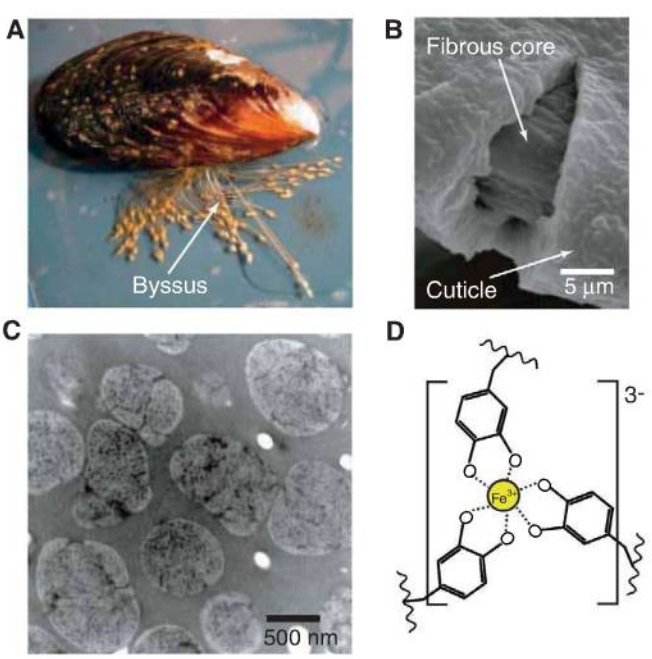

Fig. 1. Mussel byssus cuticle. (**A**) Mussels produce a byssus composed of numerous extensible, shock-absorbing byssal threads. Threads are made one at a time by the mussel foot and attached to hard surfaces by adhesive plaques. (**B**) Mytilid threads are covered by a thin (~5 μm) cuticle with a granular morphology. Strain-induced macrotearing of cuticle exposing the underlying fibrous core is evident in the SEM. The onset of macroscopic cuticle failure in some species requires strains as high as 70 to 100% despite the four- to fivefold greater hardness of cuticle vis-à-vis the extensible interior. (**C**) Granular microstructure as revealed by means of transmission electron microscopy (TEM) in an osmium-stained cuticle. (**D**) The hexadentate mononuclear tris dopa-iron coordination complex proposed to cross-link mfp-1 in the byssus coating.

dopa-metal cross-link density that alternates from high (granules) to low (matrix) (Fig. 4). This model assumes that mfp-1 is the primary structural component of the coating, and although other types of bonding are expected to contribute to the overall stabilization of the structure, we focus here only on the potential role of dopa-Fe cross-linking (*18*). At the onset of cuticle strain, mfp-1 chains [which at rest are random coils and short bent helices (*20*)] straighten out. Within this range, the granules and matrix exhibit similar (high) compliance; however, at ~30% strain most of the coiled protein domains are unraveled, and the load is transferred to the metal-based cross-links. Because of their higher cross-link density, the granules oppose further deformation at the expense of the less cross-linked matrix (Fig. 4). This is perhaps the point at which the lability of dopa-Fe complexes becomes instrumental to cuticle function by facilitating the formation of dispersed microcracks and sparing the cuticle from catastrophic failure. The relatively low forces required to completely unfold noncovalently stabilized random coil domains [~100 pN for the PEVK domain of the muscle protein titin (*28*)] versus those required to break a dopa-metal bond [~800 pN (*7*)] support the sequence of sacrificial bond breakage put forward in this model; however, alternative interpretations should still be considered.

An open question concerns the mechanism of local control over the cross-link density by the organism. There are two plausible explanations: (i) Granules represent a condensed protein phase with higher mfp-1, and consequently dopa density, than the matrix. High-resolution electron micrographs of cuticle-forming cells reveal that secretory vesicles undergo a maturation process that resembles phase separation to form a prefabricated granule surrounded by matrix (*15*). Or (ii), granules have more cross-links per protein chain (for example, mfp-1 within the granules could have more Tyr modified to dopa residues). Two populations of mfp-1 differing only in the degree of dopa modification have been identified (*18*, *21*). It should be added that the two explanations are not mutually exclusive.

The use of dopa-Fe complexes to "ironclad" a polymeric coating is also notable considering the costly cellular processing required. What is the adaptive benefit of forming redox-active dopa by means of posttranslational processing when histidine could be used for metal cross-linking at lower cost? Possibilities include using post-translational modifications to tune cross-link density [as exemplified by the two mfp-1 populations (*21*)], linking dopa-Fe redox exchange to didopa cross-link formation (table S2) (*10*), and exploiting the remarkable affinity of the dopa-Fe^{3+} complex in iron-limited marine environments (SOM text) (*24*, *29*).

This study provides in situ evidence for the peculiar metallopolymeric structures used to stabilize the load-bearing network in the byssus cuticle. In light of previous mechanical studies, these data support the notion that density and organization of metal complexation in functional biopolymers can be fine-tuned for desirable material properties. The adaptive design of the byssal cuticle is unusual in this regard because the density of metal complexation is strategically varied within the polymeric structure at the sub-micrometer scale in order to create a material that is both hard and extensible—an ideal coating for compliant substrates.

References and Notes

1. C. C. Broomell, M. A. Mattoni, F. W. Zok, J. H. Waite, *J. Exp. Biol.* **209**, 3219 (2006).
2. S. W. Werneke, C. Swann, L. A. Farquharson, K. S. Hamilton, A. M. Smith, *J. Exp. Biol.* **210**, 2137 (2007).
3. M. J. Harrington, J. H. Waite, *Biomacromolecules* **9**, 1480 (2008).
4. M. J. Harrington, H. S. Gupta, P. Fratzl, J. H. Waite, *J. Struct. Biol.* **167**, 47 (2009).
5. S. M. Lee *et al.*, *Science* **324**, 488 (2009).
6. M. M. Pires, J. Chmielewski, *J. Am. Chem. Soc.* **131**, 2706 (2009).
7. H. Lee, N. F. Scherer, P. B. Messersmith, *Proc. Natl. Acad. Sci. U.S.A.* **103**, 12999 (2006).
8. Z. S. Zhang, R. B. Jordan, *Inorg. Chem.* **35**, 1571 (1996).
9. L. Schmitt, M. Ludwig, H. E. Gaub, R. Tampé, *Biophys. J.* **78**, 3275 (2000).
10. M. J. Sever, J. T. Weisser, J. Monahan, S. Srinivasan, J. J. Wilker, *Angew. Chem. Int. Ed.* **43**, 448 (2004).
11. H. C. Lichtenegger *et al.*, *Proc. Natl. Acad. Sci. U.S.A.* **100**, 9144 (2003).
12. E. Vaccaro, J. H. Waite, *Biomacromolecules* **2**, 906 (2001).
13. N. Holten-Andersen *et al.*, *Langmuir* **25**, 3323 (2009).
14. E. Carrington, J. Gosline, *Am. Malacol. Bull.* **18**, 135 (2004).
15. L. Vitarello Zuccarello, *Tissue Cell* **13**, 701 (1981).
16. N. Holten-Andersen, G. E. Fantner, S. Hohlbauch, J. H. Waite, F. W. Zok, *Nat. Mater.* **6**, 669 (2007).
17. N. Holten-Andersen, H. Zhao, J. H. Waite, *Biochemistry* **48**, 2752 (2009).
18. C. J. Sun, J. H. Waite, *J. Biol. Chem.* **280**, 39332 (2005).
19. C. V. Benedict, J. H. Waite, *J. Morphol.* **189**, 171 (1986).
20. S. Haemers, M. C. van der Leeden, G. Frens, *Biomaterials* **26**, 1231 (2005).
21. J. H. Waite, T. J. Housley, M. L. Tanzer, *Biochemistry* **24**, 5010 (1985).
22. S. Haemers, M. C. van der Leeden, G. J. M. Koper, G. Frens, *Langmuir* **18**, 4903 (2002).
23. S. W. Taylor, D. B. Chase, M. H. Emptage, M. J. Nelson, J. H. Waite, *Inorg. Chem.* **35**, 7572 (1996).
24. A. Avdeef, S. R. Sofen, T. L. Bregante, K. N. Raymond, *J. Am. Chem. Soc.* **100**, 5362 (1978).
25. L. Öhrström, I. Michaud-Soret, *J. Am. Chem. Soc.* **118**, 3283 (1996).
26. I. Michaud-Soret, K. K. Andersson, L. Que Jr., J. Haavik, *Biochemistry* **34**, 5504 (1995).
27. C. M. Chan, J. S. Wu, J. X. Li, Y. K. Cheung, *Polymer (Guildf.)* **43**, 2981 (2002).
28. H. B. Li *et al.*, *Proc. Natl. Acad. Sci. U.S.A.* **98**, 10682 (2001).
29. S. W. Taylor, G. W. Luther, J. H. Waite, *Inorg. Chem.* **33**, 5819 (1994).

30. L. Bertinetti (University of Torino) provided technical expertise in operating diffuse-reflectance ultraviolet-vis spectrometry. S. Wasko assisted with scanning electron microscopy (SEM). P.F., M.J.H., and A.M. are grateful for support by the Alexander von Humboldt Foundation and the Max Planck Society in the framework of the Max Planck Research Award funded by the Federal Ministry of Education and Research. M.J.H. was partially funded by an Alexander von Humboldt Research Fellowship for Postdoctoral Researchers. J.H.W. was funded by a grant from NIH (R01DE018468). N.H.A. thanks the Danish Natural Science Research Council for a post-doctoral fellowship (272-08-0087). This work made use of the Materials Research Laboratory central facilities at UCSB supported by the Materials Research and Engineering Center Program of NSF under award DMR05-20415.

Supporting Online Material

www.sciencemag.org/cgi/content/full/science.1181044/DC1
Materials and Methods
Figs. S1 to S4
Tables S1 and S2
References

25 August 2009; accepted 28 January 2010
Published online 4 March 2010;
10.1126/science.1181044
Include this information when citing this paper.

Solvent-Mediated Electron Hopping: Long-Range Charge Transfer in $IBr^-(CO_2)$ Photodissociation

Leonid Sheps,[1] Elisa M. Miller,[1] Samantha Horvath,[2] Matthew A. Thompson,[1]* Robert Parson,[1]† Anne B. McCoy,[2]† W. Carl Lineberger[1]†

Chemical bond breaking involves coupled electronic and nuclear dynamics that can take place on multiple electronic surfaces. Here we report a time-resolved experimental and theoretical investigation of nonadiabatic dynamics during photodissociation of a complex of iodine monobromide anion with carbon dioxide [$IBr^-(CO_2)$] on the second excited (A′) electronic state. Previous experimental work showed that the dissociation of bare IBr^- yields only I^- + Br products. However, in $IBr^-(CO_2)$, time-resolved photoelectron spectroscopy reveals that a subset of the dissociating molecules undergoes an electron transfer from iodine to bromine 350 femtoseconds after the initial excitation. Ab initio calculations and molecular dynamics simulations elucidate the mechanism for this charge hop and highlight the crucial role of the carbon dioxide molecule. The charge transfer between two recoiling atoms, assisted by a single solvent-like molecule, provides a notable limiting case of solvent-driven electron transfer over a distance of 7 angstroms.

Chemical transformations involve the coupling of electronic and nuclear motions as reactants evolve into products, and a central goal of chemical physics is to obtain a molecular-level picture of the underlying fundamental rules that govern reaction dynamics. Such detailed understanding requires the knowledge of reactive potential-energy surfaces, and many in-

sights into chemical dynamics have come from experiments that characterized important regions of these surfaces (*1*–*4*). For example, photoelectron spectroscopy of stable anion precursors (*5*, *6*) has been used to probe unbound regions of neutral potentials that correspond to transition states of unimolecular or bimolecular reactions (*7*, *8*). Yet, ideally we wish to characterize all parts of the potential along the reaction path, not only those regions with configurations similar to the anion geometry. This task is best accomplished through time-domain experiments (*3*, *9*) that use ultrafast laser pulses and allow real-time dynamical studies, potentially involving multiple electronic states (*10*, *11*). One such technique, widely used to probe nonequilibrium dynamics, is time-resolved photoelectron spectroscopy (TRPES), in which a pump laser pulse prepares a nonequilibrium ensemble of reactants in an excited state, and a time-delayed photodetachment (photoionization) probe pulse follows their evolution to products (*12*).

We also wish to understand how a molecule interacts with its environment in the condensed phase, where most familiar reactions take place: How might solvent forces affect the nuclear motions and the flow of energy and charge in a reaction? The presence of solvent adds enormous complexity to otherwise simple reaction dynamics, and this complexity makes real-time studies of chemistry in liquids especially challenging. Electron photodetachment from partially solvated ions offers a unique approach to investigate the transition from isolated to solvated reacting systems (*12*, *13*). Gas-phase cluster ions are simple to size-select by time-of-flight methods and provide access to well-defined environments (*13*), from one solvent molecule to multiple solvent shells. Several benchmark studies of cluster ions have begun to address the fundamental questions outlined above, such as solvent effects on caging dynamics (*14*, *15*), vibrational energy transfer (*16*), and charge delocalization (*17*–*19*). Recent studies of the partially hydrated NO^+ cation, $NO^+(H_2O)_n$ (where n is the number of H_2O molecules), demonstrate that solvent configuration can have a profound impact on the reactivity of small clusters with as few as two to four solvent molecules (*20*).

Charge transfer is another example of a process that is very sensitive to molecular interactions, as emphasized by Bragg *et al.*, who examined solvent effects in atomic electron-transfer reactions in liquids (*21*). Yet, photodissociation studies of $IBr^-(CO_2)_n$ cluster anions show that solvent-driven electron transfer between atomic fragments can occur well before the completion of the first solvent shell (*22*). In the work presented here, we further reduce the problem by considering charge transfer that is mediated by a single solvent molecule. We report a TRPES study of photodissociation of $IBr^-(CO_2)$ excited to the A′ electronic state, which extends recent work on the breaking of isolated dihalide chemical bonds (*23*, *24*). We directly probe the evolving electronic structure of $IBr^-(CO_2)$ and find that the single CO_2 solvent molecule enables electron transfer from I^- to Br ~350 fs after electronic excitation, corresponding to an IBr separation near 7 Å. The experiment and accompanying analysis show that the electron transfer occurs in a configuration reminiscent of a solvent-separated pair and is made possible by charge delocalization from I^- onto CO_2, as well as by internal CO_2 vibrational excitation.

The dynamics of this process involve the four lowest-energy electronic states of IBr^- (labeled X, A, A′, and a), shown by the solid curves in the right backplane of Fig. 1. In its ground electronic state, IBr^- dissociates adiabatically to $I + Br^-$. In contrast, the only optically accessible excited state in this energy range, the A′ state, owes its oscillator strength to its partial $\sigma \rightarrow \sigma^*$ charge-transfer character (where σ and σ^* are bonding and antibonding σ molecular orbitals of IBr^-, respectively) and correlates to $I^- + Br$ products. Consistent with the molecular orbital description of these states, bare IBr^- was shown to promptly dissociate on the A′ state to form $I^- + Br$ exclusively (*23*, *25*). Yet, the presence of just one CO_2 solvent molecule changes the product distribution dramatically (*25*).

$$IBr^-(CO_2)\,(X) + h\nu\ (790\ nm) \rightarrow IBr^-(CO_2)\,(A')$$

$$\rightarrow I^- + Br + CO_2 \qquad \sim 36\% \qquad (1)$$

$$\rightarrow I^-(CO_2) + Br \qquad \sim 61\% \qquad (2)$$

$$\rightarrow I + Br^- + CO_2 \qquad \sim 3\% \qquad (3)$$

In Eq. 1 above, h is Planck's constant, and ν is the laser frequency. The initial excitation is solely to the A′ state (*22*); dynamical simulations (see below) indicate that dissociation also occasionally samples the a state, but only at times when the two surfaces are experimentally indistinguishable. Dissociation on the A′ or a state results in pathways 1 and 2, and the branching ratio between the two pathways depends on the initial geometry of the complex and vibrational energy redistribution during dissociation. However, the third exit channel must arise from a solvent-driven nonadiabatic transition to one of the lower-energy electronic states (X or A) that correlates asymptotically to $I + Br^-$. Our simulations reveal that transitions to both of these states do take place, albeit at large IBr separations where the X and A states are nearly isoenergetic. Recent experiments have shown that the electronic structure of the atomic fragments develops very early in photodissociation of dihalides, within ~200 fs after the excitation (*23*, *24*). Thus, the third exit channel physically corresponds to electron transfer between two atomic fragments partway through the dissociation, enabled by a single solvent molecule.

The present study characterizes the time scale and IBr distance involved in the charge hop,

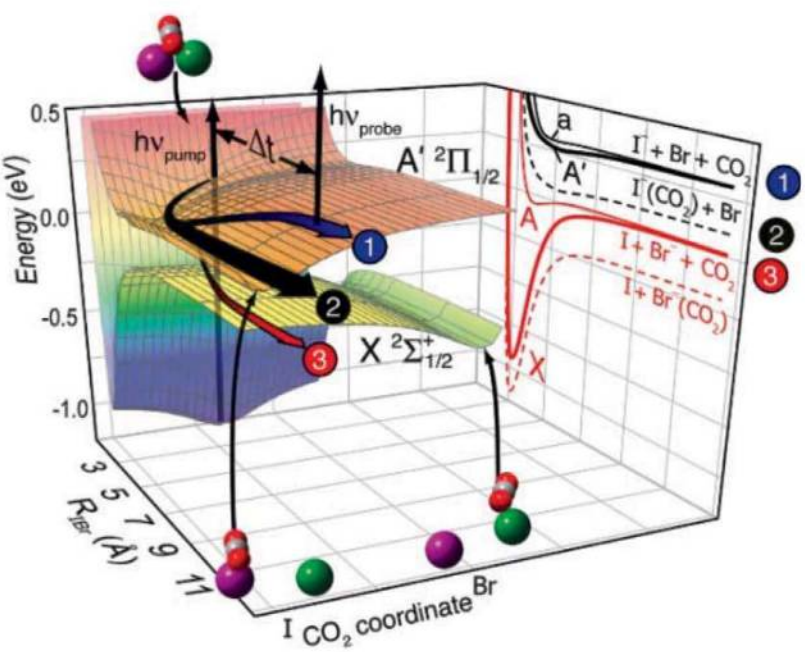

Fig. 1. Schematic X $^2\Sigma^+_{1/2}$ and A′ $^2\Pi_{1/2}$ potential surfaces of $IBr^-(CO_2)$. "CO_2 coordinate" indicates the location of the CO_2 molecule relative to I (purple spheres) or Br (green spheres). The arrows $h\nu_{pump}$ and $h\nu_{probe}$ show the pump and probe laser pulses. The three dissociation channels are labeled 1 to 3. Solid curves (right) denote the four calculated lowest-energy electronic states (X, A, A′, and a) of IBr^-. Dotted curves schematically illustrate the minimum-energy paths taken from the two-dimensional X and A′ surfaces of $IBr^-(CO_2)$. R_{IBr}, I–Br bond length.

[1]JILA, Department of Chemistry and Biochemistry, University of Colorado at Boulder, Boulder, CO 80309, USA. [2]Department of Chemistry, The Ohio State University, Columbus, OH 43210, USA.

*Present address: NASA Goddard Space Flight Center, Greenbelt, MD 20771, USA.

†To whom correspondence should be addressed. E-mail: rparson@jila.colorado.edu (R.P.); mccoy@chemistry.ohio-state.edu (A.B.M.); carl.lineberger@Colorado.edu (W.C.L.)

clarifies the crucial role of the CO_2 molecule, and proposes a mechanism for the electron transfer. The experiment combines a pulsed source of $IBr^-(CO_2)$ cluster anions, a velocity-map imaging photoelectron spectrometer, and a 100-fs laser system for pump-probe TRPES (*26*). The experimental scheme, along with a qualitative representation of the X and A′ potential-energy surfaces of $IBr^-(CO_2)$, is shown in Fig. 1. The pump laser pulse $h\nu_{pump}$ initiates the dissociation of $IBr^-(CO_2)$ on the A′ state. The three possible reaction channels are depicted by the arrows labeled 1, 2, and 3 (Fig. 1). After a delay time Δt, a probe laser pulse with energy $h\nu_{probe}$ acquires the transient photoelectron spectrum. The CO_2 coordinate in Fig. 1 represents the CO_2 position relative to I or Br. As shown by these plots, solvation of I^-, Br^-, or IBr^- by one CO_2 molecule lowers the energy by ~0.2 eV (*22*, *27*, *28*). This shift is shown schematically by the dotted curves in the right backplane of Fig. 1. Stabilization of the anions by CO_2 is also indicated by the well on the left side of the $IBr^-(CO_2)$ A′ surface and on the right side of the X surface. Equilibrium solvation by a single CO_2 molecule is insufficient to lower the energy of the A′ or a state below that of the X or A state.

The transient photoelectron spectra of dissociating $IBr^-(CO_2)$ after excitation to the A′ state are shown in Fig. 2. The photoelectron intensity is plotted versus the electron binding energy (eBE), defined as the difference between the probe photon energy and the electron kinetic energy. Background photoelectron signals have been removed, and these transient spectra reflect the time evolution of the dissociating ensemble created by the pump laser pulse. The transient spectrum gains intensity at very early pump-probe delays and shifts to higher eBE (up to $\Delta t \approx 300$ fs). Within the next 200 fs, the spectrum splits into three components that continue to shift for another 500 fs, although the integrated transient intensity stays constant. After $\Delta t \approx 1$ ps, the transient signal is invariant out to $\Delta t = 50$ ps, the longest delay time that we surveyed. The asymptotic product distribution, shown in the top panel of Fig. 2, is consistent with earlier photofragmentation studies by Thompson *et al.* and Sanford *et al.* (*22*, *25*).

The transient spectra at $\Delta t \geq 300$ fs are fit to a sum of three Gaussian functions, and their center eBE values (shown as white circles in Fig. 2) reflect the identity of the evolving dissociation products. The photoelectron peak at the lowest energy (3.06 eV) arises from the I^- product (channel 1); the peak at highest energy (3.36 eV) is attributable to Br^- (channel 3). The broad feature at eBE ≈ 3.2 eV corresponds to reaction channel 2, $I^-(CO_2)$ products, but is redshifted by ~0.05 eV from the value measured for cold $I^-(CO_2)$ (*27*). The width and the redshift of this feature provide direct evidence that the $I^-(CO_2)$ photodissociation products have a broad distribution of vibrational excitation, averaging 0.05 eV, about 25% of the $I^-(CO_2)$ well depth (*28*). The time evolution of the photoelectron signal is presented in the two top panels of Fig. 3. Panel B contains a plot of the total integrated spectral intensity as a function of Δt, which shows that the transient population of excited $IBr^-(CO_2)$ appears much faster than our experimental resolution (300 fs). After the initial rise, the constant transient signal confirms that we monitor the entire excited population en route to product formation. The transient photoelectron signal slice at eBE = 3.36 eV is plotted in Fig. 3A, along with a fit to an instrument-limited rise centered at $\Delta t = 350$ fs. Because this signal reflects the formation of Br^-, we conclude that charge transfer from I^- to Br (i.e., the transition to the X or A potential-energy surface) occurs over a 200-fs time window centered at $\Delta t = 350$ fs.

To understand the origins of the observed branching into the three product channels and, in particular, the mechanism for the nonadiabatic charge transfer from I^- to Br at ~350 fs, we performed two sets of calculations (*26*). The first is a set of nonadiabatic molecular dynamics (MD) simulations in which potential-energy surfaces for the solvent-solute system are generated "on the fly" from an effective Hamiltonian that takes into account the interaction between the solute charge distribution, which is treated quantum mechanically, and the solvent charge distribution, which is treated classically. Nonadiabatic transitions among the potential surfaces are described by a semiclassical surface-hopping algorithm. The model accounts for polarization of the solute charge distribution by the solvent, but not for charge transfer to the solvent or for solvent intramolecular vibrations (*22*, *29*). We ran 5000 classical trajectories starting from an equilibrated ensemble of $IBr^-(CO_2)$ cluster anions at internal energies ranging from 200 to 1400 cm^{-1}. These trajectories were run in groups of 1000, and the initial conditions reflect five cluster temperatures ranging from 80 to 250 K. In the second set of calculations, we took the geometries from several of these trajectories and performed high-level ab initio calculations (*30*) of the electronic energies of $IBr^-(CO_2)$ and dipole moments for IBr^-, $I^-(CO_2)$, and $IBr^-(CO_2)$. To assess the effect of the CO_2 bending motion, calculations were performed for OCO bend angles of 175°, as well as the 180° value used in the trajectory simulations (*26*).

Although the MD simulations do not include the electronic structure or internal vibrations of CO_2, they capture much of the dynamics of the photodissociation of $IBr^-(CO_2)$. Notably, these trajectories undergo prompt localization of the excess electron on iodine and reproduce the experimental result of large vibrational excitation of the $I^-(CO_2)$ cluster anion products (*26*). We find that at 80 K, all of the trajectories form $I^-(CO_2)$ + Br products (channel 2), whereas at 250 K, 30% dissociate to form I^- + Br + CO_2. This value is consistent with ~36% of the experimental signal being associated with channel 1 (*25*). Based on an analysis of the five sets of 1000 trajectories, we find that the fraction of the ensemble that follows channel 1 increases with rising internal energy of the anion before photoexcitation, a result that reflects a strong correlation between the geometry of the complex at the time of photoexcitation and the probability of three-body dissociation. Similarly, at the higher temperatures, a small number of trajectories (<1%) form Br^- (channel 3). The simulations show that channel 1 is a concerted three-body breakup, but channel 3 begins with a prompt departure of the neutral bromine atom, followed by electron transfer from I to Br and subsequent CO_2 dissociation. Details of the analysis, as well as movies of one repre-

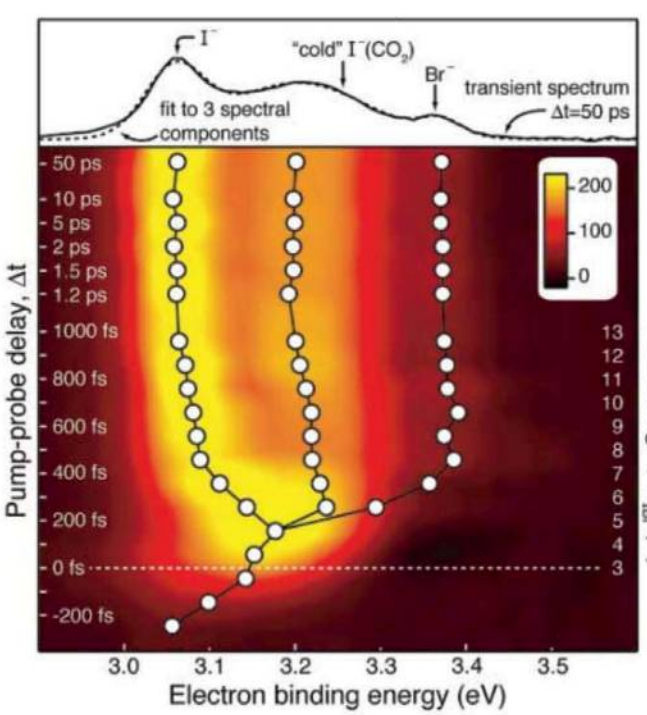

Fig. 2. Time-resolved transient photoelectron spectra of photodissociation of $IBr^-(CO_2)$ as a function of pump-probe delay. **(Top)** Transient photoelectron spectrum at Δt = 50 ps and spectral fit (dashed line). I^-, cold $I^-(CO_2)$, and Br^- are photoproduct reference eBE values. **(Bottom)** False color scale indicates the photoelectron intensity. The white circles show the centers of spectral fit components. The right vertical scale shows the approximate IBr separation at each delay time, assuming evolution in exit channel 2, $I^-(CO_2)$ + Br.

sentative trajectory for each dissociation pathway, are located in the supporting online material (*26*).

Figure 3 shows the properties derived from the representative trajectories for pathways 2 and 3. Three snapshots of cluster geometries at $\Delta t = 0$, 350, and 800 fs, taken from these trajectories, appear at the top of the figure. The trajectory that undergoes electron transfer is shown on the left-hand side. In panel C, we plot the distance between the iodine and carbon atoms (R_{IC}); in panel E, the X–A′ and A–A′ energy gaps; and in panel G, the charge on the iodine atom, based on the charge distribution for the adiabatic electronic state used to describe the classical system. Consistent with earlier studies (*24*), the charge localizes on the iodine atom within the first 200 fs. After ~350 fs, the energy gap between the A′ and A states is smaller than 0.01 eV. This reduction in the energy gap, which coincides with the $I^-\cdots CO_2$ vibration reaching its inner turning point, enables a surface hop between the A′ and A states that results in charge transfer from I to Br after ~400 fs. In summary, even though the energy gaps between the electronic states of IBr^- are too large for electron transfer when the CO_2 is in its minimum-energy geometry, motion of the CO_2 molecule reduces these energy gaps and promotes the charge-transfer process. This solvent motion is brought about by charge redistribution after electronic excitation and is further enhanced by thermal excitation of the cluster anions before photoexcitation.

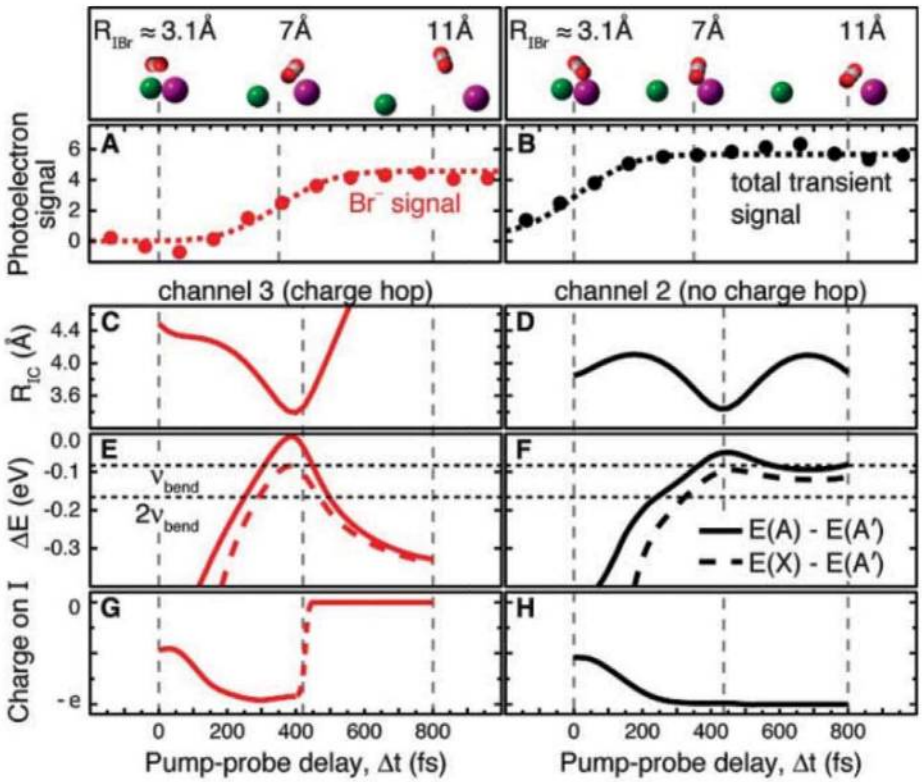

Fig. 3. (**A**) A cut through the time-resolved photoelectron spectrum at eBE = 3.36 eV, reflecting the Br^- signal. (**B**) Integrated transient intensity, reflecting the total excited state population. Data in (A) and (B) were smoothed with a three-point filter. Dashed lines in (A) and (B) are fits to instrument-limited rises, centered at Δt = 350 and 0 fs, respectively. (**C** to **H**) Calculated properties from two MD trajectories: one that exhibits electron transfer (left column, channel 3) and one that does not (right column, channel 2). Vertical dashed lines mark Δt = 0 fs, 800 fs, and the time at which the charge hop is likely to occur. (C) and (D) Distance between the I and C atoms (R_{IC}). (E) and (F) Energy gaps between the initially excited state, A′, and the two lower-energy states, A (solid curves) and X (dashed curves). In (E), the energies are obtained from the MD simulation, whereas in (F), the CO_2 molecule is bent, and the energies are calculated with electronic structure theory (*30*). The horizontal dotted lines indicate the energies of one and two quanta of CO_2 bend vibration. (G) and (H) Amount of excess charge on the I atom. The red dashed line in (G) indicates a nonadiabatic transition to the A state.

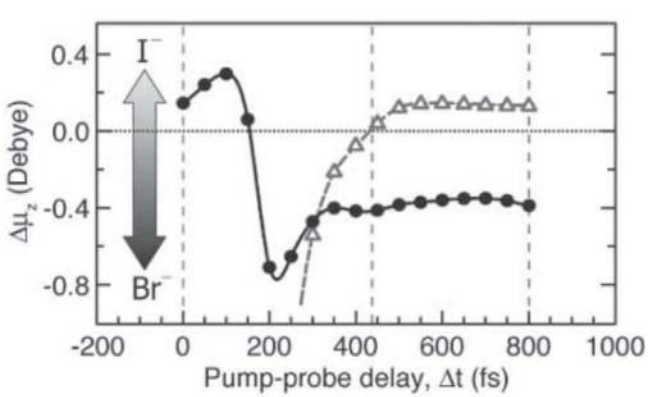

Fig. 4. Differences between the dipole moment component along the IBr bond axis ($\Delta\mu_z$) for the $IBr^-(CO_2)$ complex and either the sum of the dipole moments of IBr^- and CO_2 (solid curve and circles) or the sum of the dipole moments of $I^-(CO_2)$ and Br (dashed curve and triangles). As indicated by the arrow, a negative value of these quantities indicates more charge transfer to the Br atom, resulting from the introduction of the CO_2 molecule with a 175° OCO angle. The calculations were performed for the same MD trajectory that we used to generate the plots in the right panels of Fig. 3, and the vertical dashed lines are at the same time points as those in the right panels of Fig. 3 to aid in comparison.

Although we find several trajectories in which the charge hop occurs, the MD simulations substantially underestimate the contribution of channel 3. This discrepancy is probably due to the fact that neither vibrational excitation of CO_2 nor solvent-mediated charge transfer is included in the model. In the right panels of Fig. 3, we plot the properties for a trajectory that does not undergo a charge hop. Consistent with the results plotted in panel E, the curves in panel F show that, at the time when (R_{IC}) is minimized, the X–A′ and A–A′ energy gaps are also minimized. In contrast to panel E, these energy differences were evaluated using electronic structure theory (*30*) for an OCO angle of 175°, with all other internal coordinates taken from the classical trajectory. Similar curves were evaluated for an OCO angle of 180° and yield larger energy gaps than those shown in Fig. 3F. Although the calculated energy gaps are too large to generate a substantial transition probability for a direct hop from the A′ state to the X or A state, these gaps would be closed by adding 1 or 2 quanta of bend excitation to the CO_2 molecule (shown by the horizontal dotted lines in Fig. 3, E and F). Further evidence for participation of the CO_2 bend comes from photoelectron spectroscopy of $I^-(CO_2)$ (*27*, *31*), which indicates that in these complexes, the equilibrium value of the CO_2 bend angle is ~175°. The distortion arises from partial delocalization of the excess electron into the lowest unoccupied molecular orbital of CO_2 (*31*) and is expected to be even larger at the inner turning point of the $I^-\cdots CO_2$ vibration (fig. S9). Combining these observations, we infer that the distortion of the OCO angle upon interaction with I^- facilitates the charge hop through electronic to vibrational energy transfer.

To further investigate this mechanism, we need to assess the influence of CO_2 intramolecular vibrations and charge transfer from IBr^- to CO_2 on the IBr^- electronic structure. We focus on how the introduction of the CO_2 molecule modifies the charge distribution of IBr^- by extracting the

positions of the five atoms as a function of time from one of the MD trajectories, bending the OCO angle from 180° to 175°, and calculating the dipole moments of $IBr^-(CO_2)$, as well as the sums of the dipole moments of the $IBr^- + CO_2$ and $I^-(CO_2)$ + Br fragments, calculated at their geometries in the complex. The differences between these quantities are shown in Fig. 4. After 200 fs, the presence of the CO_2 molecule leads to a shift of the excess charge away from the iodine atom and toward the bromine atom in the complex, compared to the charge distribution in IBr^-. This shift in the charge distribution reflects both charge transfer to the bromine due to the presence of the CO_2 molecule and charge delocalization between I^- and CO_2 in the $I^-(CO_2)$ complex. Based on these results, we conclude that, for times between 200 and 500 fs, the charge distribution of $IBr^-(CO_2)$ is perturbed relative to both asymptotes with greater negative charge on the Br atom. This time range corresponds well to the time at which the $I + Br^- + CO_2$ product channel is observed in the experiment and suggests that, at the time of the charge hop, the MD simulations underestimate the coupling between the adiabatic potential curves.

Taken together, the results of the calculations lead us to a mechanism for long-range electron transfer between I and Br in the dissociation of $IBr^-(CO_2)$ on the A′ electronic state. When the $I^-\cdots CO_2$ vibration reaches its first inner turning point (typically near a time delay of ~350 fs), the energy gap between the A′ and X or A states is minimized. A small number of trajectories sample regions of the potential where the gap between the A′ and A states is ~0.01 eV, and many of the trajectories have an energy gap that is commensurate with one or two quanta of CO_2 bending vibration. At these small values of R_{IC}, the CO_2 molecule will be bent, and the distorted OCO angle projects favorably onto the bend-excited states after the charge transfer. At the same time, the changes in the dipole moment along the IBr axis indicate that the presence of the CO_2 molecule shifts the excess charge density toward the bromine atom, thereby providing a mechanism for the increased coupling between the A′ and X or A electronic states. The mechanism and time scales are consistent with the observed Br^- products at ~350 fs in the TRPES experiment. It is likely that the intimate, essential involvement of solvent internal degrees of freedom, elucidated in this simple example of long-range electron transfer, will be a major component in other electron-transfer processes taking place through solvent bridges.

References and Notes

1. D. C. Clary, *Proc. Natl. Acad. Sci. U.S.A.* **105**, 12649 (2008).
2. D. M. Neumark, *Science* **272**, 1446 (1996).
3. J. C. Polanyi, A. H. Zewail, *Acc. Chem. Res.* **28**, 119 (1995).
4. G. C. Schatz, *Science* **262**, 1828 (1993).
5. K. M. Ervin, W. C. Lineberger, in *Advances in Gas Phase Ion Chemistry*, N. G. Adams, L. M. Babcock, Eds. (JAI Press, Greenwich, CT, 1992), vol. 1, pp. 121–66.
6. D. M. Neumark, *J. Chem. Phys.* **125**, 132303 (2006).
7. D. E. Manolopoulos *et al.*, *Science* **262**, 1852 (1993).
8. P. G. Wenthold, D. A. Hrovat, W. T. Borden, W. C. Lineberger, *Science* **272**, 1456 (1996).
9. A. H. Zewail, *Angew. Chem. Int. Ed.* **39**, 2586 (2000).
10. V. Blanchet, M. Z. Zgierski, T. Seideman, A. Stolow, *Nature* **401**, 52 (1999).
11. O. Gessner *et al.*, *Science* **311**, 219 (2006); published online 15 December 2005 (10.1126/science.1120779).
12. A. Stolow, A. E. Bragg, D. M. Neumark, *Chem. Rev.* **104**, 1719 (2004).
13. A. Sanov, W. C. Lineberger, *Phys. Chem. Chem. Phys.* **6**, 2018 (2004).
14. B. J. Greenblatt, M. T. Zanni, D. M. Neumark, *Science* **276**, 1675 (1997).
15. J. M. Papanikolas *et al.*, *J. Chem. Phys.* **99**, 8733 (1993).
16. A. V. Davis, R. Wester, A. E. Bragg, D. M. Neumark, *J. Chem. Phys.* **117**, 4282 (2002).
17. A. V. Davis, M. T. Zanni, C. Frischkorn, D. M. Neumark, *J. Electron Spectrosc. Relat. Phenom.* **108**, 203 (2000).
18. D. H. Paik, N. J. Kim, A. H. Zewail, *J. Chem. Phys.* **118**, 6923 (2003).
19. D. E. Szpunar, K. E. Kautzman, A. E. Faulhaber, D. M. Neumark, *J. Chem. Phys.* **124**, 054318 (2006).
20. R. A. Relph *et al.*, *Science* **327**, 308 (2010).
21. A. E. Bragg, M. C. Cavanagh, B. J. Schwartz, *Science* **321**, 1817 (2008).
22. M. A. Thompson, J. P. Martin, J. P. Darr, W. C. Lineberger, R. Parson, *J. Chem. Phys.* **129**, 224304 (2008).
23. R. Mabbs, K. Pichugin, A. Sanov, *J. Chem. Phys.* **122**, 174305 (2005).
24. P. Wernet *et al.*, *Phys. Rev. Lett.* **103**, 013001 (2009).
25. T. Sanford, S. Y. Han, M. A. Thompson, R. Parson, W. C. Lineberger, *J. Chem. Phys.* **122**, 054307 (2005).
26. Experimental and theoretical methods are available as supporting material on *Science* Online.
27. D. W. Arnold, S. E. Bradforth, E. H. Kim, D. M. Neumark, *J. Chem. Phys.* **102**, 3510 (1995).
28. Y. X. Zhao, C. C. Arnold, D. M. Neumark, *J. Chem. Soc. Faraday Trans.* **89**, 1449 (1993).
29. M. Thompson, thesis, University of Colorado (2007).
30. H.-J. Werner *et al.*, MOLPRO, version 2008.1, a package of ab initio programs, 2008 (www.molpro.net).
31. D. W. Arnold, S. E. Bradforth, E. H. Kim, D. M. Neumark, *J. Chem. Phys.* **97**, 9468 (1992).

32. We thank the NSF (W.C.L. and A.B.M.), the Air Force Office of Scientific Research (W.C.L.), and the Office of Naval Research (A.B.M.) for support of this work, as well as the Graduate School at The Ohio State University for fellowship support (S.H.). The calculations were performed on the JILA Yotta cluster and on the Glenn Cluster at the Ohio Supercomputer Center. S.H. is grateful to K. A. Peterson for his assistance with the electronic structure calculations.

Supporting Online Material

www.sciencemag.org/cgi/content/full/science.1184616/DC1
Materials and Methods
Figs. S1 to S9
Tables S1 and S2
References
Movies S1 to S3

12 November 2009; accepted 12 February 2010
Published online 4 March 2010;
10.1126/science.1184616
Include this information when citing this paper.

Increased Silver Activity for Direct Propylene Epoxidation via Subnanometer Size Effects

Y. Lei,[1,2]* F. Mehmood,[3]* S. Lee,[1]* J. Greeley,[4] B. Lee,[5] S. Seifert,[5] R. E. Winans,[5] J. W. Elam,[6] R. J. Meyer,[2] P. C. Redfern,[1] D. Teschner,[7] R. Schlögl,[7] M. J. Pellin,[3] L. A. Curtiss,[1,3,4]† S. Vajda[1,4,8]†

Production of the industrial chemical propylene oxide is energy-intensive and environmentally unfriendly. Catalysts based on bulk silver surfaces with direct propylene epoxidation by molecular oxygen have not resolved these problems because of substantial formation of carbon dioxide. We found that unpromoted, size-selected Ag_3 clusters and ~3.5-nanometer Ag nanoparticles on alumina supports can catalyze this reaction with only a negligible amount of carbon dioxide formation and with high activity at low temperatures. Density functional calculations show that, relative to extended silver surfaces, oxidized silver trimers are more active and selective for epoxidation because of the open-shell nature of their electronic structure. The results suggest that new architectures based on ultrasmall silver particles may provide highly efficient catalysts for propylene epoxidation.

Propylene oxide is a key precursor for the production of commodity chemicals. The current methods that can produce propylene oxide on an industrial scale are either not profitable or are environmentally unfriendly because of the production of chlorinated or peroxycarboxylic waste (*1*). Thus, direct partial oxidation of propylene by molecular oxygen, as shown in Scheme 1, has received considerable attention (*2*–*8*). However, no industrial-scale heterogeneous catalytic propylene epoxidation process using molecular oxygen has yet been identified. Silver has been successfully used in the epoxidation of ethylene with high selectivity, both in the lab (*6*) and on an industrial scale (*9*). However, the use of silver in propylene ep-

[1]Chemical Sciences and Engineering Division, Argonne National Laboratory, Argonne, IL 60439, USA. [2]Department of Chemical Engineering, University of Illinois, Chicago, IL 60607, USA. [3]Materials Science Division, Argonne National Laboratory, Argonne, IL 60439, USA. [4]Center for Nanoscale Materials, Argonne National Laboratory, Argonne, IL 60439, USA. [5]X-ray Sciences Division, Argonne National Laboratory, Argonne, IL 60439, USA. [6]Energy Systems Division, Argonne National Laboratory, Argonne, IL 60439, USA. [7]Department of Inorganic Chemistry, Fritz-Haber-Institut der Max-Planck-Gesellschaft, Faradayweg 4-6, 14195 Berlin, Germany. [8]Department of Chemical Engineering, Yale University, New Haven, CT 06520, USA.

*These authors contributed equally to this work.
†To whom correspondence should be addressed. E-mail: curtiss@anl.gov (L.A.C.); vajda@anl.gov (S.V.)

oxidation has been hampered by either low conversion or poor selectivity toward propylene oxide, and the detailed mechanism of the epoxidation process is unclear (*2*, *5*, *7*, *8*, *10*).

The catalytic activity of metals can be altered when used as small metal clusters or nanoparticles (*11*–*15*), and epoxidation of propylene to propylene oxide on silver and gold nanoparticle catalysts exhibits strongly size-dependent catalytic activity (*2*, *4*, *5*, *16*). However, none of the nanocatalysts reported to date possess both high conversion and selectivity toward propylene oxide. Haruta and co-workers discovered a highly selective propene epoxidation catalyst based on titania-supported gold nanoparticles (2 to 4 nm in diameter) when hydrogen was co-fed with the oxygen and propylene mixture (*4*), but the selectivity was extremely sensitive to the gold nanoparticle size and shape. Size-preselected subnanometer gold clusters stabilized on amorphous alumina have highly selective catalysts for this reaction (*17*), and supported subnanometer Pt clusters are both highly active and selective for oxidative propane dehydrogenation (*18*).

A report that gas-phase anionic silver clusters exhibit activity in oxidation reactions at very low temperatures (*19*) led us to investigate the catalytic properties of supported silver trimers and to use quantum chemical calculations to help explain the unprecedented activity and selectivity observed for propylene epoxidation on them. In addition to size-selected silver trimers (Ag_3) supported on amorphous alumina films, we have also investigated the catalytic properties of very small nanoparticles with average size of ~3.5 nm (2 nm in height and 4 nm in diameter) resulting from agglomeration of the silver trimers at higher temperatures. The silver cluster–based catalysts were fabricated by depositing mass-selected clusters from a molecular beam on an ultrathin alumina film (~3 monolayers) produced by atomic layer deposition on top of the naturally oxidized silicon wafer (*20*). The cluster deposition apparatus has been described in detail elsewhere (*21*). Briefly, a narrow size distribution of Ag_n^+ ($n = 2$ to 4) clusters with dominant trimer contribution was mass-selected using a quadrupole mass filter and deflector assembly and deposited on the support at 2.2% atomic monolayer coverage.

$$2CH_3\text{-}CH{=}CH_2 + O_2 \xrightarrow{\text{Catalyst}} 2$$

Scheme 1.

A common problem encountered with the use of small metal particles on oxide supports is that their catalytic performance is often diminished by sintering, the agglomeration of particles caused by heating during reactions (*22*, *23*). In situ grazing incidence small-angle x-ray scattering (GISAXS) is a powerful tool to study the evolution of size and shape of supported clusters and nanoparticles under reaction conditions (*24*). GISAXS revealed that the sintering of Ag_3 clusters begins around 110°C, leading to the formation of silver particles with average size of 3.5 nm at 200°C (Fig. 1A). The analysis of the two-dimensional GISAXS data revealed particle height and diameter of 2 nm and 4 nm, respectively. These nanoparticles did not sinter further during an additional 1 hour of monitoring of the reaction. There was no evidence of any sintering of the trimers before the abrupt change at 110°C (*25*), which is consistent with the results of Buratto *et al.* (*26*), who found silver trimers to be stable on a titania surface. Because the silver trimers remain isolated only below 110°C, their catalytic properties are discussed for this temperature region.

Catalytic tests on the silver trimer and nanoparticles were performed using temperature-programmed reaction at 133 kPa and gas flow of 30 sccm (standard cubic centimeters per minute). The composition of the gas mixture was 0.67% C_3H_6 and 0.33% O_2 in helium. The reaction products were analyzed on a differentially pumped quadrupole mass spectrometer. Propylene oxide, acrolein, and carbon dioxide were identified as the dominant reaction products from the silver trimers (Fig. 1B; note that for the silver trimer, the number of surface atoms equals the number of total atoms of the cluster). The formation of acetone and propenol was excluded on the basis of analysis of the mass spectra (*25*). Beginning at room temperature, the rate of both propylene oxide and acrolein formation increased sharply with temperature. At 60°C we observed the onset of combustion. The formation of CO_2 coincided with the decrease of acrolein production, which indicates that these two channels are competitive. Figure 1C shows two regions for product selectivity below the sintering temperature. At temperatures up to 60°C, the selectivity was highest for acrolein; between 70°C and 100°C, much higher propylene oxide/acrolein product ratios (3:1) were achieved. However, this improvement is realized at the expense of an increase in CO_2 formation of 30 to 60%.

The catalytic performance of the nanoparticle aggregates was strikingly different from the performance of their subnanometer Ag_3 counterparts under identical reaction conditions (Fig. 2). The nanoparticles exhibited superior selectivity toward propylene oxide at temperatures up to 120°C while maintaining activity per surface atom comparable to that of Ag_3 clusters. Combustion on the nanosized aggregates had an onset at 130°C, a temperature 70°C higher than on Ag_3. The rate of propylene oxide molecules formed per surface silver atom was ~1 s^{-1} at 110°C for both Ag_3 and the silver aggregates, which is much greater than that reported for any silver catalyst. For example, turnover rates per surface atom (an estimated $\leq 10^{-4}$ per total atom) were reported to be 10^{-2} s^{-1} for 50- to 660-nm unpromoted silver particles at much higher temperatures [220°C (*2*)] and ~5 × 10^{-3} s^{-1} for an Ag-Ni catalyst (3:1 weight ratio)

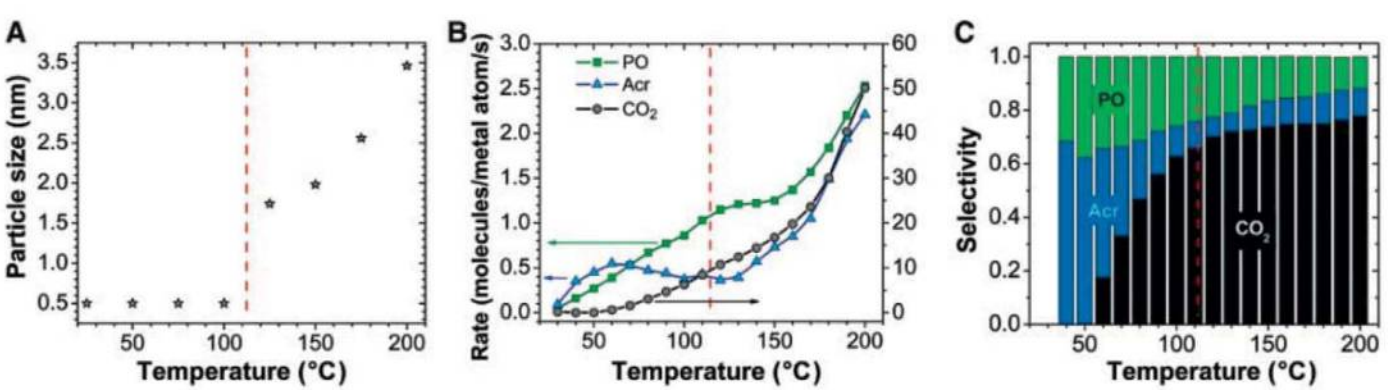

Fig. 1. (**A**) Temperature-dependent average cluster size from GISAXS. (**B**) Rate of propylene oxidation toward propylene oxide (PO), acrolein (Acr), and CO_2 per surface silver atom. (**C**) Selectivity of propylene oxide, acrolein, and CO_2 versus temperature. The vertical dashed lines indicate the temperature at which the sintering of the silver trimers begins. During an additional hour of reaction at 200°C, no change in the size of the aggregates was observed and the turnover rate for propylene oxide decreased to 1.55 s^{-1}, which likely indicates annealing of the newly formed nanostructure. The data shown are results from one run. The estimated uncertainty of GISAXS is ~ ±0.2 nm and ~5% for the turnover rates (*25*).

tested in the 150° to 300°C temperature range (*27*). Thus, the observed turnover rates in this work are orders of magnitude higher than the previously reported data (*25*). With respect to other subnanometer catalysts, the turnover rate of Ag_3 is greater by a factor of 4 than that obtained for Au_{6-10} under identical reaction conditions with comparable selectivity toward propylene oxide (*17*). Also, x-ray photoemission spectroscopy (XPS) analysis of carbon coverage yielded no evidence of degradation of the catalytic activity of the aggregates over 4 hours, nor any evidence of deactivation by carbon.

The electronic structure of small clusters and nanoparticles can control catalytic activity (*28*, *29*). We carried out an ultrahigh-vacuum x-ray photoemission (UHV XPS) experiment on the Ag_3 clusters and in situ XPS on the Ag nanoparticles in the presence of the reactants and under reaction conditions (*25*) to determine the oxidation state of silver. The Ag_3 clusters show a typical positive shift and broadening of the Ag 3d core level characteristic for small supported clusters (*29*, *30*). The 3d (5/2) core level was observed at ~368.6 eV when the energy scale was aligned according to the Si 2p (3/2) metallic core level of the substrate at 99.2 eV. The observed shift of the Ag 3d core level of the Ag_3 clusters is 0.2 to 0.4 eV less than that reported for small silver clusters of similar size (*31*, *32*), which indicates that the silver trimers are partially oxidized. (If silver is oxidized, Ag 3d is negatively shifted, as opposed to the core levels of almost all other elements.) This observation is confirmed by the results of theoretical calculations, which show increased positive charge on Ag_3 with an oxygen atom adsorbed (*25*).

An in situ XPS measurement performed on Ag particles 2 nm in height and 4 nm in diameter (*25*) showed that even these particles exhibited broadening and positive shifts in the Ag 3d spectrum relative to the metallic reference. Considering the magnitude of the shift and the size of these particles, as well as the fact that the spectrum can be described with one Gauss-Lorenz curve, it is likely that the silver nanoparticles are mostly metallic during propylene oxidation, with any oxidized contribution below 5%.

We carried out periodic, self-consistent density functional (PW91) calculations to understand the observation that Ag_3 clusters on an alumina support catalyze propylene epoxidation with only a negligible amount of carbon dioxide and high activity at low temperatures. Previous computational work on this reaction has focused exclusively on idealized single-crystal Ag surfaces (*33*). Torres *et al.* have reported a density functional theory (DFT) study of propylene epoxidation on an Ag(111) surface (*34*). They investigated two reaction pathways: (i) oxygen transfer from the silver surface to the propylene via an oxametallacycle intermediate for the formation of propylene oxide, and (ii) hydrogen abstraction from propylene by surface oxygen to form an allyl radical that is postulated to lead to combustion products. The latter pathway had a lower barrier, which is consistent with combustion being favored over epoxidation on Ag(111). In contrast, combustion products are not as favorable in ethylene epoxidation on a silver surface because it is not possible to form an allyl-like species from ethylene (*35*). The high activity and small amount of combustion products at low temperatures observed for Ag_3 suggest that the reaction mechanism is different from that at the Ag(111) surface, and this was confirmed by our DFT calculations.

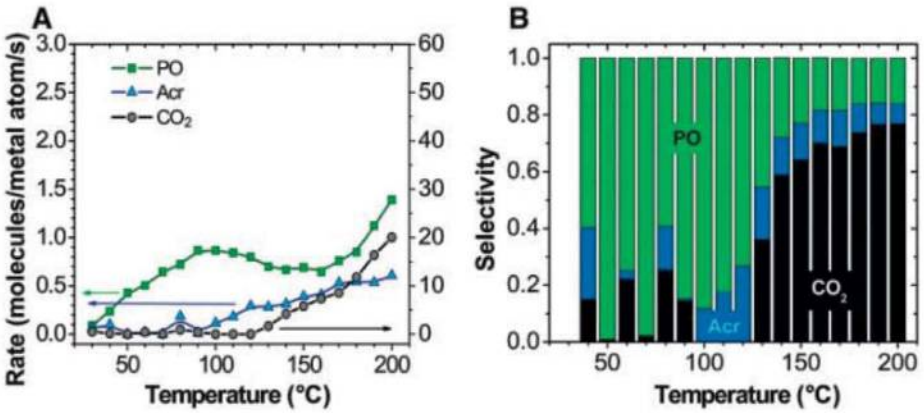

Fig. 2. (**A** and **B**) Rate of propylene oxidation toward propylene oxide, acrolein, and CO_2 per surface silver atom (A) and selectivity (B) on the nanometer-sized, sintering-resistant silver aggregates that formed from Ag_3 clusters during the first reaction cycle. The turnover rate of 1.4 s^{-1} for propylene oxide at 200°C is in agreement with the activity data obtained after annealing of the sample at 200°C. This finding and the comparable selectivities observed at 200°C (compare Fig. 1C with Fig. 2B) indicate a high stability of the ~3.5-nm catalyst during 4 hours of reaction.

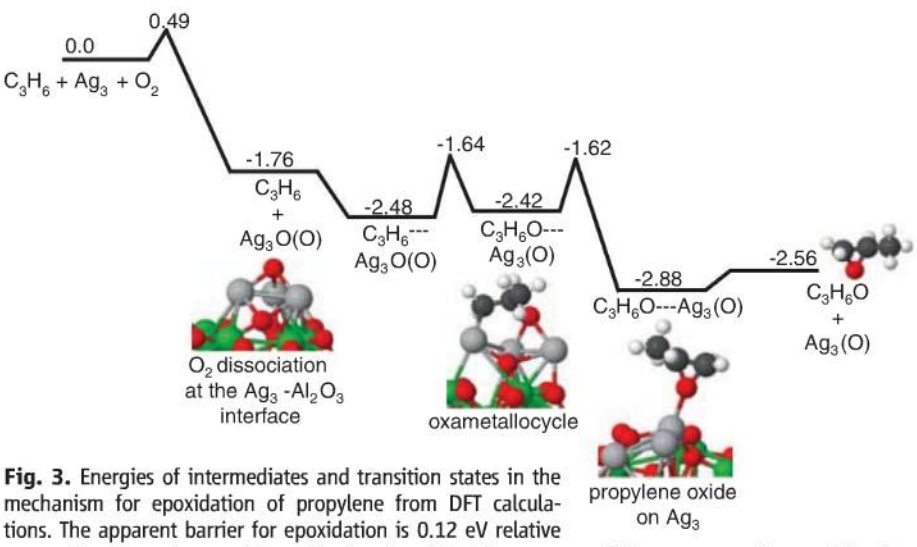

Fig. 3. Energies of intermediates and transition states in the mechanism for epoxidation of propylene from DFT calculations. The apparent barrier for epoxidation is 0.12 eV relative to gas-phase propylene and Ag_3 with dissociated O_2. There are two different oxygen sites resulting from dissociation of O_2 at the trimer-alumina surface interface: (i) the three-fold site on Ag_3, and (ii) alumina at the interface with Ag_3. The latter oxygen is indicated in parentheses. The reaction pathway as shown will result in excess interface oxygen, which can be removed either by migration to the three-fold site (calculated barrier of ~1 eV) or by diffusion and recombination on the alumina surface [diffusion on the surface should be possible according to (*37*)].

Reaction pathways for propylene epoxidation and acrolein formation were investigated; the results, including some key intermediate structures, are summarized in Figs. 3 and 4. An Ag_3 cluster adsorbed on a (010) θ alumina surface was used as a model for the catalytic reaction site. Our calculations indicate that dissociation of the oxygen molecule occurs at the interface of Ag_3 and the alumina surface with a barrier of 0.49 eV. This result suggests that two types of oxygen atoms are present at Ag_3 sites (Figs. 3 and 4): one at the interface of Ag_3 and the alumina surface, and the other in the three-fold site on Ag_3. The barrier for O_2 dissociation at the interface is much lower than the barrier of 1.19 eV on an Ag(111) surface for 0.33 monolayer of O_2. In the analysis that follows, given the low dissociation barrier and strong oxygen binding, we assume that dissociative O_2 adsorption is equilibrated and that the two types of sites available to oxygen atoms are occupied at high coverage.

The energetics of the proposed epoxidation mechanism from the DFT calculations are

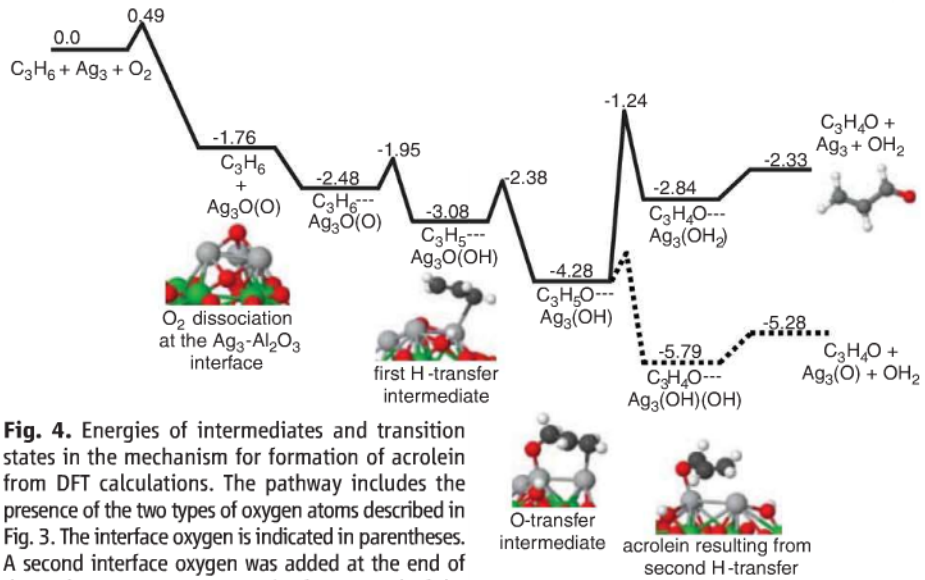

Fig. 4. Energies of intermediates and transition states in the mechanism for formation of acrolein from DFT calculations. The pathway includes the presence of the two types of oxygen atoms described in Fig. 3. The interface oxygen is indicated in parentheses. A second interface oxygen was added at the end of the pathway to assess energetics for removal of the second hydrogen. The required starting $Ag_3O(O)(O)$ configuration for this can be formed by O_2 dissociation on the $Ag_3(O)$ resulting from propylene epoxidation. Because acrolein formation involves removal of both types of oxygen atoms, it will be a closed catalytic cycle.

summarized in Fig. 3. After O_2 dissociation at the Ag_3-alumina interface, the first step involves oxygen transfer from the three-fold site to propylene to form an oxametallacyle (Fig. 3). This reaction has an apparent barrier of 0.12 eV relative to gas-phase propylene and Ag_3 with dissociated O_2 (this is the appropriate reference state for the effective barrier for epoxidation, assuming that propylene adsorption is weakly transient and does not compete directly with oxygen for adsorption sites). The second step involves oxygen addition to the double bond and is exothermic. Reaction pathways occurring from the oxametallacycle intermediate leading to the formation of other products such as acrolein, carbon dioxide, and propanal were investigated and found to be unfavorable. The apparent barrier for the first step of 0.12 eV is in good agreement with the experimental estimate for propylene oxide formation of 0.27 ± 0.1 eV (*25*).

An alternative pathway based on hydrogen abstraction from propylene leads to acrolein formation (Fig. 4). The first step involves hydrogen abstraction by the interface oxygen from the methyl group to form an allyl-like intermediate and an OH group. No barrier for this reaction is found relative to the gas-phase propylene and Ag_3 with dissociated O_2, in agreement with our experimental results (*25*). The second step involves oxygen addition to the allyl-like intermediate and is again exothermic. Formation of acrolein requires abstraction of a second hydrogen, and the DFT calculations indicate that it is highly unfavorable to transfer this additional hydrogen atom to the existing interfacial OH group (resulting in water formation). In contrast, abstraction by a second interfacial oxygen (formed during a previous catalytic cycle) to form an OH group is thermodynamically favorable. The acrolein pathway is also likely to result in combustion products, as it is usually assumed that allyl-like intermediates can initiate combustion (*34*). Further evidence for this hypothesis comes from the experimental observation that combustion and acrolein formation occur in the same reaction channel.

Our DFT investigation can account for the surprisingly high catalytic activity and selectivity found for the silver trimers. The calculations indicate that an alumina-supported Ag_3O cluster has a substantial net spin density (~0.6) on the Ag and O in the cluster. In contrast, there is no spin density present when atomic oxygen is adsorbed on an Ag(111) surface, assuming low oxygen coverage. Such a surface has a barrier to oxametallacycle formation of ~0.7 eV from our calculations and those of Torres *et al.* (*34*), which compares to 0.12 eV for the trimer. In addition, we calculated the spin density on an alumina-supported closed-shell Ag_4O cluster and found it to be zero. The barrier to formation of an oxametallacycle structure was calculated on a gas-phase Ag_4O cluster and is much higher (0.5 eV) than that of the trimer. Thus, the results for both the Ag(111) surface and the Ag_4 cluster suggest that the partially filled s-d hybridized energy level of the supported oxidized Ag_3 cluster gives it an open-shell electronic structure character, which makes it highly reactive toward the propylene double bond. This result is consistent with the observed higher activity for propylene oxide formation and the small amount of CO_2 produced at low temperatures (because CO_2 formation is initiated by C-H bond activation rather than by oxygen attack). The experimental barrier for CO_2 formation is much greater at 0.7 ± 0.2 eV (*25*), which is consistent with the calculated O_2 dissociation barrier of 0.5 eV and suggests that combustion of propylene, which requires more oxygen and involves strongly interacting propylene fragment intermediates that can impede O_2 dissociation, has O_2 dissociation as its rate-limiting step. The high activity of the 2 nm × 4 nm nanoparticles, which is the same per surface atom as the Ag_3 clusters, may also be due to electronic effects involving surface spin density sites similar to Ag_3, or possibly some other electronic structure feature. The surfaces of the nanoparticles resulting from agglomeration of the trimers are likely to have disordered structures, as extrapolated from scanning tunneling microscopy and molecular dynamics studies (*36*) of Ag nanoparticles with shapes and sizes similar to those we observed. Density functional calculations (*25*) indicate that Ag nanoclusters with structural disorder have isomers very close in energy, including some in high spin states; therefore, propylene epoxidation may be catalyzed by surface spin density on the agglomerated nanoparticles.

In the case of acrolein formation, the oxygen at the interface of the Ag_3 cluster is highly reactive for hydrogen abstraction from propylene, with no barrier for the first hydrogen abstraction step from DFT calculations. This can account for the high activity observed for acrolein formation on the silver trimer and the small amount of CO_2 produced at low temperatures. The much smaller amount of acrolein produced on the nanoparticles is consistent with an acrolein reaction mechanism based on hydrogen abstraction by the interfacial oxygen, as opposed to the oxygen adsorbed on a three-fold site; the amount of interfacial oxygen will be much smaller for the nanoparticles than for the Ag trimers. The smaller fraction of nanoparticle-alumina interfacial sites for O_2 dissociation may also explain why the combustion products desorb at a higher temperature on the nanoparticles than on the Ag trimers. The proposed acrolein reaction mechanism suggests that addition of H_2O to the feed stream could reduce the acrolein production and enhance propylene epoxidation formation, because water is a product on this pathway (Fig. 4). This expectation is in accord with the pronounced effect of water in increasing the selectivity toward propylene oxide formation observed in the case of Au_{6-10} clusters (*17*).

References and Notes

1. K. Weissermel, H.-J. Arpe, *Industrial Organic Chemistry* (Wiley-VCH, Weinheim, Germany, ed. 4, 2003).
2. J. Lu, J. J. Bravo-Suárez, A. Takahashi, M. Haruta, S. T. Oyama, *J. Catal.* **232**, 85 (2005).
3. T. A. R. Nijhuis, T. Visser, B. M. Weckhuysen, *Angew. Chem. Int. Ed.* **44**, 1115 (2005).
4. T. Hayashi, K. Tanaka, M. Haruta, *J. Catal.* **178**, 566 (1998).
5. F. W. Zemichael, A. Palermo, M. S. Tikhov, R. M. Lambert, *Catal. Lett.* **80**, 93 (2002).
6. R. M. Lambert, F. J. Williams, R. L. Cropley, A. Palermo, *J. Mol. Catal. Chem.* **228**, 27 (2005).
7. M. F. Luo, J. Q. Lu, C. Li, *Catal. Lett.* **86**, 43 (2003).
8. W. Yao *et al.*, *Catal. Lett.* **119**, 185 (2007).
9. J. G. Serafin, A. C. Liu, S. R. Seyedmonir, *J. Mol. Catal. Chem.* **131**, 157 (1998).

10. M. A. Barteau, R. J. Madix, *J. Am. Chem. Soc.* **105**, 344 (1983).
11. Z. Xu *et al.*, *Nature* **372**, 346 (1994).
12. M. S. Chen, D. W. Goodman, *Science* **306**, 252 (2004); published online 26 August 2004 (10.1126/science.1102420).
13. C. Lemire, R. Meyer, S. Shaikhutdinov, H.-J. Freund, *Angew. Chem. Int. Ed.* **43**, 118 (2004).
14. A. T. Bell, *Science* **299**, 1688 (2003).
15. F. Tao *et al.*, *Science* **322**, 932 (2008); published online 9 October 2008 (10.1126/science.1164170).
16. A. L. de Oliveira, A. Wolf, F. Schuth, *Catal. Lett.* **73**, 157 (2001).
17. S. Lee *et al.*, *Angew. Chem. Int. Ed.* **48**, 1467 (2009).
18. S. Vajda *et al.*, *Nat. Mater.* **8**, 213 (2009).
19. L. D. Socaciu *et al.*, *J. Chem. Phys.* **120**, 2078 (2004).
20. J. W. Elam, Z. A. Sechrist, S. M. George, *Thin Solid Films* **414**, 43 (2002).
21. R. E. Winans *et al.*, *Top. Catal.* **39**, 145 (2006).
22. D. H. Kim, Y. H. Chin, J. H. Kwak, J. Szanyi, C. H. F. Peden, *Catal. Lett.* **105**, 259 (2005).
23. S. Wodiunig, J. M. Keel, T. S. E. Wilson, F. W. Zemichael, R. M. Lambert, *Catal. Lett.* **87**, 1 (2003).
24. S. Vajda *et al.*, *J. Chem. Phys.* **131**, 121104 (2009).
25. See supporting material on *Science* Online.
26. L. Benz *et al.*, *J. Chem. Phys.* **122**, 081102 (2005).
27. A. Takahashi, N. Hamakawa, I. Nakamura, T. Fujitani, *Appl. Catal. A* **294**, 34 (2005).
28. R. Dietsche *et al.*, *Appl. Phys. A* **90**, 395 (2008).
29. W. E. Kaden, T. Wu, W. A. Kunkel, S. L. Anderson, *Science* **326**, 826 (2009).
30. W. F. Egelhoff Jr., *Surf. Sci. Rep.* **6**, 253 (1987).
31. R. Dietsche, thesis, Univesität Konstanz (2009).
32. K. Luo *et al.*, *J. Phys. Chem. B* **109**, 4064 (2005).
33. M. C. Zonnevylle, R. Hoffmann, P. J. Vandenhoek, R. A. van Santen, *Surf. Sci.* **223**, 233 (1989).
34. D. Torres, N. Lopez, F. Illas, R. M. Lambert, *Angew. Chem. Int. Ed.* **46**, 2055 (2007).
35. S. Linic, M. A. Barteau, *J. Am. Chem. Soc.* **125**, 4034 (2003).
36. R. E. Palmer, S. Pratontep, H. G. Boyen, *Nat. Mater.* **2**, 443 (2003).
37. P. Gamallo, R. Sayós, *Phys. Chem. Chem. Phys.* **9**, 5112 (2007).
38. Work at Argonne National Laboratory was supported by the U.S. Department of Energy, Office of Basic Energy Sciences (Chemical Sciences, Materials Sciences, and Scientific User Facilities), under contract DE-AC-02-06CH11357. We thank the BESSY staff for their support. Also supported by the American Chemical Society Petroleum Research Fund (Y.L. and R.J.M.) and the U.S. Air Force Office of Scientific Research (S.V.). We acknowledge grants of computer time at the Molecular Science Computing Facility at Pacific Northwest National Laboratory and the Laboratory Computing Resource Center at Argonne National Laboratory. A Full Utility Patent Application was filed by Argonne in March 2009, entitled "Subnanometer and Nanometer Catalysts, Method for Preparing Size-Selected Catalyst" (Application 12/402,948).

Supporting Online Material

www.sciencemag.org/cgi/content/full/328/5975/224/DC1
Materials and Methods
Figs. S1 to S27
Tables S1 to S4
References

25 November 2009; accepted 24 February 2010
10.1126/science.1185200

Metabolic Syndrome and Altered Gut Microbiota in Mice Lacking Toll-Like Receptor 5

Matam Vijay-Kumar,[1] Jesse D. Aitken,[1] Frederic A. Carvalho,[1] Tyler C. Cullender,[2] Simon Mwangi,[3] Shanthi Srinivasan,[3] Shanthi V. Sitaraman,[3] Rob Knight,[4] Ruth E. Ley,[2] Andrew T. Gewirtz[1]*

Metabolic syndrome is a group of obesity-related metabolic abnormalities that increase an individual's risk of developing type 2 diabetes and cardiovascular disease. Here, we show that mice genetically deficient in Toll-like receptor 5 (TLR5), a component of the innate immune system that is expressed in the gut mucosa and that helps defend against infection, exhibit hyperphagia and develop hallmark features of metabolic syndrome, including hyperlipidemia, hypertension, insulin resistance, and increased adiposity. These metabolic changes correlated with changes in the composition of the gut microbiota, and transfer of the gut microbiota from TLR5-deficient mice to wild-type germ-free mice conferred many features of metabolic syndrome to the recipients. Food restriction prevented obesity, but not insulin resistance, in the TLR5-deficient mice. These results support the emerging view that the gut microbiota contributes to metabolic disease and suggest that malfunction of the innate immune system may promote the development of metabolic syndrome.

Humanity is facing an epidemic of interrelated metabolic diseases collectively referred to as metabolic syndrome, the hallmarks of which include hyperglycemia, hyperlipidemia, insulin resistance, obesity, and hepatic steatosis (*1*). The increasing incidence of metabolic syndrome is widely thought to result from nutrient excess due to increased food consumption and/or reduced levels of physical activity. Such nutrient excess results in obesity and may activate endoplasmic reticulum stress pathways resulting in chronic activation of proinflammatory kinase cascades that desensitize the metabolic response to insulin (*2*). Such insulin resistance can result in hyperglycemia and, in some cases, type 2 diabetes. Recent work suggests a possible role for the gut microbiota in obesity (*3*) and, consequently, other aspects of metabolic syndrome. In both humans and mice, the development of obesity correlates with shifts in the relative abundance of the two dominant bacterial phyla in the gut, the *Bacteroidetes* and the *Firmicutes* (*4*–*6*). In addition, it has been shown that transfer of the gut microbiota from obese (*ob/ob*) mice to germ-free wild-type (WT) recipients leads to an increase in fat mass in the recipients, leading to speculation that the gut microbiota promotes obesity by increasing the capacity of the host to extract energy (calories) from ingested food (*7*).

The gut microbiota is shaped by both environment and host genetics, with the innate immune system in particular, long appreciated for its role in defending against infection by pathogenic microbes, now suggested to play a key role in regulating the gut microbiota (*8*). Thus, in addition to its role in infection/inflammation, innate immunity may play a key role in promoting metabolic health. Toll-like receptor (TLR) 5 is a transmembrane protein that is highly expressed in the intestinal mucosa and that recognizes bacterial flagellin. In previous work with mice genetically deficient in TLR5 (T5KO mice), we found that 10% of the mutant mice exhibited severe colitis and an additional 30% exhibited gross and/or histopathologic evidence of colitis (*9*). The remaining 60% of the T5KO mice exhibited broadly elevated proinflammatory gene expression but lacked the histopathologic features that define colitis; however, we observed that, by 4 weeks of age, these mice had body masses that were on average 15% higher than those of their WT littermates. To eliminate potential opportunistic pathogens that may have been present in T5KO and WT littermates, and to make their gut microbiota similar to that of mice from the Jackson Laboratory (the world's largest supplier of research mice), we "rederived" T5KO mice by transplanting embryos into mice purchased from this supplier (*10*). Such standardization of the microbiota in the T5KO mice greatly attenuated the severity of their colitis and resulted in a more uniform phenotype characterized by mild inflammation (fig. S1) and obesity (Fig. 1).

Analysis of these rederived mice showed that, at 20 weeks of age, both male and female T5KO mice had body masses that were 20% greater than those of WT mice (Fig. 1A). Magnetic resonance imaging (MRI) revealed increased fat mass throughout the body of the T5KO mice, with a particular increase in visceral fat (Fig. 1B). T5KO mice had epididymal fat pads that were about twice as large as those in WT littermates at 20 weeks of age (Fig. 1, C and D). This increase

[1]Department of Pathology, Emory University, Atlanta, GA 30322, USA. [2]Department of Microbiology, Cornell University, Ithaca, NY 14853, USA. [3]Department of Medicine, Emory University, Atlanta, GA 30322, USA. [4]Howard Hughes Medical Institute, Department of Chemistry and Biochemistry, University of Colorado, Boulder, CO 80309, USA.

*To whom correspondence should be addressed. E-mail: agewirt@emory.edu

in fat mass correlated with a substantial increase in serum levels of triglycerides and cholesterol and with an increase in blood pressure (Fig. 1, E to G), features often associated with metabolic syndrome. Ex vivo analysis revealed higher production of proinflammatory cytokines interferon-γ (IFN-γ) and interleukin-1β (IL-1β) in T5KO adipose tissue versus WT adipose tissue (fig. S2), which suggests that increased adiposity may play a role in perpetuating the low-grade chronic inflammation exhibited by the mutant mice.

We next examined blood glucose levels of T5KO and WT littermates. After an overnight (15-hour) fast, T5KO mice exhibited mild but statistically significant elevations in blood glucose relative to WT littermates (Fig. 2A). Consistent with mild loss of glycemic control, when administered a bolus of glucose, T5KO mice showed impaired ability to restore blood glucose to baseline levels (Fig. 2B). In contrast to the modest effects of T5KO deficiency on glucose homeostasis, basal insulin levels were substantially elevated in T5KO mice (Fig. 2C), as was the amount of insulin produced in response to glucose challenge (Fig. 2D). The T5KO mice also exhibited a reduced response to exogenous insulin relative to WT mice (Fig. 2E), all features consistent with a state of insulin resistance. Accordingly, T5KO mice showed elevated serum levels of the adipokine lipocalin-2 (fig. S1E), which promotes insulin resistance (*11*), and exhibited an increase in the number and size of pancreatic islets that immunostained positive for insulin (Fig. 2F and fig. S3). These data suggest that T5KO mice have mild loss of glycemic control that is likely driven by insulin resistance and partially compensated for by increased insulin production—conditions typically seen in humans with metabolic syndrome.

Development of metabolic syndrome in humans is thought to be promoted by a diet high in saturated fats. To investigate the effect of such a diet on metabolic syndrome in T5KO mice, we fed the mice a high-fat diet for 8 weeks. As expected, both WT and T5KO mice on this diet showed significant increases in body mass and fat-pad mass (fig. S4, A and B). Mice of both genotypes also had increased serum levels of triglycerides, cholesterol, leptin, and insulin (fig. S4, C to F). In contrast to WT mice, most T5KO mice on a high-fat diet had fasting glucose concentrations >120 mg/dL, indicating that they had become diabetic (Fig. 3A). High-fat-fed T5KO mice also exhibited inflammatory infiltrates in the pancreatic islets (Fig. 3B) and displayed hepatic steatosis, which is a severe manifestation of metabolic syndrome (Fig. 3B). Thus, the metabolic syndrome exhibited by T5KO mice was exacerbated by a high-fat diet.

We next investigated whether changes in food intake contributed to the development of metabolic syndrome in T5KO mice. We found that T5KO mice consumed about 10% more food than WT littermates (Fig. 3C) and, concomitantly, had greater stool output (fig. S5). Bomb calorimetry and short-chain fatty acid analysis of T5KO and WT feces indicated that loss of TLR5 did not significantly impact the efficiency of dietary energy harvest (fig. S6). We examined serum levels of major orexigenic (ghrelin and neuropeptide Y) and anorexic (leptin and GLP-1) hormones, but these experiments did not provide definitive mechanistic insight into the hyperphagic phenotype of the T5KO mice (fig. S7). To explore the role of hyperphagia in the metabolic abnormalities exhibited by T5KO mice, we performed food restriction experiments. Beginning at 4 weeks of age, groups of WT and T5KO mice were no longer given unlimited access to food but rather were given only the amount of food consumed by a control group of ad libitum–fed WT mice. Twelve weeks of this food restriction regimen prevented many of the metabolic abnormalities normally seen in T5KO mice, including increased body mass and fat-pad mass and increased serum levels of glucose, lipids, and insulin (Fig. 3, D to F, and fig. S8). However, such lean T5KO mice still exhibited a decreased response to exogenous insulin (Fig. 3G), which suggests that their insulin resistance is not entirely dependent on increased food consumption or adiposity. Given that insulin suppresses food intake (*12*), these results raise the possibility that the low-grade proinflammatory signaling in T5KO mice (*9*) attenuates insulin signaling, resulting in increased food consumption that drives other manifestations of metabolic syndrome.

In light of observations that the lipopolysaccharide (LPS) receptor TLR4 promotes diet-induced metabolic syndrome (*13*, *14*) and that TLR4 is required for T5KO colitis (*9*), we

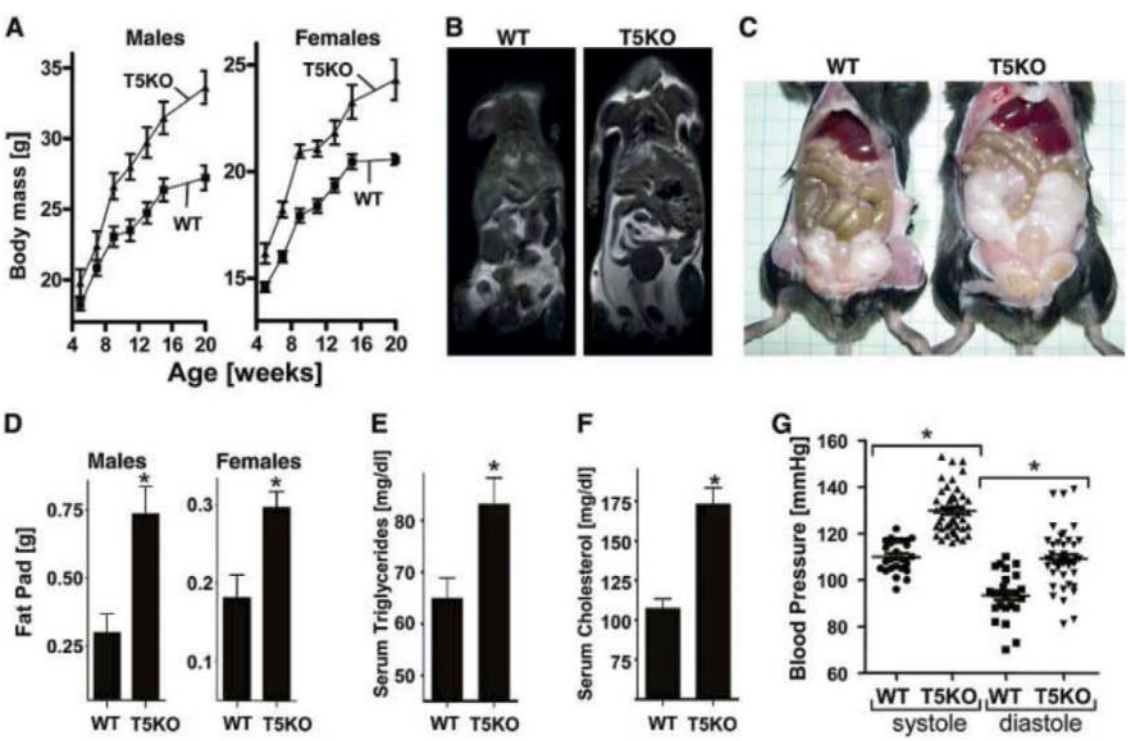

Fig. 1. T5KO mice develop obesity. T5KO mice and WT littermates were monitored for 20 weeks. **(A)** Body mass. **(B)** MRI image showing fat distribution. **(C)** Abdominal photograph of representative 20-week-old male mice. **(D)** Fat-pad mass. **(E)** Serum triglycerides. **(F)** Serum cholesterol. **(G)** Blood pressure. Results in (A) to (C) are from an individual experiment (n = 20, 10 males and 10 females) and representative of more than six distinct groups of mice. Results in (B) are representative of three separate analyses performed on mice that had median body mass of their litters. Results in (C) to (E) are from a single experiment (n = 6) and representative of several experiments. Results in (G) compare groups (n = 4) of mice with 5 to 10 independent measurements per mouse. *, $P < 0.05$.

hypothesized that TLR4 might mediate the metabolic syndrome exhibited by T5KO mice. However, loss of TLR5 in mice already deficient in either TLR2 or TLR4 still produced features of metabolic syndrome (figs. S9 and S10), arguing against this possibility. Mice lacking MyD88 did not mimic the metabolic syndrome exhibited by T5KO mice (fig. S11), suggesting a potential role for another TLR [besides TLR2 or TLR4 (all TLRs except TLR3 use MyD88)] and/or a role for cytokines such as IL-1β and IL-18 whose levels are increased in noncolitic T5KO mice (*9*) and whose receptors signal in a MyD88-dependent manner. We also observed that loss of TLR5 in RAG1-deficient mice, which lack T and B lymphocytes, still resulted in impaired glucose regulation (fig. S12), which suggests that development of T5KO metabolic syndrome does not require adaptive immunity.

We next considered the hypothesis that alterations in the gut microbiota resulting from loss of TLR5 promote the development of metabolic syndrome in these mice. To investigate this possibility, we placed T5KO mice on broad-spectrum antibiotics upon weaning for a period of 12 weeks. This treatment lowered total gut bacterial load by 90% and caused the enlargement of the ceca, as previously observed in germ-free mice (fig. S13). Analogous to observations made with mice exhibiting high-fat-diet–induced metabolic syndrome (*13*), we observed that decimation of the gut microbiota corrected T5KO metabolic syndrome relative to similarly treated WT mice (Fig. 4, A to C, and fig. S14). We next defined the extent to which loss of TLR5 altered the composition of the microbiota by pyrosequencing the 16S ribosomal RNA (rRNA) genes in the ceca. We generated a total of 22,712 partial 16S rRNA gene sequences (*15*). The relative abundance of bacterial phyla in the samples was

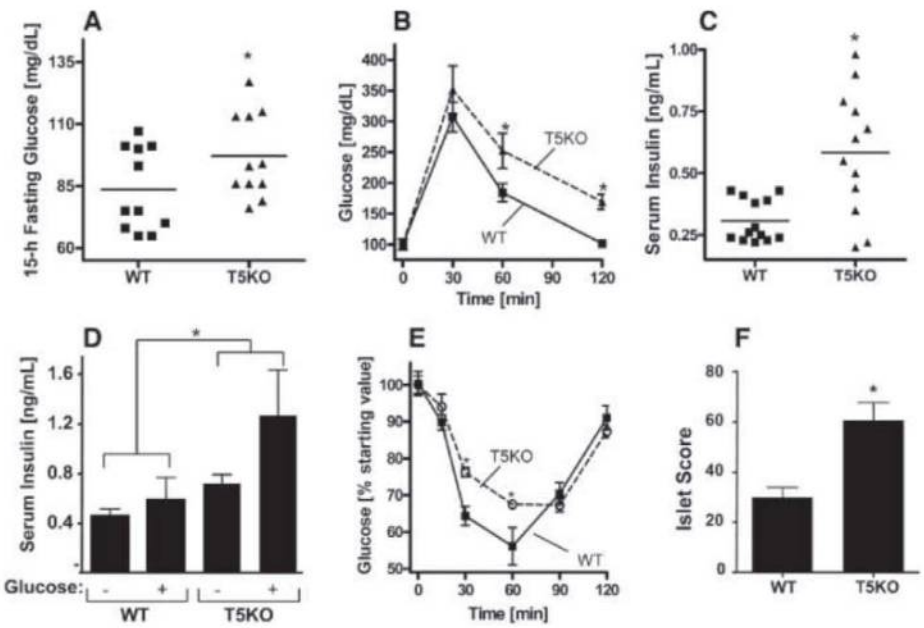

Fig. 2. T5KO exhibit hyperglycemia/insulin resistance. Twenty-week-old T5KO and WT littermate mice were assayed for various parameters of glucose homeostasis. (**A**) Fifteen-hour fasting blood glucose. (**B**) Glucose tolerance test. Mice were intraperitoneally injected with glucose (2 g per kg of body mass). (**C**) Serum insulin after a 5-hour fast. (**D**) Serum insulin levels before and 2.5 min after challenge with glucose (3 g/kg body mass). (**E**) Insulin sensitivity. Mice were fasted for 5 hours and intraperitoneally injected with insulin (1.0 U/kg body mass). (**F**) Hematoxylin and eosin (H&E) stained pancreata were blindly scored for size and number of pancreatic islets. Results in (A), (C), and (F) are from an individual experiment (n = 12 to 13) and representative of more than six distinct groups of mice. Results in (B), (D), and (E) are from a single experiment (n = 6) and representative of several experiments. *, $P < 0.05$.

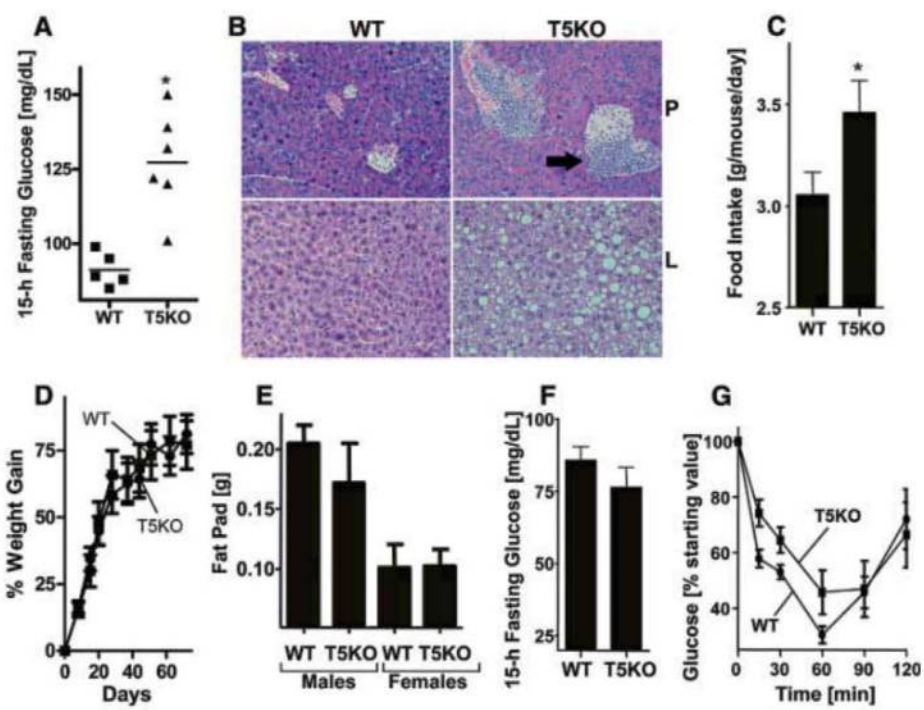

Fig. 3. T5KO metabolic syndrome depends on hyperphagia. (**A** and **B**) Four-week-old WT and T5KO mice were given a high-fat diet for 8 weeks. (A) Fifteen-hour fasting blood glucose. (B) H&E stained pancreas (P, upper panel) and liver (L, lower panel). Arrows point to inflammatory infiltrates. (**C**) Mice on a regular diet were monitored for food intake. (**D** to **G**) Mice were subjected to food restriction and assayed for (D) body mass and (E) fat-pad mass. (F) Fifteen-hour fasting glucose. (G) Insulin sensitivity measured as described in Fig. 2E. Results in (A) and (B) are from a single experiment (n = 5 to 6) and representative of two independent experiments. Results in (C) are from a single experiment (n = 6) and representative of similar results with several groups of mice. (D) to (G) is from a single experiment (n = 10) and representative of two independent experiments. *, $P < 0.05$.

similar to that reported in other studies (*Firmicutes*, 54%; *Bacteroidetes*, 39.8%; *Proteobacteria*, 1.1%; *Tenericutes*, *Actinobacteria*, *TM7*, and *Verrucomicrobia*, <0.2% of the sequences). In contrast to what has been seen with *ob/ob* mice, we found that the gut bacterial communities of T5KO and WT mice had similar relative abundances of *Firmicutes* and *Bacteroidetes*. However, UniFrac analysis, which compares bacterial communities based on the premise that similar communities are those that share a greater fraction of the overall phylogenetic tree (*16*), indicated that the gut microbiotas of T5KO and WT littermate mice were significantly different in their species composition (fig. S15). In addition, despite the marked interindividual differences in species diversity typical of mice (and humans), we observed 116 bacterial phylotypes from various phyla to be consistently enriched or reduced in T5KO mice relative to WT mice (figs. S16 and S17, and tables S1 and S2). Thus, in contrast to the *ob/ob* mouse model of obesity, where the alteration of the microbiota was characterized by a phylum-level shift without amplification or loss of particular species, here we have identified a specific suite of bacterial species whose abundance is altered by loss of TLR5. These phylotypes are typical of murine gut bacteria in general and related to a variety of gut bacteria identified by culture-independent analysis of human gut microbiota (table S3).

The inability to culture most gut bacteria makes assessment of their causal role in health and disease technically challenging. To investigate whether the changes in the gut microbiota were a cause or consequence of the metabolic syndrome in T5KO mice, we transplanted the T5KO microbiota into WT germ-free mice, which, like newborn mice, can be colonized by a diverse microbiota in a manner that preserves the complex composition of the transferred organisms (*17*). In principle, any gut microbial dysbiosis present in the host would be transferred to the recipient (*7*, *18*). We found that the transplanted T5KO microbiota conferred many aspects of the T5KO phenotype to the WT germ-free hosts, including hyperphagia, obesity, hyperglycemia, insulin resistance, colomegaly, and elevated levels of proinflammatory cytokines (Fig. 4, D to H, and fig. S18). This suggests that the changes in the gut microbiota observed in the T5KO mice are likely to be a contributing factor in the development of metabolic syndrome in the mice.

In summary, we have shown that loss of TLR5 results in a phenotype reminiscent of human metabolic syndrome. The underlying molecular mechanisms remain to be defined, but we speculate that loss of TLR5 produces alterations in the gut microbiota that induce low-grade inflammatory signaling. This signaling may in turn cross-desensitize insulin receptor signaling, leading to hyperphagia, which then drives other aspects of metabolic syndrome (fig. S19). Our results suggest that the specific composition of microbiota to which individuals are first exposed may be an important means by which early environment exerts a lasting influence on metabolic phenotype. They also suggest that the excess caloric consumption driving the current epidemic of metabolic syndrome may be caused, at least in part, by alterations in host-microbiota interactions.

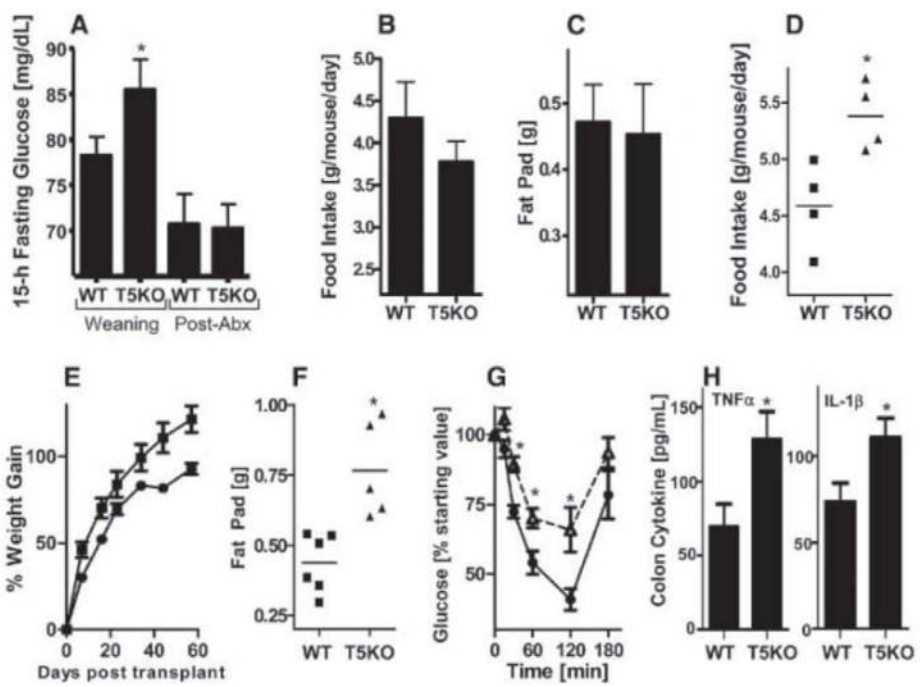

Fig. 4. T5KO gut microbiota is necessary and sufficient to transfer metabolic syndrome phenotype to germ-free mice. (**A** to **C**) Four-week-old T5KO mice and WT littermates were placed on broad-spectrum antibiotics and monitored for 12 weeks. (A) Fifteen-hour fasting glucose. (B) Food intake. (C) Fat-pad mass. (**D** to **H**) Four-week-old WT germ-free mice were intragastrically administered cecal content from WT or T5KO mice and monitored for 7 weeks. (D) Food intake expressed as average consumption per mouse per day 10 to 13 days after transplant. (E) Body mass. (F) Fat-pad mass. (G) Insulin sensitivity. (H) Colonic tumor necrosis factor–α (TNF-α) and IL-1β. Results in (A) to (C) are from a single experiment (n = 5 to 6) and representative of two independent experiments (other shown in fig. S14). Results in (D) to (H) are from a single experiment (n = 5 to 6). *, $P < 0.05$.

References and Notes

1. Y. Wang, M. A. Beydoun, L. Liang, B. Caballero, S. K. Kumanyika, *Obesity* **16**, 2323 (2008).
2. G. S. Hotamisligil, E. Erbay, *Nat. Rev. Immunol.* **8**, 923 (2008).
3. F. Bäckhed *et al.*, *Proc. Natl. Acad. Sci. U.S.A.* **101**, 15718 (2004).
4. R. E. Ley *et al.*, *Proc. Natl. Acad. Sci. U.S.A.* **102**, 11070 (2005).
5. R. E. Ley, P. J. Turnbaugh, S. Klein, J. I. Gordon, *Nature* **444**, 1022 (2006).
6. P. J. Turnbaugh *et al.*, *Nature* **457**, 480 (2009).
7. P. J. Turnbaugh *et al.*, *Nature* **444**, 1027 (2006).
8. E. Slack *et al.*, *Science* **325**, 617 (2009).
9. M. Vijay-Kumar *et al.*, *J. Clin. Invest.* **117**, 3909 (2007).
10. Materials and methods are available as supporting material on *Science* Online.
11. Q. W. Yan *et al.*, *Diabetes* **56**, 2533 (2007).
12. S. C. Woods, E. C. Lotter, L. D. McKay, D. Porte Jr., *Nature* **282**, 503 (1979).
13. P. D. Cani *et al.*, *Diabetes* **57**, 1470 (2008).
14. H. Shi *et al.*, *J. Clin. Invest.* **116**, 3015 (2006).
15. The GenBank accession number for the 16S pyrosequencing data set is SRA009446.
16. C. Lozupone, R. Knight, *Appl. Environ. Microbiol.* **71**, 8228 (2005).
17. P. J. Turnbaugh *et al.*, *Sci. Transl. Med.* **1**, 6ra14 (2009).
18. W. S. Garrett *et al.*, *Cell* **131**, 33 (2007).

19. We thank F. A. Anania, D. G. Harrison, and I. R. Williams for valuable discussions and comments, and N. Scalfone and M. Hamady for technical assistance. This work was supported by an NIH grant (DK061417 and an associated American Recovery and Reinvestment Act supplement) and a Senior Award from the Crohn's and Colitis Foundation of America (CCFA) to A.T.G. M.V.-K. is a recipient of Career Development Awards from CCFA and K01 (DK083275) from NIH. This research used a Digestive Disease Research and Development Center (DDRDC) core facility that is supported by NIH grant DK06439.

Supporting Online Material

www.sciencemag.org/cgi/content/full/science.1179721/DC1
Materials and Methods
Figs. S1 to S19
Tables S1 to S3
References

27 July 2009; accepted 19 February 2010
Published online 4 March 2010;
10.1126/science.1179721
Include this information when citing this paper.

Variation in Transcription Factor Binding Among Humans

Maya Kasowski,[1]* Fabian Grubert,[1,2]* Christopher Heffelfinger,[1] Manoj Hariharan,[1,2] Akwasi Asabere,[1] Sebastian M. Waszak,[3,4] Lukas Habegger,[5] Joel Rozowsky,[6] Minyi Shi,[1,2] Alexander E. Urban,[1,7] Mi-Young Hong,[1] Konrad J. Karczewski,[2] Wolfgang Huber,[3] Sherman M. Weissman,[7] Mark B. Gerstein,[5,6,8] Jan O. Korbel,[3,9]† Michael Snyder[1,2]†

Differences in gene expression may play a major role in speciation and phenotypic diversity. We examined genome-wide differences in transcription factor (TF) binding in several humans and a single chimpanzee by using chromatin immunoprecipitation followed by sequencing. The binding sites of RNA polymerase II (PolII) and a key regulator of immune responses, nuclear factor κB (p65), were mapped in 10 lymphoblastoid cell lines, and 25 and 7.5% of the respective binding regions were found to differ between individuals. Binding differences were frequently associated with single-nucleotide polymorphisms and genomic structural variants, and these differences were often correlated with differences in gene expression, suggesting functional consequences of binding variation. Furthermore, comparing PolII binding between humans and chimpanzee suggests extensive divergence in TF binding. Our results indicate that many differences in individuals and species occur at the level of TF binding, and they provide insight into the genetic events responsible for these differences.

Differences in gene expression have been observed in a variety of species (*1*–*3*). However, the extent to which transcription factor (TF) binding differences occur both among individuals and between closely related species, and the global relationship between TF binding and genetic variation, are largely unexplored (*4*). We used chromatin immunoprecipitation followed by sequencing (ChIP-Seq) to map nuclear factor κB (NFκB) and RNA polymerase II (PolII) binding sites in 10 humans: 5 are of European ancestry (including a parent-offspring trio), 2 of eastern Asian ancestry, and 3 of Nigerian ancestry (table S1); 9 of these have been analyzed by the HapMap (*5*) and the 1000 Genomes (*6*) projects, and one represents an individual for whom extensive structural variant (SV) maps are available (*7*, *8*). All individuals but one were females; in pairwise comparisons, modest differences in TF binding were observed between the male and 9 females; our analyses thus combined results from all 10 humans. For comparison we also analyzed PolII binding in one female chimpanzee.

We used stringent criteria to identify binding peaks (*9*), and clustered them into discrete binding regions (BRs) (*10*), yielding a total of 15,522 and 19,061 BRs for NFκB and PolII, respectively. Within BRs, most peaks were similar in position and magnitude among individuals (fig. S1A). However, significant differences in binding were observed (fig. S1A), and the Spearman correlation coefficients among replicates of different individuals (median values 0.79 and 0.90 for NFκB and PolII, respectively) were less than that of biological replicates of a given individual (median values 0.90 and 0.95, respectively) (fig. S2A and table S2). Seven and a half and 25% of the NFκB and PolII BRs, respectively, differed significantly between two individuals [analysis of variance test (*10*), Bonferroni-adjusted P value < 0.05; (*10*)] (fig. S3C), and many variable BRs exhibited more than twofold magnitude differences in binding (fig. S3D). Variable BRs for both NFκB and PolII, respectively, were often coassociated ($P < 1 \times 10^{-4}$; permutation test) (Fig. 1D and fig. S4), a correlation that is particularly strong for BRs that are less than 10 kb apart (fig. S4A). Variable NFκB and PolII regions were also often coassociated ($P = 2.80 \times 10^{-25}$, Kolmogorov-Smirnov test) (table S3 and fig. S4A), even though the NFκB and PolII data are from tumor necrosis factor–α (TNF-α)–treated and untreated cells, respectively. These results suggest that adjacent binding sites and BRs may influence one another, perhaps through cooperative binding or interactions with other proteins.

For both NFκB and PolII, BRs within 1 kb of transcription start sites (TSSs) of RefSeq genes showed less variability (6 and 25%, respectively) than intergenic peaks (8 and 28%) ($P < 1 \times 10^{-4}$; permutation test). TSS BRs also revealed stronger ChIP-Seq signals (1.2- and 2.3-fold, respectively), with many exceptions (fig. S5). The majority of binding regions (>70%) were occupied in two or more individuals, which argues against cell line artifacts (fig. S3B). The signal intensity for 40 and 53% of the BRs absent (that is, "lost") in one individual was similar to background for NFκB and PolII (*10*), respectively, suggesting complete absence of binding in these cases, rather than threshold effects.

BRs differing in TF occupancy among individuals often involve loci of potentially high interest. These include the *RPS26*, *BLK*, *SP140*, and *ZNF804A* genes for PolII, which have been associated with type 1 diabetes, systemic lupus erythematosus, chronic lymphatic leukemia, and schizophrenia, respectively, and *ORMDL3*, *PTGER4*, and *LOC253039* for NFκB, which are associated with asthma, Crohn's disease, and rheumatoid arthritis (*10*). Genes with variability in PolII binding showed a slight enrichment with immunity and defense functional gene categories ($P = 0.045$, Benjamini-Hochberg multiple testing correction) among target genes (*10*).

We examined the genetic contribution to binding variation using single-nucleotide polymorphisms (SNPs) from the 1000 Genomes project. Individual SNPs in NFκB and PolII BRs frequently affected binding (Fig. 1A and fig. S6A), and the number of SNPs in BRs correlated with the frequency of significant binding differences (Fig. 1B). SNPs altering the NFκB DNA binding motif had a strong effect, elevating the frequency of significant binding differences 2.4-fold. About 90% of the binding differences followed the expected trend in which better matches to the consensus motif yielded higher binding signals ($P < 1 \times 10^{-3}$) (Fig. 1C, table S4, and fig. S6B). SNPs that putatively affect binding are abbreviated as B-SNPs (binding SNPs).

We also searched for other associated DNA motifs, such as the Stat1 motif [previously associated with NFκB-binding (*11*)], TATA box, CAAT box, and GC box (*12*), and we performed de novo searches for enriched DNA motifs in BRs (*10*), which revealed BR enrichments for the NFκB motif and the GC box, along with additional motifs (fig. S7). We assessed the effect of genetic variation on each of the motifs. SNPs in the Stat1 motif markedly elevated the frequency of significant NFκB binding differences (1.3-fold enrichment; $P < 1 \times 10^{-3}$, permutation test) (Fig. 1B), and 71% of the alterations in the Stat1 motif changed NFκB binding in the expected direction; that is, improved Stat1 motif sequences increased NFκB binding ($P < 1 \times 10^{-3}$) (Fig. 1C, table S4, and fig. S6B). For PolII, SNPs in the CAAT box had a strong effect on binding (1.6-fold; $P < 1 \times 10^{-3}$), with 63% of cases displaying the correct trend, whereas SNPs in the TATA box and GC box had modest effects (1.5-fold and 1.3-fold, with 51 and 52%, respectively, exhibiting the correct trend). The significant covariance in the Stat1 motif with NFκB binding differences and the nuclear factor Y (NFY) CAAT box with PolII binding differences suggests a functional interaction of Stat1 with NFκB and NFY with PolII, respectively; the latter has been documented previously (*13*). We call this approach to examine covariation of motifs with variable binding regions the allele binding cooperativity test or ABC test.

We next analyzed the effect of SVs, >1-kb genomic segments displaying copy-number var-

[1]Department of Molecular, Cellular, and Developmental Biology, Yale University, New Haven, CT 06520, USA. [2]Department of Genetics, Stanford University School of Medicine, Stanford, CA 94305, USA. [3]Genome Biology Research Unit, European Molecular Biology Laboratory, Heidelberg, Germany. [4]Department of Biotechnology and Bioinformatics, Weihenstephan-Triesdorf University of Applied Sciences, 85350 Freising, Germany. [5]Program in Computational Biology and Bioinformatics, Yale University, New Haven, CT 06520, USA. [6]Department of Molecular Biophysics and Biochemistry, Yale University, New Haven, CT 06520, USA. [7]Department of Genetics, Yale University School of Medicine, New Haven, CT 06520, USA. [8]Department of Computer Science, Yale University, New Haven, CT 06520, USA. [9]European Molecular Biology Laboratory–European Bioinformatics Institute, Wellcome Trust Genome Campus, Hinxton CB10 1SD, UK.

*These authors contributed equally to this work.
†To whom correspondence should be addressed. E-mail: jan.korbel@embl.de (J.O.K.); mpsnyder@stanford.edu (M.S.)

iants (CNVs) or balanced inversions (*7*, *8*, *14*, *15*). We probed high-density microarrays to identify CNVs in seven individuals (*10*) (table S5) and combined these with CNVs from another survey (*15*). CNVs significantly elevated the frequency of BR differences between individuals by 5.1- and 2.0-fold for NFκB and PolII, respectively ($P < 1 \times 10^{-4}$, permutation test) (Fig. 2, A and B, fig. S8, and table S6). Furthermore, the effect followed the correct trend in 90 and 80% of the respective NFκB and PolII cases (Fig. 2C); deletions reduced binding signals, whereas duplications elevated them. A combined set of high-resolution SVs identified by paired-end mapping (*7*, *14*) also exhibited enrichment in binding differences for deletions intersecting with NFκB and PolII BRs [3.2-fold and 1.7-fold, respectively ($P < 1 \times 10^{-4}$, permutation test)]. We observed a 2.8-fold significant enrichment in differential binding owing to inversions affecting NFκB BRs ($P < 1 \times 10^{-4}$, permutation test), and a slight, nonsignificant enrichment due to inversions affecting PolII BRs (Fig. 2B), suggesting that inversions may affect binding. SVs that are associated with binding are abbreviated B-SVs (binding SVs).

The total fraction of significant binding differences coinciding with genetic variations was 35% for NFκB and 26% for PolII (table S7 and fig. S6C). Thirty-four percent of the NFκB BRs intersect with SNP differences between corresponding regions in different individuals (1% intersect with a known TF motif, with SNPs falling both in the NFκB or the STAT1 motif) (table S8) and 3% with SVs (some SNPs coincide with SVs). Thus, genetic differences affecting the BR can be assigned to many, but not to the majority of, binding differences. Possible reasons for the remaining BR variation include *trans*-effects, epigenetic variation, as well as B-SNPs and B-SVs that were not ascertained. Some of the binding differences could be related to the different ages of the individuals.

We examined the effect of binding variation on gene expression by generating deep RNA-Seq data from each cell line (*10*) and comparing those data with binding data (Fig. 3A and fig. S9A). A significant correlation was observed (Spearman correlation coefficients of 0.475 and 0.461 for NFκB and PolII, respectively) (Fig. 3B, fig. S9B, and table S9), suggesting an influence of binding differences on mRNA abundance. Examples of correlated genes include *UGT2B17*, *GSTM1*, and *ZNF804A*, which encode glucuronic acid and glutathione transferases, and a gene linked to schizophrenia (*10*). However, a number of BR differences were not associated with differences in gene expression and presumably compensatory (for example, feedback) mechanisms influence the expression in these cases. We also examined the effect of B-SNPs with differences in both binding and gene expression and found that both NFκB and PolII binding and expression differences correlated with the presence of B-SNPs, including those in the NFκB and Stat1 motif (for NFκB) and the CAAT, GC, and TATA box (for PolII) (Spearman correlation coefficients: 0.48 to 0.82) (Fig. 3C and table S9). Copy number differences (that is, B-SVs) also correlated with gene expression, albeit the correlation was not as strong as that of copy number differences with binding (table S10), indicating a more-direct role for genetic variation on TF binding than on gene expression.

The observation that SNPs and SVs are frequently associated with binding differences suggests a crucial role of *cis* elements in the genetics of TF binding. We thus analyzed the segregation pattern of BR occupancy in the parent-offspring trio, and observed potential Mendelian segregation in >90% of BRs (fig. S10A), although this was difficult to determine with certainty, because not all alleles that are relevant to TF binding have been ascertained in the parents. In the child, 947 and 732 BRs were occupied by NFκB and PolII, respectively, but not in the parents. This is indicative of transgression in which a binding event was evident only in the offspring (Fig. 3, A and D, fig. S10B, and tables S11, S12, and S13).

We also examined whether some BRs are specific to certain populations. Although the number of individuals analyzed was small, the NFκB data revealed a total of 14 BRs that were specifically occupied or unoccupied in the African or Asian individuals (table S14). For PolII, the chimpanzee data were used to infer gains and losses relative to the likely ancestral state of binding, and a total of 68 population-specific occupancies (gains and losses) were identified in the three population groups (table S14). Overall, we found relatively few population-specific events, ~0.1 to ~0.4%, suggesting that most alleles affecting TF binding are shared among different populations.

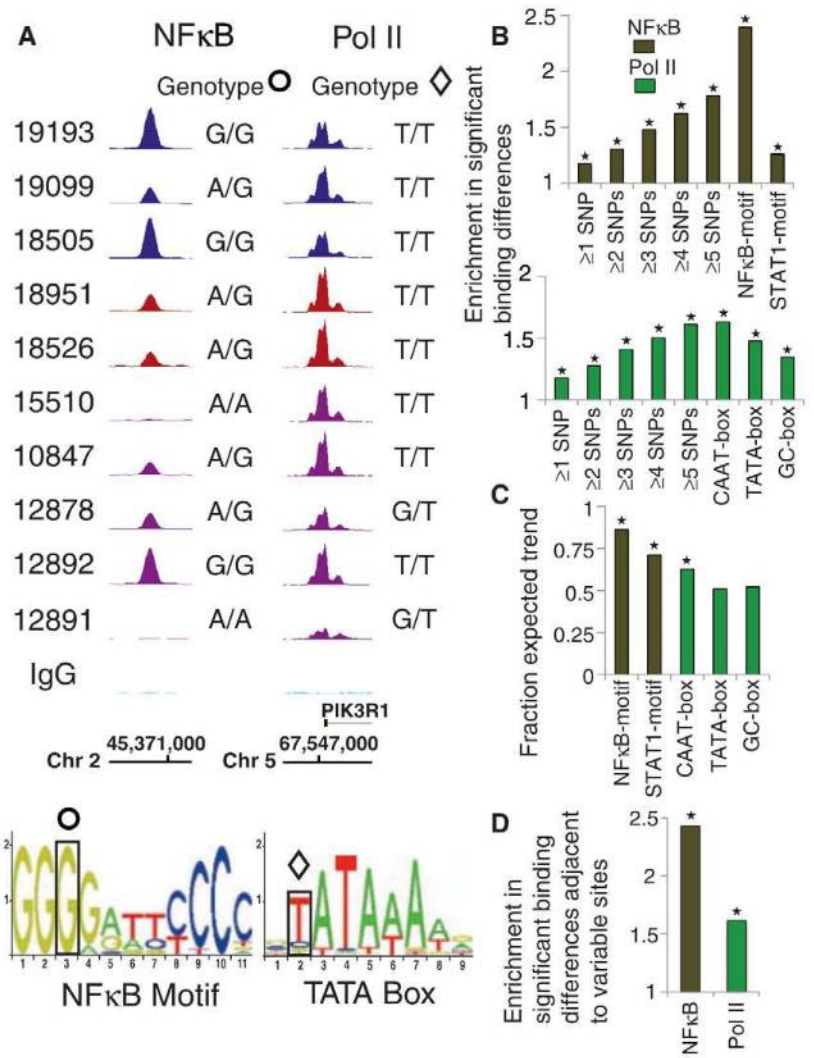

Fig. 1. Effect of SNPs on NFκB and PolII binding. (**A**) Signal tracks of a NFκB motif and a TATA box demonstrate effects of B-SNPs on TF binding, with correlations in the expected direction (that is, with correct trend). (**B**) Fold enrichments for cumulative SNP differences affecting BRs and for single SNPs affecting motifs, in pairwise comparisons between individuals relative to the overall frequency of binding differences for NFκB (7.5%) and PolII (25%). (**C**) B-SNPs affecting motifs frequently lead to binding differences with correct trend. *$P < 0.001$, based on randomization tests involving 10,000 permutations, that is, permutation tests. (**D**) BRs adjacent to differentially bound BRs are enriched for binding variation.

Because humans and chimpanzees exhibit 5 to 10% differences in gene expression (*16*), we also examined divergence of TF binding among primates by analyzing PolII binding in a single chimpanzee. We analyzed 15,418 (81%) of human BRs with corresponding syntenic regions in the chimpanzee genome. The majority of PolII BRs were occupied both in humans and chimp (fig. S11A). However, 32% of the BRs exhibited significant differences in binding (corrected P value < 0.05) (Figs. 2A and 4A), a figure higher than that for human PolII variation (25%). Genes near regions uniquely occupied in the chimp were enriched in the following functional categories: (i) nucleoside, nucleotide, and nucleic acid metabolism; and (ii) steroid metabolism (P values = 3.60×10^{-5} and 4.16×10^{-4}, respectively). Furthermore, BRs that were uniquely occupied in humans were significantly enriched in protein modification and mRNA transcription [Fischer Exact test (*10*), Benjamini-Hochberg P values = 2.22×10^{-89} and 9.08×10^{-139}, respectively] (table S15).

As in humans, relative differences identified in the chimpanzee were higher in intergenic BRs

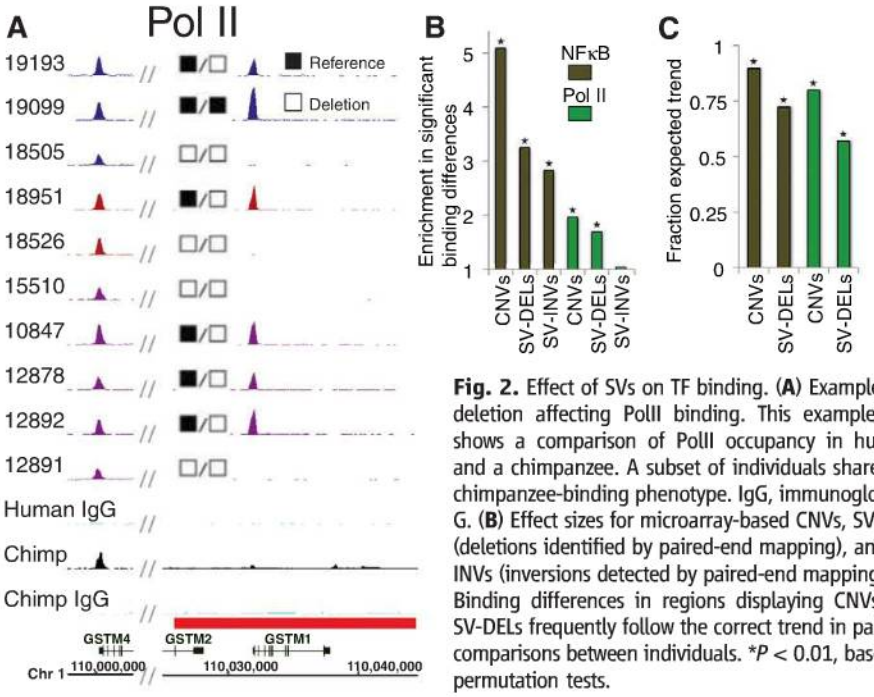

Fig. 2. Effect of SVs on TF binding. (**A**) Example of a deletion affecting PolII binding. This example also shows a comparison of PolII occupancy in humans and a chimpanzee. A subset of individuals shares the chimpanzee-binding phenotype. IgG, immunoglobulin G. (**B**) Effect sizes for microarray-based CNVs, SV-DELs (deletions identified by paired-end mapping), and SV-INVs (inversions detected by paired-end mapping). (**C**) Binding differences in regions displaying CNVs and SV-DELs frequently follow the correct trend in pairwise comparisons between individuals. *P < 0.01, based on permutation tests.

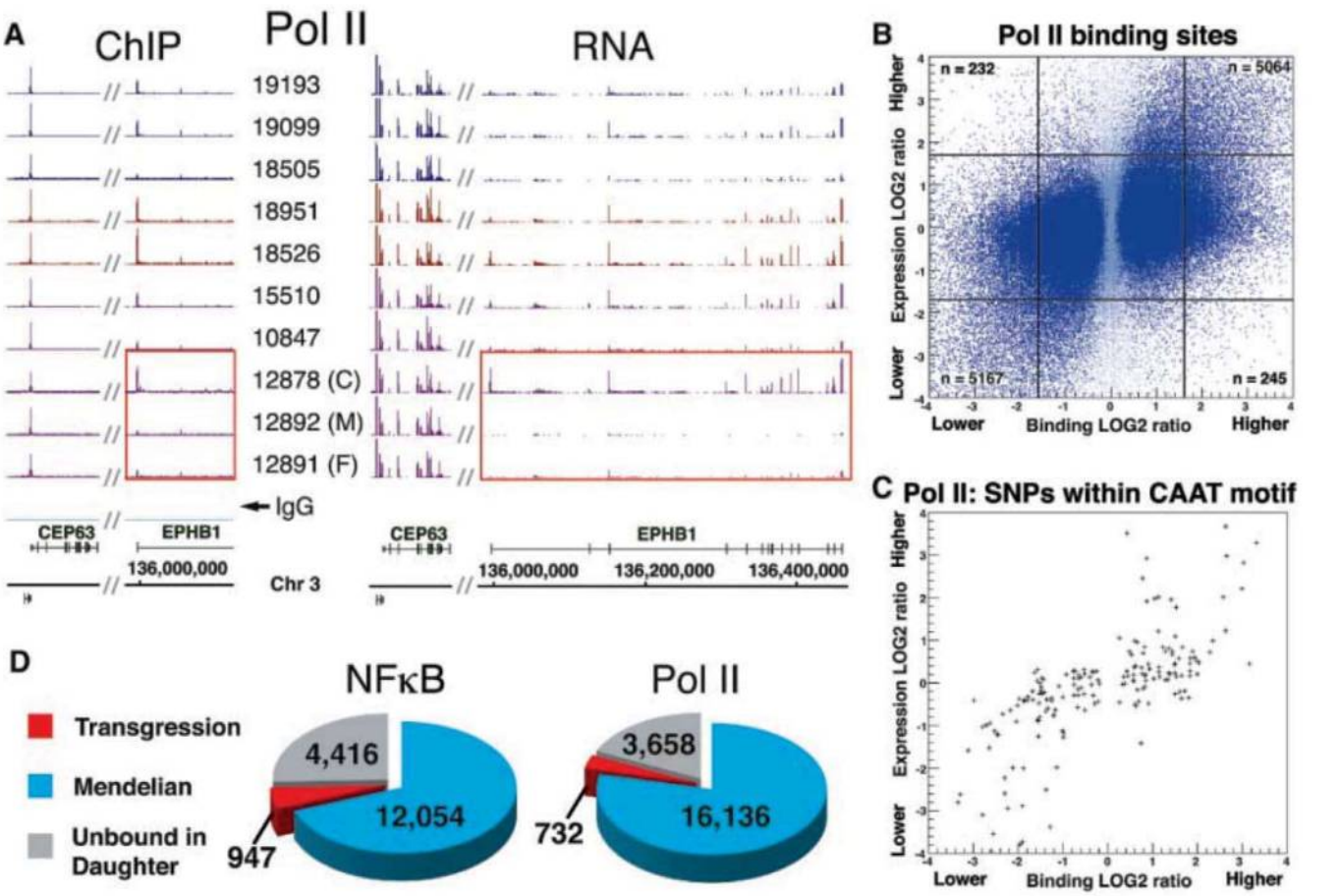

Fig. 3. Correlation and effect sizes of TF binding and gene expression. (**A**) Example showing a correlation of binding and expression. This figure also shows a transgression event, in which the daughter displays a strong increase in binding relative to the parents. Continuous signal tracks are shown in fig. S10C. (**B**) Regions with binding variation correlate with differences in expression. Dark blue dots, PolII BRs displaying significant differences in binding in pairwise comparisons between individuals; light blue dots, other BRs. The black lines demarcate data points that fall 2 SDs outside the binding ratio or gene expression distributions. Indicated counts (n) represent data points falling into the four corners for each data set. (**C**) Strong correlation between binding and gene expression at BRs in which a B-SNP intersects with the PolII-specific CAAT box. (**D**) Breakdown of segregation events in the trio showing the extent of BRs with candidate transgression events.

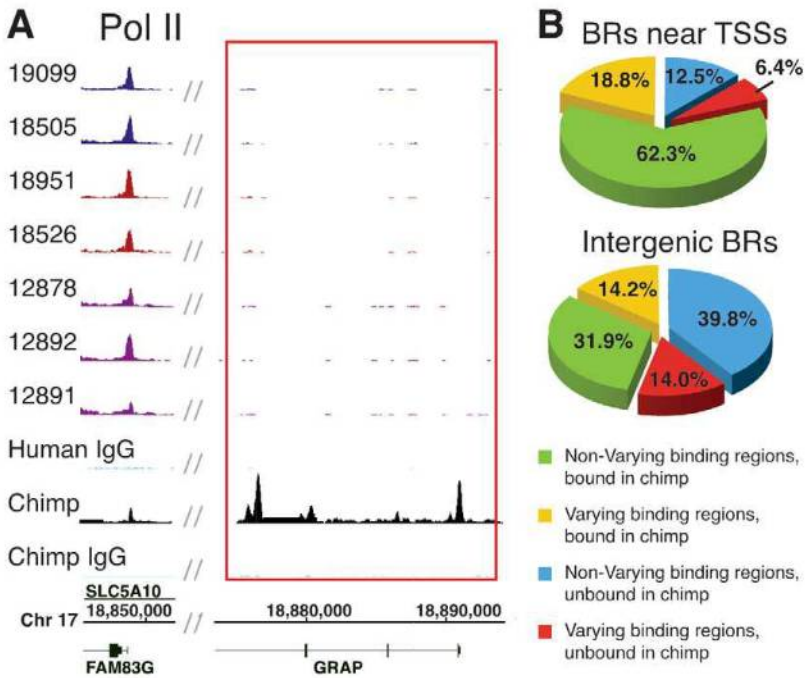

Fig. 4. Comparison of PolII binding in humans and a chimpanzee. **(A)** Signal tracks for a peak found only in the chimpanzee. All 10 individuals are shown in fig. S11B. **(B)** Pie charts displaying occupancy by PolII of genomic regions where the chimp and human genomes are in synteny.

relative to BRs within 1 kb of a TSS: 33% of the syntenic intergenic PolII BRs differed significantly from the human samples, compared with 31% near TSSs ($P < 1 \times 10^{-4}$; permutation test). Consequently, human BRs near TSSs were generally more likely to be scored as occupied in chimpanzee (81%) than intergenic BRs were (46%) (Fig. 4B). Furthermore, human BRs with strong binding signals (that is, many mapped reads) are more frequently occupied in the chimpanzee than those with weaker signals (fig. S11C), indicating either divergence of the weaker sites or signals that fell below the threshold at the low signal sites. Finally, we observed a general correlation between polymorphism and divergence in binding; that is, variable BRs in humans displayed, on average, more divergence from chimpanzee BRs (in terms of fold change in normalized read counts) than did nonvariable BRs (Spearman test, 0.68; $P = 3.9 \times 10^{-7}$) (fig. S11D).

Our data demonstrate extensive contributions of genetic variations on TF binding, many of which are expected to be functional through their effect on gene expression. Overall, the differences observed here (7.5 and 25% for NFκB and PolII, respectively, for humans; 32% for human/chimpanzee) greatly exceed estimates for sequence variation in coding sequences [estimated as 0.025% for humans (*17*) and 0.71% for human/chimpanzee (*18*)], suggesting a strong role for binding variation in human diversity. Extending mapping of B-SNPs and B-SVs for these and additional transcription factors should further inform on the genetic underpinnings of phenotypic diversity in humans and provide insights into genetic causes of human disease.

References and Notes

1. B. E. Stranger *et al.*, *Science* **315**, 848 (2007).
2. M. V. Rockman, L. Kruglyak, *Nat. Rev. Genet.* **7**, 862 (2006).
3. D. A. Skelly, J. Ronald, J. M. Akey, *Annu. Rev. Genomics Hum. Genet.* **10**, 313 (2009).
4. A. R. Borneman *et al.*, *Science* **317**, 815 (2007).
5. International HapMap Consortium, *Nature* **449**, 851 (2007).
6. More information on the 1000 Genomes project can be found at http://1000genomes.org.
7. J. O. Korbel *et al.*, *Science* **318**, 420 (2007).
8. E. Tuzun *et al.*, *Nat. Genet.* **37**, 727 (2005).
9. J. Rozowsky *et al.*, *Nat. Biotechnol.* **27**, 66 (2009).
10. Materials and methods and supporting data are available on *Science* Online.
11. O. H. Krämer *et al.*, *Genes Dev.* **20**, 473 (2006).
12. A. Sandelin, W. Alkema, P. Engström, W. W. Wasserman, B. Lenhard, *Nucleic Acids Res.* **32** (Database issue), D91 (2004).
13. M. C. Faniello *et al.*, *J. Biol. Chem.* **274**, 7623 (1999).
14. J. M. Kidd *et al.*, *Nature* **453**, 56 (2008).
15. S. A. McCarroll *et al.*, *Nat. Genet.* **40**, 1166 (2008).
16. H. Creely, P. Khaitovich, *Prog. Brain Res.* **158**, 295 (2006).
17. S. Levy *et al.*, *PLoS Biol.* **5**, e254 (2007).
18. H. Watanabe *et al.*, *Nature* **429**, 382 (2004).

19. We thank the 1000 Genomes project for early data access. This research was funded by grants from NIH (M.S., S.W., and M.G.), and by funding from the European Molecular Biology Laboratory (J.K.), a March of Dimes Foundation Grant (A.U.), and the NIH Medical Scientist Training Program grant TG T32GM07205 (M.K.). M.K. was a Howard Hughes Medical Institute Medical Research Training Fellow. Data sets are available at the Gene Expression Omnibus (GEO) database with accession number GSE19486. M.S. is on the Scientific Advisory Board and a founder for both Affymetrix and Metagenomix.

Supporting Online Material

www.sciencemag.org/cgi/content/full/science.1183621/DC1
Materials and Methods
Figs. S1 to S16
Tables S1 to S20
References

20 October 2009; accepted 12 February 2010
Published online 18 March 2010;
10.1126/science.1183621
Include this information when citing this paper.

Heritable Individual-Specific and Allele-Specific Chromatin Signatures in Humans

Ryan McDaniell,[1] Bum-Kyu Lee,[1] Lingyun Song,[2,3] Zheng Liu,[1]* Alan P. Boyle,[2] Michael R. Erdos,[4] Laura J. Scott,[4,5] Mario A. Morken,[4] Katerina S. Kucera,[2] Anna Battenhouse,[1] Damian Keefe,[6] Francis S. Collins,[4] Huntington F. Willard,[2] Jason D. Lieb,[7] Terrence S. Furey,[2] Gregory E. Crawford,[2,3]† Vishwanath R. Iyer,[1]† Ewan Birney[6]†

The extent to which variation in chromatin structure and transcription factor binding may influence gene expression, and thus underlie or contribute to variation in phenotype, is unknown. To address this question, we cataloged both individual-to-individual variation and differences between homologous chromosomes within the same individual (allele-specific variation) in chromatin structure and transcription factor binding in lymphoblastoid cells derived from individuals of geographically diverse ancestry. Ten percent of active chromatin sites were individual-specific; a similar proportion were allele-specific. Both individual-specific and allele-specific sites were commonly transmitted from parent to child, which suggests that they are heritable features of the human genome. Our study shows that heritable chromatin status and transcription factor binding differ as a result of genetic variation and may underlie phenotypic variation in humans.

Control of gene transcription is believed to be important in determining organismal phenotype and fitness. Variations in genomic DNA, such as single-nucleotide polymorphisms (SNPs), insertions, or deletions (indels), may act singly or in combination to influence gene regulation (*1*, *2*). These heritable variations have been thought to affect the binding of sequence-

specific transcription factors or to affect the physical conformation of packaged DNA, namely chromatin. Humans typically harbor two copies (alleles) of every gene, and recent studies show that for between 10% and 22% of human genes, the two copies are regulated differently—for example, one copy may be transcribed while the other is not (*3*). Such allele-specific expression can be created in part by underlying biological processes such as imprinting, but little is known about other molecular determinants of allele-specific gene regulation in humans or to what extent these events are genetically determined, given that variation in gene regulation can also be caused by nongenetic phenomena including epigenetic, environmental, or stochastic effects (*4*–*6*). To aid in our understanding of the molecular basis of allele-specific gene regulation and the separate but related topic of phenotypic variation between individuals, we have cataloged allele-specific and individual-specific variation in transcription factor binding and chromatin structure.

To assay individual variation and how it relates to the allele-specific behavior of chromatin, we used deoxyribonuclease I hypersensitive (DNase I HS) site mapping, which broadly identifies regulatory DNA elements such as promoters, enhancers, silencers, and insulators (*7*, *8*). We also performed chromatin immunoprecipitation (ChIP) for elements associated with the CCCTC-binding factor (CTCF), a multifunctional transcriptional and chromatin regulator (*9*–*12*). The combination of these two different methods, DNase I HS mapping and CTCF ChIP, allowed us to independently validate our results. Assays were performed on cell lines from one CEU (CEPH Utah reference family; residents with ancestry from northern and western Europe) family (both parents and their daughter) and one YRI (Yoruba from Ibadan, Nigeria) family (both parents and their daughter) in the 1000 Genomes Project (*13*). The study design therefore features four unrelated adults (the parents) and two children who are directly related to one pair of adults but unrelated to the other pair or each other (Fig. 1A). This design allows us to dissect individual- and allele-specific information in the context of these families, and thereby to determine heritability and the contribution from genetic or epigenetic processes. Previous studies have identified very few individual-specific sites and have not explored their heritability (*14*).

We generated DNase-seq and CTCF ChIP-seq (deep sequencing) data from two independent cell growths for each cell line (Fig. 1 and fig. S1) (*13*). Sites were classified as "constant" (present in all four unrelated parents), "individual-specific" (present in at least two of the parents and absent in the other two parents), or "singletons" (present in just one individual) (Fig. 1B, Fig. 2, A and B, fig. S2, and table S1). Global analysis of the 10,041 (DNase) or 1632 (CTCF) individual-specific sites specific to one set of parents compared to the other showed that the children's signals at those sites were closer to their own parents than to that of the unrelated family (Fig. 2, C and D). Given the large number of individual sites tested, this result shows that these chromatin signals are

[1]Center for Systems and Synthetic Biology, Institute for Cellular and Molecular Biology, Section of Molecular Genetics and Microbiology, University of Texas, Austin, TX 78712, USA. [2]Institute for Genome Sciences and Policy (IGSP), Duke University, Durham, NC 27708, USA. [3]Department of Pediatrics, Division of Medical Genetics, Duke University, Durham, NC 27708, USA. [4]Genome Technology Branch, National Human Genome Research Institute, Bethesda, MD 20892, USA. [5]Center for Statistical Genetics, Department of Biostatistics, University of Michigan, Ann Arbor, MI 48109, USA. [6]European Bioinformatics Institute, Wellcome Trust Genome Campus, Hinxton, Cambridge CB10 1RQ, UK. [7]Department of Biology, Carolina Center for Genome Sciences, and Lineberger Comprehensive Cancer Center, University of North Carolina, Chapel Hill, NC 27599, USA.

*Present address: MedImmune, 1 MedImmune Way, Gaithersburg, MD 20878, USA.

†To whom correspondence should be addressed. E-mail: greg.crawford@duke.edu (G.E.C.); vishy@mail.utexas.edu (V.R.I.); birney@ebi.ac.uk (E.B.)

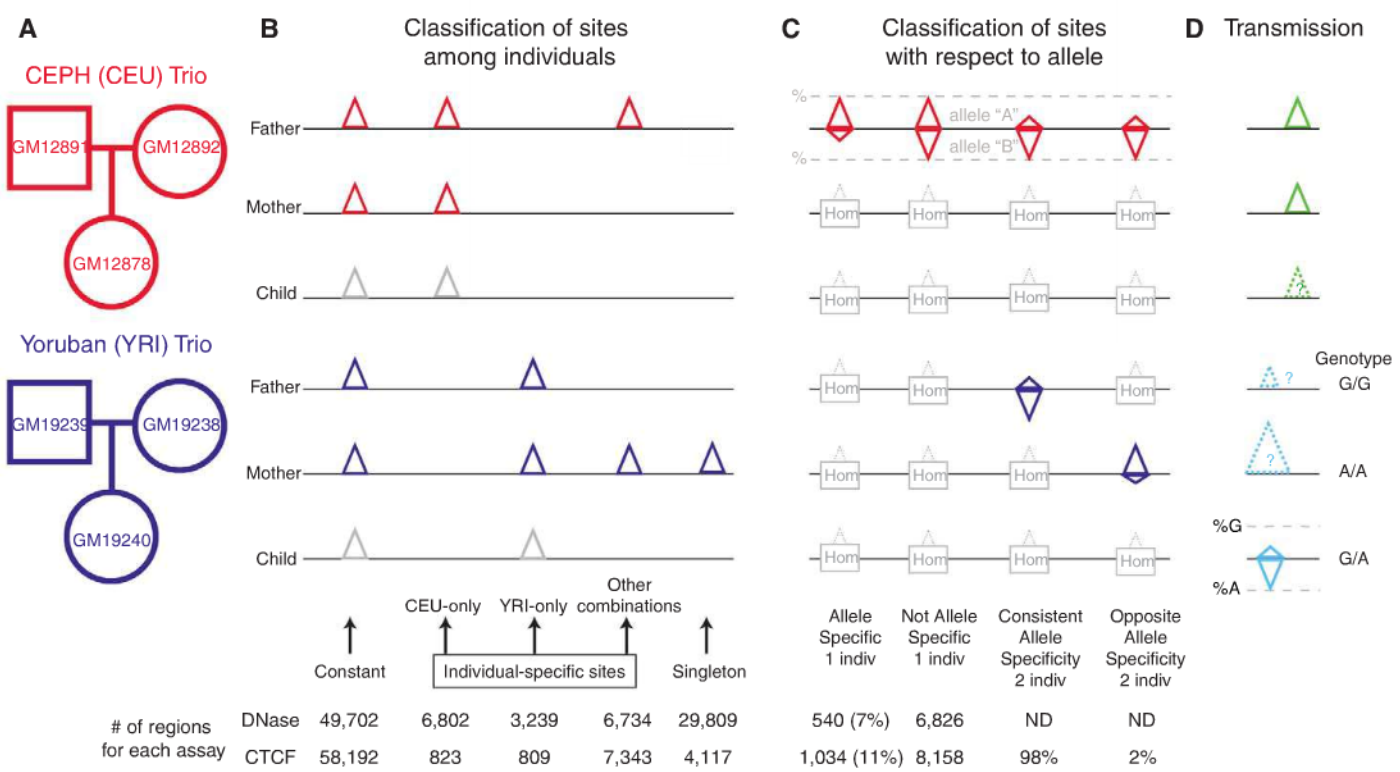

Fig. 1. (**A**) Cell lines from CEU and YRI parent-child trios. (**B**) Classification of DNase I HS or CTCF binding sites among individuals. Constant sites are those occurring in all four parents. CEU- and YRI-only sites occurred in both parents within only one population. Sites occurring in one individual (singletons) or in other combinations were also noted (table S2). Sites in children were not used in this initial classification (gray). (**C**) Sites that are allele-specific (skewed toward one allele) in one individual, not allele-specific in one individual, consistent allele-specific in two individuals, and opposite allele-specific in two individuals. Homozygous (Hom) individuals for an allele are not informative. (**D**) Transmission tests show that CEU- or YRI-only sites are more likely in children from the same population (green; see also Fig. 2), and allele-specific sites in children correspond to signal intensities in parents who are homozygous for different alleles (turquoise; see also Fig. 3). Numbers and percentages of all categories are indicated at the bottom. The orientation of the triangles indicates the two alleles that are assayed; triangle sizes indicate differences in signal strength (in terms of number of sequence reads).

heritable. However, this analysis alone cannot distinguish among genetic, epigenetic, or other causes for inheritance. The high degree of concordance at the 54,621 sites identified by both assays also supports the heritability of binding-level specificity (fig. S3).

We next examined the correlation of individual variation in these chromatin sites with variation in gene expression. The presence of an individual-specific DNase I HS site near the transcription start site of a gene was positively correlated with expression of that gene in that individual, relative to genes that were farther away (fig. S4, A and C). Individual-specific CTCF sites were associated with both activation and repression of nearby genes, suggesting a more complex relationship to gene expression (fig. S4, B and D).

The use of high-throughput sequencing allowed us to assess allele-specific chromatin signals by detecting preferential recovery of sequence reads containing one allele over the other when there was an underlying heterozygous SNP in the individual. When aligning our sequences containing such a mixture of alleles at a given heterozygous SNP to the reference human genome sequence, we found a marked preference for alignment of sequence reads containing the allele that also happened to be represented in the reference sequence (fig. S5). After correcting for this technical bias (*13*), we assessed the true allele specificity of each heterozygous SNP sequenced at sufficient depth for each assay, and found that 7% of DNase I HS sites and 11% of CTCF sites have significant allele specificity after multiple testing correction (Fig. 1C).

Although allele-specific sites occurred on all chromosomes, the X chromosome was particularly enriched for such sites. This would be expected if DNase I HS and CTCF binding on the two X chromosomes is unequal in females, provided that one of the two X chromosomes is preferentially inactivated in the cell population (fig. S6, A and B). Indeed, we established that X inactivation patterns were nonrandom in the cell lines studied, and that the paternal X was preferentially inactivated in 90% of cells in each cell line from both daughters (fig. S7A). Most X-chromosome allele-specific CTCF sites showed a bias toward the active maternal X (fig. S7B), thus demonstrating that allelic imbalance in CTCF binding is generally associated with epigenetic silencing in X inactivation. We found several sites at which CTCF bound equally to the inactive and active X alleles or preferentially bound the allele on the inactive X. These could represent CTCF binding in regions escaping inactivation, or sites involved in or otherwise reflecting epigenetic changes associated with dosage compensation (*9*).

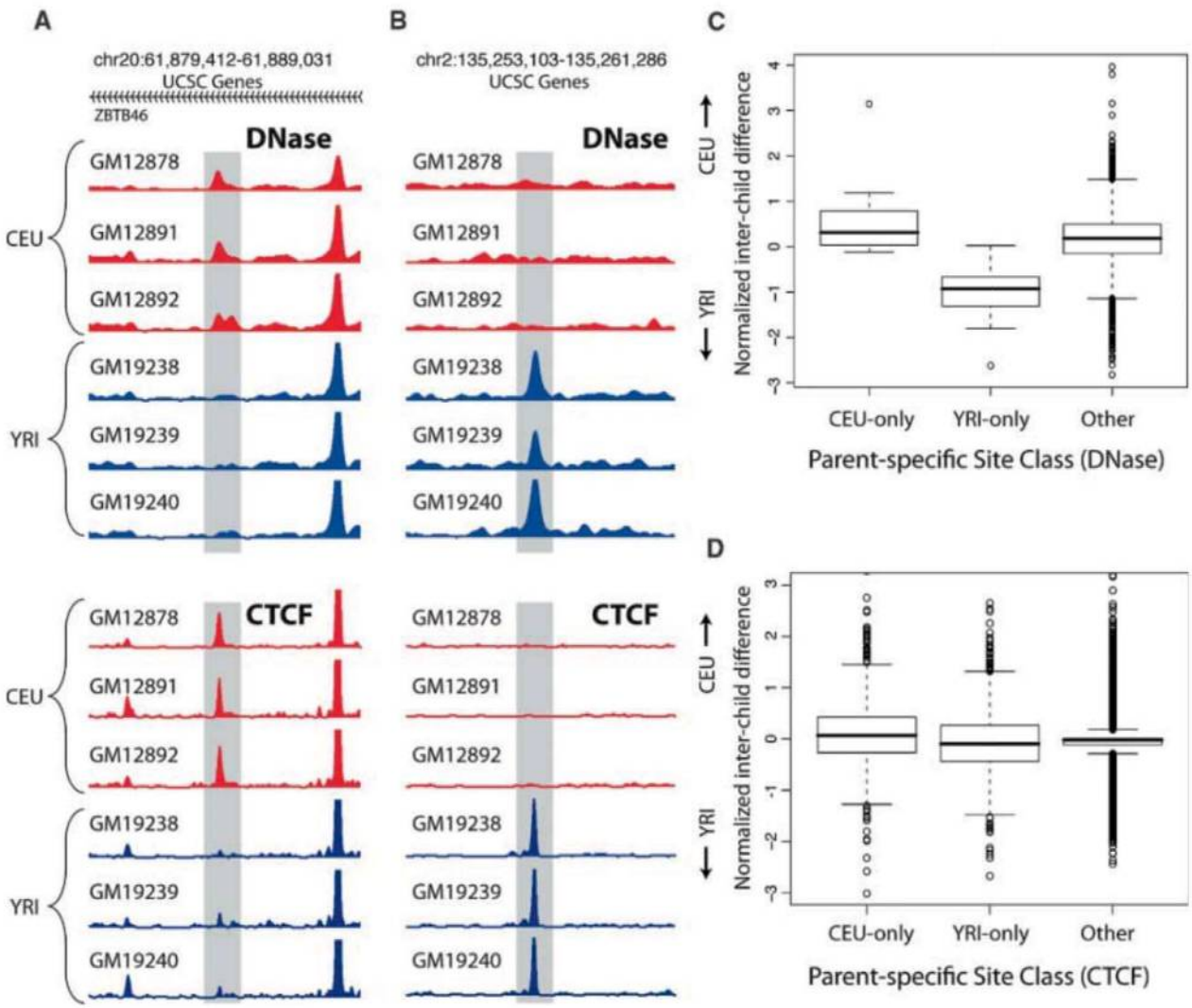

Fig. 2. Individual-specific chromatin transmission. (**A**) Example of CEU-only individual-specific DNase I HS and CTCF sites (shaded areas). (**B**) Example of YRI-only individual-specific sites. (**C** and **D**) Genome-wide individual-specific DNase I HS sites (C) and CTCF sites (D) were categorized as CEU-only, YRI-only, or other combinations. The standard box plots of the relative normalized interchild differences for these categories show that the child signal was significantly closer to the parental sites from its own population ($P < 10^{-15}$ for DNase I HS, $P < 10^{-8}$ for CTCF; Wilcoxon rank-sum test). Numbers at top of (A) and (B) are chromosome numbers followed by start-stop coordinates from the UCSC Genome Browser. In (A) the indicated sites occur in the *ZBTB46* gene, whose direction of transcription is right to left (as indicated by arrowheads).

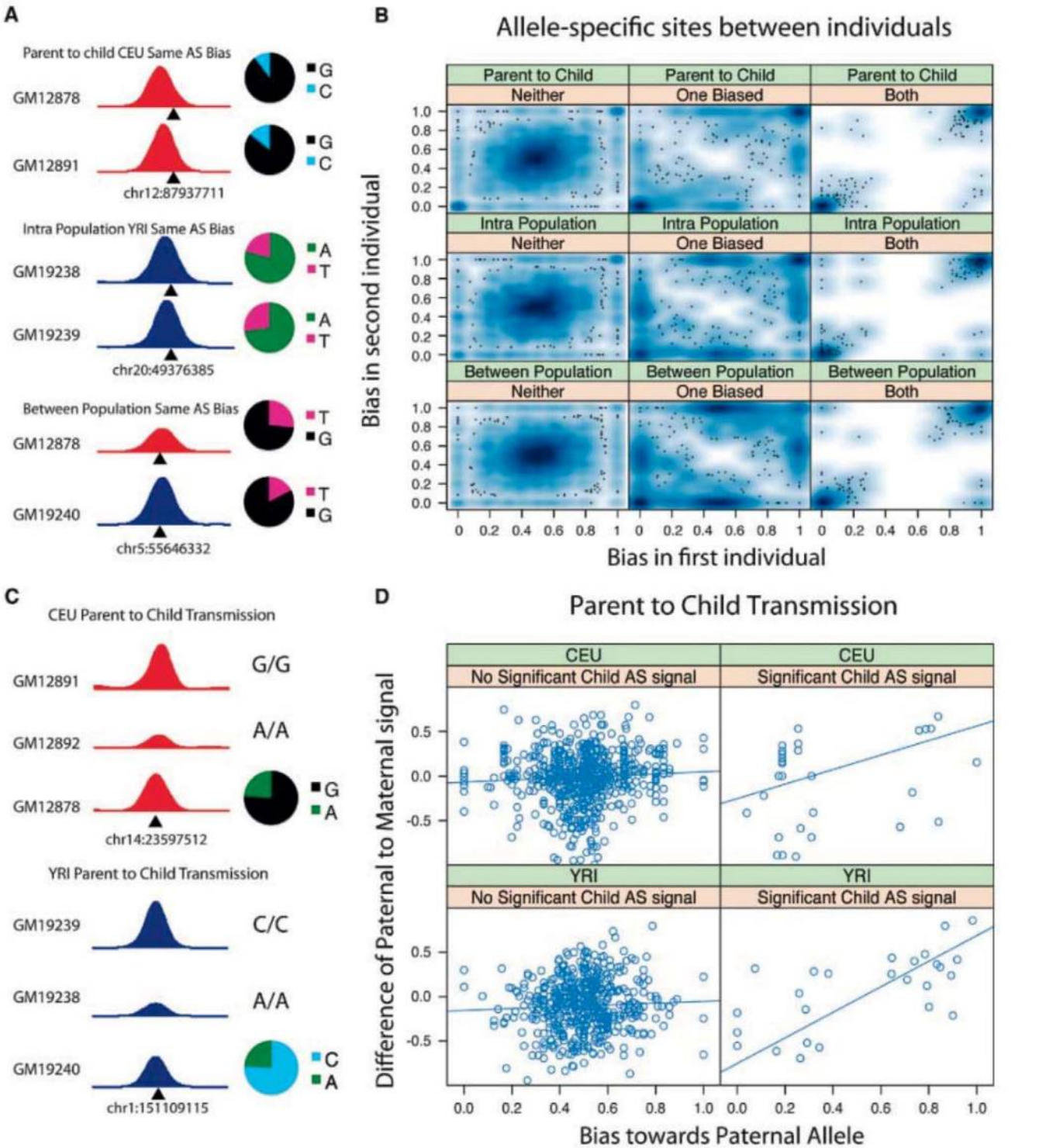

Fig. 3. Comparison of allele-specific sites between individuals. (**A**) Each subpanel shows a different allele-specific site in two individuals in the indicated category. The overlapping SNP is indicated below. Adjoining pie charts show concordant allelic bias within the ChIP-seq reads for each site. (**B**) Allele-specific CTCF site correlations, as shown by smoothed scatterplots (*13*) of biases between any two individuals (parent-child, intrapopulation, and between-population) where the bias was significant in neither, one, or both individuals. Because of the large number of sites, the density of sites is shown by shades of blue, with outlying sites to this density shown as points. In each pairwise comparison, the bias was predominantly correlated (lower left and upper right of each plot). (**C**) Allele-specific CTCF sites in a child where both parents are homozygous, showing transmissibility. Peak heights indicate relative binding strength in the parents. The parent homozygous for the allele that was overrepresented in the child has a stronger signal than the other parent. (**D**) Heterozygous CTCF sites in children where both parents were homozygous. Child sites were classified as allele-specific (right) or not (left). CTCF signal differences between parents were compared to each of the children. Zero on *x* axis represents 100% maternal bias; 1 represents 100% paternal bias.

To establish that the allele-specific CTCF binding biases were not an artifact, we tested four allele-specific and five non–allele-specific CTCF sites using matrix-assisted laser desorption/ionization–time-of-flight mass spectrometry (MALDI-TOF MS) (fig. S8A and table S4) (*15*). Each of the four allele-specific sites showed a significantly higher proportion of the enriched allele (fig. S8B), although the absolute levels of enrichment were lower as assayed by MALDI-TOF MS than by ChIP-seq. In contrast, none of the five non–allele-specific ChIP-seq CTCF sites showed significant bias by MALDI-TOF MS (fig. S8B and table S5).

Chromatin signals could be individual-specific or allele-specific as a result of nongenetic factors, such as environmental, epigenetic, or stochastic differences between individuals (*4*, *5*). If allele-specific chromatin structure has a direct genetic basis, the relationship between a specific allele and the chromatin signal should be maintained between individuals. When we considered the 10,364 shared heterozygous sites present in two or more individuals, if two individuals showed significant allele-specific CTCF binding, it was nearly always toward the same allele (Fig. 3, A and B). We next examined the prevalence of an autosomal imprinting-like process for generating allele specificity. Because the male and female parental alleles are randomly distributed with respect to any genetic haplotype, one would expect that if a site were subjected to a parent-of-origin imprinting-like process, half of such sites would have reversed allele specificity in unrelated individuals with the same heterozygous sites. However, only about 2% of interindividual pairs showed significantly opposite behavior (Fig. 1C) (*13*). This shows that an autosomal imprinting-like mechanism is not a major contributor to allelic bias, at least for CTCF binding.

Using the parent-child structure of our study, we could also examine the relationship between allele-specific information present in the children and individual-specific information in the parents. Unlike the earlier transmission test of individual-specific sites (Fig. 2), this comparison specifically assesses a genetic mechanism for generating allele specificity. At the 62 CTCF sites where there was a significant allele-specific signal in the child and where one parent was homozygous for one allele and the other parent homozygous for the other (Fig. 1D), the allele bound most strongly by CTCF in the child was most often (65%) the allele carried by the parent who showed the greatest level of CTCF binding, and the extent of parental differential CTCF binding was correlated to the extent of the child's allele specificity ($P = 6.6 \times 10^{-5}$, Spearman's correlation) (Fig. 3, C and D). These results suggest a heritable genetic rather than an epigenetic basis for a large proportion of the allele-specific binding of CTCF. There was a strong tendency for the same allele to be preferred in both the CTCF and DNase I HS assays when both could be measured (fig. S9). It is thus likely that DNase I HS sites are also correlated between individuals and are transmissible from parent to child.

SNPs underlying the allele-specific sites could directly affect transcription factor binding and chromatin. Alternatively, these SNPs could merely be markers for other cis polymorphisms such as indels that we did not incorporate into our reconstructed reference genomes. We therefore examined whether SNPs themselves disrupted the CTCF binding motif, and whether the effect of any disruption was consistent with the observed effect on CTCF binding (*13*). At sites where CTCF showed allele-specific binding, the motif score tended to be higher for the favored allele, whereas at sites lacking differences in CTCF binding, motif scores were similar (fig. S10). Moreover, strongly conserved positions in the motif were more likely to harbor allele-specific SNPs (Fig. 4). Thus, SNPs underlying many allele-specific binding sites are likely to directly affect the binding of CTCF, further suggesting that there is a genetic basis for allele-specific binding.

Our results suggest a strong genetic component for allele-specific differences at the level of transcription factor binding and chromatin structure. In addition to the genetic effects, we expect that some individual-specific differences may be due to nongenetic or epigenetic differences between individuals, such as DNA methylation, which could vary without regard to the underlying genotype. Our results are not consistent with widespread random allelic inactivation in lymphoblastoid lines (*16*), and they place limits on the extent of an imprinting-like process affecting transcription factor binding and chromatin structure. Chromatin structure is thought to be an important reservoir of epigenetic information as well as part of the means by which genetic and epigenetic changes affect phenotypes. Because we can now reliably measure individual differences in chromatin structure, our data may have implications for the identification and characterization of common noncoding polymorphisms associated with disease risk.

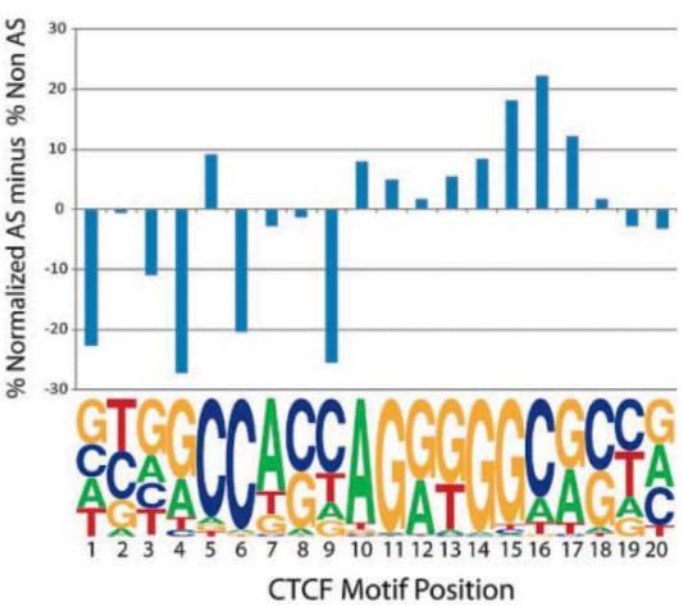

Fig. 4. Representation of allele-specific and non–allele-specific SNPs across the CTCF binding motif (*17*). The *y* axis indicates the difference between the two as a percentage of normalized total SNPs. Higher bars indicate an increased representation of allele-specific SNPs relative to other positions, which tends to occur at conserved positions.

References and Notes

1. V. G. Cheung, R. S. Spielman, *Nat. Rev. Genet.* **10**, 595 (2009).
2. M. Morley *et al.*, *Nature* **430**, 743 (2004).
3. K. Zhang *et al.*, *Nat. Methods* **6**, 613 (2009).
4. E. Hatchwell, J. M. Greally, *Trends Genet.* **23**, 588 (2007).
5. S. B. Montgomery, E. T. Dermitzakis, *Hum. Mol. Genet.* **18**, R211 (2009).
6. H. Yan, W. Yuan, V. E. Velculescu, B. Vogelstein, K. W. Kinzler, *Science* **297**, 1143 (2002).
7. D. S. Gross, W. T. Garrard, *Annu. Rev. Biochem.* **57**, 159 (1988).
8. C. Wu, P. M. Bingham, K. J. Livak, R. Holmgren, S. C. Elgin, *Cell* **16**, 797 (1979).
9. G. N. Filippova, *Curr. Top. Dev. Biol.* **80**, 337 (2007).
10. A. Lewis, A. Murrell, *Curr. Biol.* **14**, R284 (2004).
11. A. Lewis, W. Reik, *Cytogenet. Genome Res.* **113**, 81 (2006).
12. J. E. Phillips, V. G. Corces, *Cell* **137**, 1194 (2009).
13. See supporting material on *Science* Online.
14. M. Kadota *et al.*, *PLoS Genet.* **3**, e81 (2007).
15. K. L. Mohlke *et al.*, *Proc. Natl. Acad. Sci. U.S.A.* **99**, 16928 (2002).
16. V. Plagnol *et al.*, *PLoS ONE* **3**, e2966 (2008).
17. T. H. Kim *et al.*, *Cell* **128**, 1231 (2007).

18. We thank T. Severson, F. Ye, and L. Bukovnik at the Duke IGSP Sequencing Core Facility and K. Moon and S. Luo at Illumina for sequencing; S. Tenenbaum and S. Chittur at the State University of New York, Albany, for expression data; J. Lucas and Z. Zhang at Duke for gene expression analysis; the Texas Advanced Computing Center for computational infrastructure; and the 1000 Genomes Project for genotypes. E.B. has been a paid consultant to EagleGenomics, UK. Supported by National Human Genome Research Institute (NHGRI) ENCODE Consortium grant U54 HG004563-03 and NHGRI grant Z01 HG000024. Raw data from this paper are available at Gene Expression Omnibus (GSE15805 and GSE19622) and at the University of California, Santa Cruz (UCSC) Genome Browser.

Supporting Online Material

www.sciencemag.org/cgi/content/full/science.1184655/DC1
Materials and Methods
Figs. S1 to S11
Tables S1 to S5
References

13 November 2009; accepted 25 February 2010
Published online 18 March 2010;
10.1126/science.1184655
Include this information when citing this paper.

Arsenic Trioxide Controls the Fate of the PML-RARα Oncoprotein by Directly Binding PML

Xiao-Wei Zhang,[1*] Xiao-Jing Yan,[1*] Zi-Ren Zhou,[2] Fei-Fei Yang,[3] Zi-Yu Wu,[3] Hong-Bin Sun,[4] Wen-Xue Liang,[1] Ai-Xin Song,[2] Valérie Lallemand-Breitenbach,[5] Marion Jeanne,[5] Qun-Ye Zhang,[1] Huai-Yu Yang,[6] Qiu-Hua Huang,[1] Guang-Biao Zhou,[7] Jian-Hua Tong,[1] Yan Zhang,[1] Ji-Hui Wu,[4] Hong-Yu Hu,[2] Hugues de Thé,[5,8] Sai-Juan Chen,[1,8]† Zhu Chen[1,8]†

Arsenic, an ancient drug used in traditional Chinese medicine, has attracted worldwide interest because it shows substantial anticancer activity in patients with acute promyelocytic leukemia (APL). Arsenic trioxide (As_2O_3) exerts its therapeutic effect by promoting degradation of an oncogenic protein that drives the growth of APL cells, PML-RARα (a fusion protein containing sequences from the PML zinc finger protein and retinoic acid receptor alpha). PML and PML-RARα degradation is triggered by their SUMOylation, but the mechanism by which As_2O_3 induces this posttranslational modification is unclear. Here we show that arsenic binds directly to cysteine residues in zinc fingers located within the RBCC domain of PML-RARα and PML. Arsenic binding induces PML oligomerization, which increases its interaction with the small ubiquitin-like protein modifier (SUMO)–conjugating enzyme UBC9, resulting in enhanced SUMOylation and degradation. The identification of PML as a direct target of As_2O_3 provides new insights into the drug's mechanism of action and its specificity for APL.

Oncogenic fusion proteins are a characteristic feature of many human leukemias and they often play a key role in driving the development and progression of the disease. These proteins arise when chromosomal rearrangements juxtapose two unrelated genes, and the resultant fusion gene produces an aberrant hybrid protein containing amino acid sequences corresponding to each gene. Because these oncogenic fusion proteins are selectively expressed in cancer cells, they have been extensively investigated as potential targets for anticancer therapies (*1*, *2*).

PML-RARα, a fusion protein found specifically in over 98% of human acute promyelocytic leukemia (APL), is produced as a result of a t(15;17) chromosomal translocation (*3*, *4*). It contains sequences from the promyelocytic leukemia protein (PML), a zinc finger protein whose function is not fully understood, and retinoic acid receptor alpha (RARα) (*4*). In vitro and in vivo studies have shown that PML-RARα is crucial for the pathogenesis of APL (*1*, *3*). Two drugs in clinical use for APL, arsenic trioxide (As_2O_3) and all-*trans* retinoic acid (ATRA), both act by promoting degradation of PML-RARα (*5*–*8*). When used as a combination therapy, these drugs lead to durable remission of APL (*9*). As_2O_3 induces degradation of PML-RARα and PML in NB4 cells, a human APL cell line (Fig. 1, A and B), by promoting a specific posttranslational modification (SUMOylation) of the PML moiety (*7*, *10*–*12*). The precise molecular mechanisms by which As_2O_3 regulates SUMOylation of these proteins remain obscure, however.

To investigate whether As_2O_3 directly alters the biochemical features of the PML proteins, we examined the effects of the drug on PML-RARα, PML, and RARα when these proteins were overexpressed in human embryonic kidney (HEK) 293T cells by DNA-mediated transfection (*13*). We found that as early as 10 min after exposure, As_2O_3 induced a shift of PML and PML-RARα, but not RARα, from the supernatant of cell lysates to the detergent-insoluble pellet (Fig. 1C) (*7*, *11*). After 30 min of As_2O_3 exposure, high-molecular-weight species corresponding to the modified forms of PML and PML-RARα were detected in the pellet fraction. Parallel experiments demonstrated the modifications to be the small ubiquitin-like protein modifiers SUMO-1, SUMO-2/3, and ubiquitin conjugations (fig. S1), consistent with previous studies (*11*). The rapid and specific effects of As_2O_3 on PML or PML-RARα pointed to a possible direct interaction of arsenic with these proteins. If arsenic binds directly to PML, it should be present together with PML in the detergent-insoluble pellet. We indeed observed that the arsenic content of the pellet from cells

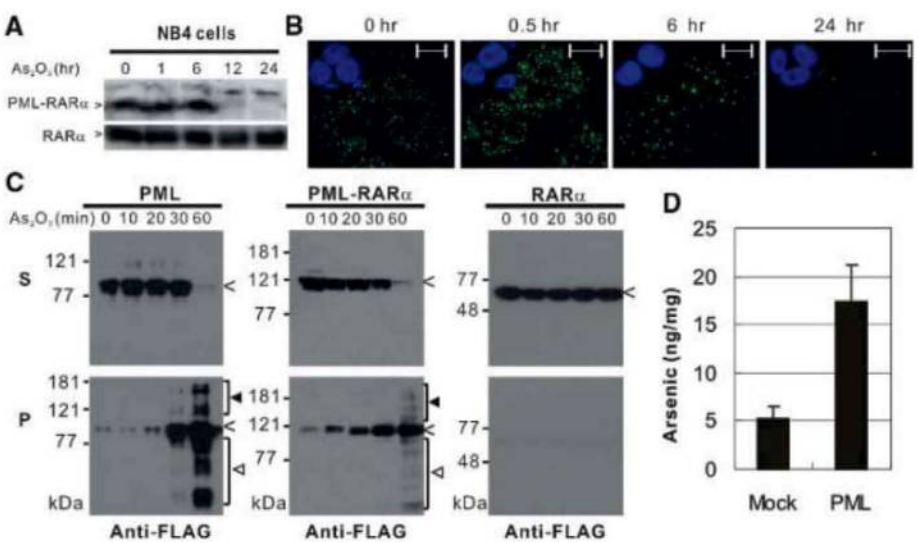

Fig. 1. The effect of As_2O_3 on the posttranslational modification and degradation of PML-RARα and PML is rapid and specific. (**A** and **B**) As_2O_3-induced degradation of PML-RARα in the APL cell line NB4 cells, as assessed by Western blotting with RARα antibody and immunofluorescence staining with PML antibody (green). The cells were treated with 1 μM As_2O_3. Scale bar, 10 μm. (**C**) A time-course study showing the effects of As_2O_3 on PML, PML-RARα, or RARα. (<) points to parental proteins, (▼) to modified proteins, and (▽) to degraded fragments. Transfected HEK 293T cells were treated with 2 μM As_2O_3 and then lysed in RIPA buffer and fractionated into supernatants (S) and pellets (P) by centrifugation. (**D**) The arsenic content of pellets from HEK 293T cells that had been mock-transfected or transfected with a vector encoding PML.

[1]State Key Laboratory of Medical Genomics, Shanghai Institute of Hematology, Rui Jin Hospital affiliated to Shanghai Jiao Tong University School of Medicine, 197 Rui Jin Road II, Shanghai 200025, China. [2]State Key Laboratory of Molecular Biology, Institute of Biochemistry and Cell Biology, Shanghai Institutes for Biological Sciences, Chinese Academy of Sciences (CAS), Shanghai 200031, China. [3]National Synchrotron Radiation Laboratory, University of Science and Technology of China and Beijing Synchrotron Radiation Facility, Institute of High Energy Physics, CAS, Beijing 10004, China. [4]Hefei National Laboratory for Physical Sciences at Microscale and School of Life Sciences, University of Science and Technology of China, Hefei, Anhui 230026, China. [5]Université de Paris 7/INSERM/CNRS UMR 944/7151, Equipe Labellisée No. 11 Ligue Nationale Contre le Cancer, Hôpital St. Louis, Avenue C. Vellefaux, 75475 Paris CEDEX 10, France. [6]Shanghai Institute of Materia Medica, Shanghai Institutes for Biological Sciences, CAS, Shanghai 201203, China. [7]Laboratory of Molecular Carcinogenesis and Targeted Therapy for Cancer, State Key Laboratory of Biomembrane and Membrane Biotechnology, and Key Laboratory of Stem Cell Development, Institute of Zoology, CAS, Beijing, China. [8]The Pôle Sino-Français de génomique et de Sciences du vivant de l'Hôpital Rui-Jin, 197 Rui-Jin Road II, Shanghai, China.

*These authors contributed equally to this work.
†To whom correspondence should be addressed. E-mail: zchen@stn.sh.cn (Z.C.); sjchen@stn.sh.cn (S.-J.C.)

overexpressing PML was substantially greater than that of the pellet from control, mock-transfected cells (Fig. 1D).

Arsenic is a metalloid element known to exert some of its biological effects through direct interaction of the trivalent arsenite anion (AsO_3^{3-}) with the thiol groups of vicinal cysteines in target proteins (*14*, *15*). Notably, the N-terminal structure of PML that is retained in all PML-RARα isoforms harbors a cysteine-rich RBCC domain (*16*, *17*). This domain includes one RING domain (R), two B box motifs (B1 and B2), and a coiled-coil domain (CC). Contained within the PML-R and PML-B box are zinc fingers (ZFs), cysteine-rich structural regions that potentially could be involved in arsenic binding (fig. S2) (*17*–*19*).

To explore whether arsenic binds directly to PML and PML-RARα in cells, we used as probes two organic arsenicals with effects similar to those of As_2O_3, *p*-aminophenylarsine oxide (PAPAO) and ReAsH (fig. S3). PAPAO was conjugated to biotin (designated as Biotin-As) (*20*). Analysis by a streptavidin agarose affinity assay revealed that Biotin-As bound to PML and PML-RARα, but not to RARα, and that this binding could be attenuated by As_2O_3 or unlabeled PAPAO (Fig. 2A).

We next performed experiments with ReAsH, an organic arsenic derivative whose red fluorescence is quenched until its arsenic moieties bind to vicinal thiols in target proteins (*21*). PML localizes in a distinctive fashion to punctate PML nuclear bodies (NBs), whereas PML-RARα exhibits a microspeckled pattern (*7*, *22*). We found that ReAsH, like As_2O_3, induced the aggregation of PML NBs (Fig. 1B and 2B). Moreover, ReAsH colocalized with PML signals in NB4 cells (Fig. 2B), which suggested that ReAsH directly binds to PML-RARα and/or PML. This colocalization was attenuated by a pretreatment with As_2O_3 but not $ZnSO_4$ (Fig. 2B).

To further investigate arsenic binding, we transiently overexpressed proteins that were fused to EGFP (enhanced green fluorescent protein). ReAsH colocalized with EGFP-PML and EGFP-PML-RARα in a relatively specific manner (Fig. 2C and fig. S4). To clarify which region(s) of PML are involved in the interaction with ReAsH, we constructed various deletion mutants of the protein (fig. S2A). We observed that EGFP-PML 1–394 (containing the RBCC domain) was strongly labeled by ReAsH, whereas EGFP-PML ΔRBCC displayed no colocalization with ReAsH (Fig. 2C). There was almost no ReAsH colocalization signal detected in experiments with EGFP-PML ΔR, and the colocalization signal was significantly attenuated in experiments with EGFP-PML ΔB2. In contrast, EGFP-PML ΔB1 still showed significant colocalization with ReAsH. Collectively, these results suggest that arsenic directly binds PML through its RING domain, as well as its B2 motif (Fig. 2C).

The PML-R domain plays a central role in PML SUMOylation (*23*), and the structure of this domain has been determined by nuclear magnetic resonance (NMR) (*18*). We therefore used the isolated PML-R domain as a model to investigate the characteristics of arsenic interaction with the complete PML protein. We prepared recombinant apo-PML-R (PML-R without zinc) and determined arsenic binding activity by matrix-assisted laser desorption/ionization–time-of-flight (MALDI-TOF) mass spectrometry (MS) with the rationale that each molecule of arsenic bound to the protein should be identified by a mass increment of 75 (atomic mass of arsenic) as compared to the parental protein (*14*). In experiments involving a clinically relevant concentration of As_2O_3, we found that apo-PML-R bound to one or two arsenic (Fig. 3A). Optical absorbance of PML-R increased in the range of 250 to 340 nm with addition of As_2O_3 (Fig. 3B), which indicated that arsenic-sulfur bonds had formed (*24*). Extended x-ray absorption fine structure (EXAFS) and x-ray absorption near-edge structure (XANES) spectroscopy (*25*) indicated that arsenic tended to coordinate with three sulfur atoms from the three conserved cysteines in both PML-R-ZFs (C60, C77, C80 in ZF1 and C72, C88, C91 in ZF2), whereas zinc exhibited the typical tetrahedral coordination with conserved cysteine and histidine residues (Fig. 3, C and D, fig. S5, and tables S1 and S2). Consistent with this, the PML mutants with the double mutation C77/C80A (Cys^{77} Cys^{80} replaced by Ala) and C88/91A showed an attenuated affinity to arsenic and had no response to As_2O_3 modulation in terms of the pellet transfer and high-molecular-weight modification (fig. S6).

Proteins can adopt different conformations upon coordination with different metals, which affects both their function and stability (*26*). Circular dichroism (CD) showed that As-PML-R (apo-PML-R titrated with As_2O_3) adopted fewer secondary structures than Zn-PML-R (stabilized by zinc binding) (Fig. 3E), as previously shown with other proteins (*27*). NMR hetero-

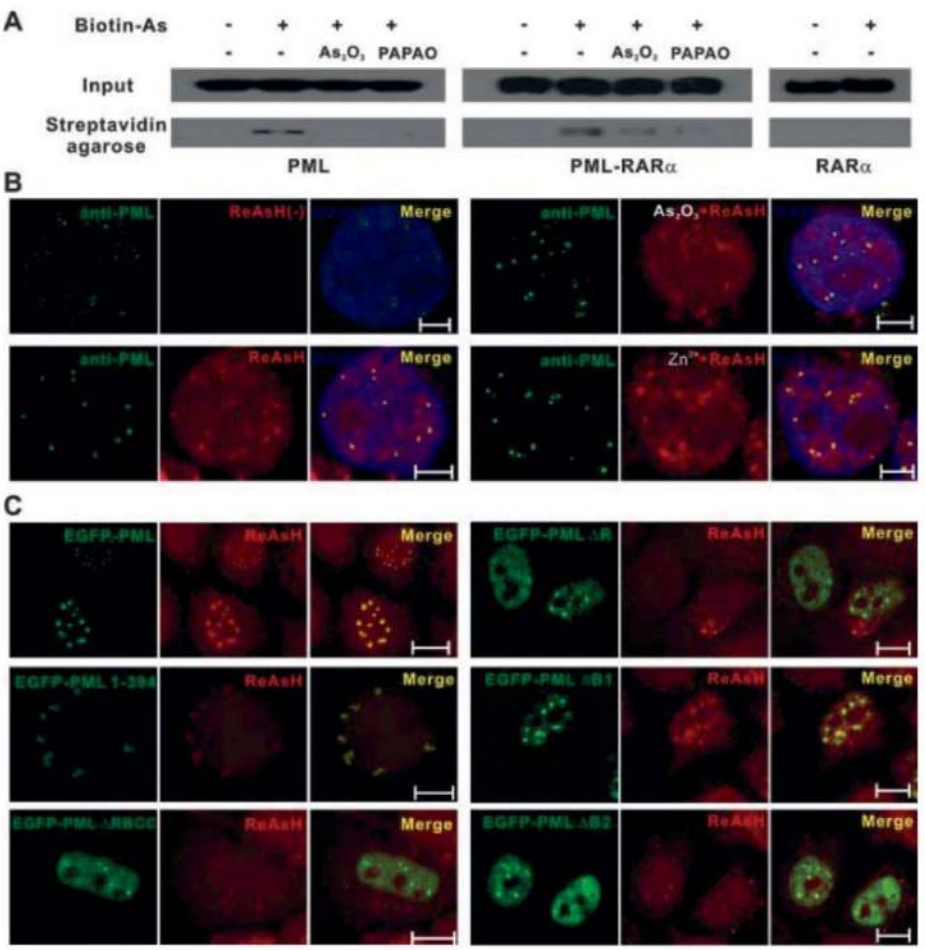

Fig. 2. Arsenic binds to PML-RARα and PML in cultured cells. (**A**) The arsenic binding proteins PML and PML-RARα, but not RARα, were identified in a streptavidin agarose affinity assay in which a biotinylated derivative of the organic arsenical PAPAO (Biotin-As) was used as a probe. (**B**) Colocalization of PML and PML-RARα with the fluorescent organic arsenical ReAsH in NB4 cells. As_2O_3+ReAsH, pretreatment with As_2O_3; Zn^{2+}+ReAsH, pretreatment with $ZnSO_4$. Scale bar, 5 μm. (**C**) Colocalization of EGFP-labeled PML and various EGFP-labeled PML deletion mutants with ReAsH in HeLa cells. Schematic structures of the deletion mutants are provided in fig. S2A. Scale bar, 10 μm.

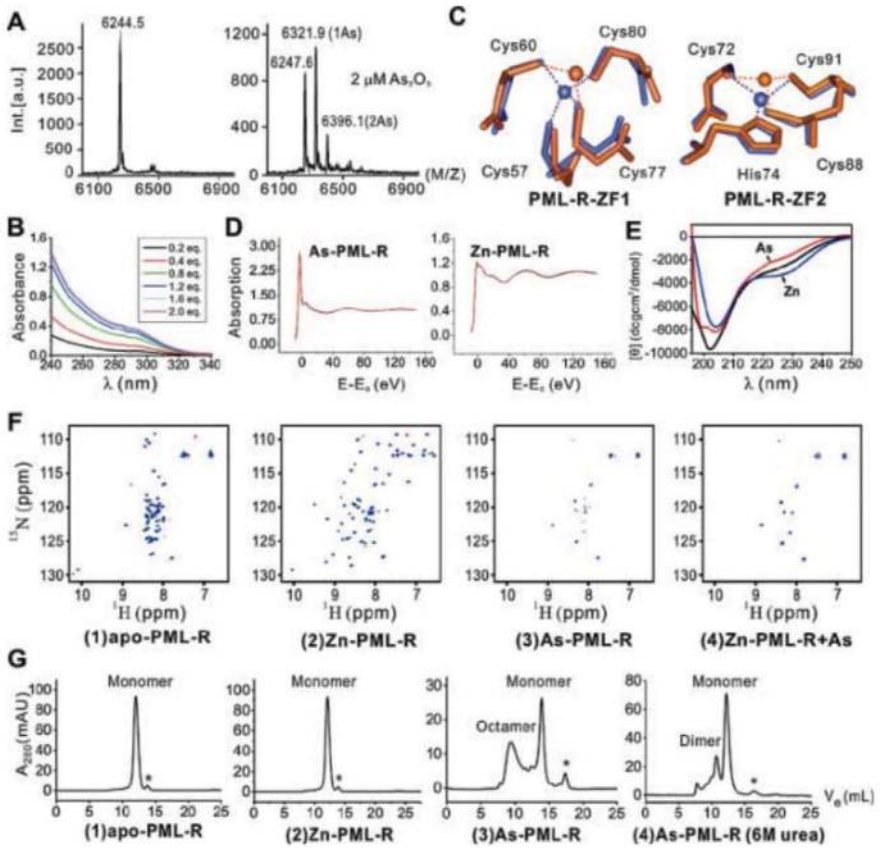

Fig. 3. Arsenic binds to PML-R and induces a conformational change in this protein domain in vitro. (**A**) The interaction between apo-PML-R and arsenic. Apo-PML-R was incubated with As_2O_3 (As-PML-R) and then analyzed by MALDI-TOF mass spectrometry. The numbers shown in parentheses near the peaks represent the number of arsenic atoms bound to the parental peptides. (**B**) Near-ultraviolet absorbance spectrometry assay of apo-PML-R titrated with As_2O_3. (**C**) Local structure showing conserved cysteines and/or histidine around metal ions of Zn-PML-R (orange) or As-PML-R (blue), obtained by XANES and EXAFS analysis. (**D**) XANES spectra. Black curves represent experimental data and red lines, the best fit (*13*). (**E**) CD spectra of apo-PML-R (black line) titrated with $ZnCl_2$ (blue) or As_2O_3 (red). (**F**) NMR HSQC spectra of (1) apo-PML-R, (2) Zn-PML-R, (3) As-PML-R, and (4) Zn-PML-R titrated with 10 eq. of As_2O_3. PML-R in NaAc buffer (pH 5.6) was titrated stepwise with $ZnCl_2$ or As_2O_3 under NMR HSQC monitoring. (**G**) Gel filtration of (1) apo-PML-R, (2) Zn-PML-R, (3) As-PML-R, and (4) As-PML-R in 6M urea buffer. *Impurity.

nuclear single-quantum coherence (HSQC) spectra further demonstrated that As-PML-R tended to oligomerize as indicated by the disappearance of most of its resonance peaks (Fig. 3F, panel 3), different from the well-folded Zn-PML-R (Fig. 3F, panel 2). It was noteworthy that Zn-PML-R oligomerized when excessive As_2O_3 (10 eq.) was added (Fig. 3F, panel 4) and showed an HSQC spectrum similar to that of As-PML-R (Fig. 3F, panel 3). This observation suggests that arsenic might replace the zinc in Zn-PML-R under these conditions.

Gel filtration studies revealed that the PML-R oligomers induced by arsenic binding were primarily octamers (Fig. 3G, panel 3). Under denaturing condition such as 6M urea, a small portion corresponding to homodimers remained, probably because of arsenic-mediated cross-linking between two PML-R molecules (Fig. 3G, panel 4). This hypothesis is consistent with our observations that As_2O_3 promotes PML NBs aggregation in cells (Fig. 1B and fig. S7A) and that these aggregates are resistant to disruption by detergent-containing buffers, such as RIPA and 3M urea buffer (fig. S7B). This resistance could be responsible for the rapid transfer of PML from the supernatant of cell lysates to the pellet after As_2O_3 treatment (fig. S7C). Since transfer of PML to the pellet preceded its appearance as a high-molecular-weight species (Fig. 1C and fig. S7C), it is possible that arsenic-induced oligomerization of PML facilitates the protein's subsequent modification by SUMOylation and ubiquitination and enhances its degradation.

We therefore performed an in vitro SUMOylation assay to investigate whether these posttranslational modifications might be due to structural changes of PML induced by arsenic binding. Note that As_2O_3-pretreatment of PML enhanced its SUMO-2 modification in vitro (Fig. 4A). This

Fig. 4. Biological consequences of the structural change in PML that is induced by arsenic binding. (**A**) Arsenic binding enhances SUMO-2 (S2) modification of PML. For determination of the effect of As_2O_3 on SUMO conjugation, anti-FLAG (FLAG antibody–labeled) M2 beads with FLAG-PML (F-PML) were incubated with As_2O_3 and then stringently washed to remove free arsenic before in vitro SUMOylation. E1: SAE1/SAE2, SUMO activating enzyme. (**B**) Arsenic binding enhances the PML-R-mediated interaction between PML and UBC9 in vitro. (**C**) Arsenic enhances the interaction between PML and UBC9 in HeLa cells. The interaction of PML and UBC9 was determined by mammalian two-hybrid assay. RLA, relative luciferase activity. (**D**) A working model of the mechanism by which As_2O_3 controls the fate of PML and PML-RARα.

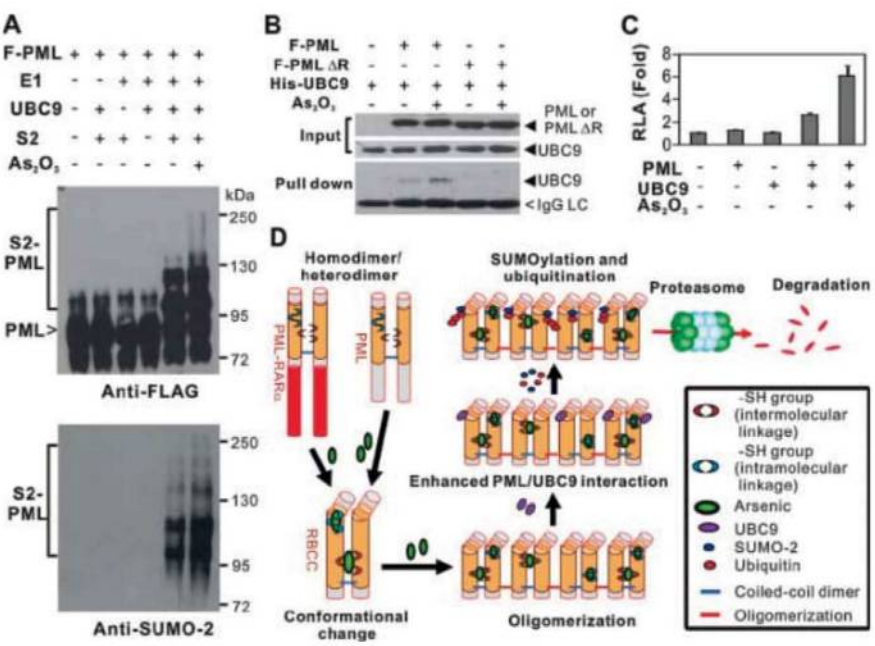

was accompanied by an enhanced interaction between PML and UBC9, the E2 SUMO-conjugating enzyme (Fig. 4B); this enhanced interaction also occurred in intact cells, as measured by a mammalian two-hybrid assay (Fig. 4C). The interaction of PML with UBC9 was mediated by PML-R (Fig. 4B), which points to an important role of PML-R in regulating SUMOylation. Predictions from structural modeling indicate that amino acid residues Q58 and Q59 in ZF1 of PML-R could directly contact UBC9 (fig. S8). The conformational change in ZF1 that is induced by arsenic binding might alter the conformation and position of Q58 and/or Q59 and increase the binding affinity of UBC9 for PML-R, which in turn might lead to enhanced SUMOylation of PML-R.

On the basis of our data and previous observations that PML-RARα and PML are capable of homodimerization or heterodimerization through the PML coiled-coil domain (*16*, *17*), we propose the following mechanistic model for arsenic-induced degradation of PML and PML-RARα: Arsenic binds to cysteines in the ZFs of the PML RBCC domains either intramolecularly or by forming cross-links between the two RBCC molecules in the homodimer. The resultant conformational changes may facilitate further oligomerization of PML-RARα or PML and promote SUMOylation of these proteins through enhanced interaction of PML with the enzymes that catalyze this modification (such as UBC9) or through enhanced exposure of the modification sites. Ultimately this would lead to enhanced ubiquitination and degradation of PML and the PML-RARα oncoprotein (Fig. 4D) (*7*, *11*). The structural and molecular basis for the exquisite sensitivity of PML ZFs to arsenic merits further investigation.

In summary, we have demonstrated that arsenic binds directly to the PML-RARα oncoprotein that drives the development of APL. This interaction is likely to explain, at least in part, why As_2O_3 is a clinically effective therapy for patients with APL (*9*, *28*). The identification of PML as a direct target of As_2O_3 opens new perspectives for optimizing the use of this ancient remedy in future leukemia therapies (*29*).

References and Notes

1. Z. Y. Wang, Z. Chen, *Blood* **111**, 2505 (2008).
2. J. Zhu, Z. Chen, V. Lallemand-Breitenbach, H. de Thé, *Nat. Rev. Cancer* **2**, 705 (2002).
3. G. B. Zhou, J. Zhang, Z. Y. Wang, S. J. Chen, Z. Chen, *Philos. Trans. R. Soc. London B Biol. Sci.* **362**, 959 (2007).
4. H. de Thé, C. Chomienne, M. Lanotte, L. Degos, A. Dejean, *Nature* **347**, 558 (1990).
5. Z. X. Shen *et al.*, *Blood* **89**, 3354 (1997).
6. M. E. Huang *et al.*, *Blood* **72**, 567 (1988).
7. J. Zhu *et al.*, *Proc. Natl. Acad. Sci. U.S.A.* **94**, 3978 (1997).
8. J. Zhu *et al.*, *Proc. Natl. Acad. Sci. U.S.A.* **96**, 14807 (1999).
9. J. Hu *et al.*, *Proc. Natl. Acad. Sci. U.S.A.* **106**, 3342 (2009).
10. V. Lallemand-Breitenbach *et al.*, *J. Exp. Med.* **193**, 1361 (2001).
11. V. Lallemand-Breitenbach *et al.*, *Nat. Cell Biol.* **10**, 547 (2008).
12. M. H. Tatham *et al.*, *Nat. Cell Biol.* **10**, 538 (2008).
13. Materials and methods are available as supporting material on *Science* Online.
14. G. Jiang, Z. Gong, X. F. Li, W. R. Cullen, X. C. Le, *Chem. Res. Toxicol.* **16**, 873 (2003).
15. J. Lu, E. H. Chew, A. Holmgren, *Proc. Natl. Acad. Sci. U.S.A.* **104**, 12288 (2007).
16. A. Melnick, J. D. Licht, *Blood* **93**, 3167 (1999).
17. K. Jensen, C. Shiels, P. S. Freemont, *Oncogene* **20**, 7223 (2001).
18. K. L. Borden *et al.*, *EMBO J.* **14**, 1532 (1995).
19. K. L. Borden *et al.*, *Proc. Natl. Acad. Sci. U.S.A.* **93**, 1601 (1996).
20. X. Zhang *et al.*, *Cancer Lett.* **255**, 95 (2007).
21. B. R. Martin, B. N. Giepmans, S. R. Adams, R. Y. Tsien, *Nat. Biotechnol.* **23**, 1308 (2005).
22. G. Q. Chen *et al.*, *Blood* **89**, 3345 (1997).
23. E. Duprez *et al.*, *J. Cell Sci.* **112**, 381 (1999).
24. A. M. Spuches, H. G. Kruszyna, A. M. Rich, D. E. Wilcox, *Inorg. Chem.* **44**, 2964 (2005).
25. M. Benfatto, S. Della Longa, C. R. Natoli, *J. Synchrotron Radiat.* **10**, 51 (2003).
26. H. Bhattacharjee, B. P. Rosen, *J. Biol. Chem.* **271**, 24465 (1996).
27. A. M. Spuches, D. E. Wilcox, *J. Am. Chem. Soc.* **130**, 8148 (2008).
28. R. Nasr *et al.*, *Nat. Med.* **14**, 1333 (2008).
29. K. Ito *et al.*, *Nature* **453**, 1072 (2008).

30. We thank E.-D. Wang, K.-K. Wang, J. Zhu, and X.-J. Sun for constructive comments on the work; Y.-Y. Shi, H.-L. Jiang, J.-H. Mao, C.-F. Wu, Y.-Y. Xie, Y.-G. Chang, Y.-J. Jiang, and W.-S. Chu for experimental assistance; X.-D. Xi, N. Kieffer, and J. Zhu for critical reading of the manuscript; and all members of Shanghai Institute of Hematology for their encouragement. This work was supported in part by 863 Program (2006AA02A405), 973 Project (2010CB529201, 2006CB910305), the National Natural Science Foundation of China (30801372, 30623010, 30772744, 30830119, 10734070), the Shanghai Municipal Commission for Science and Technology (07DZ05908 and 08DZ2200100), and the Samuel Waxman Cancer Research Foundation Co-Principal Investigator Program.

Supporting Online Material

www.sciencemag.org/cgi/content/full/328/5975/240/DC1
Materials and Methods
Figs. S1 to S8
Tables S1 and S2
References

16 October 2009; accepted 9 March 2010
10.1126/science.1183424

Transnuclear Mice with Predefined T Cell Receptor Specificities Against *Toxoplasma gondii* Obtained via SCNT

Oktay Kirak,[1]* Eva-Maria Frickel,[1] Gijsbert M. Grotenbreg,[1]† Heikyung Suh,[1] Rudolf Jaenisch,[1,2]* Hidde L. Ploegh[1,2]*

Mice that are transgenic for rearranged antigen-specific T cell receptors (TCRs) are essential tools to study T cell development and function. Such TCRs are usually isolated from the relevant T cells after long-term culture, often after repeated antigen stimulation, which unavoidably skews the T cell population used. Random genomic integration of the TCR α and β chain and expression from nonendogenous promoters represent additional drawbacks of transgenics. Using epigenetic reprogramming via somatic cell nuclear transfer, we demonstrated that T cells with predefined specificities against *Toxoplasma gondii* can be used to generate mouse models that express the TCR from their endogenous loci, without experimentally introduced genetic modification. The relative ease and speed with which such transnuclear models can be obtained holds promise for the construction of other disease models.

The resolution of an infectious disease requires careful orchestration of innate and adaptive immunity. B and T cells specific for infectious agents are not easily obtained in abundant and pure form, yet their availability is crucial in defining their activation requirements and protective properties, either as a single clone or as an ensemble of different specificities. During the peak of an immune response, as many as 30% of all $CD8^+$ T cells may be pathogen-specific (*1*, *2*). For viral pathogens such as vaccinia virus or mouse herpes virus-68, several dozen antigens may be recognized by $CD8^+$ and $CD4^+$ T cells (*3*–*5*). Existing T cell receptor (TCR) transgenic mouse models have all been constructed from T-cell clones or hybridomas selected for survival and response to antigens in vitro. Whether these transgenic mouse models accurately reflect the affinities and activation requirements of lymphocytes triggered during a physiological response to an infection is not known.

Somatic cell nuclear transfer (SCNT) allows the generation of embryonic stem cells (ESCs)

[1]Whitehead Institute for Biomedical Research, Cambridge, MA 02142, USA. [2]Department of Biology, Massachusetts Institute of Technology, Cambridge, MA 02142, USA.

*To whom correspondence should be addressed. E-mail: kirak@wi.mit.edu (O.K.); jaenisch@wi.mit.edu (R.J.); ploegh@wi.mit.edu (H.L.P.).

†Current address: Immunology Programme and Departments of Microbiology and Biological Sciences, National University of Singapore, 117456 Singapore.

and mice from any somatic cell through epigenetic reprogramming without the introduction of genetic modifications (*6*–*8*). The specificity of TCRs or B cell receptors (BCRs) is determined by site-specific recombination of their V, D, and J gene segments. Consequently, when SCNT is applied to lymphocytes of known specificity, these genetic V(D)J rearrangements are transferred to the SCNT-ESCs and the mice derived from them, whereas epigenetic marks are reset (Fig. 1A). Natural killer T cells (NKTs) carrying an invariant TCR, as well as T and B cells of unknown specificity, have been used as donor cells for SCNT, demonstrating that mice can be cloned from such cells and that their rearranged TCR- or Ig-loci can be transmitted through the germline (*9*–*12*).

We applied this approach to create a new mouse model by using effector $CD8^+$ T cells specific for *Toxoplasma gondii*, isolated at the height of resolving an acute infection (*13*). We focused on these cells because protective immunity against this protozoan critically depends on interferon (IFN)–γ produced by $CD8^+$ T cells (*14*, *15*). We had identified two naturally processed epitopes, L^d-Tg-Rop7$^{161\text{-}169}$ (R7) and L^d-Tg-Gra4$^{107\text{-}115}$ (G4), restricted by the major histocompatibility complex antigen (MHC-I) H-$2L^d$ and recognized by $CD8^+$ T cells (*16*). Using a similar approach, a screen for epitopes recognized by H-$2K^b$ or H-$2D^b$ led to the identification of one H-2^b–restricted epitope, K^b-Tg-tgd057$^{59\text{-}66}$ (T57), a protein of unknown function (*17*). One additional H-2^d epitope, L^d-Tg-Gra6$^{215\text{-}224}$, was identified in parallel (*18*). However, there has been no mouse model that provides access to naïve antigen-inexperienced *T. gondii*–specific T cells.

We used $CD8^+$ T cells specific for R7, G4, and T57 on the BL/6 x Balb/c F1 (B6CF1) background as donor cells for SCNT, a procedure that is more efficient for donor nuclei of mixed background (*6*). To improve nuclear reprogramming, we made use of trichostatin A (TSA), an inhibitor of histone deacetylases (Fig. 1B). We generated SCNT-blastocysts with an overall efficiency of 7.2% per pseudo-pronucleus (PPN) in all three conditions and obtained ESCs when using TSA treatment for 6 hours (four ESC lines) or 10 hours (one ESC line), but none in the absence of TSA. As a control, fertilized blastocysts on the B6CF1 background yielded 47 ESCs per 48 blastocysts (fig. S1A). When $CD8^+$ T cells from a pure Balb/c background were used as donor cells, we derived two SCNT-ESC lines with similar efficiency (fig. S1B), but only after 10 hours of TSA treatment, confirming reports that TSA indeed facilitates cloning of inbred mice (*7*, *19*).

We generated chimeric mice using the five SCNT-ESC lines from the B6CF1 background, all of which showed pronounced populations of tetramer-positive $CD8^+$ T cells in the absence of infection with *T. gondii* (Fig. 1C). Chimeric mice derived from the two SCNT-ESC lines on the Balb/c background also yielded $CD8^+$ T cells of correct specificity (fig. S1C). We thus cloned T cells of desired specificity in seven out of seven cases, a rate that depends on both TSA treatment and the ability to obtain donor cells of sufficient purity. We refer to these animals as transnuclear (TN) mice because such mice, generated via SCNT of T cells (or B cells) with preselected specificity, represent a new type of mouse model.

To test for germline transmission and to establish TN mouse lines, chimeric mice with T57 T cells (H-2^b–restricted) were backcrossed onto the MHC-matched BL/6 background. Offspring with agouti coat color indicated germline transmission (fig. S1D). Chimeric mice with H-2^d–restricted T cells (G4 and R7) were backcrossed onto the MHC-matched Balb/c background, and offspring with a white coat color indicated germline transmission (fig. S1D). All litters from transmitting males were analyzed by means of either polymerase chain reaction (PCR) or flow cytometry in order to identify offspring carrying the corresponding TCR (fig. S1, E to G). We secured germline transmission of the respective TCRs in five out of five SCNT-ESC lines derived from the B6CF1 background. No

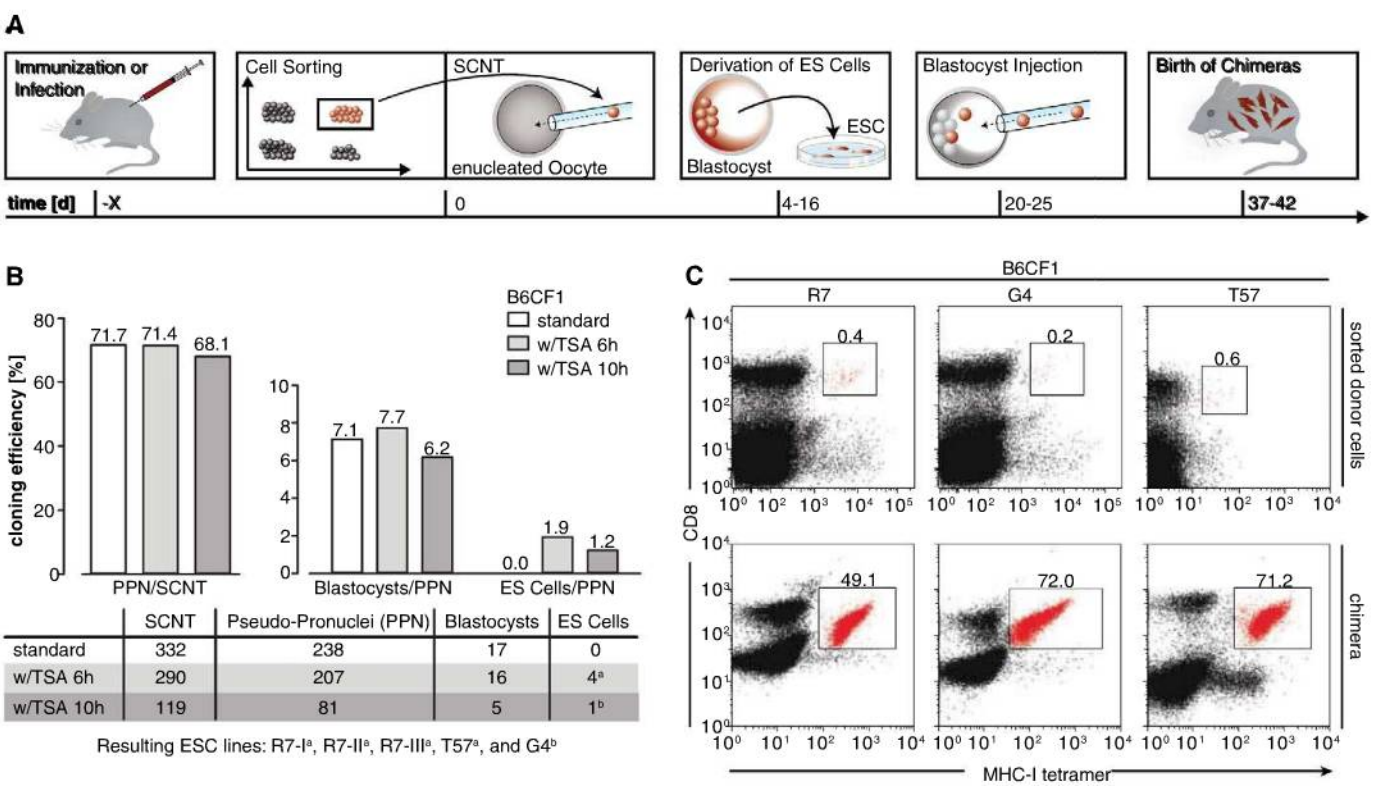

	SCNT	Pseudo-Pronuclei (PPN)	Blastocysts	ES Cells
standard	332	238	17	0
w/TSA 6h	290	207	16	4[a]
w/TSA 10h	119	81	5	1[b]

Resulting ESC lines: R7-I[a], R7-II[a], R7-III[a], T57[a], and G4[b]

Fig. 1. SCNT of predefined T cells. (**A**) Schematic representation of the underlying strategy and timeline. (**B**) Absolute and relative numbers of SCNT performed with $CD8^+$ T cells and derived ESCs in B6CF1 background. (**C**) (Top) Representative flow cytometry plots of B6CF1 background mice infected with *T. gondii*. Gate and number (percent per total $CD8^+$ T cells) indicates sorted $CD8^+$ T cells with defined specificity used as donor cells. (Bottom) Representative flow cytometry analysis of chimeric mice injected with SCNT-ESCs derived from corresponding donor cells in top panels. Gate and number (percent per total $CD8^+$ T cells) indicates the presence of specific $CD8^+$ T cells in chimeric mice.

germline transmission was achieved for the two SCNT-ESC lines from the Balb/c background. The resulting animals represented three different TCR specificities (T57, G4, and R7), restricted by two different MHC-I alleles (H-2L^d and H-2K^b).

We next identified the genomic TCR rearrangements from the TN mice on the B6CF1 background (Fig. 2A and fig. S2, A and B) by means of rapid amplification of cDNA ends (RACE)–PCR. Examination of the cDNA sequences obtained showed that the three SCNT-ESC lines specific for R7 were different from each other. A comparison of their amino acid sequences revealed no obvious pattern of the complementary determining region 3 (CDR3) that would explain their shared specificity (fig. S2C).

To characterize TN mice, we compared splenocytes from the T57 line with B6CF1 wild-type mice and a widely used TCR transgenic line also restricted by H-2K^b, OT-I, which is specific for a chicken ovalbumin–derived peptide (SIINFEKL) (*20*). A comparison of T cells (CD3$^+$) and B cells (B220$^+$) showed that the TN line had a relative increase in the CD3$^+$ population (35.6% for TN versus 12.8% for B6CF1 wild type) and that this population consisted mainly of CD8$^+$ T cells (91.3% for TN versus 43.1% for wild type) (Fig. 2B). A skewing in the CD8$^+$ population was also apparent in the OT-I line (84.8%), but without a relative increase in CD3$^+$ cells (17.7%). The majority of CD8$^+$ TN cells were CD44^{low} CD62L$^+$, which is indicative of a naïve phenotype (64.1% for T57 versus 69.6% for wild type). We also compared the TN line G4 to the transgenic line 2C (Fig. 2C). The alloreactive 2C line was derived from a Balb/b mouse (H-2^b) injected with H-2^d cells (H-2^b anti H-2^d). Its response against the QL9 peptide is particularly well-characterized (*21*–*23*). Similar patterns were observed for the two TN lines G4 and T57. TN mice expressing only a single copy of a pre-rearranged endogenous β-chain had no major changes in T cell subsets, whereas TN mice expressing a single copy of a pre-rearranged endogenous α-chain had an increase in CD3$^+$ CD4$^-$ CD8$^-$ cells in the spleen (fig. S3, A and B). Finally, we found that T-cell development in TN mice T57 and G4 in all aspects examined resembles that of B6CF1 wild-type mice and of some transgenic lines (fig. S4, A to D, and fig. S5, A and B).

Because TN CD8$^+$ T cells were generated from freshly isolated effector CD8$^+$ T cells, we hypothesized that TN T cells may have MHC-binding characteristics that are distinct from conventional TCR transgenic mice. In a MHC-I–tetramer dissociation assay, the TN CD8$^+$ T cells of H-2L^d haplotype dissociated faster from their cognate

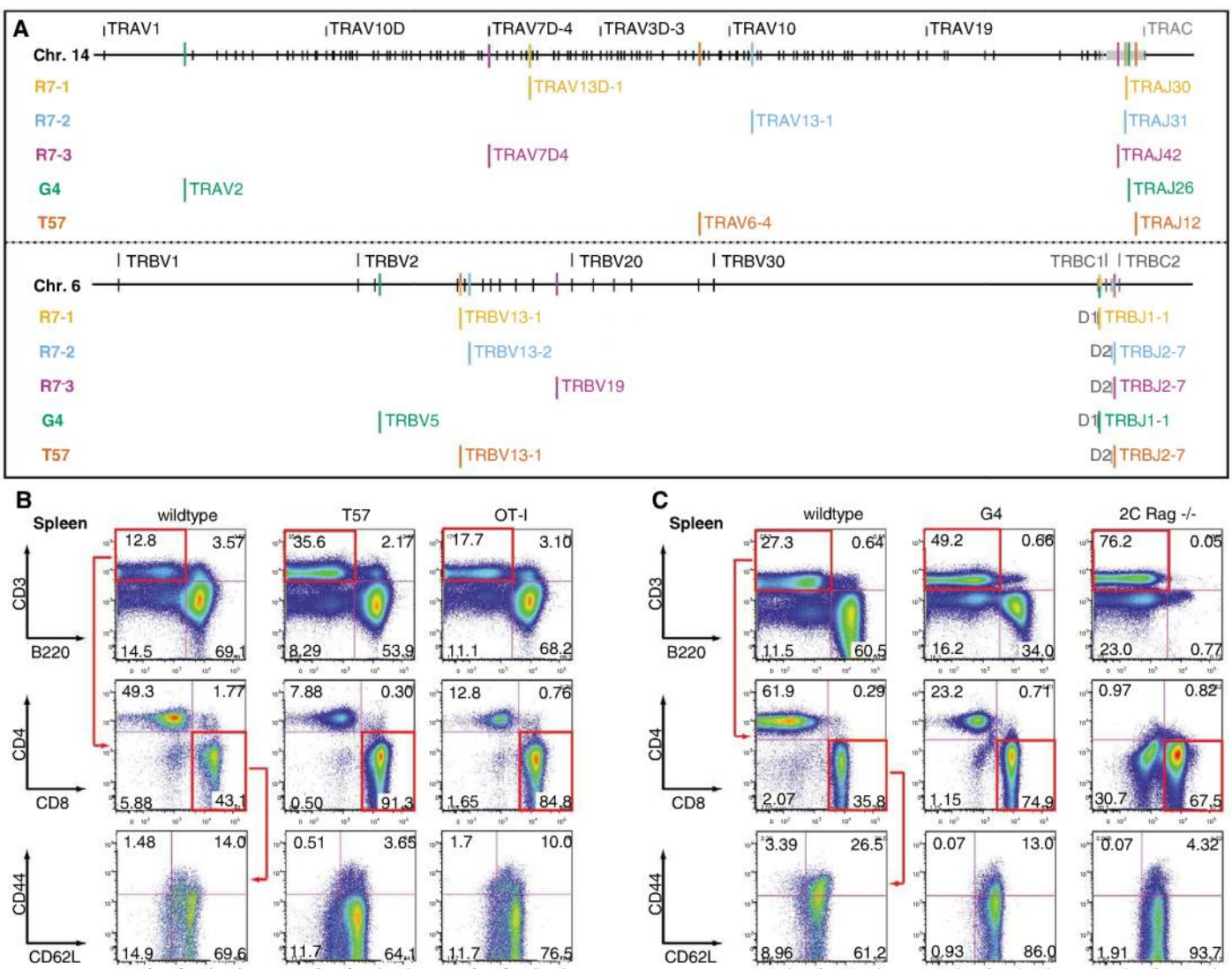

Fig. 2. TCR sequence and comparison of TN T cells with wild-type and transgenic mice. (**A**) Schematic representation of the V(D)J rearrangements at the TCR-α (top) and TCR-β locus (bottom) in TN mice. Top row represents wild-type configuration and some regions for orientation (data are based on www.ensembl.org). (**B** and **C**) Representative flow cytometric analysis of splenocytes from (B) wild-type, T57, and OT-I mice or (C) wild-type, G4, and 2C *Rag*$^{-/-}$ mice (two mice per genotype were analyzed).

peptide–MHC-I complex than did transgenic 2C cells (Fig. 3A). The observed differences in dissociation rate of the H-2L^d T cells are not due to differences in peptide-MHC interactions because the peptides QL9, G4, and R7 stabilized H-2L^d in transporter of antigen processing (TAP)–deficient cells equally well (Fig. 3B). Although we are aware of the limitations of tetramer dissociation as a surrogate parameter for TCR affinity (*24*), we consider it possible that the average *T. gondii*–specific H-2L^d–restricted TCR may well be of lower affinity than the highly selected 2C. A comparison of TN T57 with transgenic OT-I cells showed similar dissociation rates (Fig. 3C). We examined the ability of TN CD8$^+$ T cells to produce IFN-γ upon stimulation with peptide-loaded antigen-presenting cells in vitro. TN T cells secreted IFN-γ only when stimulated with the corresponding peptide (Fig. 3D).

To assess the extent to which the presence of only the TCR α- or β-chain suffices to yield TCRs of specificity similar to that of the TN αβ pair, we analyzed mice that carry only the TN α- or only the TN β-chain of T57 or G4 (fig. S6A). There was no increase in tetramer-positive T cells in mice carrying the TN β-chain or α-chain only.

We next compared the in vivo response of wild-type BL/6 and TN CD8$^+$ T cells to an infection with *T. gondii* (Fig. 4, A and B, and fig. S6, B to E). In wild-type mice, we detected T57 tetramer-positive CD8$^+$ T cells mainly between day 9 to 15 after infection, with a maximum frequency of about 7% (fig. S6B). When T57 CD8$^+$ T cells were adoptively transferred into wild-type mice, the kinetics of expansion were comparable but with a much higher frequency of T57 tetramer-positive CD8$^+$ TN T cells (about 60%) (Fig. 4, A and B). We detected little or no response from the endogenous CD8$^+$ T cells in these mice that received TN T cells (Fig. 4A and fig. S6C). Similarly, when carboxyfluorescein diacetate succinimidyl ester (CFSE)–labeled CD8$^+$ T cells from wild-type or T57 mice were transferred into recipient mice which were then infected with *T. gondii*, up-regulation of CD69 and dilution of CFSE was observed only in mice receiving T57 T cells (fig. S6, D and E).

We next investigated the protective potential of CD8$^+$ T cells from T57 TN mice. Animals infected with a lethal dose of *T. gondii* die around day 10, and some of the CD8$^+$ T-cell responses do not peak before that time (*16*–*18*). When B6CF1 mice were challenged with a lethal dose of *T. gondii*, four out of seven mice receiving CD8$^+$ T cells from T57 TN mice survived the acute phase of infection, as compared with one out of seven in the control group (Fig. 4C). Using live imaging in the course of a lethal challenge with luciferase-expressing *T. gondii*, we observed a significant reduction in parasite load at day 7 after infection in the group that received CD8$^+$ T cells from T57 (Fig. 4D). Further experiments will show whether all five TN lines are equally capable of controlling *T. gondii* and help establish the number of specific cells needed, as well as the cell type (naïve, effector, or memory T cell) that is most effective at protection.

Transgenic mouse models have long been used to study various aspects of the immune system. Their generation involves long-term culture and repeated stimulation of T cells with antigen, isolation of the TCR α- and β-chains as cDNA or genomic fragments under the control of a non-endogenous promoter, and integration of the TCR into the mouse genome at non-homologous sites (*25*–*27*). This inevitably leads to variation in expression levels, kinetics, and development even in mice expressing the same TCR (*28*). Further

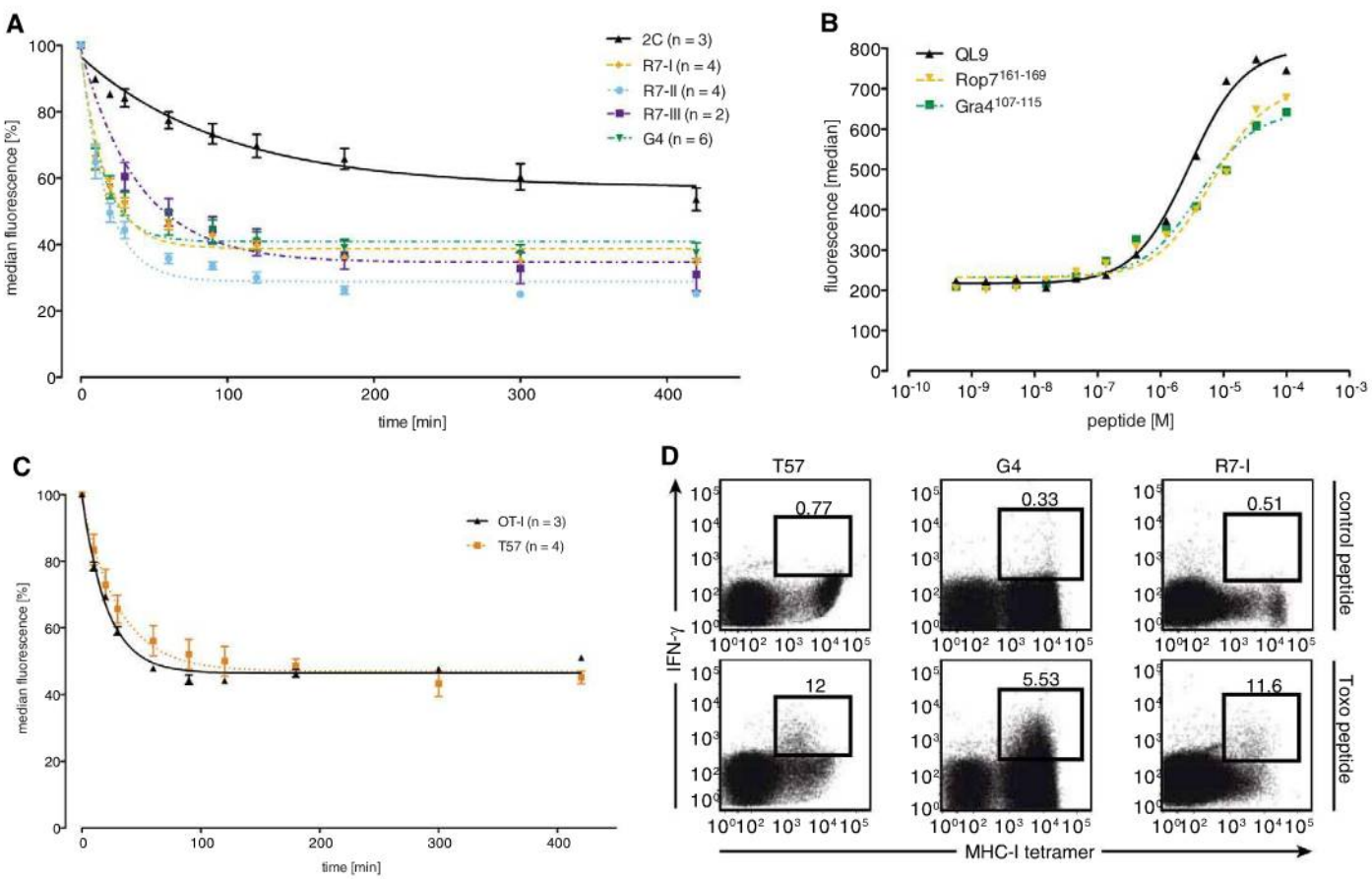

Fig. 3. TN T cell function in vitro. (**A**) Dissociation of peptide-L^d tetramers from CD8$^+$ T cells was measured for the transgenic line 2C *Rag*$^{-/-}$ (L^d-QL9) and the TN lines R7 I-III and G4 by use of flow cytometry and plotted over time. Number of repeats (*n*) is shown in brackets. Data plotted represents mean ± SEM. (**B**) Stabilization of H-2L^d on the surface of TAP-deficient cells via titration of QL9, R7, or G4 peptide [analyzed by use of GraphPad Prism software (GraphPad Software, La Jolla, CA)]. (**C**) Dissociation of the peptide-K^b tetramers from CD8$^+$ T cells for the transgenic line OT-I and the TN line T57. Number of repeats (*n*) is shown in brackets. Data plotted is mean ± SEM. (**D**) Flow cytometry analysis of IFN-γ secretion upon stimulation of TN T cells with antigen-presenting cells loaded with control peptide (top) or corresponding specific peptide (bottom).

studies of suitable TCR transgenic lines are governed mostly by random selection of a "best responder." To show that somatic cells can be reprogrammed, a mouse line had been generated from a randomly chosen T cell (*10*). This mouse showed skewed T-cell development, with a strong increase in the CD4-CD8 DN population (45% in LN3 compared to 5% in wild type), attributed to aberrant expression of the α-chain (*11*). Besides a relative shift in the DN1-4 stages toward the DN4 phase, we did not observe an increase in the CD4-CD8 DN population in the TN mice reported here. TN mice have no additional experimentally introduced genetic modifications. Consequently, the differences observed amongst TN lines must be due to position effects within the rearranged TCR locus or derive from the intrinsic properties of the expressed TCR. A comparison of different TN mouse lines might therefore allow a detailed dissection of these properties without the confounding effects of transgenic artifacts.

The time-consuming generation of transgenic mouse models has led to the widespread use of a limited number of surrogate antigens, such as ovalbumin (recognized by the OT-I and OT-II transgenic mice) to study the immunobiology of infectious disease. Pathogens engineered to produce fragments of ovalbumin, and the immune reaction against it, are unlikely to capture all essential aspects of the physiological response. As an example, we show that T57 TN CD8$^+$ T cells proliferate upon infection with *T. gondii* and significantly reduce the parasite-burden but provide limited protection against an acute lethal challenge with *T. gondii*. Are responses against all epitopes equally protective? What is the best cell type to provide protection? Do responses against some epitopes protect from *Toxoplasma*-induced encephalitis? The answers to such questions require ready access to T cells that accurately reflect the natural response against the pathogen, and TN T cells arguably meet these requirements

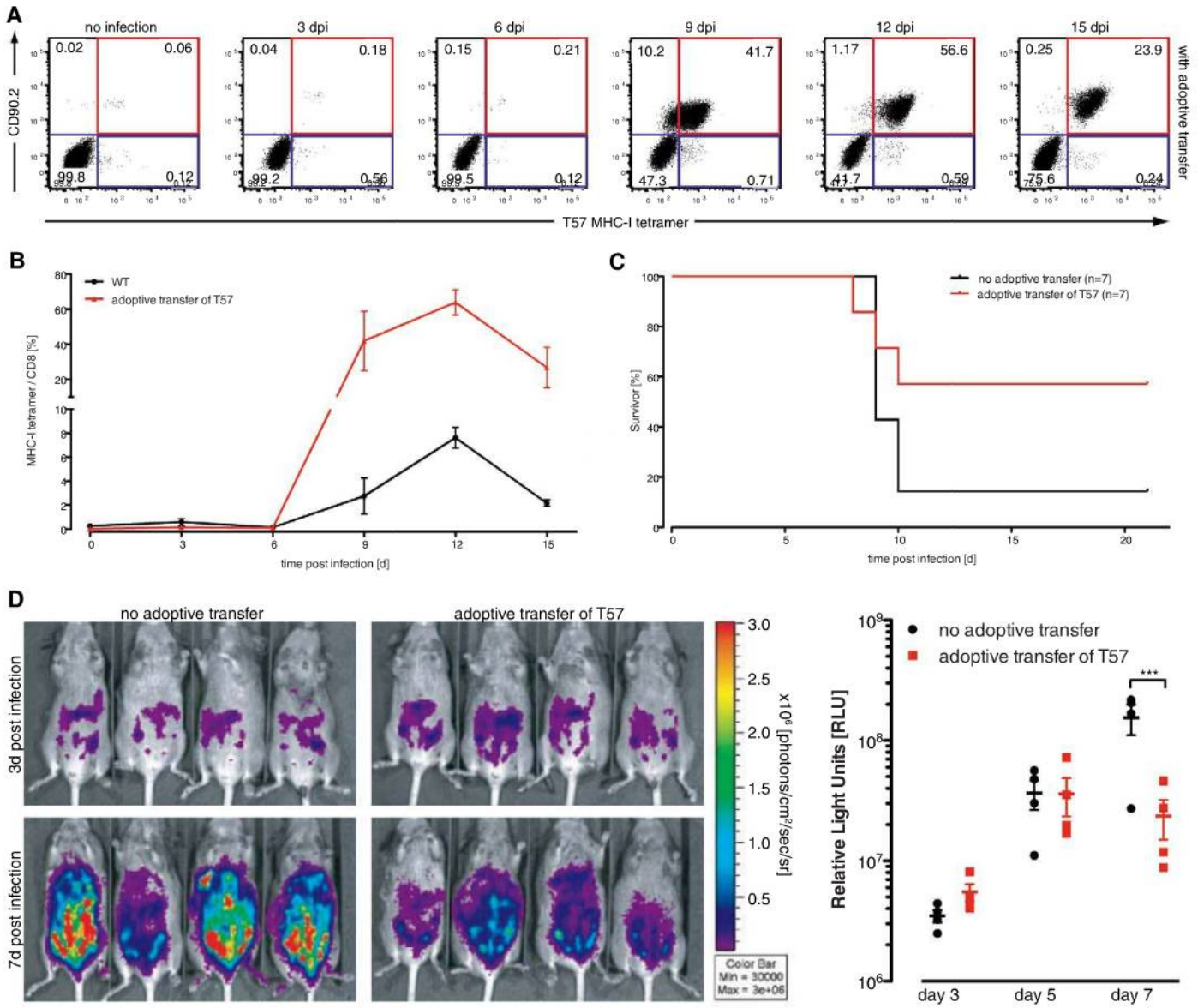

Fig. 4. TN T57 T-cell function in vivo. (**A**) In vivo response of wild-type BL/6 mice having received an adoptive transfer of TN T57 CD8$^+$ cells (three mice per time point per group). Representative flow cytometric analysis at different time points after infection, with the boxes showing the percentage of T57-specific cells among CD8$^+$ T cells, are shown. TN cells (red boxes) and endogenous cells (blue boxes) can be distinguished by use of CD90.2. (**B**) Graphical representation of the flow cytometric results showing the kinetics of wild-type (black curve) and TN (red curve) T57-specific CD8$^+$ T cells (analyzed by use of GraphPad Prism software). (**C**) Survival curve of wild-type B6CF1 mice infected with lethal dose of tachyzoites ($n = 7$ mice for each group). (**D**) Optical imaging of luciferase-expressing *T. gondii* during a lethal challenge (left) and quantification of signal (right) ($n = 4$ mice per group). Data plotted are mean ± SEM. Triple asterisk indicates significant difference (two-way analysis of variance, $P < 0.001$).

best. Taken together, TN mice obtained by means of SCNT can be generated rapidly from freshly isolated specific $CD8^+$ T cells. As long as methods for identification of antigen-specific lymphocytes can be applied, this strategy should also be applicable for $CD4^+$ T cells and B cells. TN mice resemble a new type of mouse model that express their TCR α- and β-chains from their endogenous loci under the control of their endogenous promoters without further genetic modification, thus avoiding genetic footprints at the site of integration, which is an unavoidable hallmark of transgenics.

References and Notes

1. P. Wong, E. G. Pamer, *Annu. Rev. Immunol.* **21**, 29 (2003).
2. I. J. Amanna, M. K. Slifka, S. Crotty, *Immunol. Rev.* **211**, 320 (2006).
3. L. E. Harrington, R. van der Most, J. L. Whitton, R. Ahmed, *J. Virol.* **76**, 3329 (2002).
4. S. Gredmark-Russ, E. J. Cheung, M. K. Isaacson, H. L. Ploegh, G. M. Grotenbreg, *J. Virol.* **81**, 10300 (2008).
5. M. Moutaftsi *et al.*, *Nat. Biotechnol.* **24**, 817 (2006).
6. T. Wakayama, R. Yanagimachi, *Mol. Reprod. Dev.* **58**, 376 (2001).
7. S. Kishigami *et al.*, *Biochem. Biophys. Res. Commun.* **340**, 183 (2006).
8. K. Eggan *et al.*, *Proc. Natl. Acad. Sci. U.S.A.* **98**, 6209 (2001).
9. K. Inoue *et al.*, *Curr. Biol.* **15**, 1114 (2005).
10. K. Hochedlinger, R. Jaenisch, *Nature* **415**, 1035 (2002).
11. T. Serwold, K. Hochedlinger, M. A. Inlay, R. Jaenisch, I. L. Weissman, *J. Immunol.* **179**, 928 (2007).
12. S. B. Koralov, T. I. Novobrantseva, K. Hochedlinger, R. Jaenisch, K. Rajewsky, *J. Exp. Med.* **201**, 341 (2005).
13. Materials and methods are available as supporting material on *Science* Online.
14. Y. Suzuki, J. S. Remington, *J. Immunol.* **144**, 1954 (1990).
15. F. S. Dzierszinski, C. A. Hunter, *Parasite Immunol.* **30**, 235 (2008).
16. E. M. Frickel *et al.*, *J. Infect. Dis.* **198**, 1625 (2008).
17. D. C. Wilson *et al.*, *PLOS Pathogen* **6**, e1000815 (2010).
18. N. Blanchard *et al.*, *Nat. Immunol.* **9**, 937 (2008).
19. S. Kishigami *et al.*, *J. Reprod. Dev.* **53**, 165 (2007).
20. K. A. Hogquist *et al.*, *Cell* **76**, 17 (1994).
21. D. M. Kranz, D. H. Sherman, M. V. Sitkovsky, M. S. Pasternack, H. N. Eisen, *Proc. Natl. Acad. Sci. U.S.A.* **81**, 573 (1984).
22. W. C. Sha *et al.*, *Nature* **336**, 73 (1988).
23. J. Chen, H. N. Eisen, D. M. Kranz, *Microbes Infect.* **5**, 233 (2003).
24. X. L. Wang, J. D. Altman, *J. Immunol. Methods* **280**, 25 (2003).
25. V. Kouskoff, K. Signorelli, C. Benoist, D. Mathis, *J. Immunol. Methods* **180**, 273 (1995).
26. H. Pircher, K. Bürki, R. Lang, H. Hengartner, R. M. Zinkernagel, *Nature* **342**, 559 (1989).
27. C. Mamalaki *et al.*, *Dev. Immunol.* **3**, 159 (1993).
28. M. J. Barnden, J. Allison, W. R. Heath, F. R. Carbone, *Immunol. Cell Biol.* **76**, 34 (1998).

29. The authors are thankful to H. Eisen, M. J. Gubbels, K. van Grinsven, E. Guillen, A. Drake, V. Mahajan, Q. Gao, and G. Yap for fruitful discussions and reagents; J. Dausman, R. Flannery, and J. Jackson for assistance with the management of the mouse colony; P. Wisniewski for FACSorting; and J. Saeij and K. Jensen for the Pru PA7 and assistance with the in vivo imaging. E.M.F. was supported by the Human Frontiers Science Program. R.J. was supported by NIH grants RO1-HD045022 and R37-CA084198. H.L.P. was supported by grants from NIH. We thank L. Clay for financial support. The Whitehead Institute has filed a patent related to the generation of mice with defined antigen receptor specificity using epigenetic reprogramming (international patent application PCT/US2009/049596). The sequences have been submitted to the European Molecular Biology Laboratory Nucleotide Sequence Database, accession number FN601337-FN601346.

Supporting Online Material

www.sciencemag.org/cgi/content/full/328/5975/243/DC1
Materials and Methods
Figs. S1 to S6
References

2 July 2009; accepted 9 February 2010
10.1126/science.1178590

EXOME SEQUENCING:
A FLASH IN THE PAN?

It's an interesting time for genome scientists. With next generation technologies outpacing Moore's Law and prices plummeting, human genomes—once multimillion-dollar propositions—today cost tens of thousands of dollars, about the same as a car. Yet multiply those prices by the sample numbers required to triangulate disease genes—not to mention the burden of collecting, storing, and analyzing the resulting data—and expect genomic sticker shock. There is an alternative. Supported by some $76.5 million in federal spending since 2008, plus a clutch of commercial products, exome sequencing proved its mettle in 2009 with a trio of papers highlighting its clinical possibilities. No wonder *Science* named exome studies one of five "areas to watch" in its December "Breakthrough of the Year" issue. **By Jeffrey M. Perkel**

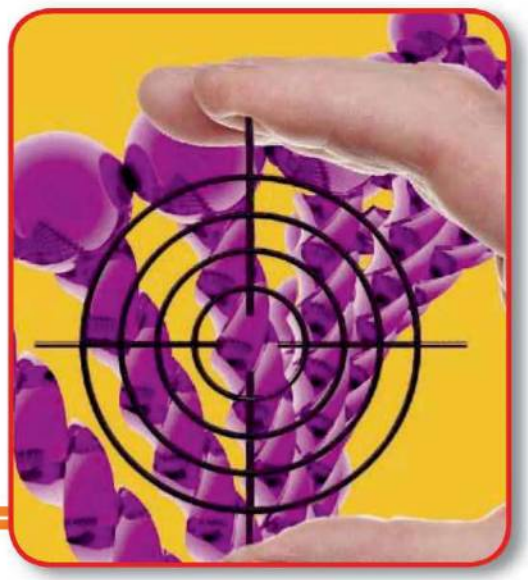

CREDIT: (PHOTO ILLUSTRATION) SCIENCE; ISTOCKPHOTO.COM\SIRER; ISTOCKPHOTO.COM\OSULEO

The human genome weighs in at some 3 billion base pairs. The human "exome," or total exon complement, is just 1 percent as large, its 180,000 exons comprising a mere 30 Megabases (Mb) of DNA.

The rationale for sequencing that 1 percent is a mixture of science, economics, and pragmatism.

The vast majority of diseases map to protein-coding genes or their regulatory elements. Since researchers don't know what to make of most noncoding variants anyway, it makes sense to focus on the interpretable regions, especially given limited resources.

And resources are limited. At the **Baylor College of Medicine** Human Genome Sequencing Center in Houston, 20 **ABI** SOLiDs, each producing about 30 gigabases (Gb) per run, crank out some 2 terabases of sequence per month, says Donna Muzny, director of operations—about 666 human genomes' worth. One complete human genome at 30x coverage requires 90 Gb, and typically consumes three machines for one 10-day run, Muzny says; a 30 Mb exome ideally requires just 900 Mb to achieve comparable coverage, though in practice about 5-6 Gb are collected. Still, that means one machine can collect five to six complete datasets, a significant savings in both time and money, especially for studies requiring several hundred samples, such as the facility's ongoing cancer and autism work.

"If you want to get and sequence whole genomes for these studies," Muzny says, "that's still a lot more sequence to generate than capacity and cost will allow right now."

Those bases cost money on the back end, too. "The cost of sequencing is dropping significantly faster than the cost of data storage," says **Yale University** geneticist Richard Lifton. Yale's genome center has 1 petabyte of storage and 768 processors dedicated to processing and storing the data pouring out of its 12 **Illumina** sequencers. Yet at 500 gigabytes of storage and 3,000 processor-hours of CPU time per genome, compared to 10 gigabytes and 60 processor-hours per exome, those resources can fill fairly quickly.

Recognizing the need to balance these issues against the profound clinical potential of genome sequencing, the **US National Heart, Lung, and Blood Institute (NHLBI)** in 2008 awarded $12 million for exome sequencing technology development (the "Exome Project") to the **Broad Institute of MIT and Harvard, Harvard Medical School,** and the **University of Washington** (UW). This past October, NHLBI pushed the project into "production mode" with another $64.5 million—$25 million each to UW and the Broad Institute for sequencing, and the balance for data and sample management.

"The cost of sequencing is dropping significantly faster than the cost of data storage."

Today, thanks partly to that funding, as well as the independent efforts of other researchers and tool developers, genome scientists' toolboxes are stocked with targeted sequencing options. Short term, these approaches balance the benefits of whole-genome approaches against their practical and financial shortcomings. Longer term, given the steep decline in sequencing costs to date, that balance could shift.

In the opinion of Exome Project awardee and Harvard geneticist George Church, "From a data collection standpoint, exomics is going to be a flash in the pan."

EXOME SEQUENCING IN THE CLINIC

Credit two research teams—one led by Lifton, the other by Deborah Nickerson, Jay Shendure, and Michael Bamshad at continued »

UPCOMING FEATURES

Flourescent Labels—April 16

Proteomics 1: Mass Spectrometry—May 14

Breakthroughs in Imaging—June 18

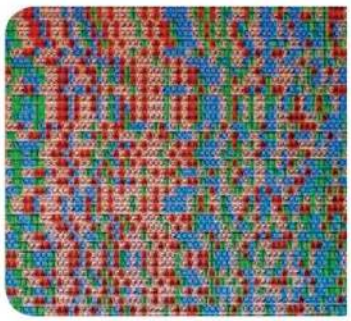

"We already had two examples of [correcting a misdiagnosis] in the first three exome papers."

UW—with showcasing the clinical potential of exome sequencing in 2009.

The Exome Project–funded UW team got the ball rolling in August. The team published 12 human exomes—eight normal HapMap samples and four individuals with Freeman-Sheldon syndrome (FSS), an autosomal dominant disease. Though FSS had previously been mapped to *MYH3,* the authors used their data—and some clever filtering algorithms—to demonstrate that exome sequencing could pinpoint disease-causing mutations.

The team then applied that approach to Miller's syndrome, a rare autosomal recessive disorder whose cause was unknown. Sequencing four individuals from three families, the team mapped the mutation to the gene *DHODH,* which is involved in pyrimidine biosynthesis. They published their findings in November.

Meanwhile Lifton, working with researchers in Lebanon and Turkey, used exome sequencing to diagnose a five-month-old Turkish boy suffering from dehydration and chronic diarrhea. The child's doctors suspected a renal disorder such as Bartter syndrome, but could not identify the cause.

Instead, exome analysis indicated the child harbored a mutation in *SLC26A3* (encoding a chloride/bicarbonate exchange transporter) and a diagnosis of congenital chloride diarrhea—a finding the Yale team subsequently confirmed in five additional patients also thought to have Bartter's; they published their findings in October.

"We already had two examples of [correcting a misdiagnosis] in the first three exome papers," marvels Shendure (the second being two subjects in the Miller's study who were thought to also have cystic fibrosis, but who instead had primary ciliary dyskinesia). "That blows me away a little bit—we are just getting into this, and we're starting to see this. It just makes you wonder how much else is out there."

HYBRIDIZATION STRATEGIES

All three studies used the same capture strategy, array hybridization. The UW team enriched its genomic DNA on custom, 244,000-probe **Agilent** DNA microarrays representing 26.6 Mb from the NCBI (US National Center for Biotechnology Information) Consensus Coding Sequence database, collecting 6.4 Gb per exome (51x coverage) for the FSS analysis and 5.1 Gb per exome (40x coverage) for Miller's syndrome. Lifton's team captured its DNA on 2.1-million-oligo **Roche NimbleGen** arrays (after first optimizing them for use with Illumina sequencing chemistry), sequencing 34 Mb representing 18,673 genes to about 40x coverage.

Despite these successes, the technique has a critical weakness: Microarray processing isn't easily scaled.

"It's a difficult process to perform. You've got to be dexterous to set the array hybridizations up, and there's a limit to the number a single person can do," says Daniel Turner, head of sequencing technology development at the **Wellcome Trust Sanger Institute** near Cambridge, UK.

That isn't true of solution-based hybridization, however, and at the Sanger, where 35 Illumina Genome Analyzer IIs (GAIIs) push out some 700 Gb of purity-filtered sequence per week, such approaches are gaining traction. "When you do this in solution," Turner explains, "your throughput can increase dramatically. It's just manipulating liquids and using a magnet. You don't need anything more specialist than that."

The approach is also making inroads at Baylor. "We can better process-manage the solution-based strategy [than the array-based one]," Muzny explains. "You don't need a hybridization station; it's done in a thermocycler. So you can automate and get higher throughput."

Agilent and Roche NimbleGen both offer solution-based hybridization systems in custom and off-the-shelf designs. Agilent's SureSelect Human All Exon Kit, based on work by Andreas Gnirke and colleagues at the Broad Institute, hybridizes fragmented genomic DNA to some 330,000 biotinylated 120-mer RNAs in solution—long enough to efficiently catch SNPs and short in-dels, says Fred Ernani, marketing manager at Agilent Technologies. NimbleGen's SeqCap EZ Exome captures essentially the same targets on 2.1 million biotinylated DNA oligos—roughly 10 available per exon, or enough to adjust oligo design for maximal capture uniformity, says Xinmin Zhang, senior product manager. In both cases, the resulting hybrids are harvested using strepavidin beads, enabling unbound material to be washed away.

AVOIDING FUZZY EDGES

At Harvard, Church takes a completely different approach to exome capture: molecular-inversion probes (MIPs, also called "padlock" probes).

MIPS are 70-mer oligonucleotides consisting of a 30-base central common segment flanked by target-specific 20-mers. These probes effectively "hug" specific genomic segments using their targeting arms, forming a semicircular structure whose gap flanks the targeted sequence. This gap is then sealed with DNA polymerase and ligase, after which the closed circles are amplified to produce a sequencing library.

Hybridization approaches, Church explains, tend to capture more sequence than researchers want. "Something that pulls out the general area [such as hybridization] is going to have 'fuzzy edges'," he says. "As you get to the fuzzy edges, you get low enough coverage to not be useful, but high enough coverage to be wasteful." MIPS, in contrast, yield "sharp edges—99 percent is what you want."

Highly flexible in theory, the approach initially fared poorly in practice. In a preliminary 2007 study Church, with his then–graduate student Shendure, created 55,000 MIPs covering 6.7 Mb, of which just 18 percent (10,000 exons) was recovered. In 2009 Shendure and Nickerson optimized the method, using the same 55,000 MIPs to successfully target 50,000 exons (91 percent). continued »

Researchers can also obtain sharp edges using PCR. In 2006 **Johns Hopkins University** researchers Bert Vogelstein, Kenneth Kinzler, and Victor Velculescu took on the Herculean task of PCR amplifying some 135,000 fragments representing 13,023 genes from 11 breast and 11 colorectal cancer cell lines, as well as two normal controls. Some 3.4 million independent PCR and Sanger sequencing reactions later, the team identified 1,149 mutated genes.

Today, researchers have an easier option. **RainDance Technologies'** RDT 1000 system combines the benefits of PCR with the company's RainStorm microdroplet technology, allowing millions of single-plex picoliter-scale PCR reaction vessels to be assembled in a single 200-μL tube. Each droplet contains template, buffer, and one of 20,000 PCR primer pairs, allowing scientists to enrich up to 10 Mb of sequence.

According to Scott Kennedy, chief scientific officer at RainDance, the company's solution is more about "targeted sequence enrichment" than "sequence capture." Exome targeted strategies, he says, are essentially "discovery-based." RainDance, on the other hand, enables customers to target specific regions of interest, where they have already formulated a hypothesis. "Most customers want to focus in on genomic regions that are relevant to their area of biology or translational research," Kennedy explains.

PROBLEMS WITH GENOME CAPTURE

For all their convenience, exome sequencing strategies aren't perfect. For one thing, the strategies don't capture only the desired targets. In Lifton's case, just 38 percent of sequenced bases mapped to the targeted DNA. Though far better than the specificity the team would have seen with whole-genome sequencing, this still represents a considerable waste of sequence. Also, some targeted bases are never read adequately—10 percent worth in Vogelstein's study, for instance.

Targeted capture methods may also alter the composition of the resulting libraries if, say, different alleles are captured at different rates. Imagine, Ernani says, that at a particular chromosomal location, one chromosome may contain either a T or a G. If the alleles are captured equally, at 20x coverage you should see either 10 Ts and 10 Gs or, say, 20 Ts and 0 Gs. "But what about 19-to-1 or 18-to-2?" asks Ernani. Are those few Gs sequencing errors, or a poorly captured allele? "You need to have about the same number of reads to say it is a heterozygous SNP."

Similarly, researchers may report an exome was read to 40x depth "on average," but that doesn't mean each base was actually read 40 times; some are read only occasionally, others are heavily oversampled—a problem of "uniformity."

"Uniformity is the killer," says Turner. Given 80 percent specificity, for instance, you should only need, say, one extra GAII lane to collect the missing sequence, he says. "But if the uniformity is variable—if some regions are covered at 100x and others at 5x for a given amount of sequencing—you need to do much more sequencing to bring the underrepresented sequences up."

Sanger researchers tend to run two to three lanes per exome, or 5–7.5 Gb worth of 54-base paired–end reads, Turner says. "So we are doubling or trebling the amount of sequencing we have to do compared to the ideal situation just because of uniformity and specificity," he says.

FEATURED PARTICIPANTS

Agilent Technologies
www.agilent.com

Applied Biosystems
(now part of Life Technologies)
www.appliedbiosystems.com

Baylor College of Medicine
www.bcm.edu

Broad Institute
www.broadinstitute.org

Harvard Medical School
www.hms.harvard.edu

Illumina
www.illumina.com

Johns Hopkins University
www.jhu.edu

RainDance Technolgies
www.raindancetechnologies.com

University of Washington
www.washington.edu

US National Heart, Lung, and Blood Institute
www.nhlbi.nih.gov

US National Human Genome Research Institute
www.genome.gov

Wellcome Trust Institute
www.sanger.ac.uk

Yale University
www.yale.edu

THE BOTTOM LINE

Researchers and companies continue to address these problems. Yet no amount of tweaking can overcome two fundamental shortcomings, the first being coverage: Exome sequencing ignores both noncoding sequence variations and genomic rearrangements. It also is relatively expensive: that 1 percent costs more than 1 percent of a whole genome to obtain. At February's Advances in Genome Biology and Technology (AGBT) meeting, the Broad Institute's Stacey Gabriel was quoted as saying her team was sequencing exomes at 1/15th the cost of whole genomes. Lifton's study cost about $2,500, $1,500 for one lane of a GAII run, and $1,000 for targeting. By comparison, in its 2009 publication of three complete human genomes, **Complete Genomics** estimated consumables for 40x coverage cost just $1,500.

Nevertheless, efforts are under way to migrate the technology from rare, monogenic diseases like Miller's, to more common, complex conditions like cancer and Alzheimer's. "The studies we did provide a framework both technically and analytically for how to think about these things moving forward, at least a starting point," says Shendure, who has funding from both NHGRI and NHLBI to address that problem. "But I think it's certainly going to be challenging as we try to move from things that are really monogenic and simple and Mendelian to things that are more complicated."

Challenges notwithstanding, *Science* magazine's 2010 prediction seems off to a good start, with sequencing centers queuing up thousands of exomes. At AGBT, Gabriel said the Broad would sequence some 5,000 this year; Nickerson said UW would produce about the same number within two years. "We're likely to see at least 10,000 exomes by 2011," Nickerson predicts.

Jeffrey M. Perkel is a freelance science writer based in Pocatello, Idaho.

DOI: 10.1126/science.opms.p1000042

NEW PRODUCTS: GENOMICS

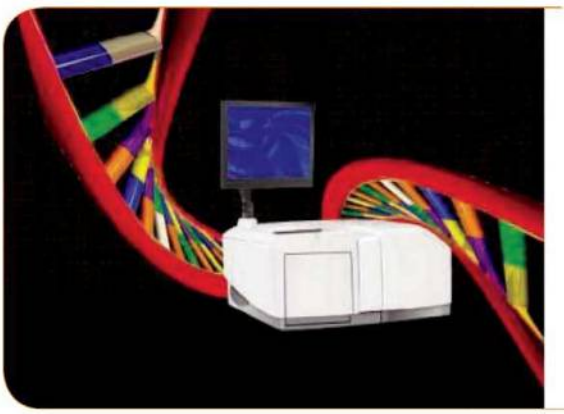

NEXT GENERATION SEQUENCING

The Access Array integrated fluidic circuit (IFC) eases the burden of library preparation for resequencing or long-range polymerase chain reaction (PCR) because it facilitates the amplification and barcoding of 48 samples in parallel, with minimal time and labor, and in as few as three hours with yields that are equimolar and routinely at 100,000,000 or 1,000,000,000 amplicons. Because every sample can be identified by its barcode, all 48 samples can be multiplexed at the sequencing step. This capability dramatically reduces the time and money required for large-scale projects. Scientists interested in large cohort studies can relatively easily sequence specific genes of interest from hundreds of individuals in a matter of weeks.

Fluidigm Europe

For info: +33-44-259-386 | www.fluidigm.com

WHOLE REFERENCE GENOMES

Whole reference genomes are available for NextGENe second-generation sequence analysis software. Human, mouse, and rat genomes are currently available in formats for use with data from the Illumina GA systems, Roche Genome Sequencer FLX systems, and AB SOLiD Systems. Maize and bovine genomes are in development. The current version of NextGENe software includes a whole-genome builder, which allows users to construct a completely annotated reference of any species. Reference genome annotation includes gene name, chromosome position, reference nucleotide, reported variants, amino acid sequence, and dbSNP identification, as well as a direct link to the dbSNP database.

SoftGenetics

For info: 814-237-9340 | www.softgenetics.com

INSERTION SEQUENCE DETECTION KIT

The White Glove IS Detection Kit tests for the presence of transposable insertion sequence (IS) elements in the genomes of commonly used *E. coli* strains. The kit can also be used to determine which elements have transposed from these genomes into a plasmid of interest propagated in these strains. Scarab Genomics also offers Clean Genome strains of *E. coli,* which do not contain the IS elements naturally present in the genomes of *E. coli* strains commonly used for protein and plasmid production. IS element transposition is known to be stimulated by the cell stress response and can lead to the "hopping" of IS elements into plasmid DNA or into other regions of the bacterial chromosome. The transposition of IS elements into an expression vector can interfere with the expression of a foreign protein in *E. coli.*

Scarab Genomics

For info: 888-513-7075 | www.ScarabGenomics.com

AUTOMATED SAMPLE PREPARATION FOR SEQUENCING

A new automated bead-washing system based on the Freedom EVO 75 workstation has been developed to reduce the manual sample preparation needed for next generation sequencing. In the new system, the Freedom EVO 75 bead-washing station is equipped with a two-channel LiHa arm, a Te-MagS magnetic separation module, and all the racks and carriers required for parallel preparation of 24 templated bead samples. The system's software features washing protocols developed by Life Technologies for optimal sequencing performance of the SOLiD System.

Tecan Group

For info: +41-44-922-81-11 | www.tecan.com

AUTOMATED MICROFLUIDICS

The LabChip XT is an automated nucleic acid fractionation instrument designed to remove a key bottleneck in the workflow of next generation sequencing by replacing the tedious gel isolation and purification steps used for size selection of sheared genomic DNA. The LabChip XT and its software make use of a multichannel microfluidic chip to quickly process samples independently and without the potential for cross-contamination.

Caliper Life Sciences

For info: 781-684-6548 | www.caliperLS.com

MICROARRAYS

Three new CytoSure ISCA aCGH arrays were designed in collaboration with the International Standard Cytogenomic Array (ISCA) Consortium to meet all resolution, multiplexing, and budget requirements. The 8 by 60k, 4 by 180k, and 4 by 44k CytoSure ISCA formats provide powerful arrays focusing on genome regions associated with diseases and syndromes in addition to offering whole genome coverage. Through a proprietary 60-mer probe design and multiple rounds of optimization, the CytoSure ISCA arrays can ensure reliability and confident detection of genetic aberrations with high signal-to-noise ratios. Each array is supplied with CytoSure Interpret analysis software for effortless translation of data into meaningful results.

Oxford Gene Technology

For info: +44-(0)-1865-856828 | www.ogt.co.uk

Electronically submit your new product description or product literature information! Go to **www.sciencemag.org/products/newproducts.dtl** for more information.

Newly offered instrumentation, apparatus, and laboratory materials of interest to researchers in all disciplines in academic, industrial, and governmental organizations are featured in this space. Emphasis is given to purpose, chief characteristics, and availabilty of products and materials. Endorsement by *Science* or AAAS of any products or materials mentioned is not implied. Additional information may be obtained from the manufacturer or supplier.

Faculty Position in Computational Genomics

Group Leader – Computational Genomics (Ref: 80616)

The Wellcome Trust Sanger Institute invites applications from outstanding individuals to join our Faculty and lead key project work in computational genomics. A possible primary research interest is in computational integrated genomics: with the large scale data collection projects at the Institute, such as 1000 Genomes, WTCCC, targeted mutagenesis in mouse and zebrafish and transcriptomics, the challenge is to connect genotype, transcription and function. The successful candidate will benefit from the Sanger's very substantial informatics resources and the strong interactions with the European Bioinformatics Institute, computational research groups at the University of Cambridge and the Cambridge Microsoft Research Institute.

As a member of our Faculty the successful candidate will enjoy access to unparalleled facilities to support the delivery of projects and the generation of data and biological resources on a large scale. Our core technologies include high throughput sequencing, genotyping and core IT support which underpin our global position in these areas. During the coming years we aim to make a major contribution to the understanding of gene function, similar in impact to our role in genome sequencing.

We are seeking to appoint a Group Leader at Career Development Fellow level, for a 6 year fixed term. Further details of our Faculty model can be found at **http://www.sanger.ac.uk**. The expectation is that at this level Group Leaders will have the opportunity to develop the intellectual basis, biological resources and data to sustain a scientific programme in the long term and will pursue their career elsewhere at the end of the term.

Applicants for this role will have a strong computational biology background, having excelled as postdoctoral scientists and will be able to demonstrate that they have the capability and personal qualities to lead a research team and direct independent work, possibly for the first time. Applications from women are particularly encouraged, although we welcome approaches from any scientists with relevant research interests. Salary range from £36,772 dependent on experience.

Contact for informal enquiries: Tim Hubbard **th@sanger.ac.uk**

Closing date for applications is 28th May 2010.

Postdoctoral Fellow - Computational Genomics (Ref: 80615)

A comprehensive description of regulatory regions is a major missing component of the annotation of genome sequences. With the availability of sensitive computational algorithms (e.g.NestedMICA, capable of large scale ab initio motif discovery) and large scale experimental datasets of regulatory elements from projects such as the ENCODE project, there is great potential to generate improved regulatory annotation for large vertebrate genomes at the motif level.

This post is within Tim Hubbard's research group **http://www.sanger.ac.uk/research/faculty/thubbard/research.html** to develop and apply machine learning algorithms such as NestedMICA to build comprehensive motif libraries and annotate large genomes. The post would suit individuals with a strong mathematical background and experience of algorithm development. Tim's research group works closely with the major vertebrate genome annotation projects of Ensembl, Havana and GENCODE (ENCODE) of which he is PI. The Sanger Institute has extensive computational resources suitable for large scale calculations envisaged for this research.

Applicants must have a PhD in a relevant subject area (e.g. Computational / Statistical Genomics, Physics, Bioinformatics, Biophysics, Engineering, Computer Science) and have a genuine interest in biological regulation with strong programming skills (e.g. C++, Perl) in UNIX environments.

The Salary range is £28,000 to £34,433 dependent on experience. This position is for a fixed term of 3 years. Successful applicant(s) who have submitted their PhD thesis and are awaiting their PhD award to be confirmed will be placed on a transitional pay point, currently £25,845. On confirmation of award applicants will be moved on to the pay scale above.

Closing date for applications is 30th April 2010.

For further information and details on how to apply, go to: http://www.sanger.ac.uk

General queries can be directed to: hrservices@sanger.ac.uk

Registered Charity No: 1021457

wellcome trust sanger institute

SYSTEMS BIOLOGY AND BIOINFORMATICS:

SOMETHING FOR EVERYONE

Systems biology and bioinformatics want you. These highly collaborative fields are looking for biologists, engineers, chemists, mathematicians, and computer programmers. If you can work in a diverse team, says Bernhard Palsson of the University of California, San Diego, "It's an era of unprecedented opportunity." **By Chris Tachibana**

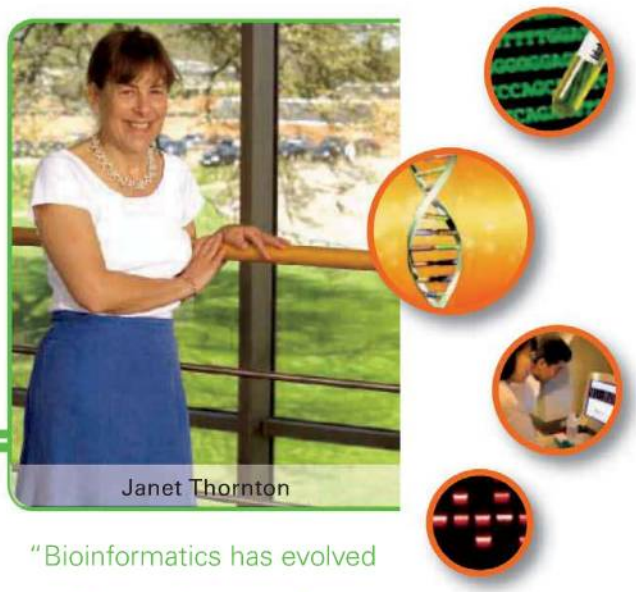

Janet Thornton

"Bioinformatics has evolved rapidly over the past 15 years and is now quite ubiquitous."

Lynn Hlatky, director of the center of cancer systems biology at St. Elizabeth's Medical Center, Tufts University, agrees, saying, "For people who are changing careers, and for new investigators, there is funding, and new systems biology centers are being established worldwide."

The job opportunities aren't necessarily tied to a specific geographic location, either. Collaborators can work remotely on a common project. Wet-lab data generated at one site might be analyzed by group members cyber-networking from a distance. "It's more about getting the right people together to address the problem, no matter where they are," says Hlatky. Systems biologists just need "the ability to see the big picture and to have an open mind. Anyone can get into this game."

Actually, all researchers need to get into the game, according to **Jens Nielsen,** professor of systems biology at Chalmers University of Technology, Göteborg, Sweden. "The tools, techniques, and approaches of systems biology are becoming standard in research and industry," he says. "To get a life science job in 10 or 20 years, you will simply be expected to have competency in these areas."

Combining High Tech with Old School

The list of specific areas within systems biology is almost comically long, and includes everything from cutting-edge computer science to traditional life sciences. Fortunately, in this field, collaboration is the name of the game. Galetti Professor of Bioengineering at the University of California, San Diego (UCSD) **Bernhard Palsson** says systems biology includes "an understanding of networks, biological systems and linear algebra, genomics and genetics, the biochemistry of gene products, and how everything fits into the three-dimensional architecture of the cell." Hlatky says that attacking the complex, nonlinear nature of biology requires "a team of individuals collectively versed in the traditional biological as well as the quantitative sciences, from cell and molecular biology to physics, chemistry, computer science, and mathematics."

Systems biology even needs expertise in fields that have fallen a bit out of fashion. Remember Linnaeus? "Taxonomy is a field of increasing importance, particularly combined with molecular techniques," says **Stephan Schuster** of the Center for Comparative Genomics and Bioinformatics at Penn State University and the Department of Biochemistry and Molecular Biology. Knowledge of physiology, "but now with quantitative and molecular tools," is valuable, says Hlatky. "We also need people who have training in population levels of thinking—developmental specialists, physicists, and ecologists."

The multidisciplinary systems biology group is like a multicellular organism, explains Hlatky, with robustness coming from specialization and a division of labor. This diversity allows the team to tackle dynamic problems with multiple variables. For example, she says, "In cancer biology, we used to think a number of oncogenes, tumor suppressors, and DNA repair genes drove the whole process, but now we are identifying thousands of genetic alterations in cancers. This means we're not going to figure it out by tracking a few or even dozens of genetic endpoints. We need computation and bioinformatics to address this part of the puzzle."

Like two organs in one body, systems analysis and bioinformatics are separate, but interdependent. "Bioinformatics extracts knowledge from the data that underlie systems biology, for creating hypotheses and models," says **Janet Thornton,** director of the European Molecular Biology Laboratory, European Bioinformatics Institute (EMBL-EBI). Bioinformatics is a growth area, says Thornton, because "almost every experiment now involves multiple sources of data, requiring the ability to handle those data and to draw out inferences and knowledge. Bioinformatics has evolved rapidly over the past 15 years and is now quite ubiquitous." continued »

UPCOMING FEATURES

Bio/Pharma: Mythbusting about Industry—April 23
Careers in Water Science (Online Only)—May 14
Focus on Spain—June 11

CAREERS IN BIOINFORMATICS/SYSTEMS BIOLOGY

"Together with genomics, the most important research will be in bioinformatics, where you can correlate temporal or genomic profiles with chemical, mass spectrometry, and genetic data."
—Stephan Schuster

Bioinformatics Opportunities in Service and Discovery

Careers in bioinformatics can be in the applied or services field, or in basic research. These two areas are very different in philosophy and practice, offer diverse opportunities, and attract different personality types. Structured, long-term, large-scale thinkers excel in the services field. "These people deliver a professional service, so they have to have robust software, and a very clear development process," explains Thornton. "They serve a large community of users, so they can't just change things overnight. Changes are planned months in advance, and occur while running 24 hours a day, and accepting data from all over the world." This area especially needs developers and testers. "They say it takes one month to write a program, but 10 to make it robust," says Thornton. Bioinformatics service also involves curation, or annotation of genes, proteins, metabolites, and other elements. Here again, says Thornton, "the annotator has to follow clear processes, and do it the same way with every gene or protein. You can't suddenly decide to do it differently one day. The goals of service are reliability, robustness, utility, and ease of use."

Research opportunities in the bioinformatics service field usually focus on making databases faster and more efficient. But the bottom line for the service side is scheduling new releases and data exchanges, and sticking to clearly defined criteria, protocols, and deadlines. Also, Thornton acknowledges, "Service bioinformaticians must make absolutely sure that no data are lost, which is something research scientists have been known to do."

Bioinformatics discovery is "for blue sky researchers" who can think of new ways to apply bioinformatics techniques or new directions to take the field, says Thornton. "Bioinformatics researchers need curiosity to answer biological questions. They need to write good software, but it doesn't have to be perfect, and this is not usually the primary goal. It's more important for researchers to ask the right questions. In my opinion, most good bioinformatics research is rooted in answering a specific biological question, but these can be rather grand questions, such as, How does the expression of all genes change as an organism ages?" And bioinformatics researchers can go where their imagination and interests lead them. "They have the freedom to explore multiple organisms, which is usually not the situation for an experimental biologist," says Thornton. "To a computational biologist, it doesn't matter if the data are protein interactions or metabolism, the methods are the same. An attraction of this field is that you aren't spending your life looking at a single organism or protein, but can be flexible and take a broader view."

The future career possibilities are encouraging. Penn State's Schuster says that "together with genomics, the most important research will be in bioinformatics, where you can correlate temporal or genomic profiles with chemical, mass spectrometry, and genetic data. This really opens up opportunities for people who are coming from many different directions." But right now, Thornton says, "Bioinformatics needs people driven by biology questions who want to take computational routes to answering those questions."

Opportunities for Bioengineers, Entrepreneurs, and Academics

Systems biology needs all-around researchers, according to Nielsen of Chalmers. He advises his students and postdocs to get experience in as many areas as possible, "from engineering to statistical analysis to molecular verification," and to do this as part of their project. Palsson of UCSD agrees, saying, "The best training might be classwork in the quantitative methods, while at the same time doing hands-on research in the lab in an environment that provides an in-depth understanding of what biology is all about."

For scientists with a broad range of skills, Nielsen says, "job prospects in industry are fairly good right now, considering that it's a tough time everywhere." Many of his students train for careers in industry with applied projects, addressing issues like improving fungal strains for commodity chemical production. Nielsen says that drug development firms, pharmaceutical companies, and commodity producers have been "investing in systems biology technology, so now they need people who can use it." The demand is particularly great for "people who can analyze data, who approach biology in a quantitative fashion and can integrate information from different areas."

Palsson has been involved in several startup companies and holds 28 US patents. He says the current demand for systems entrepreneurs is in "bioprocessing and metabolic engineering to make commodity and fine chemicals, and biopolymers." Both Palsson and Schuster see renewable energy and biofuels as a potential growth area with many challenges to meet. "We already see money being earned in sustainable energy fields, and they need information from broad systems studies in environmental areas and biodiversity," says Schuster. EMBL-EBI's Thornton also sees business opportunities for bioinformaticians. "Large pharmaceutical companies are moving away from in-house bioinformatics resources," she explains. "There's too much data, and they can't handle the storage, and don't have the personnel to keep things running. There may be opportunities for small and medium enterprises to develop software solutions for companies to handle their data effectively."

Academics and educators are not left behind as the demand for systems analyzers and bioinformaticians grows. "In 10 or 20 years, systems biology will just be part of an integrated biology education, so the need for faculty in this area will increase dramatically in the future," says Nielsen. Universities also need bioinformaticians, says Thornton. "Every biology research department will need computational experts." continued »

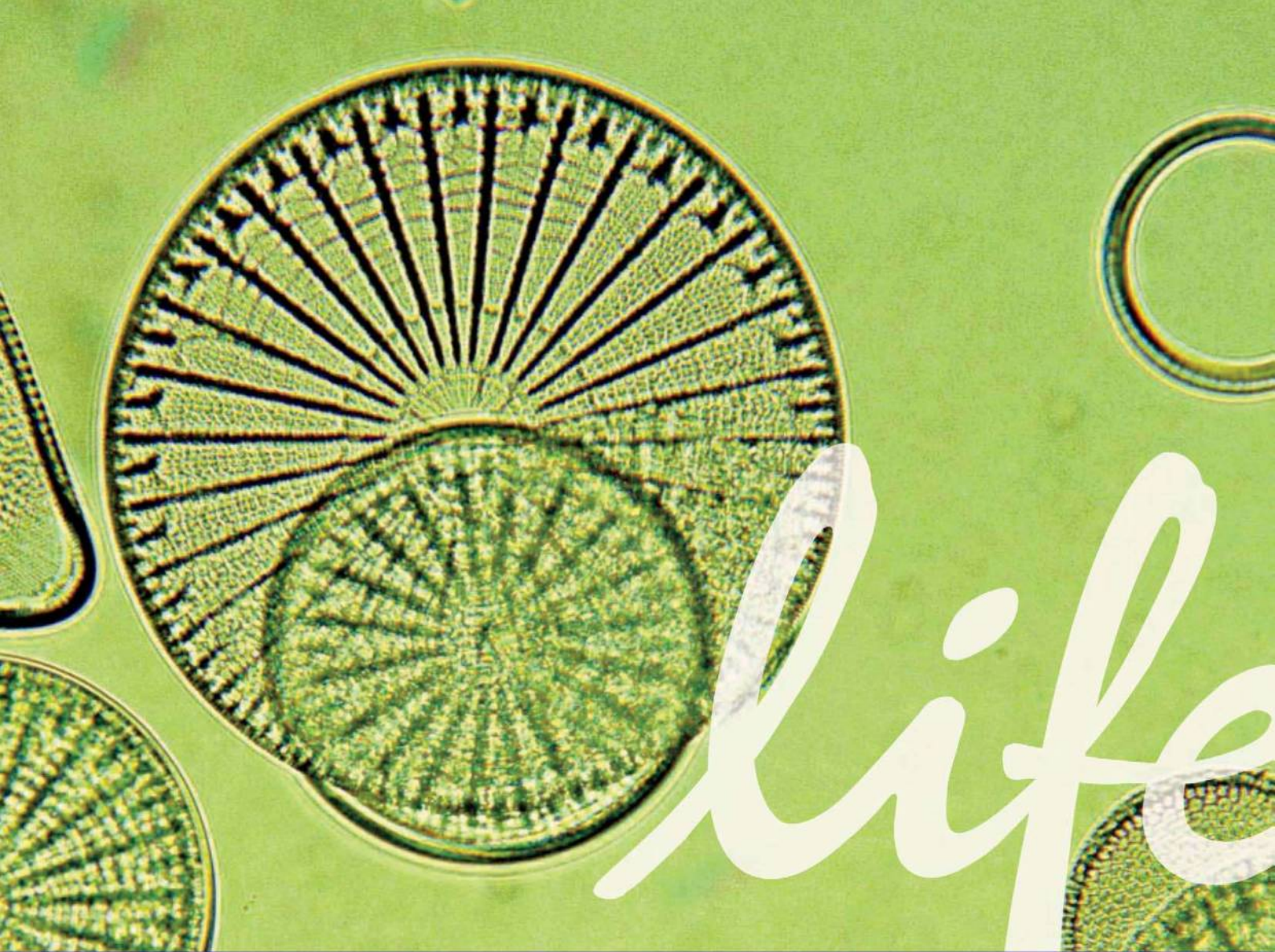

Life Even Better™

We believe in the power of science to transform life and the power of people to make it happen. Created through the combination of Invitrogen Corporation and Applied Biosystems, Life Technologies is a global biotechnology tools company dedicated to improving the human condition. We enable people to accelerate scientific exploration, driving to discoveries and developments that make life even better.

Join us in discovering the infinite surprises and solutions that science — and you — can reveal.

www.lifetechnologies.com/careers

EOE

life technologies™

applied biosystems | invitrogen

FEATURED PARTICIPANTS

Chalmers University of Technology
www.chalmers.se/en

European Molecular Biology Laboratory, European Bioinformatics Institute
www.ebi.ac.uk

Institute for Systems Biology
www.systemsbiology.org

Penn State University
www.psu.edu

Tufts University
www.tufts.edu

University of California
www.universityofcalifornia.edu

Medicine in the Era of Systems Biology and Bioinformatics

Another booming area is systems medicine. Clinical applications are limited today, but leaders in the field believe that radical changes are coming to health care and medical research. Hlatky of Tufts predicts that progress in analyzing physiological networks, integrating data from multiple levels, and monitoring biological changes over time will have a major impact. Future physicians, take note. "We'll pay more attention to all the parts, and recognize connections between different medical disciplines, like cancer and cardiology," she says. "Medicine will become more of what it is supposed to be, an integrated treatment of the individual." Hlatky says that stem cell biology is another area where a systems approach has strong potential, because of the complexity of the cells, and their impact on everything from neurological diseases, to chronic conditions, to regenerative medicine.

Systems medicine will also create job opportunities in bioinformatics. Thornton says, "In the future, we'll need people at the interface of databases and clinical trials, people who can handle all that computational work. Those data will be used in many different ways, to identify and measure interactions, and to determine concentrations. We need to develop computational tools for handling those data, including the variants."

At a more personalized level, **Lee Hood,** founder of the Institute for Systems Biology in Seattle, put forward his vision of the future of diagnosis in a recent talk. He described "an annual wellness assessment by blood prick that will analyze 2,500 protein biomarkers, for an organ-by-organ report on an individual's health status." Accumulation of individual data points over time will make every person a little longitudinal study, and "every patient will be his or her own control." To make this happen, scientists need to advance nanotechnology and imaging technology, and to create new computational tools. For those interested in business-oriented careers, Hood predicts "an explosion in health care companies, as emphasis shifts from disease to wellness."

Penn State's Schuster has a different angle on how systems biology researchers and bioinformaticians will contribute to human health and welfare. "Changes to the environment will affect flora, fauna, microenvironments, and may have geologic aspects. This will shift patterns of pathogens, and changes in pathogens will impact human populations and food supplies. This will carry over to human health and the stability of societies." Awareness of how environmental changes affect health and society is growing, providing research opportunities for systems biologists. "I believe funding cycles for environmental projects are on the upswing," he says.

Seeing the Big Picture

To find other areas of expansion in systems biology and bioinformatics, you don't have to look very far. Analysis of the interactome, or how cell components interact with their neighbors, is "big in the field now" says Nielsen of Chalmers. "This will be especially challenging, because it is not a static thing. Protein A may act with Protein B, but that interaction depends on how we set up the experiments."

Tufts' Hlatky adds, "We need to take the multiscale, dynamic interactions among molecules, cells, and tissues and knit them together in a quantitative construct." Thornton of the EMBL-EBI also sees integrating different levels of information as the next step, particularly in processing, storing, and interpreting imaging data. "We're developing advanced imaging tools from the cellular, to the organ, and up to the whole organism level." These methods have to be automated, and the data they generate need to be processed, integrated, and analyzed. Thorton says, "The opportunities are clearly in understanding biology at all different scales, bridging information from molecules to cells to organs to the whole organism, and being able to bring all those aspects together, basically to interpret the entire genome at all levels."

The field needs researchers who are comfortable working with data from all these levels, and grand thinkers who can come up with unifying theories. Hlatky says the next goal is to find the overarching biological principles in systems data, the models that allow researchers to "explain and predict." In any case, there's no escaping the power of systems biology and bioinformatics. Echoing Nielsen's remark that systems methods and bioinformatics will become standard practice, Hlatky says, "It's how we do biology now."

Chris Tachibana is a science writer based in Seattle, USA, and Copenhagen, Denmark.

DOI: 10.1126/science.opms.r1000087

CAREERS IN BIOINFORMATICS/SYSTEMS BIOLOGY

The Virginia Bioinformatics Institute at Virginia Tech

The Virginia Bioinformatics Institute (VBI) at Virginia Tech (www.vbi.vt.edu) is a premier bioinformatics, computational biology, systems biology, and health IT research facility that uses transdisciplinary approaches to science combining information technology, biology, and medicine. Research at the institute involves integration of diverse disciplines such as mathematics, computer science, general, synthetic, systems and micro-biology, medicine, plant, animal and human pathology, biochemistry, engineering, physics, statistics, economics, and other social sciences.

VBI wishes to build on its strengths as a world-class research institute by recruiting outstanding individuals for the following positions:

Assistant Professor or Associate Professor (two positions) Two faculty with demonstrated experience in the development of software tools for clinical and/or translational data are sought to interface between VBI and the recently created Virginia Tech Carilion Research Institute (www.vtc.vt.edu/research).

Postdoctoral positions (multiple) Outstanding candidates are sought for a wide range of postdoctoral positions including medical informatics, genomics/genetics, nutritional immunology, computational synthetic biology.

Director, Core Computational Facility & Research Computing Infrastructure (www.vbi.vt.edu/core_computational_facility) The candidate will oversee the maintenance, development, and expansion of VBI's high-performance computing infrastructure and a broad set of embedded, maintained, and ready-to-use national and international databases (-omic, text, image and other). The candidate should have demonstrated experience in the leadership and management of large-scale information technology projects in a customer service oriented, multidisciplinary, biomedical and/or life science research environment.

For a full description of each position please consult
https://www.vbi.vt.edu/careers or contact **hr@vbi.vt.edu**

To apply, please visit **www.jobs.vt.edu** and search by the department name "Virginia Bioinformatics Institute".

VBI Virginia Bioinformatics Institute — VirginiaTech

POSITIONS OPEN

vetmeduni vienna

At the
University of Veterinary Medicine, Vienna
there is a vacancy for a Professor of
Virology

The responsibilities involve research, teaching, further education and the provision of services related to the field. A research profile in the area of virology relevant to commercial application is desirable, with a specialization on viral diseases of domestic animals, preferentially of farm animals. This would facilitate integration in current research relating to infectious diseases and to clinical work, which forms the focal points of research in the Departments and Clinics, in particular in the Dept of Pathobiology and the Dept of Farm Animals and Public Health. Experience in clinical and diagnostic veterinary virology including the use of domestic animals and model systems for studies of infection are also desirable.

Further information may be found under:
www.vetmeduni.ac.at/professuren

Applications should be submitted by **June 11th, 2010** to:
The Office of the Senate
University of Veterinary Medicine, Vienna,
Veterinärplatz 1, 1210 Vienna, Austria.

ANNOUNCEMENTS

KATHOLIEKE UNIVERSITEIT
LEUVEN

The K.U.Leuven, founded in 1425, is Belgium's largest university. As a leading European research institution, it offers a wide variety of academic programmes in Dutch and English, nurtured by internationally acclaimed, high quality interdisciplinary research, both in the university and in its associated hospitals. More than 6,000 researchers from over 120 countries participate in investigatory and strategic frontier research, as well as targeted and demand-driven research. The university's interaction with its external partners is very intense. As a comprehensive university, K.U.Leuven offers 3-year Bachelor's and 1-or 2-year Master's programmes in almost all disciplines. The Leuven doctoral schools organise the international PhD tracks of close to 4,000 doctoral candidates.
Leuven is a safe, agreeable and multicultural town, with a vibrant student community, only a short train ride away from Brussels, Paris and London.

The **Science, Engineering and Technology** Group at K.U.Leuven invites applications for vacant academic positions in:

- Telecommunication
- Nano-electronics and Nanotechnology
- Algorithms and Software for Computational Science
- Heat and Mass Transport in Building Materials and Building Components
- Structural Design in Architecture
- Differential Geometry
- Theoretical High-energy Physics
- Biomolecular Network Dynamics
- Teacher Training in Geography / Environmental Sciences
- Smart Grids

Detailed descriptions of these profiles and information on how to apply can be found at **www.set.kuleuven.be/vacancies.**

The K.U.Leuven pursues a policy of equal opportunity and diversity.

TULANE UNIVERSITY SCHOOL OF MEDICINE

Department of Pathology and Laboratory Medicine

Cancer Research Faculty Positions

The Department of Pathology and Laboratory Medicine at Tulane University School of Medicine invites applications from outstanding scientists who are qualified for tenure-track or tenured faculty positions at the level of Assistant, Associate or Full Professor. Candidates should have Ph.D, M.D. or M.D./Ph.D. and will be expected to develop and maintain rigorous externally funded research programs in cancer biology, broadly defined, to complement the basic and translational research. Applicants should have substantial peer-reviewed publications that demonstrate research productivity and the ability to perform cutting edge research. Candidates for Assistant Professor should have adequate postdoctoral research experience and show good promise in developing independent research programs. Applicants for Associate or Full Professor should have substantial research productivity and history of grant support and academic service.

Salary: commensurate with the candidates' experience and qualifications. Competitive startup fund: provided. Starting date: negotiable. If interested: submit a current CV, research plan, and names of 3-5 potential referees via email (**jfrois@tulane.edu**) or regular mail to: **Tong Wu, M.D., Ph.D., Professor and Chairman, Dept. of Pathology and Laboratory Medicine, Tulane University School of Medicine, 1430 Tulane Ave., SL-79, New Orleans, LA 70112**.

Tulane University School of Medicine is an Affirmative Action/Equal Opportunity Employer.

FACULTY POSITIONS AT THE ROCKEFELLER UNIVERSITY

The Rockefeller University seeks exceptional, interactive, and creative scientists to join its faculty. We invite applications from outstanding candidates for tenure-track positions and also encourage tenured scientists to apply, provided that they are at an early stage of their career.

The Rockefeller University provides strong financial support for the research work of its faculty. The positions offer highly competitive salary, benefits and start-up funds, new or recently renovated laboratory space, access to numerous state-of-the-art core facilities and extensive opportunities for collaboration both within the University and with neighboring institutions. The University also provides very strong continuing support for research work beyond start-up, including full support for graduate students.

The University has a laboratory-based organization structure that fosters interdisciplinary research in the following areas:

- **Chemical & Structural Biology**
- **Immunology, Virology & Microbiology**
- **Medical Sciences & Human Genetics**
- **Molecular, Cell & Developmental Biology**
- **Neurosciences & Behavior**
- **Organismal Biology, Evolution & Ecology**
- **Physical & Mathematical Biology**

Details about specific subjects of research can be found at:
http://www.rockefeller.edu/facultysearch.

Applications are being accepted electronically through our **Online Application System** at **http://oas.rockefeller.edu.** Applicants should follow the online application procedure.

The deadline for receipt of applications is May 14, 2010.

If you have questions regarding submitting an application, please contact our Administrator at **facultysearch@rockefeller.edu.**

The Rockefeller University is an Affirmative Action/Equal Opportunity/VEVRAA Employer and solicits applications from women and under-represented minorities.

TEXAS TECH UNIVERSITY
Edward E. Whitacre Jr. College of Engineering

The Maddox Chairs *in Energy* at Texas Tech University

The Edward E. Whitacre Jr. College of Engineering at Texas Tech University is committed to leveraging these **two exceptionally large endowed chairs at over $7 million each**, to become one of the nation's leaders in finding solutions to the world's energy challenges. The college is seeking world-class researchers in solar and sustainable energy as candidates for the Maddox Chairs.

Donovan Maddox Distinguished Engineering Chair *in Solar Energy*

Candidates are expected to have national and international reputation in solar energy based on research publications. In addition, a record of acquiring external resources to support research, team building, and mentoring of associates and graduate and undergraduate students is necessary. The holder of the Donovan Maddox Chair will be expected to not only bring his or her own research activities to the Whitacre College of Engineering, but also to build a collaborative community of scholars at Texas Tech dedicated to solar energy research, thereby building a world-class research program. The appointment will be as a full professor in the Whitacre College of Engineering.

Jack Maddox Distinguished Engineering Chair *in Sustainable Energy*

Candidates with exceptional and diverse backgrounds in energy sciences and engineering are sought for this endowed position. The successful candidate will demonstrate a national and international reputation for contributions to the solution or advancement of the state of the art on a variety of research issues in the sustainable energy fields including energy efficiency, biofuels, wind power, tidal power, geothermal, and energy storage. The successful candidate, along with the Donavan Maddox Chair in Solar Energy, will set the tone, vision, and the path in order to build a nationally and internationally recognized program at Texas Tech University in sustainable energy research. The appointment will be as a full professor in the Whitacre College of Engineering.

Screening will begin upon the receipt of applications and will continue until the position is filled. Candidates names will not be made public until the final stages of the search. Curriculum vitae and the names and contact information of at least four references should be submitted at www.coe.ttu.edu/maddox. To nominate a colleague for these chairs, visit www.coe.ttu.edu/maddox. Nominations can be made anonymously.

Questions about the Jack Maddox or Donovan Maddox Chairs should be directed to:
Jack Maddox and Donovan Maddox Search Committees
Texas Tech University | Whitacre College of Engineering
Box 43103 | Lubbock, Texas 79409-3013 | engineeringdean.coe@ttu.edu | 1.800.528.5583

Texas Tech University | Whitacre College of Engineering
1.800.528.5583 | www.coe.ttu.edu/maddox

An Affirmative Action/Equal Opportunity/Americans with Disabilities Employer

Department of Health and Human Services
National Institutes of Health

Director, National Institutes of Health Induced Pluripotent Stem Cell Center

The NIH invites applications from outstanding candidates to establish and direct an Induced Pluripotent Stem Cell (iPSC) Center in its Intramural Research Program. This new Center will be administered by the National Institute of Arthritis and Musculoskeletal and Skin Diseases. The successful candidate will hold a doctoral degree in a relevant field and be a recognized leader in the field of stem cell biology. S/he must have a strong track record in generating iPSCs and investigating their biology and potential therapeutic uses.

The Director will lead the newly established iPSC Center, the mission of which is to bring this exciting new technology to clinical reality within the NIH Intramural Research Program and the NIH Clinical Center. The Director will be expected to create a world-class research group that will catalyze new approaches and uses of iPSCs and differentiated cells derived from them, and/or cells trans-differentiated from somatic cells for the entire biomedical research community. The Center will collaborate with researchers to apply iPSC technologies to support their research endeavors, with a focus on the generation of clinical applications for iPSCs and/or trans-differentiated cells, and derivation of new disease-specific cell lines. The iPSC Center will promote the use of this technology and provide researchers with training to facilitate clinical development of iPSCs. The ideal candidate will be highly interactive and collaborative, and will actively engage members of the NIH intramural and the extramural research communities to identify and develop projects that have the prospect of moving to clinical trials within the NIH Clinical Center. The Director will have the opportunity to partner with the NIH Chemical Genomics Center to utilize small molecules and siRNA technologies to optimize the generation and differentiation of iPS cells. The Director will also be provided resources to direct an intramural laboratory to develop a vibrant research program in the area of stem cell biology and its clinical applications.

Salary will be commensurate with experience. A full package of benefits, including retirement, health, life, long-term care insurance, and a Thrift Savings Plan, is available.

Review of applications will begin on or about June 1, 2010, with applications being accepted until the position is filled.

Interested individuals should send a CV, a vision statement for directing the NIH iPSC Center, a statement of research interests and goals, and the names of up to five references to: Ms. Wanda White at wanda.white@nih.gov or mailed to the address below by May 31, 2010:

Bldg 31, Room 4C-12
31 Center Drive, MSC 2350
NIAMS - NIH
Bethesda, Maryland 20892-2350

DHHS and NIH are Equal Opportunity Employers.

THE UNIVERSITY OF HONG KONG
香 港 大 學

Founded in 1911, The University of Hong Kong is committed to the highest international standards of excellence in teaching and research, and has been at the international forefront of academic scholarship for many years. Ranked 24th among the top 200 universities in the world by the UK's *Times Higher Education*, the University has a comprehensive range of study programmes and research disciplines spread across 10 faculties and about 100 sub-divisions of studies and learning. There are over 23,400 undergraduate and postgraduate students coming from 50 countries, and more than 1,200 members of academic and academic-related staff, many of whom are internationally renowned.

Non-Clinical Professor in the Department of Pharmacology and Pharmacy (Ref.: 20100157)

Applications are invited for appointment as Non-Clinical Professor in the Department of Pharmacology and Pharmacy, from as soon as possible thereafter, on a three-year fixed-term basis.

Applicants should possess a Ph.D. in Pharmaceutical Sciences, a Pharm.D. or an equivalent qualification: and have teaching experience in pharmacy at both undergraduate and postgraduate levels. They should have working experience in a tertiary institution in a leadership capacity, and should possess a track record in pharmacy research. Candidates with working experience in pharmacy practice and/or pharmacy programme development, assessment and evaluation, would have an advantage. The appointee will contribute to teaching and curriculum development of the pharmacy programme, as well as other research and scholarly activities of the Department. Administrative responsibilities are part of the portfolio, and he/she is expected to take on a leadership role in the Department, including supervision of junior academic staff and research programme development. He/She will develop, lead innovations and contribute to leadership and strategic direction setting in pharmacy, fostering excellence in teaching and learning, research and professional engagement in pharmacy. The appointee should exhibit effective verbal and written communication, well-developed interpersonal skills, dedication to education, and a commitment to establish himself/herself in academic pharmacy. Information about the Department can be obtained at http://www3.hku.hk/pharma/current/.

Annual salary for Non-Clinical Professorship will be in the range of HK$848,820 – 1,188,900 (approximately US$1 = HK$ 7.8) (subject to review from time to time at the entire discretion of the University). The appointment will attract a contract-end gratuity and University contribution to a retirement benefits scheme, totalling up to 15% of basic salary, as well as leave, and medical/dental benefits. Housing benefits will also be provided as applicable. At current rates, salaries tax does not exceed 15% of gross income.

Applicants should submit a completed application form, a full C.V., at least 3 reference letters with specific comments on the academic competence of the applicants, together with an indication of research orientation. **Further particulars and application forms** (152/708) can be obtained at http://www.hku.hk/apptunit/; or from the Appointments Unit (Senior), Human Resource Section, Registry, The University of Hong Kong, Hong Kong (**fax:** (852) 2540 6735 or 2559 2058; **e-mail:** senrappt@hku.hk). **Review of applications will continue until the post is filled.** Candidates who are not contacted within 4 months of the date of application may consider their applications unsuccessful.

The University is an equal opportunity employer and is committed to a No-Smoking Policy

EMORY UNIVERSITY
SCHOOL OF MEDICINE

Endowed Chair Professorship in Cancer Nanotechnology

Supported by the Brock Family, the Georgia Research Alliance and the Georgia Cancer Coalition

Emory University School of Medicine seeks an MD, PhD, or MD/PhD scientist with national and international stature in the emerging discipline of Nanomedicine. Candidates should have a track record of well-funded research, broadly cited publications, and a collaborative/entrepreneurial spirit. The candidate's research interests should complement or reinforce existing strengths of the NIH-designated Emory-Georgia Tech Center for Cancer Nanotechnology Excellence and the Winship Cancer Institute. The Winship Cancer Institute at Emory is a National Cancer Institute designated Cancer Center.

Potential research areas include, but are not limited to, cancer molecular imaging probe development, novel nanocarriers and in vivo delivery methods for targeted therapy of cancer, and new cancer detection and treatment strategies. The chosen candidate will receive a competitive startup package and an endowed chair professorship with his/her primary appointment in an appropriate Department.

Applications with a curriculum vitae and names and contact information for three references should be sent to: **Lisa Simmons, Administrator, The Wallace H. Coulter Department of Biomedical Engineering, Emory University School of Medicine, 101 Woodruff Circle, Suite 2001, Atlanta, GA 30322 (Phone: 404-727-9875; e-mail: lsimmon@emory.edu)**. Please reference position number **15562BR**.

Emory University is An Equal Opportunity/Affirmative Action Employer.

Chief, Division of Endocrinology, Diabetes and Metabolism

The Department of Medicine at the University of Wisconsin School of Medicine and Public Health invites applications/nominations for the position of Chief of the Division of Endocrinology, Diabetes and Metabolism to direct and expand its research, educational and clinical activities.

The new Chief of Endocrinology will be an acknowledged academic scientist with demonstrated excellence as a clinician, educator and administrator with Endocrinology fellowship training. Candidates must demonstrate a record of scholarly achievements qualifying him/her for a tenured appointment at the University of Wisconsin.

To learn more about the UW Madison, please visit:
http://www.wisc.edu/employment/madison.php

Please apply with a CV to: **sa@medicine.wisc.edu**

Sanjay Asthana, MD, Head of Search Committee
Department of Medicine, School of Medicine and Public Health
2870 University Avenue Suite #106
Madison, WI 53705

The UW Madison is an AA/EEO employer; Caregiver and open records laws apply. A background check will be conducted prior to employment.

UNIVERSITY OF WISCONSIN-MADISON
SCHOOL OF MEDICINE AND PUBLIC HEALTH

THE UNIVERSITY *of* TEXAS
MEDICAL SCHOOL AT HOUSTON
A part of The University of Texas Health Science Center at Houston

PROFESSOR AND CHAIR OF MICROBIOLOGY AND MOLECULAR GENETICS

The University of Texas Medical School at Houston is seeking applications and nominations for the position of Professor and Chair of the Department of Microbiology and Molecular Genetics. The successful candidate will be an internationally recognized, outstanding scientist with demonstrated success in research, teaching, graduate training and service to the academic community. The Department of Microbiology and Molecular Genetics (**http://mmg.uth.tmc.edu**) is one of 24 Departments and 23 Centers in the Medical School, which has $120 million in research expenditures. The Department has major research programs in prokaryotic and eukaryotic microbial molecular biology, genetics, pathogenesis, cell signaling and cellular interactions. The new Chair will be provided with resources to recruit additional faculty in order to grow the department, and implement his/her vision for the future of Microbiology within The University of Texas Health Science Center at Houston. The Medical School is located within the Texas Medical Center, which includes the UT Health Science Center at Houston, Baylor College of Medicine and UT M. D. Anderson Cancer Center.

Applications should include a letter of interest, a *Curriculum vitae*, a bibliography and the names of at least three references and should be sent by email to: **ms.ibp.applicants@uth.tmc.edu** or addressed to **Dr. John F. Hancock, Chair of the MMG Search Committee, University of Texas Medical School at Houston, P.O. Box 20708, Houston, TX 77225**.

The University of Texas is an Equal Opportunity Employer and encourages applications from women and minorities.

MSSM

MOUNT SINAI SCHOOL OF MEDICINE

Tenure track faculty positions in Immunology

The Mount Sinai Immunology Institute is seeking outstanding scientists to develop rigorous independent research programs in basic or translational immunology. Applicants whose programs address inflammatory bowel disease, mucosal immunity, bacterial-epithelial interactions, and intravital imaging are encouraged to apply. The Immunology Institute is a diverse, interactive group interested in basic and translational immunology and mechanisms of immune-mediated diseases, **www.iisinai.org**. Applicants may have MD, PhD or MD/PhD degrees and may be appointed at the Assistant, Associate or Full Professor levels, at Mount Sinai School of Medicine with a generous start-up package.

Applicants should submit a CV, research plan and the names of three references to Immunology Institute Faculty Search Committee, email: **Zaida.Newman@mssm.edu**. Review of applications will begin **April 30, 2010**.

New Faculty Position - Neuroscience Berlin

The Charité – Universitätsmedizin Berlin/Medical School of the Freie Universität Berlin and the Humboldt-Universität zu Berlin invites applications for a new faculty position (W3 full professor). This is part of an ambitious recruitment effort aiming to expand and diversify the Berlin interdisciplinary neuroscience community within the Cluster of Excellence 'NeuroCure'.

Of particular interest are neuroscientists with broad expertise in neuroanatomy and cell biology. Researchers with a specific interest in mechanisms of neuronal damage, endogenous neuroprotection, regeneration, interaction of the nervous system with the immune system, as well as neurodevelopmental/developmental disorders and mechanisms of neuronal plasticity will allow us to further complement our interdisciplinary network.

Demonstrated excellence in research, rather than specific research area, is the focus for evaluation of applications; hence, the primary criteria for appointment will be outstanding records of innovative research and academic performance, including landmark papers in leading journals, and the potential for establishing a rigorous and innovative independent research program with fruitful collaborations and inspiring mentorship.

The successful candidate will be involved in basic research training for medical students, and in mentoring graduate students with a strong interest in basic science and translational research. In addition, we maintain a highly regarded MD/PhD program. Further, state-of-the-art genomics, proteomics, and neuroimaging facilities, as well as extensive dedicated animal housing are available to all members of the neuroscience community. The successful applicant will be expected to develop and maintain an externally funded research program and to teach at the undergraduate and graduate levels. Preference will be given to individuals whose interests are synergistic with ongoing research programs in the Cluster.

The Charité is an equal opportunity employer, committed to the advancement of individuals without regard to ethnicity, religion, sex, age, disability or any other protected status.

Please send a curriculum vitae and a description of achievements and research interests (see: http://www.charite.de/en/charite/organization/careers/employment_market/internship/) to:

Dean Prof. Dr. Grüters-Kieslich
Charité – Universitätsmedizin Berlin
Charitéplatz 1, 10117 Berlin, Germany
e-mail: neurocure@charite.de

The search will continue until the position is filled. To ensure full consideration, applications should be received by 25.04.2010. The electronic submission of your documents is encouraged. For additional information on research programs and facilities, see www.neurocure.de.

The successful candidate will join an interactive group of investigators in state-of-the-art research facilities at the Charité Campus Berlin Mitte.

www.neurocure.de

Science Careers is the window that displays your vision.

Visit our ENHANCED WEBSITE!

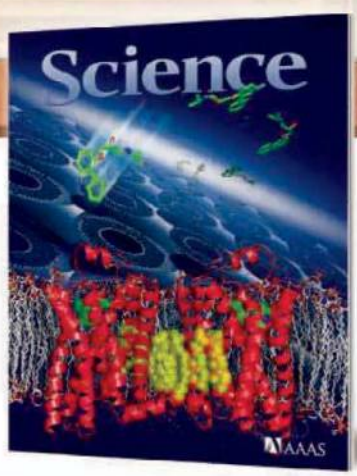

Revealing your vision to employers is our job. We're your source for connecting with top employers in industry, academia, and government. We're the experts and entry point to the latest and most relevant career information across the globe.

Our newly designed website offers a set of tools that reveal career opportunities and your personal potential. Whether you're seeking a new job, career advancement in your chosen field, or ways to stay current on industry trends, *Science* Careers is your window to a limitless future.

Your Future Awaits.

Improved Website Features:

- » Relevant Job E-mail Alerts
- » Improved Resume Uploading
- » Content Specific Multimedia Section
- » Facebook Profile

Job Search Functionality:

- » Save and Sort Jobs
- » Track Your Activity
- » Search by Geography
- » Enhanced Job Sorting

Science Careers

From the journal *Science* AAAS

ScienceCareers.org

10 Ways to Improve Your Chances of Securing Research Funding

RESEARCH APPLICATIONS NETWORKING

HOPING WISHING TANTRUM

RABBIT'S FOOT SLOTS SELF-FINANCING

JOINING

There are many approaches to securing funding, but not all are effective. That's why the American Association for the Advancement of Science is committed to offering its members a variety of resources to help them locate the money they need—including an ongoing analysis of R&D budgets and funding, and an extensive directory of funding opportunities. Join us. Together we can make a difference. **aaas.org/plusyou**

AAAS + U = Δ

ESH
EUROPEAN SCHOOL OF HAEMATOLOGY

8th International Conference on

MECHANISMS OF CELL DEATH AND DISEASE: ADVANCES IN THERAPEUTIC INTERVENTION AND DRUG DEVELOPMENT

Chairs: T.J. McDonnell, J.A. Hickman, K-M. Debatin

Hotel Quinta da Marinha, Cascais, Portugal / 14-18 October , 2010

Deadline for abstracts and scholarships: September 6, 2010

Invited Speakers

D. Altieri (Worcester), M. Bolognesi (Milano), G. Cohen (Leicester), F. Colland (Paris), K.M. Debatin (Ulm), C. Dive (Manchester), V. Dixit (San Francisco), S. Fawell (Cambridge, USA), W. Fraser Symmans (Houston), H. Fricke (Frankfurt), S. Fulda (Ulm), J. Gillard (Montreal), J.A. Hickman (Croissy sur Seine), P. Holland (San Francisco), D. Huang (Melbourne), R. Humphreys (Rockville), R. Khosravi-Far (Boston), D. Komander (Cambridge), P. Krammer (Heidelberg), S. Lowe (Cold Spring Harbor), T.J. McDonnell (Houston), P. Meier (London), K. Pfizenmeier (Stuttgart), M. Shi (Hannover), J. Silke (Victoria), D. Vucic (San Francisco), H. Walczak (London), D. Wallach (Rehovot), I. Wistuba (Houston), L. Zawel (Cambridge)

The conference seeks to address translational aspects of current fundamental science in the field of genetically controlled cell death. In 2010, the main focus is on the Death Receptor Family, some 20 years after their discovery, and on the IAP family of proteins. There will be presentations on both the fundamental aspects of death receptor signalling and IAP function, from opinion leaders in the field, and the clinical utilisation of this knowledge. Following from this, the rapidly emerging field of the control of cell death by ubiquitination / de-ubiquitination will be addressed. A round table discussion on the use of clinical biomarkers to measure apoptotic cell death will provide a lively translational forum. Keynote presentations from Vishva Dixit and Scott Lowe open and close this exciting program of fundamental science in the field of cell death and its clinical translation.

Main topics:

- Death receptor
- IAP inhibitors
- Biomarkers and round table discussion
- Updates and new targets

For further information
WWW.ESH.ORG or contact ghyslaine.lebougault@univ-paris-diderot.fr

hgm 2010

14th HUMAN GENOME MEETING

NEXT GENERATION GENOMICS AND MEDICINE

18–21 MAY 2010 | LE CORUM, MONTPELLIER FRANCE

register at www.hgm2010.org

CONFERENCE SYNOPSIS

Next generation sequencing and genotyping coupled with computational advances have allowed the comprehensive and precise investigation of complex biological systems. Such advances have provided new insights in biology and new understandings of human disease. The complex and massive datasets require new systems approaches to data analysis and open up the possibility of synthetic reconstructions of biological systems.

The HGM 2010 will explore the interface between these next generation technologies and human biology and pathophysiology. The focus will be on the integration of biology, computational sciences, and genomic technologies towards resolving complex biological and medical questions. We will discuss the necessary processes such as biobanking that will enable this integration. The impact of this science on ethics and society and on the aspirations of emerging countries will also be explored.

CONFIRMED SPEAKERS (BY ALPHABETICAL ORDER)

- Anne C Ferguson-Smith (UK)
- C. Augustine Kong (USA)
- Christina D. Smolke (USA)
- Bartha-Maria Knoppers (Canada)
- Ben van Ommen (Netherlands)
- David B. Goldstein (USA)
- David Cox (USA)
- Doug Lauffenburger (USA)
- Edison T Liu (President HUGO) (Singapore)
- Edward Rubin (USA)
- Emmanouil Dermitzakis (Switzerland)
- Eran Segal (Israel)
- Felix Li Jin (China)
- Frank Johannes (Netherlands)
- Gil Ast (Israel)
- Gil McVean (UK)
- Hans A. Lewin (USA)
- Henry Yang Huanming (China)
- Hiroki R. Ueda (Japan)
- Hiroki Kitano (Japan)
- Jay D. Keasling (USA)
- Jean-Christophe Glaszmann (France)
- Jennifer Harris (Norway)
- John Mattick (Australia)
- Lance Miller (Singapore)
- Luis Serrano (Spain)
- Mark McCarthy (UK)
- Martin Vingron (Germany)
- Michael Synder (USA)
- Peer Bork (Germany)
- Robert Feil (France)
- Ruan Yijun (Singapore)
- Stanislav Dusko Ehrlich (France)
- Stephen Baylin (USA)
- Stephen W. Scherer (Canada)
- Susan E. Ozanne (UK)
- Yoshihide Hayashizaki (Japan)

PROGRAMME AT A GLANCE

Plenaries
- Human Genome Variation in Evolution and Disease
- Epigenetics in Development and Human Disease
- An Expanding RNA World
- Synthetic and Systems Genomics

Symposia
- Quantitative Genomics (GWAS, QTL, Expression cosettes)
- Pathways, Networks and Systems Biology
- Nutrigenetics and Nutrigenomics
- Next Generation Sequencing – 1000 Genome Project and Beyond
- Microbial Genomics and Meta Genomics
- Biobanking

ABOUT MONTPELLIER

Montpellier is a beautiful city in southern France, very close to the Mediterranean Sea. It is a city in which medicine has been a vocation since the 11th Century, with the oldest, existing medical faculty in the west. The fine reputation of its Law and Arts Faculties, together with the venerable Faculty of Medicine, makes it one of France's foremost university cities.

Find out more about Montpellier at www.ot-montpellier.fr/en

HUGO – OECD Symposium on Genomics & Bioeconomy
17 May 2010, Le Corum - Montpellier France
visit www.bioeconomy2010.org to find out more

Organisers: HUGO Inserm Supported by:

Genomics Automation Congress

6 - 7 May, Boston, MA, USA

The conference will be co-located with the RNAi & miRNA World Congress and Epigenetics World Congress. Registered delegates will have access to all three meetings ensuring a very cost-effective trip.

Distinguished Faculty to include:
Francois Vigneault, Ragon Institute Fellow, Harvard Medical School
Chad Creighton, Assistant Professor, Division of Biostatistics Dan L. Duncan Cancer Center
Greg Caporaso Colorado University
Steven Jones, Genome Sciences Centre, British Columbia Cancer Research Centre
Corey Nislow, Assistant Professor, Department of Molecular Genetics University of Toronto
Micheal Metzker, Associate Professor, Human Genome Sequencing Center Baylor College of Medicine

For sponsorship and exhibition opportunities contact Aaron Woodley
tel: +44 (0) 1787 315129
email: a.woodley@selectbiosciences.com

Agenda Topics :

- Sample Preparation and Storage
- Liquid Handling and Sample Management
- Next Generation Sequencing
- Data Handling and Analysis
- 3rd Generation Sequencing Technologies

GENOMICSAUTOMATION.COM

SELECT BIOSCIENCES
Delivering Difference

Genomics Automation Europe
14-15 September 2010

POSITIONS OPEN

FACULTY POSITIONS IN TRANSLATIONAL NEUROSCIENCE

The Sanders-Brown Center on Aging at the University of Kentucky invites applications for two tenure-track faculty positions at the **ASSISTANT** or **ASSOCIATE PROFESSOR** level in the area of translational neuroscience. Basic or clinical research programs that focus on early mechanisms underlying neurodegenerative disorders, identification of novel drug targets, or development of mammalian preclinical animal models of central nervous system disorders are of special interest. A Ph.D., M.D., or M.D.-Ph.D. degree with relevant postdoctoral experience is required. To apply, electronically submit a single PDF file that includes a complete curriculum vitae, a brief statement describing your area of expertise and career goals, research plans, and contact information of at least three references to **e-mail: rs_sbcoafacsrch@email.uky.edu**. Evaluation of applicants begins in May 2010.

The University of Kentucky is an Equal Opportunity Employer and encourages applications from minorities and women.

BioArray Solutions in Warren, New Jersey, is looking to fill a **SENIOR RESEARCH SCIENTIST** position. We are seeking a **POLYMER CHEMIST/CHEMICAL ENGINEER** self-starter with at least two to five years of postdoctoral experience. The position requires demonstrated expertise in laboratory-scale polymer-microparticle synthesis using emulsion/dispersion/suspension polymerization and their characterization along with solid working knowledge of colloid/surface chemistry. Please apply via **website: http://www.immucor.com**. *BioArray Solutions is an Equal Opportunity Employer.*

POSITIONS OPEN

PROGRAM ASSOCIATE POSITION, DEEP CARBON OBSERVATORY
Carnegie Institution of Washington

The Deep Carbon Observatory (DCO) is an international, multidisciplinary, decade-long effort dedicated to achieving a transformational understanding of carbon's chemical and biological roles in Earth's interior. The research of the DCO is organized around three Science Directorates: Deep Carbon Reservoirs and Fluxes, Deep Life, and Energy, Environment and Climate. The DCO Secretariat, located at the Carnegie Institution of Washington's Geophysical Laboratory, plays a central role in coordinating the efforts of an international community to identify scientific needs and opportunities in deep carbon science. The Secretariat is engaged in fund raising from industrial, governmental, and foundation sources; outreach to the scientific community through the sponsorship and organization of workshops, international meetings, and conferences; and public education and outreach related to deep carbon science. The Secretariat is supported with a grant from the Alfred P. Sloan Foundation.

The DCO Program Associate, a full-time position, will provide both scientific and administrative assistance with the organization of workshops, calls for proposals, fellowship applications, and engagement in fund raising from industrial, governmental, and foundation sources. The Program Associate will report to the Program Director who is responsible for the day-to-day operations of the Secretariat. The ideal candidate would have experience as a postdoctoral scientist, although candidates with a Ph.D. or Master's degree in the geosciences, physical sciences, materials sciences, or biological sciences with significant experience would also be considered. In addition to interactions with researchers from around the world, duties will include writing and editing materials for the website, meeting minutes, DCO reports and proposals, and beginning to develop education and outreach components for the DCO. Excellent interpersonal skills, writing, and organizational skills are essential. The position will require periodic travel. Salary level is competitive and will be based on the qualifications of the candidate.

Completed applications (including resume and contact information for two references) should be submitted electronically to **Lauren Cryan, e-mail: lcryan@ciw.edu** indicating "Program Associate for Deep Carbon Observatory" in the subject line.

Equal Opportunity Employer.

Denison University, a selective liberal arts college, invites applications for two-year position for an **ORGANISMAL BIOLOGIST** to begin August 2010. Teaching load for this position is two courses with laboratories each semester; all courses have enrollments of 24 or fewer. Teaching responsibilities include a sophomore-level course in ecology and evolution, upper-level majors courses (including a biological diversity course focusing on the study of a major taxonomic group; preference will be given to candidates who can also teach animal behavior), and a nonmajors course in the candidate's area of interest (visit **website: http://www.denison.edu/biology/** for a detailed description of the department, its curriculum, and this position). Demonstrated ability in undergraduate teaching is expected and a Ph.D. is preferred (all but dissertation acceptable). Please submit electronic application materials (a cover letter clearly indicating advanced course preferences, curriculum vitae, statement of teaching philosophy, undergraduate and graduate transcripts, and three letters of recommendation) online at **website: https://employment.denison.edu**. Review of applications will begin immediately and continue until position is filled.

In a continuing effort to diversify our campus community, we actively encourage applications from people of color, women, veterans, people of diverse sexual identities/orientations, and others who may contribute positively to the diversification of ideas and perspectives. For additional information and resources about diversity at Denison, please see our Diversity Guide at ***website: http://www.denison.edu/offices/humanresources****. Denison University is an Affirmative Action/Equal Opportunity Employer.*

POSITIONS OPEN

USGS science for a changing world

RESEARCH FISHERY BIOLOGIST/ASSISTANT UNIT LEADER, United States Geological Survey–Cooperative Fish and Wildlife Research Unit, Corvallis, Oregon. See **website: http://www.usajobs.gov. Announcement #WR-2010-0260.**

ASSISTANT PROFESSOR OF VIROLOGY
Department of Molecular Genetics and Microbiology
University of Florida College of Medicine

The Department of Molecular Genetics and Microbiology in the College of Medicine is seeking to expand its basic research faculty in the area of virology. The Department is internationally recognized for its strength in virology and boasts nine faculty members whose primary research is in virology from among a faculty of 23. The successful candidate will build upon these existing strengths in virology and have opportunities for strong, multidisciplinary collaborations with other virologists in the Genetics Institute, cancer center, and the newly established Emerging Pathogens Institute. Those with research interests in the areas of molecular virology, viral pathogenesis, or viral immunology are encouraged to apply. BSL-3 and ABSL-3 facilities and a wide range of excellent biotechnology core facilities are currently available within the Health Sciences Center.

The successful candidate will have a Ph.D., M.D., or M.D.-Ph.D. degree and at least three years of postdoctoral experience. This is a full-time, 12-month, tenure-track faculty appointment at the rank of Assistant Professor and includes a competitive startup package and salary and excellent laboratory space. The salary and startup funds are negotiable and will be commensurate with experience and needs.

Applicants should provide a letter of application, curriculum vitae, and the names of three references to: **David C. Bloom, Ph.D., Chair of the Search Committee, University of Florida, P.O. Box 100266, Gainesville, FL 32610-0266. Or by e-mail: virologistsearch@mgm.ufl.edu**. Applicants should also apply online at **website: https://jobs.ufl.edu,** referencing **requisition number 0804466.** The review of applicants will begin on May 1, 2010, and will continue until the position is filled.

The University of Florida is an Equal Opportunity Institution dedicated to building a broadly diverse and inclusive faculty and staff. Minorities, women, and those from other underrepresented groups are encouraged to apply.

MARKETPLACE

INTERNATIONAL SCIENCE & ENGINEERING
VISUALIZATION CHALLENGE

CALL FOR ENTRIES

ENTRY DEADLINE: SEPTEMBER 15, 2010

SCIENCE AND ENGINEERING'S MOST POWERFUL STATEMENTS
ARE NOT MADE FROM WORDS ALONE

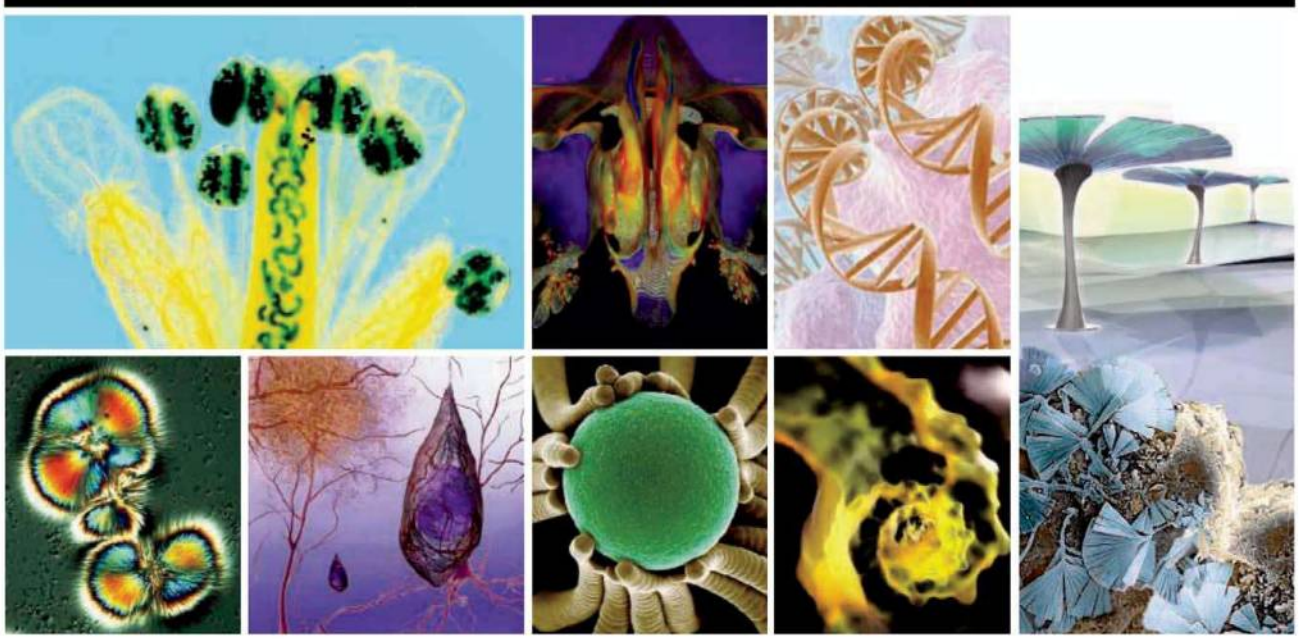

Visualization in all its forms has the power to illuminate and educate. It explains and makes clear all aspects of the world around us. It feeds insight and provokes curiosity.

The National Science Foundation (NSF) and the journal *Science*, published by the American Association for the Advancement of Science, invite you to participate in this year's Challenge. The competition recognizes scientists, engineers, visualization specialists, and artists who produce innovative work in visual communication.

Winning entries will be published in *Science* and *Science* Online, and will be displayed on the NSF web site.

Award Categories

- Photography
- Illustrations
- Informational Posters and Graphics
- Interactive Games
- Non-Interactive Media

COMPLETE ENTRY INFORMATION:
WWW.NSF.GOV/NEWS/SCIVIS

NSF

Science
AAAS

R&D Systems MultiAnalyte Profiling Kits for Cancer Research

Cancer is a disease of context-dependent cellular dysfunction that can involve a range of biological activities. Because of its complexity, quality research tools designed to simultaneously study multiple cancer-related factors are crucial for rapidly advancing our understanding of cellular transformation. R&D Systems Proteome Profiler™ Antibody Arrays allow for the concurrent detection of multiple intracellular or secreted proteins without the need for individual Western blot experiments or specialized laboratory equipment.

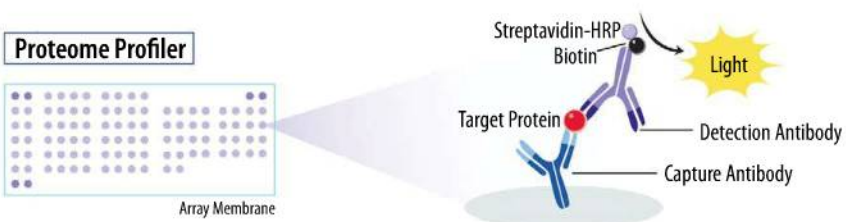

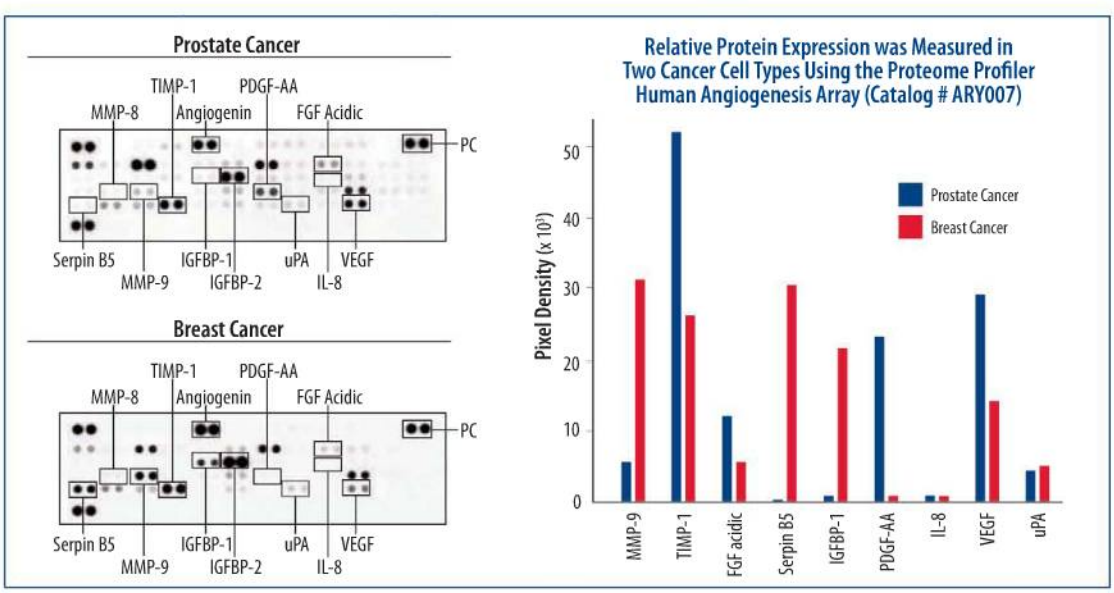

For more information visit our website at **www.RnDSystems.com/go/ProteomeProfiler**

For research use only. Not for use in diagnostic procedures.

R&D Systems, Inc. www.RnDSystems.com

R&D Systems Europe, Ltd. www.RnDSystems.co.uk

R&D Systems China Co., Ltd. www.RnDSystemsChina.com.cn

R&D SYSTEMS®